

**CRANFIELD UNIVERSITY**

**AZFAR ALI SYED**

**SURFACE ENHANCED RAMAN SPECTROSCOPY  
FOR ULTRA-SENSITIVE DETECTION OF ENERGETIC MATERIALS**

**DEFENCE COLLEGE OF MANAGEMENT AND TECHNOLOGY**

**PhD THESIS**

**CRANFIELD UNIVERSITY**

DEFENCE COLLEGE OF MANAGEMENT AND TECHNOLOGY

DEPARTMENT OF MATERIALS AND APPLIED SCIENCE

PhD THESIS

Academic Year 2004-2007

Azfar Ali Syed

Surface Enhanced Raman Spectroscopy  
for Ultra-Sensitive Detection of Energetic Materials

Supervisors: Dr SR Ahmad & Dr J Bellerby

June 2007

© Cranfield University 2007. All rights reserved. No part of this publication may be reproduced without the written permission of the copyright owner.

## ABSTRACT

The prospect of ultra-sensitive detection of molecular species, particularly those of energetic materials, has prompted the present research initiative. The combination of metal surface nano-technology and Raman spectroscopy has given rise to 'Surface Enhanced Raman Spectroscopy' (SERS). This is a very sensitive technique and has proved to be capable of detecting a single molecule.

SERS was demonstrated by recording Raman spectra of the sample molecules adsorbed on various specially prepared SER-active surfaces both in the form of a colloidal suspension and on the solid roughened surfaces. Using a gold colloidal suspension, pyridine has been detected down to  $10^{-11}$  molar (M) concentration. A silver slab was roughened to a dimension of a nano-scale by etching in nitric acid solution to make SER-active surface. Pentaerythritol Tetranitrate (PETN) explosive was detected using this surface after its  $10^{-2}$  M solution was dropped, dried and washed (of any residue) from the surface. Lithographically engineered silver structures in the form of nano-arrays having a number of silver structures of approximately  $10^6$  in a region of  $0.1 \text{ mm}^2$  have been used for SERS. The major noise contribution to the scattering from impurities in an ordinary glass substrate has been eliminated by replacing glasses as substrates with pure quartz discs. The headspace vapours from peroxide explosives, Triacetone Triperoxide (TATP) and Hexamethylene Triperoxide Diamine (HMTD), were detected at approximately 70 parts per million (ppm) and 0.3 ppm concentrations respectively using a portable commercial Raman Spectrometer. PETN was also detected from its headspace vapour at about 18 parts per trillion (ppt) in spite of it having a much lower vapour pressure.

The possibility of desorption of adsorbed molecules from a nano-structured surface by laser irradiation has been demonstrated experimentally with the aim of reusability of SER-active surfaces. Also demonstrated was the enhancement in Raman intensity through resonance Raman effect spectroscopy for the future use in surface enhanced resonance Raman spectroscopy (SERRS).

## ACKNOWLEDGMENT

ALL THANKS BE TO ALLAH, THE MOST GRACIOUS THE MOST GIVING.

I am truly grateful to Dr R Ahmad not only as a supervisor but also as a mentor. His enthusiasm and devotion to work has made a deep impression on me. This thesis would not have been completed if not for his encouragement and guidance. He has taught me the art of quality research and independent thinking. I am indebted for his continued support even after his retirement. I am deeply thankful to Dr J Bellerby for his help and guidance, firstly as chairman of the thesis committee and then as a supervisor on the retirement of Dr R Ahmad. His advice and guidance during the research as well as during the writing up thesis were extremely helpful. I am equally indebted to Dr M Cartwright for his multi-role involvement in my research right from the time of the formulation of research proposal, as my co-supervisor and finally as chairman of the thesis committee. Apart from his trust in my work and his continuous encouragement all along, his particular help in procurement of a Raman spectrometer made the research possible. I am also grateful to Professor IG Wallace as head of the Department of Materials and Applied Science for providing me with an excellent work environment during the past years and Mrs S Hardy and Mrs P Pye for their cheerful assistance.

I also owe thanks to many others who helped me in my work: Dr X Fang for his help throughout my stay, especially for the time we spent in doing work on resonance Raman spectroscopy; Mr E Billiet for his help and technical support in the operation of the equipment and in designing various experimental setups; Dr A Bellamy for provision of peroxide explosive samples; Dr J Coath from the electro-optics group for letting me use sputtering equipment and for numerous fruitful discussions. His advice to remain focused on the main tasks greatly helped me finish in time; Mr R Hall for helping me with substrate shaping; Dr J Painter and Dr J Rock for helping me in obtaining electron micrographs; DR M Moniruzzaman for showing me how to use the profiler; Mrs J Lovell and Ms M Harris for providing me with the laboratory chemicals and equipment from time to time; I must also thank Dr A Russell who was a constant source of motivation and guidance during the difficult times. I appreciate his sincere and timely advice and for tolerating me as an office mate.

My special thanks to Dr JVG Ramos and Dr SS Cortez from the Institute of Material Structure, Madrid, Spain for inviting me to a three-week training session in some of the latest techniques in SERS and to the European Science Foundation for funding the trip. I am also grateful to Dr N Stone at Biomedical Research Institute, Gloucester for inviting me and letting me use the Renishaw Raman microscope.

I dedicate this thesis to my parents especially to my mother. Their prayers and motivation kept on the course. I am extremely grateful to my wife and children for accompanying me to England away from their family and friends and supporting me throughout. I must thank my colleagues from Pakistan for helping me in administrative and academic capacities.

I am grateful to the HEC and NUST, Pakistan for sponsoring my PhD and for the financial support.



# LIST OF CONTENTS

<b>ABSTRACT</b>	ii
<b>ACKNOWLEDGEMENT</b>	iii
<b>LIST OF CONTENTS</b>	iv
<b>LIST OF FIGURES</b>	viii
<b>LIST OF TABLES</b>	xv
<b>GLOSSARY</b>	xvi
<b>1 INTRODUCTION</b>	1
1.1 Rationale	1
1.2 Backdrop	3
1.3 Recent Breakthroughs in Raman Spectroscopy	6
1.4 Viability of Raman Spectroscopy as Explosive Detection Technique	7
1.5 Goals and Objectives	8
<b>2 REVIEW OF LITERATURE</b>	10
2.1 Overview	10
2.2 Explosive detection with Raman Spectroscopy	12
2.3 Advanced Raman Techniques	16
2.3.1 State of the Art in Resonance Raman Spectroscopy	16
2.3.2 State of the Art in SERS	17
2.4 SER-active surface fabrication techniques	21
2.4.1 SERS with metal colloids	23
2.4.2 SERS with solid SER-active surfaces	28
2.5 Application of SERS	34
2.6 Conclusions	38
<b>3 THEORETICAL CONSIDERATIONS</b>	40
3.1 Raman Scattering and Resonance Raman Spectroscopy	40
3.2 Surface Enhanced Raman Spectroscopy (SERS)	46
3.2.1 Electromagnetic (EM) enhancement	46
3.2.2 Charge transfer (CT) or chemical enhancement	51
3.3 Summary	52
<b>4 SAMPLES AND CHARACTERISCS</b>	53
4.1 Introducrion	53
4.2 Pyridine	55

4.3	Nitrobenzene	56
4.4	Acetone	57
4.5	Pentaerythritol Tetranitrate (PETN)	58
4.6	Triacetone Triperoxide (TATP)	61
4.7	Hexamethylene Triperoxide Diamine (HMTD)	62
<b>5</b>	<b>EXPERIMENTAL - INITIAL WORK</b>	<b>65</b>
5.1	Introduction	65
5.2	Specifications of equipment	65
5.2.1	Modified spectrofluorometer	65
5.2.2	UV-vis-NIR spectrometers	66
5.2.3	Spex 1404 Raman spectrometer - high resolution	66
5.2.4	Renishaw RM2000 Raman microscope	66
5.2.5	Ocean Optics R-3000 Raman system	67
5.2.6	Digital surface profiler	67
5.2.7	Microscopes	67
5.2.8	Scanning electron microscopes	67
5.2.9	Magnetron sputtering equipment	67
5.3	Results and analysis	68
5.3.1	Preliminary Raman Spectroscopy with a non laser source	68
5.3.2	Excitation laser wavelengths dependence	69
5.3.3	Surface enhanced Raman spectroscopy with metal colloids	76
5.3.4	SERS with prepared solid surfaces	82
5.4	Conclusions	98
<b>6</b>	<b>EXPERIMENTAL – SUBSTRATE FABRICATION</b>	<b>99</b>
6.1	General	99
6.2	Instrumentation	100
6.3	Glass-based substrates	100
6.3.1	Materials	101
6.3.2	Surface Fabrication Procedure	101
6.3.3	Nanosphere Lithography	101
6.3.4	Silver Deposition	102
6.3.5	Nanosphere removal	103
6.3.6	Variation 1 - Deposition of Pre-NSL Silver layer	105
6.3.7	Variation 2 – Deposition of Post-NSL Silver layer	105
6.4	Quartz-based substrates	105

6.4.1	Materials	105
6.4.2	Surface Fabrication Procedure	105
6.5	NSL Structure Characterisation	107
6.5.1	Glass Based Substrates	107
6.5.2	Quartz based substrates	121
6.6	Characterisation of SPR of the SER-active surfaces	124
6.7	Summary	128
<b>7</b>	<b>EXPERIMENTAL – SERS RESULTS</b>	<b>130</b>
7.1	Introduction	130
7.2	The limitations of Glass Substrate	131
7.3	SERS results as per the types of SER-active surfaces	135
7.4	Glass-based substrates with pre-NSL silver layer	136
7.5	SERS analysis with Glass-based substrates with thin silver overlayer	142
7.6	SERS analysis with Quartz-based substrates	148
7.6.1	SER spectroscopy of Pyridine	148
7.6.2	SER spectroscopy of Nitrobenzene	152
7.6.3	SER spectroscopy of TATP	154
7.6.4	SER spectroscopy of HMTD	157
7.6.5	SER spectroscopy of PETN	159
7.7	Photo-desorption	163
7.8	Heat desorption	167
7.9	Summary	168
<b>8</b>	<b>CONCLUSIONS AND RECOMMENDATIONS</b>	<b>169</b>
8.1	Conclusions	169
8.2	Recommendations	171
	<b>REFERENCES</b>	<b>173</b>
	<b>APPENDICES</b>	<b>185</b>
A	Summary of Raman spectroscopy of explosive materials	186
B	Summary of reported results on Surface Enhanced Raman Spectroscopy	187
C	SPEX FluroMax, Spectrofluorometer	190
D	Perkin Elmer Lambda 9 UV/vis/NIR Spectrophotometer	191
E	Cintra-5 UV/vis Spectrophotometer	192
F	Custom built high-resolution Raman spectrometer	193
G	Renishaw Raman microspectrometer RM2000	194
H	Ocean Optics Raman Spectrometer R-3000	195

I	MicroXAM 3D Interferometric Surface Profiler	196
J	Scanning electron microscopes	197
K	Magnetron sputtering equipment	199
L	Preparation of gold surfaces for SERS study by laser ablation technique	200
M	Glass and optical fused quartz characteristics	202
N	Geometry of silver nano-structures	204
O	Raman and SER spectra of sample molecules discussed in Chapter 7	208

## LIST OF FIGURES

Figure 1.1	C.V. Raman’s equipment (a) and spectrum of CCl <sub>4</sub> taken in 1923 (b). A modern Raman microscope (c) and Raman spectrum of CCl <sub>4</sub> recorded with it (d).	4
Figure 1.2	Schematic representation of Rayleigh and Raman scattering process.	5
Figure 2.1	Graph showing effect of laser power density on Raman intensity for explosives.	14
Figure 2.2	Relative fluorescence intensity of explosives at 2 different wavelengths.	15
Figure 2.3	Effect of high power pulsed laser on colloids. Silver colloids before (a) and after exposure (b)	25
Figure 2.4	AFM image of silver nano-wires (a) and SER spectra after adding analyte molecules recorded at different wavelengths (b)	26
Figure 2.5	RR spectrum of R6G molecule recorded with 514.5 nm laser wavelength (A) and its SER spectrum shows decrease of fluorescence and increase in S/N (B)	26
Figure 2.6	A calixarene causes aggregation in colloids (bottom) and links to PAH (top) simultaneously	28
Figure 2.7	Fibre optic SER sensor made of silver coated etched optical fibres.	30
Figure 2.8	Etched silver foil for 3 minutes in HNO <sub>3</sub> .	31
Figure 2.9	Partial silver layer on silica coated glass substrate(a). Silica beads coated by silver particles (b).	31
Figure 2.10	Polystyrene micro-sphere assembly on gold substrate (a) and hexagonal silver nano-network achieved after thermal pressing and removal of micro-spheres (b)	32
Figure 2.11	SEM images crystalline assembly of polystyrene spheres of 400 nm diameter (a) and periodic array of silver particles left on the substrate (b).	33
Figure 2.12	AFM image of 51 nm high silver patterns left after removal of polystyrene nanospheres	33
Figure 2.13	Schematics of a single structural array formed from single layer (A) and double layer (B) configurations. AFM image of single layer arrays on mica substrate formed with nanosphere diameter of 542 nm (C), 401 nm (D), 264 nm (E) and 165 nm (F).	34
Figure 2.14	UV-vis spectra showing change in LSPR ( $\lambda_{\max}$ ) region with change in height of the nano-structures formed with 301 nm diameter nanospheres.	35
Figure 3.1	Dipole moment induced in the electronic cloud of the molecule by the laser incident field that results in scatterings.	40
Figure 3.2	Simplified graphical representation of resonance Raman process.	44
Figure 3.3	Schematic diagram of Raman, resonance Raman and SER effect.	48
Figure 3.4	Graphical representation of SER effect on metal sphere.	48
Figure 4.1	Diagram showing the sample presentation setup for the vapour detection. The SER-active surface is fabricated and analyte is put	

	in the vial (a) and surface is put face down on the vial where it is exposed to vapour from the analyte (b). .....	54
Figure 4.2	Raman spectrum of pyridine recorded with a 785 nm excitation wavelength. ....	55
Figure 4.3	Raman spectrum of nitrobenzene recorded with 785 nm laser wavelength. ....	57
Figure 4.4	Raman spectrum of acetone taken with an excitation wavelength of 785 nm . ....	58
Figure 4.5	Raman spectrum of PETN recorded with an excitation wavelength of 514 nm. ....	59
Figure 4.6	Raman spectrum of PETN recorded with an excitation wavelength of 785 nm. ....	60
Figure 4.7	Raman spectrum of TATP recorded with a 785 nm excitation wavelength. ....	62
Figure 4.8	Raman spectrum of HMTD recorded with a 785 nm excitation wavelength. ....	63
Figure 5.1:	Raman spectrum of liquid acetone at $\lambda_i = 350$ nm. ....	68
Figure 5.2	REP of $\text{CH}_3$ asymmetric stretch at $2995\text{ cm}^{-1}$ of acetone within $\lambda_i = 350$ to $450$ nm. ....	69
Figure 5.3	Schematic layout of equipment setup for collection of Raman scatterings at $90^\circ$ . ....	70
Figure 5.4	Absorption spectrum of PETN over the UV-vis-NIR wavelength showing the maximum absorption at $\sim 330$ nm. ....	71
Figure 5.5	Raman spectra of PETN recorded with six different wavelengths; 514.5, 496.5, 488, 476.5, 465.8 and 457.9 nm. ....	72
Figure 5.6	Raman spectra of PETN recorded with six different wavelengths showing increase in Raman intensity of peak at $1287\text{ cm}^{-1}$ with the decrease in laser wavelength. ....	73
Figure 5.7	Graph showing the effect of changing $\lambda_i$ on IR for the PETN peak at $1287\text{ cm}^{-1}$ . There is an ncrease in IR with the decrease in $\lambda_i$ . Trend line for the excitation wavelengths from 465.8 nm to 514.5 nm is shown by the dotted line. ....	73
Figure 5.8	REP for five different Raman bands of PETN showing resonance enhancement of Raman scattering. ....	75
Figure 5.9	UV-vis absorption spectra of silver colloids prepared by three different methods. ....	78
Figure 5.10	UV-vis absorption spectrum of gold colloid prepared by the Lee and Meisel method. ....	78
Figure 5.11	SER spectra of pyridine from gold colloidal solution recorded with $\lambda_i = 785$ nm; pure pyridine Raman spectra (a), at $10^{-5}$ M (b), at $10^{-8}$ M (c) and at $10^{-11}$ M (d) concentrations. ....	80
Figure 5.12	SER spectrum of $10^{-3}$ M pyridine in silver colloidal solution recorded with $\lambda_i = 514.5$ nm showing spurious band. ....	81
Figure 5.13	Raman spectra of PETN in bulk and on copper disc recorded with $\lambda_i = 785$ from a diode laser. $t_i = 30$ seconds. ....	82
Figure 5.14	Raman spectra of RDX in bulk and on Cu disc recorded with $\lambda_i = 785$ nm. $t_i = 20$ seconds. ....	83

Figure 5.15	SEM images of silver slab before etching at 20 magnifications (a) same slab after etching in nitric acid solution at different magnifications (b-f). .....	85
Figure 5.16	Surface profiles of etched silver slab showing 300 to 1000nm high needle like structures.....	85
Figure 5.17	Raman spectra from etched silver slab before PETN droplet as background and of bulk for reference. SER spectra after putting small droplet of PETN solution, washing and drying and after 24 hours. $\lambda_i = 785 \text{ nm}$ . $t_i = 50 \text{ seconds}$ . .....	86
Figure 5.18	SEM images of Silver slab before etching at 20 magnifications (a) same slab after etching for 2.5 minutes at different magnifications as indicated (b-f). .....	87
Figure 5.19	Raman spectra of PETN (reference) and of etched silver slab after fabrication. SER spectrum of adsorbed PETN molecules. $t_i = 100 \text{ seconds}$ . .....	88
Figure 5.20	Surface profile of glass substrate with 20 nm silver layer. ....	90
Figure 5.21	Profile images of 100 nm silver film spotted with 10 $\mu\text{l}$ of 0.08% PETN solution, showing uniform crystal like pattern giving roughness 400 to 600 nm (a) and digital profile images of the features (b and c). .....	92
Figure 5.22:	Profile images of 100 nm silver layer spotted with 10 $\mu\text{l}$ spot of 1% PETN solution, showing crystal like structures having roughness of 400 to 600 nm. ....	93
Figure 5.23	Raman spectrum of PETN and SER spectra from 100nm silver film sputtered on glass slide at 400 $^{\circ}\text{C}$ , spotted with 0.08% PETN. $\lambda_i = 785 \text{ nm}$ . $t_i = 100 \text{ seconds}$ . ....	93
Figure 5.24:	Raman spectrum of PETN and SER spectrum of 1% PETN in acetone spotted on 100 nm silver film sputtered on glass slide at 450 $^{\circ}\text{C}$ . $\lambda_i = 785 \text{ nm}$ . $t_i = 40 \text{ seconds}$ .....	94
Figure 5.25:	Profile images from glass slide with 100 nm silver film before spotting (a), rough patterns after PETN spot (b), magnification of 'b' at the edge (c), and the area in centre of spot (d and e).....	95
Figure 5.26	Raman spectrum of PETN and its SER spectra of 1% PETN in acetone and in butanone. The surfaces were fabricated with 100 nm silver film deposited on glass slides at 450 $^{\circ}\text{C}$ . $t_i = 60 \text{ seconds}$ .....	96
Figure 5.27	Raman spectrum of pyridine and SER spectrum after a drop of $10^{-2}$ M pyridine solution was put on 100nm silver film that was etched for 2 minute in $\text{HNO}_3$ solution. $t_i = 5 \text{ seconds}$ . ....	97
Figure 6.1	Schematic of NSL process. The measured quantity of nanosphere solution is placed on inclined substrate (a) and the solution spread and flow to form mono-layer on evaporation of solvent (b).....	102
Figure 6.2	Photograph of the substrates coated with monolayer of nanospheres placed in the chamber of magnetron sputtering equipment.....	103
Figure 6.3	Removal of nanospheres by ultra-sonication in ethanol. ....	103

Figure 6.4	The basic NSL method (a) and the two variants for preparation of SER-active glass-based substrates (b) and (c). Enlargement of part of (b) is shown as (d). .....	104
Figure 6.5	The diagrammatic layout of the method for preparation of SER-active quartz-based substrates.....	106
Figure 6.6	Schematic representation of the substrate fabrication stages in a Lithographic method. Glass substrate (a), with nanospheres (b), with silver layer (c) and after the nanospheres are removed (d).....	107
Figure 6.7	Surface fabrication stages by NSL technique. Glass substrate (a), with nanospheres (b), and after silver layer and the removal of the nanospheres (c). .....	107
Figure 6.8	Configuration of a single silver structural array formed by the assembly of six nanospheres.....	108
Figure 6.9	SEM image of multilayer of polystyrene nanospheres over treated glass surface. ....	111
Figure 6.10	SEM image of nanosphere monolayer formed at $6^{\circ}$ slope (A) converts to multilayer at the lower end (B). ....	111
Figure 6.11	SEM image showing uniform monolayer assembly of substrate kept at $8^{\circ}$ slope from the horizontal. ....	112
Figure 6.12	SEM image of a typical assembly of nanosphere in a monolayer. The circled areas show defects occurring due to the variations in particle size. ....	113
Figure 6.13	SEM image of a defective patch on a substrate kept at $6^{\circ}$ slope from the horizontal (a) and the similar patch after removing PNS (b).....	114
Figure 6.14	SEM image of uniform PNS monolayer over glass substrate kept at $8^{\circ}$ slope coated with 150 nm silver layer (a), uniform nanostructures formed after removal of nanospheres (b), one cluster of six structures (c) and a 3D digital profile image of the same substrate (d).....	114
Figure 6.15	Surface prepared with undiluted nanospheres while the glass was kept at $10^{\circ}$ from the horizontal.....	115
Figure 6.16	Surface prepared with undiluted nanospheres while the glass was kept at $12^{\circ}$ slope, show the widely dispersed nanospheres over the entire surface. ....	116
Figure 6.17	Microscopic image of surface prepared similar to the one in figure 6.16 with nanosphere removed (a) and further enhanced SEM image showing large silver islands (b).....	116
Figure 6.18	Glass substrate with 10nm (non-uniform) silver layer coated at $6^{\circ}$ slope showing partial silver. ....	117
Figure 6.19	Glass substrate with 15nm silver under-layer coated at $6^{\circ}$ slope with undiluted nanospheres, showing PNS mono-layer devoid of ideal geometrical packing. ....	118
Figure 6.20	Surface fabrication process of a glass-based surface with 15 nm silver under-layer coated at a $6^{\circ}$ slope. Glass surface (a) with a 15 nm silver layer (b) with a monolayer of the nanospheres (c) and with the nanospheres removed (d). ....	118



Figure 6.21	Glass substrate with 15nm (non-uniform) silver under-layer coated at $8^{\circ}$ slope with undiluted nanospheres, showing a highly defective region. ....	119
Figure 6.22	Electron micrograph of glass substrate coated at $8^{\circ}$ slope with undiluted nanospheres and sputtered with 250 nm thick silver layer.....	120
Figure 6.23	Microscope image of glass substrate coated at $8^{\circ}$ inclination with undiluted nanospheres and sputtered with 40 nm thick silver layer. ....	121
Figure 6.24	SEM image of partially removed PNS from quartz substrate etched for 2 hours, coated at $8^{\circ}$ slope with undiluted nanospheres and sputtered with 50 nm silver layer.....	122
Figure 6.25	Surface fabrication process of a quartz-based surface with 60 nm silver layer coated at a $6^{\circ}$ slope. Quartz substrate (a) with a monolayer of the nanospheres (b) and after silver coating and the nanospheres removed (c). ....	123
Figure 6.26	SEM image of quartz-based substrate with 60 nm silver layer showing good monolayer assembly.....	124
Figure 6.27	Microscope image of quartz-based substrate fabricated with 70 nm silver layer and its profile image.....	124
Figure 6.28	UVN spectra of SER-active surfaces fabricated with different heights of nano-structures .....	127
Figure 6.29	UVN spectral values showing increasing transmittance values at 785 nm wavelength for the corresponding decrease in the heights of nano-structures.....	128
Figure 7.1	Typical spectrum of a glass substrate showing a characteristic background, ( $t_i = 3$ seconds). ....	132
Figure 7.2	SER spectrum of $10 \mu\text{l}$ drop coating of Pyridine $10^{-2}$ M solution on glass-based surface, Raman spectra of bulk pyridine and of glass surface are also included for reference. ....	133
Figure 7.3	The Raman spectrum of the clean quartz substrate with $t_i = 3$ seconds.....	134
Figure 7.4	The Raman spectra of the glass and quartz substrates recorded with $t_i = 3$ seconds each. ....	135
Figure 7.5	Normal Raman spectra of $10^{-2}$ M solution of Pyridine in a cuvette (a) and the SER spectrum of the adsorbed molecules on a SER-active glass-based surface. ....	137
Figure 7.6	Raman spectrum of SER-active surface before pyridine exposure, spectrum of $10^{-2}$ M pyridine in cuvette and SER spectra of pyridine exposed surface with $t_i = 5$ and 10 seconds. ....	138
Figure 7.7	Raman spectrum of pure pyridine in cuvette, SER spectrum of surface before Pyridine exposure and after surface was exposed to pyridine vapour for 10 seconds with $t_i = 3$ and 5 seconds as indicated.....	139
Figure 7.8	Raman spectrum of nitrobenzene in cuvette and SER spectrum of surface exposed to its vapours for 20 seconds .....	140
Figure 7.9	SER spectrum recorded with $t_i = 10$ seconds, from surface exposed to pyridine vapour for 15 seconds. Raman spectra of pyridine in	

	cuvette and of background from substrate without exposure to analyte are also shown. ....	144
Figure 7.10	SER spectrum ( $t_i = 10$ seconds) from a glass-based surface exposed to pyridine vapour for 10 seconds showing ring vibration modes. ....	145
Figure 7.11	SER spectrum ( $t_i = 10$ seconds) from a glass-based surface having 225 nm high of nano-structures with 20 nm silver overlayer when exposed to headspace vapour from PETN. ....	146
Figure 7.12	Raman (reference) and SER spectra ( $t_i = 10$ seconds) from a glass-based surface having 250 nm high of nano-structures with 20 nm silver overlayer when exposed to headspace vapour from HMTD. ....	147
Figure 7.13	Normal Raman spectrum of pyridine and SER spectrum recorded from a surface having 300 nm high silver structures exposed to the vapour from pyridine for 10 seconds. ....	149
Figure 7.14	Normal Raman spectrum of pyridine and SER spectrum recorded from a surface exposed to the vapour from pyridine for 20 seconds having 250 nm high structures. ....	150
Figure 7.15	Normal Raman spectrum of pyridine and SER spectrum recorded from a surface exposed to the vapour from pyridine for 20 seconds having 200 nm high structures. ....	151
Figure 7.16	Normal Raman spectrum of pyridine and SER spectrum recorded from a surface exposed to the vapour from pyridine for 10 seconds having 50 nm high structures. ....	152
Figure 7.17	SER spectrum of nitrobenzene (vapour) absorbed on SER-active surface with 250 nm structure height recorded with Renishaw Raman Microscope. ....	154
Figure 7.18	Normal Raman spectrum of TATP and its SER spectrum recorded from a surface (quartz-based) exposed to the headspace vapour, prepared with 250 nm of sputtered silver layer. ....	155
Figure 7.19	Normal Raman spectrum of TATP and its SER spectrum recorded from a surface (quartz-based) exposed to the headspace vapour, prepared with 225 nm of sputtered silver layer. ....	156
Figure 7.20	Normal Raman spectrum of TATP and its SER spectrum recorded from a surface (quartz-based) exposed to the headspace vapour, prepared with 80 nm of sputtered silver layer. ....	157
Figure 7.21	Normal Raman and SER spectra recorded from a quartz-based surface with 250 nm silver structural height exposed to the headspace vapour of HMTD. ....	158
Figure 7.22	Normal Raman and SER spectra recorded from a quartz-based surface with 60 nm silver structural height exposed to the headspace vapour of HMTD. ....	159
Figure 7.23	Normal Raman spectrum of solid PETN and its SER spectrum recorded from a quartz-based surface having 250 nm silver structural height, exposed to the headspace vapour. ....	160
Figure 7.24	Normal Raman spectrum of solid PETN and its SER spectrum recorded from a quartz-based surface having 200 nm silver structural height, exposed to the headspace vapour. ....	161

Figure 7.25	Normal Raman spectrum of solid PETN and its SER spectrum recorded from a quartz-based surface having 60 nm silver structural height, exposed to the headspace vapour.....	162
Figure 7.26	Normal Raman spectrum of solid PETN and its SER spectrum recorded from a quartz-based surface having 40 nm silver structural height, exposed to the headspace vapour.....	162
Figure 7.27	Some of the 13 consecutive SER spectra showing initial increase in the peak intensity of the pyridine with the decrease in quantity of adsorbed molecules.....	164
Figure 7.28	Some of the 39 consecutive SER spectra showing decrease in the peak intensity of the Pyridine with the decrease in quantity of adsorbed molecules.....	164
Figure 7.29	Number 1, 6, 13, 21, 31, 41 and 52 spectra indicated from 1 to 7 respectively showing initial increase and subsequent decrease in the peak intensity of the pyridine vapour adsorbed on a quartz-based surface.....	165
Figure 7.30	The initial increase and subsequent decrease in the peak intensity of the pyridine vapour adsorbed on a SER surface (quartz-based substrate) with the increase in duration of laser exposure.....	166
Figure 7.31	The removal of pyridine molecules from the quartz-based surface shown in term of decreasing Raman intensity with the increasing exposure to the laser radiation.....	167

## LIST OF TABLES

Table 4.1	Basic properties of pyridine. ....	55
Table 4.2	Characteristic Raman modes of pyridine. ....	56
Table 4.3	Basic properties of nitrobenzene. ....	56
Table 4.4	Characteristic Raman modes of nitrobenzene. ....	57
Table 4.5	Basic properties of acetone. ....	57
Table 4.6	Characteristic Raman modes of acetone. ....	58
Table 4.7	Basic properties of PETN. ....	59
Table 4.8	Characteristic Raman modes of PETN. ....	60
Table 4.9	Basic properties of TATP. ....	61
Table 4.10	Characteristic Raman modes of TATP. ....	62
Table 4.11	Basic properties of HMTD. ....	63
Table 4.12	Characteristic Raman modes of HMTD. ....	64
Table 5.1:	Increase in Raman intensity in order of magnitude of five different PETN bands with excitation wavelengths approaching resonance region. ....	76
Table 5.2	Fabrication of SER surfaces using silver films deposition on different substrates. ....	89
Table 5.3	Parameters and results of 100 nm silver film etched in HNO <sub>3</sub> solution to produce rough SER-active surface. ....	97
Table 6.1	Effects on substrate's morphology with the changes in PNS concentration and angle of coating. ....	110
Table 6.2	Effects of angle of coating on assembly of nanospheres. ....	122
Table 6.3	UVN spectral readings of SER surfaces fabricated with different heights of nano-structures with corresponding transmittance values at 785 nm wavelength. ....	127
Table 7.1	Summary of experiments conducted with glass-based substrate with pre-NSL silver layer. ....	136
Table 7.2	Summary of experiments conducted with glass-based substrate with silver overlayer. ....	143
Table 7.3	Summary of experiments conducted using pyridine with quartz- based surfaces. ....	148
Table 7.4	Summary of experiments conducted using nitrobenzene with quartz-based surfaces. ....	153
Table 7.5	Summary of SERS results recorded with quartz-based surfaces showing detection of headspace vapour from TATP having concentration of 70 ppm. ....	155
Table 7.6	Summary of SERS results recorded with quartz-based surfaces showing detection of headspace vapour from HMTD having concentration of 0.29 ppm. ....	157
Table 7.7	Summary of SERS results recorded with quartz-based surfaces showing detection of headspace vapour from PETN having concentration of 18 ppt. ....	160
Table 7.8	Some of the peak intensity changes due to the desorption of pyridine molecules from the SER surface. ....	165

## GLOSSARY

3D	Three dimensional
$\alpha$	Polarisability
$\lambda$	Wavelength
$\lambda_{\max}$	Wavelength of maximum absorption
$\nu$	Frequency
AFM	Atomic force microscopy
$c$	Velocity of light
C4	Composition 4
CCD	Charge coupled devices
cps	Counts per second
CT	Charge transfer
CW	Continuous wave
DIPAM	Diaminohexanitrodiphenyl; dipicramide
DODECA	Dodecanitroquaterphenyl
EDS	Explosive detection system
EM	Electromagnetic
FTR	Fourier transform raman
fwhm	Full width half maximum
GC	Gas chromatogram
GRH	Gloucester royal hospital
$h$	Planck's constant
HE	High explosives
HMTD	Hexamethylene triperoxide diamine
HMX	Cyclotetramethylene tetranitramine
HNBP	Hexanitrobiphenyl
HNS	Hexanitrostilbene
HNS BIB	HNS and Hexanitrobiphenyl
HNSSUP	HNS superfine
ICCD	Integrated charge coupled devices
IED	Improvised explosive device
IMS	Ion mobility spectrometer
InGaAs	Indium gallium arsenide
IR	Infrared
LOD	Limit of detection
LSP	Localized surface plasmon
LSPR	Localized surface plasmon resonance
M	Molar
MS	Mass spectroscopy

Nd:YAG	Neodymium yttrium aluminium garnet
NIR	Near infrared
NONA	Nonanitroterphenyl
NQ	Nitroguanidine
NSL	Nanosphere lithography
NTO	Nitrotriazolone
OMA	Optical Multi-channel Analyser
ONT	Octonitroterphenyl
PAH	Polycyclic aromatic hydrocarbons
PETN	Pentaerythritol tetranitrate
pH	Hydrogen potential
PMT	Photomultiplier Tube
PNS	Polystyrene nanospheres
ppb	Parts per billion
ppm	Parts per million
ppt	Parts per trillion
R6G	Rhodamine 6G
RDX	Cyclotrimethylenetrinitramine
REP	Raman excitation profiles
rms	Root mean square
RRS	Resonance raman spectroscopy
S/N	Signal-to-Noise Ratio
SEM	Scanning electron microscope
SER	Surface enhanced raman
SERRS	Surface enhanced resonance raman
SERS	Surface enhanced raman spectroscopy
STP	Standard Temperature and Pressure
TATB	Tri-amino-trinitro-benzene
TATP	Triacetone triperoxide
TCNB	Trichlorotrinitrobenzene
TDW	Tri distilled water
TEFO	Trinitrophenyl formal
TEM	Transmission electron microscopy
TNB	Trinitrobenzene
TNBA	Trinitrobenzaldehyde
TNN	Tetranitronaphthalene
TNT	Trinitrotoluene
UHV	Ultra high vacuum
UV	Ultraviolet
UVN	UV-vis-NIR
UV-vis	Ultraviolet and visible

# 1 INTRODUCTION

## 1.1 Rationale

There has been a sudden upsurge in the development of techniques and methods for the detection of energetic materials. This has been triggered by the onset of asymmetric warfare all over the world. Whereas explosive detection has become more challenging at airports, it has become equally vital to deploy a versatile *Explosive Detection System* (EDS) virtually at every security checkpoint, like entrances to public and government buildings, public transport accesses, and entertainment places etc. There are a number of systems available many of which are based on state of the art technologies, but each due to its unique limitations cannot be deployed at all the places, either due to the lack of cost effectiveness or portability or due to the inability to detect all types of explosives. There is no single completely foolproof automated technology currently available for effective monitoring of explosive vapour. It has been a constant struggle for the law enforcement and security agencies to acquire new techniques and equipment to address the problem and thus provide the rationale for the present research.

Raman Spectroscopy is a very powerful analytical technique for molecular analysis that allows molecular identification, detection and also its quantification in an environmental matrix. Such specific and sensitive molecular analysis is of great scientific and practical importance in many fields of modern technology. For instance in environmental studies, pharmaceutical and biological studies, forensic archaeology, law enforcement for detection of chemical, biological and explosive materials and so on. In fact, in all the areas of research where molecular investigations are required, Raman spectroscopy has proved extremely useful. Raman spectra are so specific that chemical identification is possible by using a search algorithm against digital databases.

However, advantages afforded by the specificity and high spectral purity of Raman lines are traded off by low cross-section (efficiency) of the Raman scattering process. In normal Raman scattering processes in the visible wavelength band, one Raman scattered photon is produced for approximately 10 million incident photons compared to only about 10 thousand incident photons that generate one Rayleigh scattered photon. This drawback can be overcome, to an extent, by excitation at a wavelength close to the isolated adsorption lines of the molecule, known as near-resonance excitation that provides a few orders of magnitude enhancement in Raman cross-section. However, not all molecules exhibit resonance enhancement and despite such excitation, the sensitivity of the Raman scattering process is not high enough for effective application in real world detection of trace contaminants of energetic materials.

*Surface enhanced Raman spectroscopy (SERS)* has been known to provide a method for very sensitive detection of molecular species and in some cases detection of single molecule has been reported. This emerging technology promises to provide the sensitivity needed for practical applications in the field of explosive detection. Reported results have shown that the technology has the capability to detect explosives vapour at very low concentrations. It is, therefore, considered feasible to use a field portable Raman spectrometer to detect explosives adsorbed on specially fabricated surfaces in a matter of seconds without the need for extended data analysis or background subtraction. Once the surface is ready, it can simply be exposed to the explosive vapour under normal laboratory environment and analysed without further sample preparation. Therefore, the technique has the potential not only for the ultra-sensitive detection but also for real time monitoring of energetic materials.

The explosives selected for our experiments are difficult to detect by ordinary detection techniques due to unusual structures or very low vapour pressures. Triacetone Triperoxide (TATP) is nitrogen free unlike other explosives and is undetected by most of the existing EDS that rely on nitrogen-oxygen contents for detection. Hexamethylene Triperoxide Diamine (HMTD) molecule has two nitrogen atoms but in a complex configuration that is again unlike a typical explosive. Both these explosives, due to their



simple preparation from household materials and high explosive properties, have been recently used for various terrorist activities. These peroxide explosives were detected by their headspace vapour concentration of about 70 parts per million (ppm) and 0.3 ppm respectively. Pentaerythritol Tetranitrate (PETN), although a typical explosive, has a very low vapour pressure that makes it difficult to detect. It was also detected by its headspace vapour concentration of around 18 parts per trillion (ppt). Detection at these concentrations in a matter of few seconds (mostly within 10 seconds) by portable equipment without the need of sample preparation or long time data analysis has shown the potential of surface enhanced Raman spectroscopy in the field of explosive detection for organisations responsible for security, forensics as well as for advanced research.

## 1.2 Background

Raman Spectroscopy is an essential tool in the field of analytical chemistry. The Raman effect was first predicted by *Smekal* in 1923 but first observed by *C.V. Raman* in 1928. The advancement has been tremendous in this field of technology since that time, which is clear by comparing original Raman equipment with most modern one in figure 1.1. Raman Spectroscopy has always intrigued scientists for its potential as a very powerful analytical technique. Work to exploit its potential in variety of applications has resulted in rapid development in both theory and hardware.

Phenomenologically, the Raman scattering process is explained as follows:

When the light interacts with molecules and distorts the electron cloud around the nuclei it forms a transitory, i.e. an extremely short-lived, state called, '*virtual state*'. This may or may not influence nuclear motion. If only the electron cloud is distorted the photons will be scattered with no frequency change and the process is called elastic scattering (Rayleigh scattering) which is the dominant process. However if nuclear motion is affected during the scattering process there will be transfer of energy and therefore a change in frequency will occur. The process will be inelastic and the scattering process is called Raman scattering. There are few photons (approximately 1 in  $10^7$ ) that undergo a change in wavelength and typically the intensity of Raman scattering is  $10^{-8}$  of the intensity of the incident radiation. The scattering occurs with the changes in the vibrational and rotational energies of the molecule.

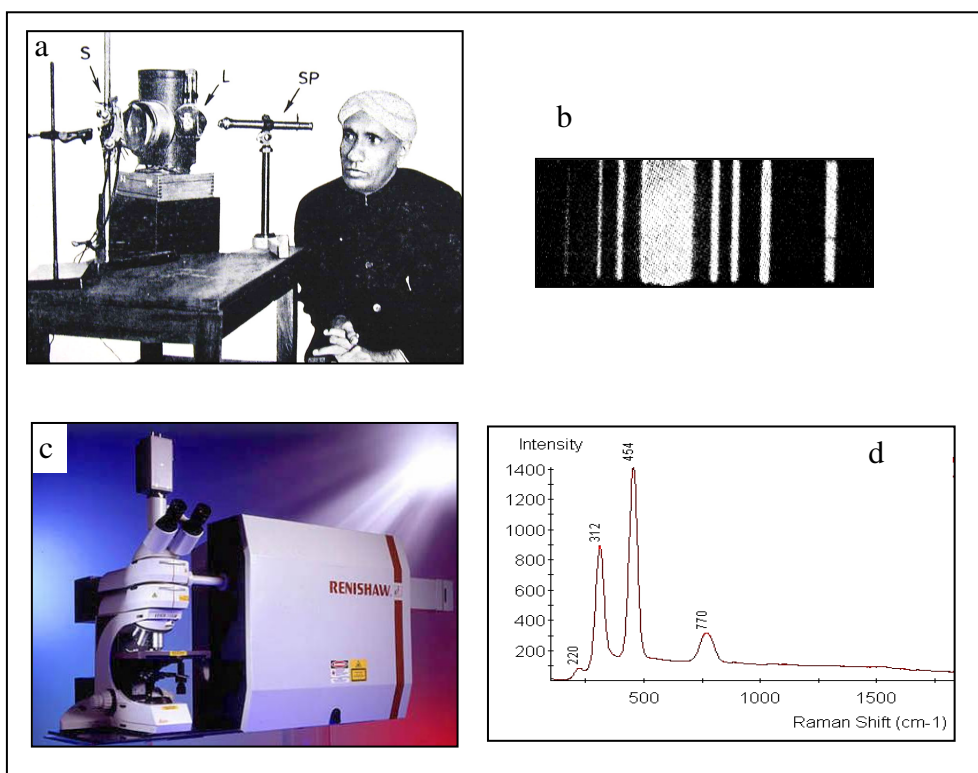


Figure 1.1 C.V. Raman's equipment (a) and spectrum of  $\text{CCl}_4$  taken in 1923 (b). A modern Raman microscope (c) and Raman spectrum of  $\text{CCl}_4$  recorded with it (d).

The whole effect is best understood by the energy level diagram in figure 1.2, in which it is shown that the '*Stokes scattering*' occurs when the incident light has higher photon energy than that of the scattered light and vice versa for the '*anti-Stokes scattering*'. Stokes scattering is much more intense than anti-Stokes because for the latter to occur the molecules have to be in a vibrationally excited state. Usually the Raman spectrum is recorded at a low energy level to give Stokes scatterings.

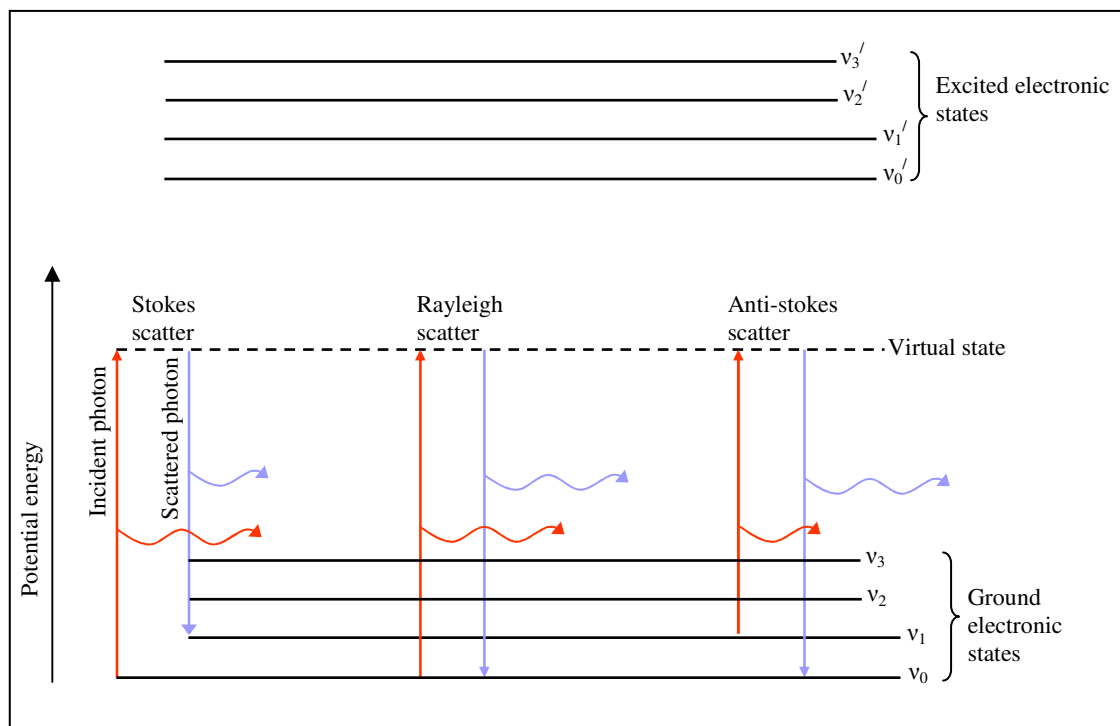


Figure 1.2 Schematic representation of Rayleigh and Raman scattering process.

A Raman spectrum is composed of a plot of Raman shift versus the intensity of the scattered radiation. A diatomic molecule can have one vibrational mode as it has only one degree of freedom, but in molecules where there are more degrees of freedom there are more vibrational modes. For a molecule with  $N$  atoms, the vibrational degree of freedom i.e. the number of fundamental vibrational modes, will be given as  $n = 3N - 6$  for a non-linear molecule (like water) and  $n = 3N - 5$  for linear molecules (like carbon dioxide). Each mode gives a characteristic shift in frequency (called characteristic group frequencies). In practice, in any inelastic interaction process, there will be more Raman lines than the fundamental modes due to the overtones and combination modes. Therefore, every molecule (in isolation or in abundance) would give a unique vibrational spectrum depending upon its composition and the selectivity of the Raman transitions governed by complex symmetry rules. This makes Raman spectroscopy a molecular or molecular site-specific analytical technique.

### **1.3 Recent Breakthroughs in Raman Spectroscopy**

The limitations of the applicability of Raman spectroscopy is imposed mainly by two factors; comparatively high background *fluorescence* and relatively very low signal intensity. Fluorescence can be effectively minimised by a host of modern techniques and data processors, and is discussed later. The low sensitivity is mainly due to the extremely small cross section for Raman scattering, typically  $10^{-30}$ - $10^{-25}$  cm<sup>2</sup>/molecule, and the larger values occurring only under favourable resonance Raman conditions. Such small Raman cross sections require a large number of molecules to achieve adequate conversion rates from excitation laser photons to Raman photons, thereby precluding the use of Raman spectroscopy as a method for highly sensitive measurements. Recent development in the field are mainly aimed at increasing the sensitivity and have led to development of more complex and sophisticated techniques like Resonance Raman Spectroscopy (RRS), FT Raman Spectroscopy (FTR), Surface Enhanced Raman Spectroscopy (SERS) and Surface Enhanced Resonance Raman spectroscopy (SERRS). Each of these offers specific advantages which are discussed in the next chapter. Although these techniques are being used widely, still there is a lot to be explained both on theoretical aspects as well as its practical manifestation.

Sensitivity or the limit of detection in Raman analysis is parameterised by signal-to-noise ratio (S/N). The comparatively small Raman cross section means small S/N, therefore very high limit of detection. In the last decade or so there has been a technological revolution of solutions to drastically increase the S/N for a given sample concentration. Introduction of multi-channel and multiplex techniques has been a result of such efforts. Raman systems have been developed to use longer wavelength excitation lasers as well as low noise Charge Coupled Devices (CCD) detectors to reduce background noise as the multi-channel gives rise to little fluorescence noise. More sophisticated techniques like SERS, RRS and SERRS are mainly developed for increasing the Raman signal strength. An enhancement in Raman intensity of up to  $10^4$  has been achieved using resonance Raman spectroscopy (RRS) and of  $10^8$  using SERS. The RRS involves using a laser line close to the absorption region (electronic transition) for the target molecule where the effect of resonance enhances the Raman signal many folds. On the other hand, in SERS the target molecules are allowed to be adsorbed on

highly polarisable surfaces of coinage metals (gold, silver, copper) roughened at the nano-metric scale, (usually less than the wavelength of incident light) which, due to a combination of charge transfer (CT) and electromagnetic (EM) effects, results in enhancement in Raman intensity up to hundred million times. Detection of a single molecule has also become possible with SERS which makes it the most sensitive detection tool available for analysts. These techniques will be the focus of the research and will be discussed in further detail in Chapter 2.

#### **1.4 Viability of Raman spectroscopy as an explosive detection technique**

It has been a constant struggle for the law enforcement and security agencies to acquire new techniques and equipment to thwart off the terrorist threat of chemical, biological and explosive attack. It is becoming more and more challenging to detect every type of explosive at all sensitive locations which demands more comprehensive methods of explosive detection to be developed. Explosive detection methods currently in use range from simple portable devices to highly sophisticated screening devices. At present a single analytical technique or device is not capable of addressing all explosive detection under a myriad of conditions which has again boosted the efforts to search for newer, more sensitive and versatile detection techniques.

Much research and development has also been done in developing reliable explosive detection and identification system based on *Raman spectroscopy*. Its main advantage being a very high specificity in which the molecules are identified by their characteristic vibrational frequencies in a complex matrix of gas, liquid or solid states with no or very little sample preparations in a matter of a few seconds. Use of fibre optics for Raman spectroscopy to reach areas inaccessible to other analytical methods is a major advantage. Comprehensive spectral information of known chemicals, including explosives, has been compiled which can be stored as a data base in the computer controlling the Raman Spectrometer. The whole system is capable of automation in which a Raman spectrum of unknown chemical is instantly compared with the stored 'finger print' to give a positive identification. Raman spectroscopy is useful in explosives analysis even in sealed transparent containers where it is possible to expose the sample in bulk to a laser and collect the scattered light. But for a well concealed

explosive having very low vapour pressure, the low sensitivity associated with Raman spectroscopy makes it less likely to be detected even with the most modern of Raman instruments.

The breakthrough in molecular analysis has taken place with the development of surface enhanced Raman spectroscopy (SERS), as it is now possible to overcome the inherent problem of low sensitivity. Although more than 5000 papers have been published on SERS since its discovery 28 years ago, its underlying principle is still not fully understood. However despite this drawback, with further development in nano-technology of metal surfaces and Raman instrumentation, the prospects of sensitive optical detection of explosives are bright.

Compared to other detection techniques, SERS seems to have better prospects in terms of sensitivity, selectivity, portability and cost effectiveness. The source (light) has negligible hazard value and is much cheaper in comparison to those used in some of the nuclear and X ray based techniques widely deployed presently. The combination of high sensitivity of surface enhancement and selectivity attributed to Raman means that the signal should be able to detect extremely low quantities of explosives (single molecule detection) with negligible false alarms. The system also offers prospects of a portable EDS which would be relatively easy and economical to be deployed at a variety of security stations. The combinational arrangement in parallel or in line with other EDS is also possible.

### **1.5 Goals and Objectives**

SERS has already been accepted as a versatile and effective technique under development for chemical analysis. Raman instruments are fast becoming smaller and economical. Advances in nano-science have solved many problems encountered in SER-active surface preparation and its interaction with the target chemical entity. Research into the theory and practice of SERS may open new research avenues, not only in the field of explosive detection but also in wider aspects of chemical and biological analysis.

In this thesis an effort is made to evaluate the potential of Raman spectroscopy to achieve ultra-sensitive detection limits for explosive in real time. The detection of novel explosives (peroxide based; TATP and HMTD) and of that with a very low vapour pressure (PETN) is attempted at trace level. The aim is therefore to improve the practical understanding of SERS so that economical, reproducible and sufficiently stable SER-active surfaces could be developed which would mark a definite progress in the development of an EDS based on SERS as well as for many related medical and environmental applications.

With the above background, the main objectives set for the research are as follows:

- a. Evaluate and critically review the existing literature on the Raman scattering process with a special emphasis on RRS and SERS.
- b. Experimentally verify the enhancement in sensitivity of the Raman process with RRS and SERS for sensitive detection of trace molecular species, particularly energetic materials.

Within the above theoretical and experimental broad objectives, the detailed tasks are as follows:

- a. Critically review up-to-date literature and theory pertaining to SERS and evaluate the explanation of SER effect.
- b. Conduct preliminary experiments using well-characterised (Raman scattering) samples for the initiation of SERS work.
- c. Undertake the preparation of SER-active surfaces, their characterisation and suitability for adsorbing desired chemical species (explosives).
- d. Conduct SERS experiments for trace detection of target species; TATP, HMTD and PETN.

## 2 REVIEW OF LITERATURE

### 2.1 Overview

Raman Spectroscopy has always provided chemists with an excellent tool for specific molecular characterisation, but physicists, apart from specificity, have more interest in the limits of detection; '*Raman intensity*'. Therefore, sensitivity has been the main focus of recent developments in Raman spectroscopy and has led to the development of advanced techniques supported by sophisticated equipment. Now Raman Spectroscopy can promise its usefulness for the detection of energetic materials at *limits of detection* (LOD) comparable or even lower than those afforded by the existing *Explosive Detection Systems* (EDSs).

Non-invasive detection of leaked vapour from highly concealed explosives at check points remains a challenging unresolved problem. As terrorists and other potential bombers become more sophisticated, both in their choice of explosive materials and in the way these materials are procured, transported, and concealed, detection methods must be improved concomitantly. Most of the deployed EDSs, based on Gas chromatography/Mass spectrometry (GC/MS), Ion mobility spectrometry (IMS), Nuclear, X ray etc, have limitations in terms of target specificity, LOD, portability or high cost. Many reviews <sup>1-7</sup> have been published to establish their viability and usefulness, especially for their capability to meet the future threat. At present no single analytical technique or device, let alone a real-time method, is capable of addressing the problem of detection of different types of explosives under different circumstances <sup>8</sup>.



Raman Spectroscopy has been used over the last few decades primarily to provide a ‘fingerprint’ of the molecular structure, thus permitting qualitative analysis of an individual compound. This is done either by direct comparison of the spectrum of a known material with that of an unknown one run consecutively or by comparison of the spectrum of an unknown compound with a ‘catalogue of reference spectra’. Therefore, Raman spectroscopy has found application in a variety of tasks, such as the detection and analysis of environmental pollutants in soil, air and water <sup>9</sup>, biological <sup>10</sup> and chemical agents <sup>11</sup>, explosive materials <sup>10</sup>, geological materials and skeletal remains/past materials <sup>12</sup>.

These extraordinary capabilities of Raman spectroscopy has prompted extensive research initiatives for ultra-sensitive and versatile detection<sup>1</sup> based on such a technique. Modern Raman techniques like *surface enhanced Raman spectroscopy* (SERS) having the ability to detect only a few molecules have already attracted attention in the field of explosive detection. Although SERS is under active research and development for many years now, still much work is needed to develop it into a reliable method for a sensitive EDS. Before going into the scope of SERS in the application of explosive detection, the overall contribution of Raman spectroscopy so far in this field is reviewed below.

## 2.2 Explosive detection with Raman Spectroscopy

Although major advances have taken place in field of Raman spectroscopy, its application and scope for explosive detection and identification conducted over a decade is still limited. The limitation is imposed primarily by the background fluorescence. It is possible to record the Raman spectrum of an explosive in bulk or in a mix where the explosive concentration is very high (~1%), but an efficient detector is required to detect very low concentrations (ppm - ppb) of explosive in a matrix as laid down by *Committee on the Review of Existing and Potential Standoff Explosives Detection Techniques* <sup>8</sup>. Although Raman spectroscopy is highly specific and that there has been much development in its hardware and software, its limited sensitivity makes it less likely as an effective detection system for wide application and commercial use. Before getting into the experimental Raman spectroscopy, two major decisions needs to

be made; the type of the spectrometer to be used and the suitability of the laser (wavelength) for explosive detection.

### **Multi-channel Vs Multiplex spectroscopy**

The modern systems are being built to utilise the benefits from the multi-channel detector affording short analysis time and multiplex (Fourier Transform Raman - FTR) spectrometers providing high sensitivity. A multi-channel spectrometer consists of multiple detectors capable of detecting multiple wavelengths from the dispersed light simultaneously, whereas a multiplex system (FTR) uses a single detector to detect a single beam having all the wavelengths (frequency modulated) and analyse each wavelength one after the other taking relatively longer time. The merits of the two systems have been discussed in publications <sup>9,13</sup>. Therefore, the analysis time for a multi-channel spectrometer is well within the real time detection limits compared to that offered by the FTR spectrometer, and that factor alone overwhelms the other effects in which an FTR spectrum may have the advantage, like resolution, spectral coverage, signal magnitude and S/N.

With the modern sensitive multi-channel detectors based on charge-coupled device (CCD), S/N achieved with 785 nanometers (nm) excitation wavelength was found to be similar to that by using Fourier Transform Raman (FTR) system, albeit with much longer analysis time. This is due to the fact that germanium (Ge) or indium gallium arsenide (InGaAs) detectors used in FTR are relatively noisier. The CCD based detector does not perform well at wavelengths above 1064 nm but has been used effectively by Lewis et al <sup>14</sup> to record anti-Stokes Raman spectra using Nd:YAG (Neodymium-doped yttrium aluminium garnet) laser. However, due to the inherent weakness of anti-Stokes Raman lines as compared to Stokes scatterings this process would have much lower detection limits. Although one can get good spectra of solid explosives for building spectral libraries and sample characterisation with high power 1064 nm (FTR) in fluorescence free excitation region, yet the utility of such a system for trace analysis in real time is considered to be limited.

### Laser wavelength selection

Lewis et al <sup>15</sup> studied Raman spectra of 30 different explosives for three different laser excitation wavelengths; 632 nm, 785 nm and 1064 nm. The spectra were recorded using explosives in bulk (quantities above 50mg) and concluded that the excitation at longer wavelengths (1064-785 nm) gives better *signal to noise ratio* (S/N). This is mainly because of the fluorescence background noise from the explosives is negligible <sup>14</sup> at near infrared (NIR) and infrared (IR) wavelengths, thus giving a good S/N. However for this, longer integration time was needed to record a useful spectrum. Therefore, despite some improvement in sensitivity, such a system had the big disadvantage of longer analysis time, and was not suitable for use at a security portal or for real time monitoring.

In the work reported by Haywood <sup>16</sup>, 632 nm laser wavelength was used effectively in detecting Semtex H (Cyclotrimethylene trinitramine (RDX) based explosive) even in a fingerprint residue using a fibre optic probe. Semtex was extremely fluorescent even at 785 nm excitation <sup>15</sup> and gave a very weak Raman intensity at 632 nm when analysed in isolation. In the presence of other fluorescent impurities in real life samples, it is not expected to get any useful Raman signal retrievable from the background noise. In a recent work Carter et al <sup>17</sup> recorded Raman spectra of PETN, RDX, Trinitrotoluene (TNT) and their stimulants (4-8% explosives in silica matrix) at a distance of 50 meters using a 532 nm frequency from a doubled Nd:YAG laser in ambient conditions. The work was useful for identifying bulk explosives from a safe distance but not practicable for vapour detection work because of higher fluorescence <sup>15</sup> as well as the photo-degradation effect of shorter wavelength laser. The tendency of laser degradation of explosives was reported by Carter et al <sup>17</sup> and results have been reproduced in figure 2.1. The graph shows the relation of Raman peak intensity and laser power density for the explosives RDX and TNT. Raman intensity of RDX started to become stable at a higher laser power density of  $\sim 3.4 \times 10^6$  W/cm<sup>2</sup> with no signs of degradation, whereas, TNT started to degrade at less than 1 W/cm<sup>2</sup> laser power density. The use of high power lasers, therefore, has to be avoided when targeting photo/thermal degradable explosives or unknown samples that may contain these explosives, as the presence of these may not be detected.

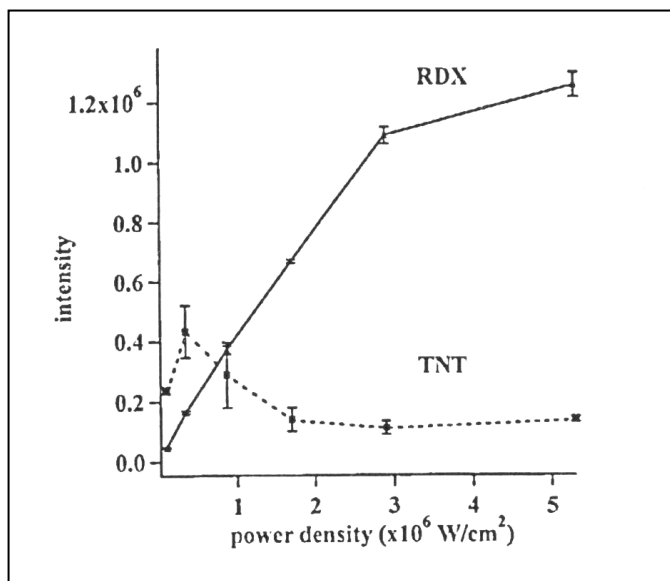


Figure 2.1 Graph showing effect of laser power density on Raman intensity for explosives (reproduced from reference 17).

This effect was more pronounced if the target molecule was in the gas phase (low concentration) or in a very small quantity. UV lasers at  $\sim 266$  nm had been demonstrated to provide better Raman intensity and a fluorescence free window with minimum chance of sample degradation<sup>9,18,19</sup>. It might be useful for laboratory based forensic work where the target sample could be separately analysed, but in the real time field detection, the usefulness of UV laser was considered limited. The application of UV Raman spectroscopy was also limited to the range of wavelength where materials do not absorb radiation to seriously affect Raman spectrum. However, its usefulness in *resonance Raman spectroscopy* (RRS) will be discussed later.

Newer Raman systems are based on superior spectrometers, high sensitivity-CCD detectors and efficient excitation wavelength blocking filters (holographic, Chevron) which, when used with near infrared (IR) diode lasers can give S/N comparable to that of FTR. Such systems are cheaper, portable and less complex and hence suitable for field use<sup>20</sup>. In recent studies by Lewis et al<sup>21,22</sup> different laser lines were used to record explosive spectra for comparison. The group concluded that with the available technology, working with 785 nm to 830 nm laser lines with CCD detectors gave the optimum results. At these wavelengths, only a few explosives gave fluorescence and that also was within the acceptable limits. Figure 2.2 shows the relative fluorescence



3. Sample degradation was also directly related to laser power. RDX started to degrade with the power of 18 mW from 785 nm wavelength laser and did not degrade even at 50 mW from 830 nm.

Similar work has been done by others<sup>23-34</sup> and some of it related to explosive detection with Raman spectroscopy is summarised in appendix A.

Raman spectroscopy, therefore, has many useful aspects with various combinations of spectrometers, detectors, lasers etc. when carefully chosen for specific tasks. However, to settle down for a single setup best suitable for real time explosive detection would have to be carefully decided. Even so, the sensitivity of a normal Raman spectrometer is likely to be too poor to be considered as an EDS in spite of the recent advancement in equipment. The best a normal Raman spectrometer can do may be the detection of small particles of explosive (~1 picogram in mass)<sup>35</sup> by focussing the laser directly onto the particle or down to a small percentage by mass (1.5-14%)<sup>20</sup> in a matrix. To be able to utilise the specificity afforded by Raman spectroscopy, the sensitivity has to be improved by a million or 100 million times, which is only possible by employing advanced Raman techniques discussed below.

## **2.3 Advanced Raman techniques**

### **2.3.1 State of the art in resonance Raman spectroscopy (RRS)**

Resonance Raman spectra are obtained when the frequency of the incident light comes close to that of an isolated electronic transition of the scattering species and Raman scattering enhancement of up to  $10^4$  has been observed<sup>36</sup>. The Raman intensity is dependent on the fourth power of the frequency, but in resonant conditions the intensity is also dependent on how close is the excitation frequency to that of the frequency of an allowed electronic transition. Whenever lasers capable of causing resonance have been used, some absorption also took place in addition to scattering, the magnitude of which was dependent on the material property and could not be easily predicted<sup>9,13</sup>. Resonance excitation invariably increased fluorescence and was likely to result in sample degradation.

Therefore, RRS is unsuitable for most fluorescent (coloured) materials especially in a matrix. Much depends upon the relative efficiency of the scattering and fluorescence process. UV RRS at around 266 nm has been reported<sup>18,19</sup> to give good Raman intensity and negligible fluorescence for non absorbing materials, yet it cannot be employed for all materials as this is a zone in which most explosives absorbs. Specific electronic information about a molecule could be obtained from the intensities of the bands found in resonance excitation<sup>36,37</sup>. This makes it a material-specific technique and its employment for forensic and explosive detection is limited where the target sample is always a complex matrix of different and unknown materials.

It may be a valuable analytical technique for laboratory work, but its applicability as an explosive detection technique is presently limited. Development of a portable and tuneable UV laser in future may increase the utility in explosive detection. However, its importance in combination with *surface enhanced resonance Raman spectroscopy* (SERRS), where fluorescence is completely quenched, appears to offer the best prospect for explosive detection in trace concentrations such as those that may escape as vapour from concealment.

### 2.3.2 State of the Art in SERS

The discovery of SERS twenty eight years ago paved the way to addressing the problem of lack of sensitivity in Raman spectroscopy and according to a survey<sup>38</sup> more than 5000 papers have already been published on the subject. The basic understanding of SERS is clearly a very important development in the study of surface chemistry and surface physics. The combination of molecular information and extraordinary sensitivity provides a valuable probe for surface structure and behaviour analysis<sup>12</sup>. SERS has been found to give an enhancement of up to  $10^6$  in scattering efficiency (more in some cases) over normal Raman scattering<sup>13</sup>. Therefore, it may be used as an in-situ and ultra-sensitive analytical technique that can provide detailed structural information and orientation of molecules on the surface<sup>9</sup>. The application of SERS has been widely recognised in chemical, biological and environmental analysis<sup>10,11,39</sup>.

### **SERS mechanism**

SERS mechanism has been discussed in many publications<sup>9,13,36,38-48</sup> some of which have adopted different approach from the others. What all agreed on was that when a Raman spectrum was recorded for a molecule adsorbed on a specially prepared rough metal surface its intensity might be enhanced by a factor of  $10^6$  or more. Therefore, the surface needs to be able to adsorb the molecule for the enhancement to take place; such a surface is mostly referred to as surface enhanced Raman active (SER-active).

The recording of SER scattering is not as simple as that for normal Raman scattering. Raman processes involve target molecules and laser interaction, whereas to obtain a SER spectrum, a metal-molecule component is added that raises the complexity of the measurement and adds to the controversial character of the SERS<sup>49</sup>. The differences in interpretation of SER spectrum owing to the complexity of the process has resulted in a large variation with in the published data. The theoretical differences between Raman and SER spectrum will be discussed in the next chapter.

### **Surface material**

The usual metals surfaces used are silver, gold and copper in the order of effectiveness for most systems<sup>41</sup>. It is possible that any substrate carrying free electrons could show the SER-effect. However, the intensity of such emissions would depend upon the free electron density, and other properties such as electrical conductivity, which is best exhibited by silver, gold and copper<sup>13</sup>. However, the SER-effect has been recorded with other materials like transition metals<sup>50-52</sup> and aluminium<sup>53</sup>. A major contribution to SER mechanism was found to be from surface phenomenon in the metal complex as compared to the adsorbed molecule<sup>42</sup>. Irrespective of the adsorbed molecule being Raman active or not, the enhancement is not possible without the metal surface being SER-active, although it is the polarisability of the molecule that dictates Raman intensity. The Raman intensity undergoes a change in magnitude when the molecule is adsorbed onto the metal. It is the poor conductivity of the metal (transition metals) that causes the electronic scattering to become the predominant process which reduces the SER-effect. Therefore when all the conditions are kept constant, silver has been found to give a better SER effect than gold and copper<sup>13,41</sup>. That is why silver has been used



more effectively in fabrication of SER-active surfaces by different techniques.

### **Morphology of SER-active surface**

In general, it can be concluded from extensive studies on morphology of the SER-active surfaces that the metal particles need to be smaller than the wavelength of light for the SER effect to occur<sup>41</sup>. It was also established that the minimum size of the roughness should be larger than the analyte molecule. So the usual roughness (aggregated colloids or the height of the structures) required for the SER-active surface was found to be between 5-500 nm<sup>41,42,54,55</sup>. However, the upper limit depends, to a great extent, on the wavelength of the excitation light, therefore, for the system having a laser in the NIR region, the roughness feature may be higher. In general, when all other parameters were kept constant, the variation in the dimension of metal roughness was found to affect the SERS results<sup>56</sup>. The roughness feature in colloidal system is normally its diameter and for solid rough metal surfaces<sup>57</sup> it is the size of surface protrusions<sup>43</sup>.

SERS is a complex process and there are many factors which affect the enhancement obtained through metal-molecule linkage, most of which are not fully understood<sup>41</sup>. Apart from the metal type and its size discussed above, other morphological and chemical characteristics have been found to play an important role, e.g. shape of the roughness feature, the spacing between the protrusions of a solid SER-active surface<sup>38,57,58</sup> and aggregation for a colloidal system<sup>36</sup>.

Even the hydrogen potential (pH) of the colloidal solution affects, in addition to the aggregation, the adsorption of target molecule and thus the SER signal<sup>55</sup>. The importance of laser wavelength has been mentioned above and will be further elaborated later. The ability of metal to adsorb the analyte molecule was found<sup>42</sup> to be not only a feature of metal property but also depend on the environment in which SER-active material was kept and on the sample presentation method.

### **Limitations of SERS**

The acceptance of SERS in analytical chemistry and physics is evident from the sudden increase in published work<sup>38</sup>. Although it is being used for basic research in advancing

the knowledge of surface science, its potentials as an effective tool in forensic and real time in situ analysis are currently being widely and extensively explored. Some of the limitations associated with SERS reported in many published works are mentioned below:

1. Not all the variables associated with SERS could be controlled<sup>46</sup>. For example if the particle's roughness size and shape was controlled, surface chemistry generally remained unstable<sup>9,59,60</sup>. Contamination or deterioration of the delicate surface resulted in deterioration of the SER spectrum.

2. Target molecule had to be adsorbed on the surface for the SER-effect. The compatibility of the molecule and the SER-active surface was found<sup>50</sup> to be a vital issue. Not all types of surfaces supported all types of molecules. It would be ideal to develop a surface whose properties could be controlled to facilitate the adsorption of a variety of analyte molecules.

3. SER scattering was found<sup>12</sup> to be dependent on the types of chemical species being used as analyte. Adsorbate molecules differed greatly in their interaction with the surface and environmental contamination could prevent that altogether<sup>42</sup>. Therefore, SERS is very sensitive to both surface chemistry as well as adsorbate-surface interaction.

4. Anomalous bands have been reported<sup>54,59,60</sup> to keep appearing in the SER spectrum that apparently had no origin from the adsorbate or surface chemicals. These bands were a source of confusion and error in the interpretation of a spectrum. For example, Rhodamine-like bands, which were probably due to a universal dye existing at a very low concentration, appeared in many types of colloids when working with 514.5 nm laser wavelength<sup>59</sup>. Knowledge of these bands is important to avoid misinterpretation.

5. The SER spectrum often differed from the Raman spectrum of the bulk material<sup>9</sup>. The Raman spectrum obtained by the interaction of a laser with the adsorbed molecule is determined by selection rules different from that of normal Raman

scatterings<sup>49</sup>. This was due mainly to the difference in vibrational freedom between free and adsorbed molecules or changes in its centre of symmetry on adsorption<sup>41,42</sup>. The surface selection rules are determined by the orientation and binding properties of the molecules at the surface nano-structure.

6. In a SER spectrum some peaks may not be visible altogether and a few forbidden vibrations may appear<sup>45</sup>. This makes the identification of an analyte difficult. One way of tackling this is to make the SER spectral library with the lowest concentrations possible and avoid comparison of spectra with normal Raman spectra during SER investigations.

7. In SERS, being a very sensitive technique, even a minute amount of contaminant sticking strongly on the surface was found to produce a dominant signal in the spectrum<sup>13,59</sup>. The problem of positive identification would then become a problem. The contaminant could be very small and could be from the environment or left behind during a previous experiment on any one part of the sampling system.

8. A SER-active surface suitable for field work should have a long shelf life, should be reproducible and economical for commercial use. Most of the types of surfaces reported<sup>39,53,55,59</sup> are being produced by a delicate laboratory controlled fabrication protocol. Surfaces used in the tests are fabricated shortly before use for a specific experimental requirement.

#### **2.4 SER-active surface fabrication techniques**

As discussed earlier, the difference between normal Raman spectroscopy and SERS is in the analyte-surface system, otherwise hardware remains the same. In an analyte-surface system, it is the latter which can be varied in physical and chemical properties to get the best results. Therefore, the different SERS techniques or SERS applications involve fabricating, controlling and modifying the surface properties for optimised enhancement<sup>36</sup>.

Concurrent to the development of the modern Raman equipment, there has been a tremendous amount of work done to develop better techniques of fabricating SER-active surfaces. These include electrode surfaces roughened by oxidation-reduction cycle<sup>13,44</sup>, island films on warm substrate formed by layers of vapour deposition<sup>54</sup>, deposition of metal films on porous glass<sup>61</sup>, cold deposited films<sup>57</sup>, lithographically produced metal spheroid assemblies<sup>46</sup>, roughened fibre optics tips<sup>62</sup>, metal colloids<sup>63</sup>, mechanical polishing<sup>46</sup>, etched silver surfaces<sup>64</sup> and metal coated nano-beads<sup>65</sup>.

Surfaces have also been prepared by a variety of methods and some by using combination of two or more simple techniques. Most of them are customarily prepared in the laboratory for a particular use and still no single substrate is known to have met the needs of all areas of study<sup>61</sup>. This is, therefore, the foremost active research area in SERS. The second is the selection of laser wavelength which is compatible with the metal-molecule complex<sup>9,66,67</sup>. The conditions/rules of adsorption for sample molecule on metal surface is the third area being explored by researchers<sup>13,68</sup>.

Many techniques have been developed for substrate preparation based on the basic methods reviewed above. Some of those that seem to be important and advanced, especially having some utility in the detection field, will now be reviewed for their viability. These methods can be broadly divided into two groups; those composed of metal colloids and those based on solid SER-active surfaces.

In order to compare the SER-active surfaces fabricated by different experimental protocols, there are some important factors which must also be considered. These are the type of the metal, type of substrate, excitation laser wavelength for SER analysis and the type and concentration of analyte used. With this in view, these experimental details of a few of the relevant techniques have been tabulated in appendix B and the same will be referred in the text.

#### **2.4.1 SERS with metal colloids**

Three widely used techniques for the preparation of metal colloid differ as per the type of reducing agent used for the reduction of silver and gold salts. An efficient method

was suggested by Lee and Meisel<sup>81</sup>, which used Trisodium Citrate ( $C_6H_5O_7Na_3$ ) as reducing agent. In another method proposed by Leopold and Lendl<sup>70</sup> metal colloids were prepared with Hydroxylamine Hydrochloride ( $NH_2OH.HCl$ ) as reducing agent. Creighton et al<sup>82</sup> used Sodium Borohydride as reducing agent. The three methods differed in the procedure of preparation but were reported to yield similar results<sup>53,70,82</sup>. The size of silver colloids was around 10 to 15 nm in diameter and from 50 to 60 nm for gold colloids. The absorption maximum of silver colloids formed from these methods remained within 395-415 nm, whereas for gold colloids it was between 510-530 nm. This showed abundance of bigger particle sizes in gold colloids. Citrate reduction method<sup>53</sup> was more widely used<sup>39,56,63,69,71,81,83</sup> because of the narrow size distribution and stability of colloids.

The most commonly used form of SER-active surface is silver colloidal solutions<sup>63</sup> having particle sizes around 10-15 nm when prepared and 50-200 nm on aggregation. gold colloids were found to be a little bigger in size, with diameters of around 40 to 50 nm, and formed much bigger colloids on aggregation than silver. Usually the aggregated silver colloids have a combination of rod like and spherical particles whereas the gold colloids are mostly spherical in shape<sup>70</sup>. The control on aggregation of these colloids is very important as it affects the sensitivity of SERS measurements.

Vidal and Pendry<sup>47</sup> have demonstrated that an isolated single particle (as in un-aggregated colloids) was a poor model for real SER-active system. Most SER-active systems were actually assemblies, sometimes very large assemblies, of coupled nanoparticles. The EM field strength at interstitial locations in the aggregate was greatly increased as compared to a single particle and these could correspond to the most chemically active sites too. It was shown<sup>70</sup> that the adsorbate molecule might be strongly bonded to such chemically active sites after landing on a randomly rough surface. It was here where very strong electromagnetic fields and field gradients were available, and were called “hot spots” of the fractal colloidal silver cluster.

Therefore, the molecules involved in the SER effect were predominantly those adsorbed on aggregates that were favourable for surface plasmon resonance (SPR). The existence

of “hot spots” at a given excitation wavelength depends strongly on the geometry of the aggregates<sup>42,46</sup>. The SPR depends on both the morphology of the nano-particle and the excitation wavelength of laser. A SER-active surface of a specific morphology possesses specific resonance properties where the surface plasmon shows highest values and whenever the coinciding laser wavelength is used, drastic enhancement in SER scatterings are observed. Application of SPR in SERS is discussed later. The surface-enhanced Stokes Raman signal is proportional to the Raman cross section of the adsorbed molecule, the excitation laser intensity, and the number of molecules that are involved in the SERS process<sup>39</sup>. The morphology of the particles is a significant factor, determining the distribution of the local enhanced electromagnetic field above the aggregates and the adsorbed molecules.

In the Lee-Meisel<sup>81</sup> colloid, a great variety of shapes, from spheres and cubes to rods and needles, could be found, whereas the particles in the hydroxylamine reduced silver colloid were predominantly spherical with some variation in size. Higher aggregation of colloidal solution and poor quality Raman systems resulted in the observation of low enhancement of detection efficiencies. Likewise the analyte-colloid interaction (adsorption) was a vital aspect<sup>43</sup>. Many techniques have been used to facilitate the adsorption of target molecule and its orientation onto the colloidal surface<sup>46</sup>. Colloids were generally prepared to be used within weeks and prolonging the shelf life of colloids is still an active research field.

### **Effect of Laser Wavelength on SERS**

In the SERRS study done by Littleford et al<sup>67</sup>, they gave useful suggestions on the choice of laser. The high powered pulsed lasers were found not very efficient for such work as compared to the low-powered continuous wave (CW) lasers. With the use of high power pulsed laser precipitation of the colloid was observed, indicating that the intense radiation permanently destabilised the colloids, possibly through sintering of already aggregated colloids as evident from the electron microscope pictures reported by Littleford et al<sup>67</sup> and reproduced in figure 2.3. It also might have resulted in breaking of the inter analyte-colloidal bond, pushing analyte molecules away from the surface and leading to a decrease in SERS intensity. Additionally, transient heating of

the colloidal particles caused by the pulsed laser lead to plasmon shifts and changes in absorption intensity, and decomposition of the silver particle due the extreme temperature conditions.

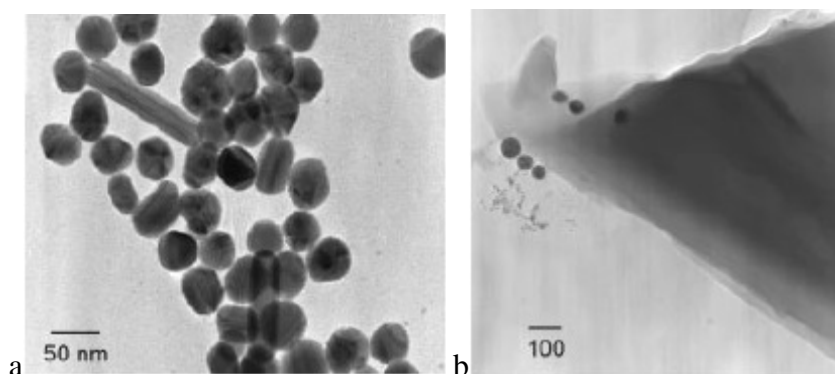


Figure 2.3 Effect of a high power pulsed laser on the colloids. Silver colloids before (a) and after exposure (b) (reproduced from reference 67).

SERS has also been successfully conducted with lasers in the visible as well as in the IR region. The work mentioned in appendix B in reference 73 showed the effect of laser wavelength while keeping all the parameters constant. The sensitivity of SER scattering was much better in the longer wavelength region due to the reasons already discussed above. The other important aspect was that the intensity of Raman peaks in the fingerprint region decreased sharply with the decrease of the wavelength of the exciting laser radiation. The AFM image of silver nano-wires and the SERS spectra after adding analyte molecules recorded at different wavelengths are reproduced<sup>73</sup> in figure 2.4.

The only drawback of using longer wavelengths was a weakening SERR response which otherwise increased the chances of enhanced sensitivity for single molecule detection. SERRS with a laser in the visible region, when used carefully, had been reported<sup>66</sup> to give very high enhancement in Raman intensity. The capability of SERRS in fluorescence quenching when recording spectra in the near-resonance region using 514.5 nm laser wavelength was demonstrated and a comparison of resonance Raman and surface enhanced resonance Raman spectra are reproduced in figure 2.5 A and B respectively<sup>66</sup>.

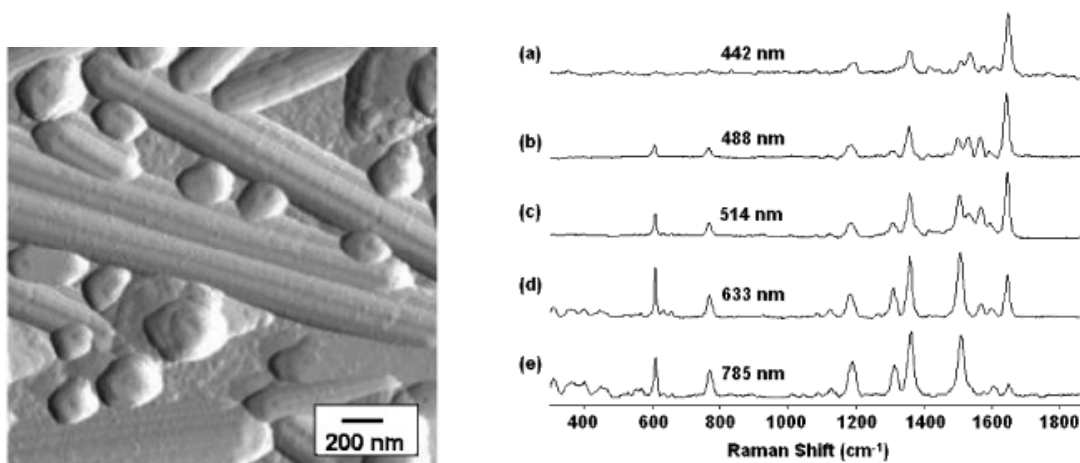


Figure 2.4 AFM image of silver nano-wires (a) and SER spectra after adding analyte molecules recorded at different wavelengths as indicated (b) (reproduced from reference 73).

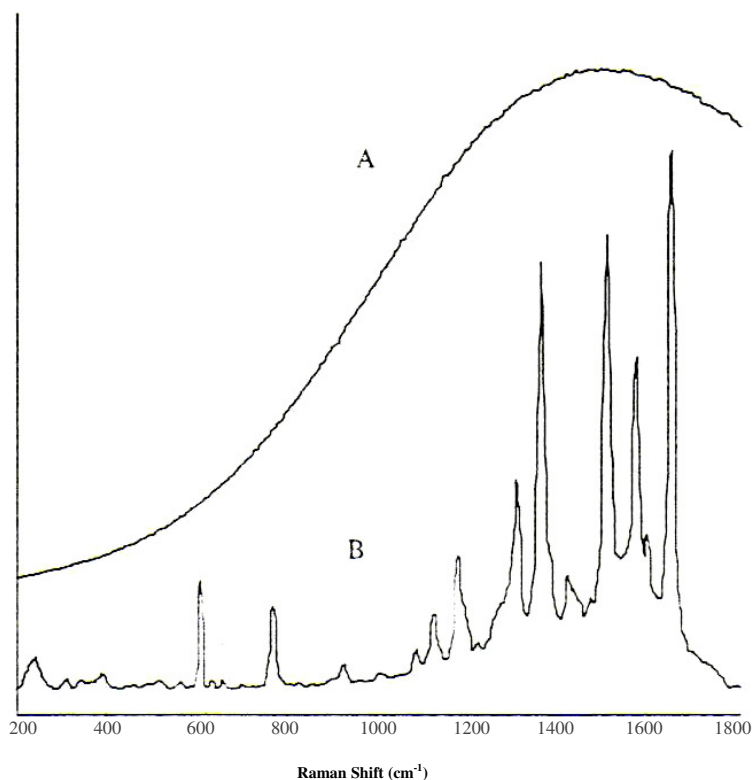


Figure 2.5 Resonance Raman spectrum of Rhodamine 6G molecules recorded with 514.5 nm laser wavelength (A) and its SER spectrum shows decrease of fluorescence and increase in S/N (B) (reproduced from reference 66).

In figure 2.5, the SERR spectrum (B) and the resonance Raman spectrum (A) of the same concentration of Rhodamine 6G dye was recorded using 514.5 nm excitation



wavelength. The Resonance Raman spectrum was completely obscured by the fluorescence, whereas the SERR spectrum was clearly observed as most of the fluorescence was quenched. This ultra high S/N in SERR scattering gave it an advantage over all other techniques of Raman spectroscopy. It should be kept in mind that for such a system to work the laser wavelength has to be selected specifically for an analyte and it becomes impracticable for the analysis of unknown materials in the environmental matrix.

The unprecedented sensitivity of SERS has been reported widely<sup>9,13,39,42,71,79</sup>. Mostly the relative concentrations justifying the single molecule adsorbed on single metal particle was reported<sup>39</sup> whenever the analyte concentration was of the order of  $10^{-12}$  to  $10^{-14}$  M and colloidal volume was of the order of pico litres. Two classes of systems capable of producing super-hot sites were small nano-particle and its aggregates in which interstitial sites were the super-enhancing locations, and secondly the large fractal aggregates in which the hot spots arise from the symmetry breaking. It was these hot spots that were considered to be responsible for the enhancements high enough to allow almost routine detection of a Raman signal from a single molecule as reported by Kneipp<sup>39</sup>, Sasic et al<sup>71</sup> and Moskovits-Jeong<sup>79</sup>.

### **Effects of surface conditions**

One of the limitations of SERS is the possible lack of compatibility of an analyte molecule with the adsorbate. Development of surfaces capable of adsorbing a molecule of choice or a wide variety of them is still an area of active research. A promising technique being developed involves adding a ‘buffer’ molecule that sticks to the surface and to the analyte, making a bond between the two. Leyton et al<sup>68</sup> did interesting work in this field while working with Polycyclic Aromatic Hydrocarbons (PAH). They used calixarenes on silver metal colloidal suspensions and nano-particle immobilized films. It was found that the calixarene host molecule adsorbed onto the metal surface captured the PAH molecule close enough to the surface for the detection by SERS, as is shown in figure 2.6. The optimum aggregation was achieved by controlling the adsorbate concentration. From the analysis of the SER spectra, useful information could be obtained about the importance of the calixarene affinity for PAH and metal surfaces.

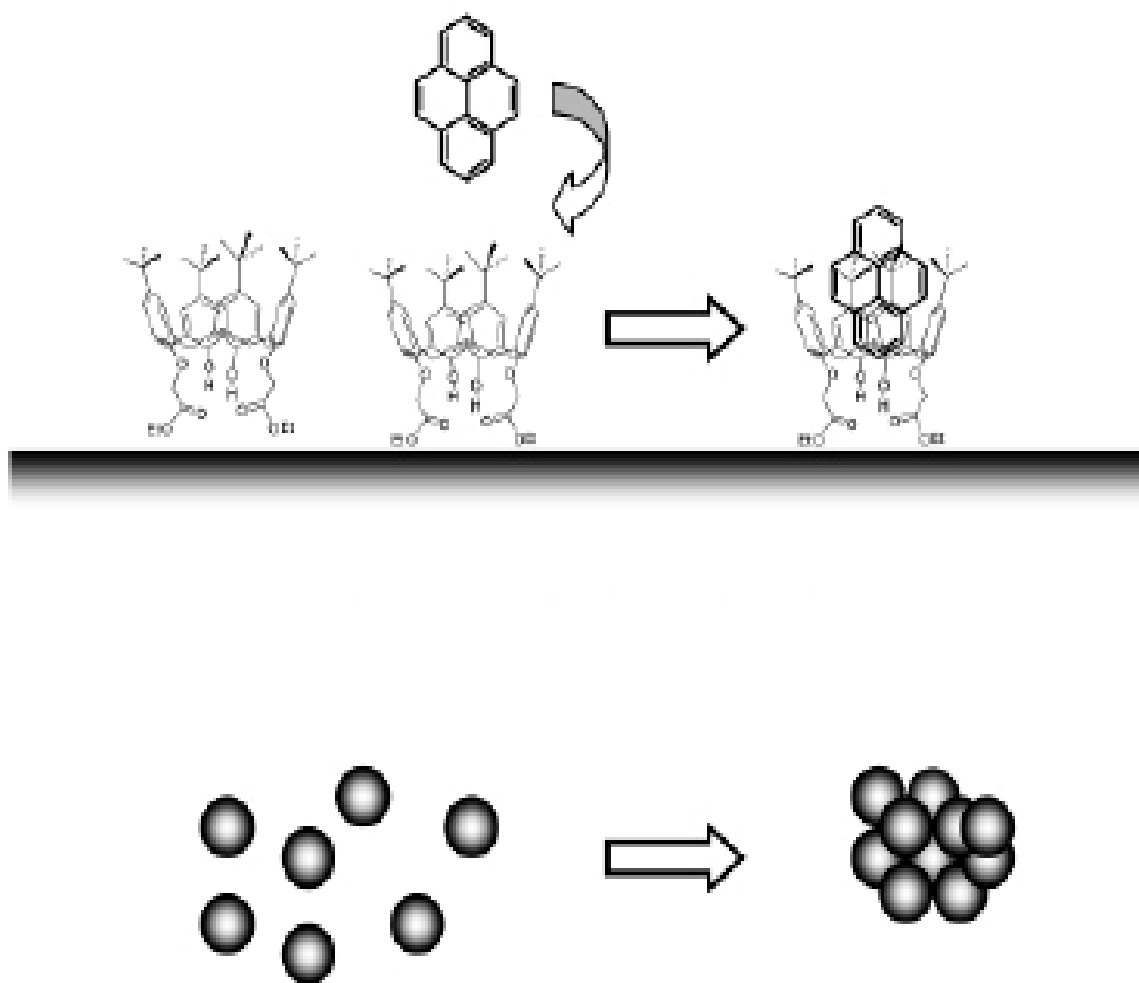


Figure 2.6 A calixarene causes aggregation in colloids (bottom) and links to PAH (top) simultaneously (reproduced from reference 68).

#### 2.4.2 SERS with solid SER-active surfaces

Unlike colloidal solutions, large SER-active metal surfaces are also being used for SERS study. The process involves making the metal surface rough at nano-scale to get the SER enhancement. The initial SER effect was experimentally observed from a roughened electrode surface<sup>9,13,50,54</sup>. A number of techniques have been used since to produce such roughness on the metal surface. Mostly the surfaces were fabricated either by molecular deposition or by roughening the metal surfaces. Different techniques have been used for these and are reviewed in detail in several publications<sup>46,49,54,57,61-65,84-92</sup>. Some of the more relevant ones are discussed here.

The most commonly used method for preparing solid SER-active surface was found to be vapour deposition of metal on solid substrates<sup>85-87</sup>. The deposition was achieved by

either chemical evaporation or through sputtering. Both methods have been used to produce highly SER-active surfaces, but it was found that the deposition can be controlled more precisely in sputtering<sup>88,89</sup>. In this method the molecules were made to sputter out of a target metal, mostly silver, after being hit by Argon ions in a vacuum chamber and were deposited uniformly on a substrate. The control on the rate of deposition, layer thickness, substrate temperature and vacuum pressure resulted in highly controlled surface film morphology. In addition, sputtering has also been done in the presence of various gases which gave a variety of options in achieving the surface roughness. In one such technique reported by Buchel et al<sup>89</sup>, silver oxide layers were deposited at various concentrations of oxygen in the chamber used to produce SER-active surfaces.

In another method reported by Lee et al<sup>84</sup>, the metal surface was hit by controlled high powered laser pulses. That resulted in ablation of metal particle from the surface. The surface roughness of the metal was controlled by verifying the laser power output and duration of laser pulse during ablation. Although a satisfactory SER enhancement was reported, the surface could not be roughened uniformly nor was the roughness optimum for SERS. Therefore, this method is not being used commonly. The ablated silver and gold particles from the metal surfaces were reported<sup>84</sup> to remain in suspension and could be used as SER-active surface, but were found to have a wide variation in particle sizes and therefore, this also was found to be an unsatisfactory technique. The advantages of laser ablation, however, are its simplicity and the absence of chemical reagents or ions in the final preparation.

Fibre optic SER sensors were prepared by coating etched fibre tips with metal layers<sup>74</sup>. The SEM images are reproduced in figure 2.7. Although the diameter of each fibre was around 30-40 nm, the roughness and the arrangement of the roughened edges did not give very high enhancement. Similar work was reported by Viet and Hill<sup>62</sup> where they mechanically roughened the fibre tips before coating them with a silver film. Again, the concentration of analyte was  $10^{-2}$  M which was not low enough to show enhancement usually associated with SERS.

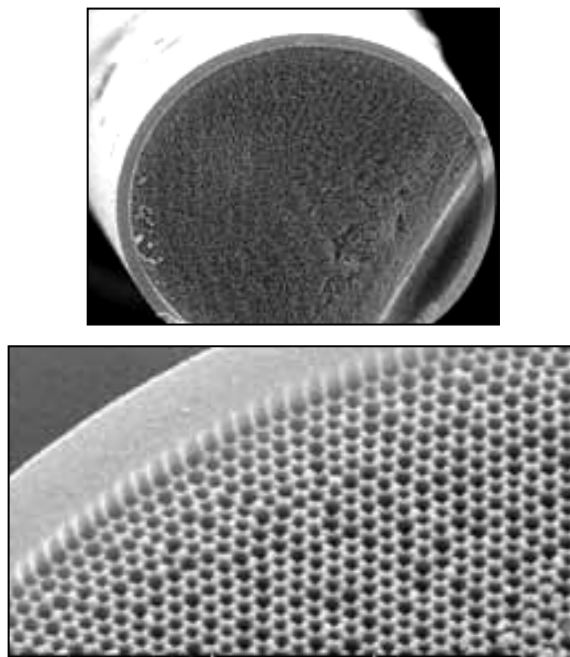


Figure 2.7 Fibre optic SER sensor made of silver coated etched optical fibres (reproduced from reference 74).

Perez et al <sup>64</sup> produced simple SER-active surface by etching silver foil with nitric acid for different time durations. The results obtained were related to the corresponding capacity of the treated substrate for strong SER signals. A magnified image of silver foil etched for 3 minutes in nitric acid solution (8:20 in water) is reproduced in figure 2.8. His work concluded that the maximum increase in the SER signal was obtained after 3 minutes of etching with the given concentration of nitric acid. Longer etching times caused a decrease in signal strength and subsequently resulted in the complete dissolution of the silver foil. The etched foil did not have uniform roughness and its use as SER-active surface for sensitive detection was limited.

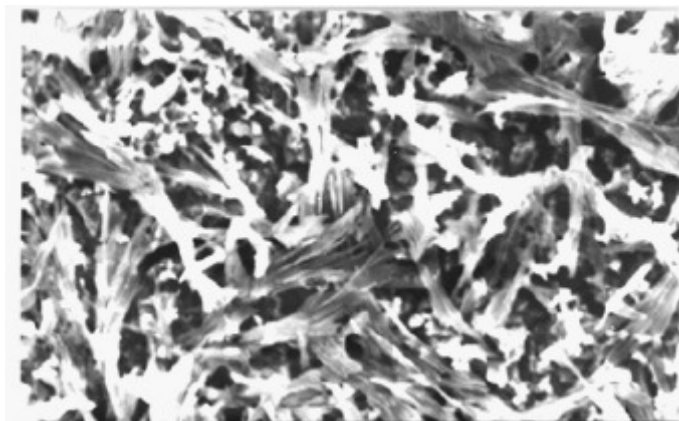


Figure 2.8 Silver foil etched for 3 minutes in solution of HNO<sub>3</sub><sup>64</sup>.

There are many techniques for preparing SER-active surfaces by depositing metal layers on a suitable substrate as described in appendix B as well as in earlier discussions. Work of Drachev et al<sup>76</sup> used a silica layer on a glass substrate and then added a partial layer of silver on it to prepare SER-active surface. The partial layer created protrusions of 10 to 13 nm height on the surface which gave a reasonably high Raman signal. The SEM image of a partial silver layer is reproduced in figure 2.9 (a)<sup>76</sup>. Bao et al<sup>65</sup> coated various sizes of silica beads with the silver particles to obtain SER effect but the enhancement effect seemed to be mainly from the silver particles sticking on to the silica beads and not from the silica beads themselves as is shown in figure 2.9 (b).

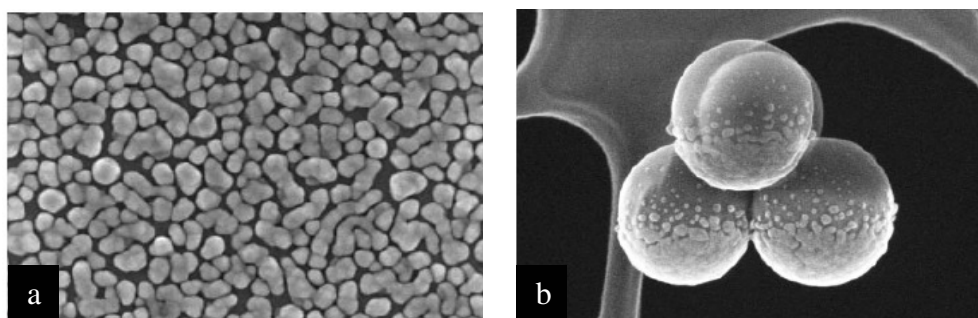


Figure 2.9 Partial silver layer on silica coated glass substrate (a). Silica beads coated with silver particles (b) (reproduced from references 76 and 65 respectively).

Several lithographic techniques have been used to prepare nano-structured SER-active surfaces. Of these ion beam lithography<sup>93</sup>, nano-imprint lithography<sup>94</sup> and nanosphere

lithography are promising ones. Ion beam lithography was found very costly in terms of time and resources whereas nano-imprint lithography was comparatively simple in process, yet its mould formation at nanoscale was very complex. Nanosphere lithography was found better than the rest is discussed here in detail.

### Nanosphere Lithography (NSL)

A very exciting method for producing uniform surface roughness by nano-sphere lithography was reported by Sun et al <sup>95</sup>. They used 265 nm diameter polystyrene micro-spheres assembled on a gold substrate, pressed thermally to achieve a non-spherical layer. A silver layer was put on it and the micro-spheres were washed away to get an hexagonal silver nano-network. SEM images of the assembled micro-spheres and final surface achieved by the authors are reproduced in figure 2.10.

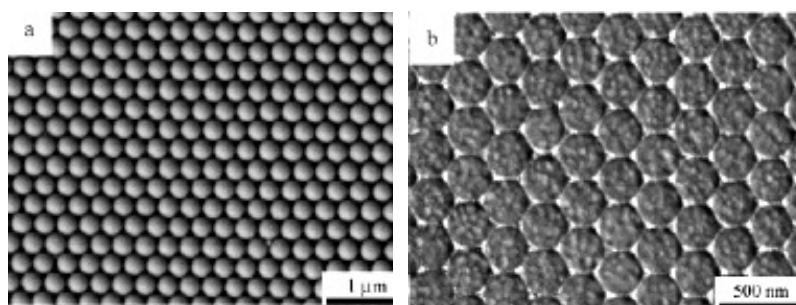


Figure 2.10 Polystyrene micro-sphere assembly on gold substrate (a) and hexagonal silver nano-network achieved after thermal pressing and removal of micro-spheres (b) (reproduced from reference 95).

Astilean <sup>96</sup> demonstrated an even simpler form of nano-spheres lithography by assembling a monolayer of 400 nm diameter polystyrene nano-spheres on silica and then coating with thermally evaporated silver. Polystyrene beads were removed to get a periodic array of silver particles. The SEM images of both before removal of beads and final silver rough surface are shown in figure 2.11. Extensive work on nanosphere lithography (NSL) has been done by Van Duyne's group <sup>58,80,97-99</sup>. In one case <sup>80</sup>, 400 nm diameter polystyrene nano-spheres were coated in a monolayer on a glass substrate and then 50 nm thick silver film was deposited before removing the nanospheres from the substrate. The rough silver surface was capable of detecting analyte concentrations down to  $10^{-13}$  M. An AFM image of the final SER-active surface is reproduced in figure

2.12 showing arrays of silver nano-structures, each small structure being ~231nm apart (centre to centre) and ~93nm in size (perpendicular bisector of the triangle).

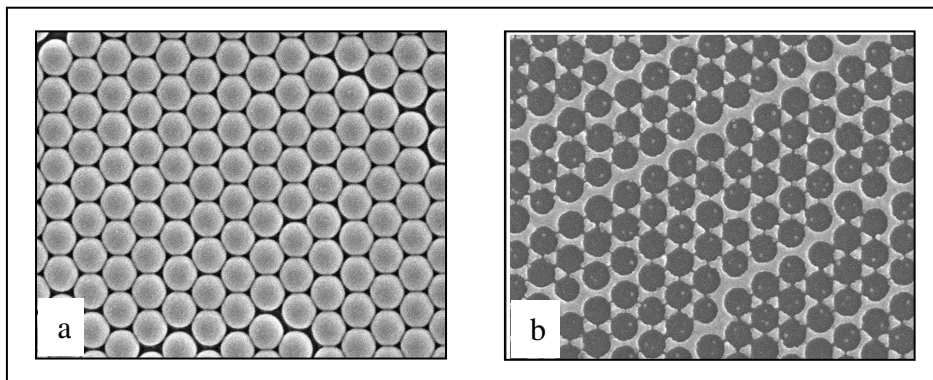


Figure 2.11 SEM images of crystalline assembly of polystyrene spheres of 400 nm diameter (a) and periodic array of silver particles left on the substrate (b) (reproduced from reference 96).

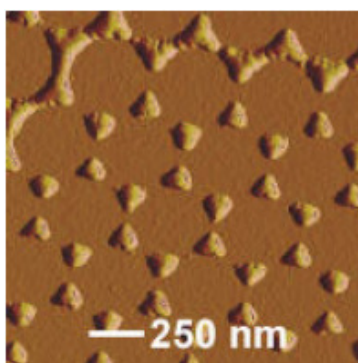


Figure 2.12 AFM image of 51 nm high silver patterns left after removal of polystyrene nanospheres (reproduced from reference 80).

Schmidt et al <sup>100</sup> has claimed SER enhancement of the order of up to  $10^6$  for rhodamine 6G dye molecule when using an ordered silver nano-cluster array using 900 and 400 nm diameter latex nanospheres. Although higher enhancement of Raman intensity has been achieved with colloidal system in suspension than with the large surfaces, the latter offers many other advantages for field deployment. Silver coated substrates were found to be more robust than colloidal solutions and are expected to withstand a field environment better. Systems like fibre optic SER sensors <sup>62,74</sup> that did not require changing the substrate for every test seem promising.

## 2.5 Application of SERS

It has been discussed already that the most critical stage of development in SERS is the SER-active surface having high concentration of ‘hot spots’ and also capable of adsorbing desired analyte<sup>36,39,49</sup>. It is considered that large EM field enhancement in the metal-molecule complex combined with chemical enhancement by a charge transfer mechanism gave a large SER cross-section, making a single-molecule detection feasible<sup>13,42,46,101</sup>. Routine detection, however, at such a high sensitivity is not yet possible due to poor reproducibility of the surfaces, variations in the surface roughness, and variability in colloidal size.

It was reported that the morphology of the structures in terms of shape, size and height could be controlled<sup>98</sup>. The size and shape were systematically modified by varying both the size of the nanospheres, figure 2.13 A and B, and by the monolayer/double layer configurations, figure 2.13 C-F. A specific morphology was achieved within a nanostructure cluster.

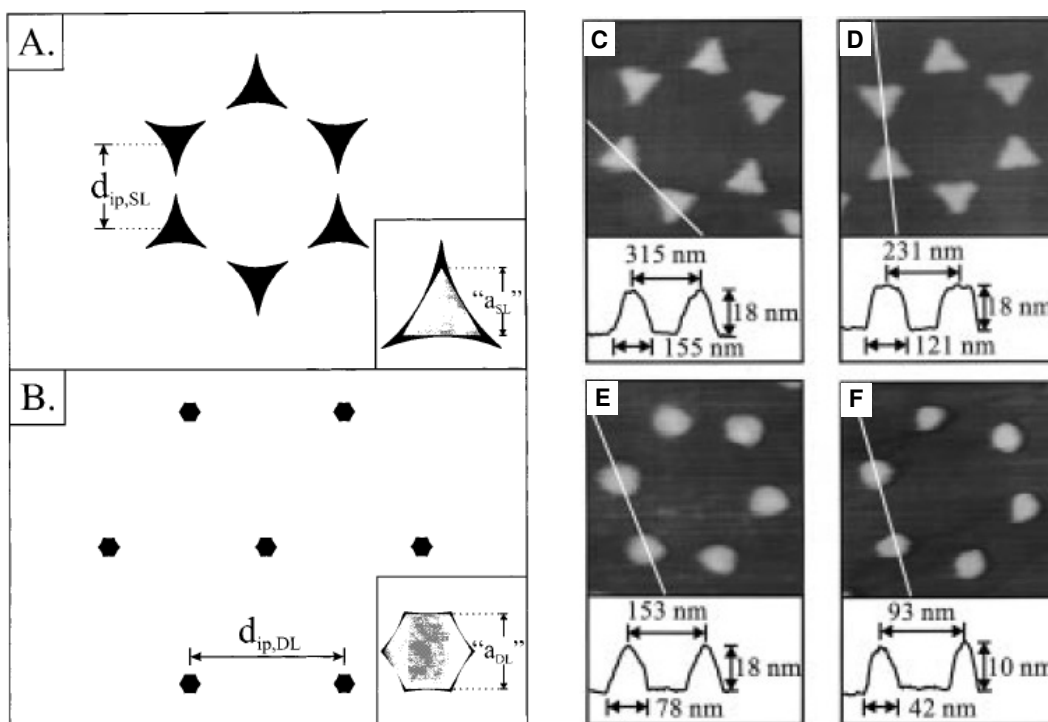


Figure 2.13 Schematics of a single structural array formed from single layer (A) and double layer (B) configurations. AFM image of single layer arrays on mica substrate formed with nanosphere diameter of 542 nm (C), 401 nm (D), 264 nm (E) and 165 nm (F). (Reference 98)



Achievement of local surface plasmon (LSP) was found to be dependent on the resonance conditions. LSP resonance (LSPR) was studied by Van Duyne's group<sup>58,98,99,102</sup> and others<sup>49,101</sup>. It was found that the LSPR depended on the morphology of the silver nano-structures. Not only the shape and size of the nano-structure but the height of the structure had a major impact on the LSPR values. Jensen et al<sup>58</sup> did a UV-Visible extinction study on surfaces fabricated with ~301 nm diameter nanospheres with varying height of the silver structures (thickness of silver layer). The results are reproduced in figure 2.14. Note that the LSP resonance (LSPR) occurs at the wavelength of highest absorption. So, with the increase in the height 'h' (nm) of the silver structures the LSPR value (wavelength of maximum absorption,  $\lambda_{\max}$ ) decreased. Therefore, the SER-active surface could be tuned to be in the LSPR region depending on the laser wavelength used to achieve higher enhancement in the Raman scatterings. In the same study a surface fabricated using 542 nm diameter nanospheres and a silver layer ~50 nm thickness showed maximum absorption at the wavelength of 782 nm.

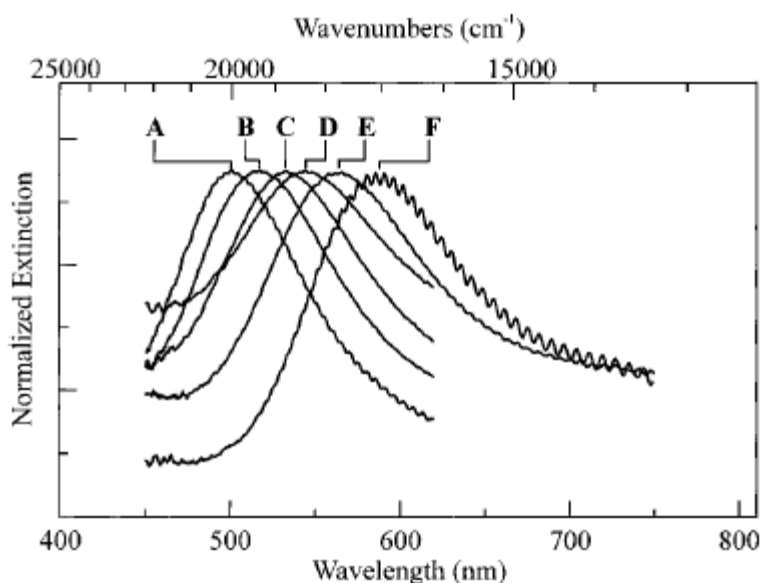


Figure 2.14 UV-visible spectra of surfaces fabricated with 301 nm diameter nanospheres.  $h = 58$ ,  $\lambda_{\max} = 501$  (A),  $h = 53$ ,  $\lambda_{\max} = 517$  (B)  $h = 43$ ,  $\lambda_{\max} = 533$  (C),  $h = 38$ ,  $\lambda_{\max} = 544$  (D),  $h = 33$ ,  $\lambda_{\max} = 563$  (E) and  $h = 23$ ,  $\lambda_{\max} = 585$  (F) (reference 58)

The enhancement of SER scattering occurs when the excitation wavelength of the laser is in/near resonance either with the surface plasmon or with the target molecule or both.

This combination of SERS and resonance enhancement SERRS, has been reported<sup>66,103,104</sup> to give even higher enhancements of Raman scattering than  $10^{10}$ , with complete quenching of the fluorescence that was otherwise a major limitation in RRS. This would be of particular interest for in-situ remote detection in the presence of background species.

In SERRS the signals relate more to molecular scattering than to surface-molecule interaction and the additional sensitivity means that less laser power could be used<sup>101</sup>. This was found to reduce decomposition and give reduced background signals. SERRS has enabled the detection of sub-monolayer coverage of adsorbate in observation times of  $\sim 1$  second<sup>101</sup> and facilitated important technological developments in optical instrumentation (for instance diode lasers, fibre optics, collection optics, holographic notch filters, and sensitive low-noise multi-channel detectors)

Research has shown the potential of SERS to detect and to identify trace chemicals. The limit of detection (LOD) and quantification achievable by SERS improved in recent times, especially with the demonstration by many researchers of its capability of single-molecule detection discussed above. Recently Vo-Dinh et al<sup>105-107</sup> also achieved very low detection limits for a variety of chemical agents. Adsorption and detection of drugs on silver colloids was done recently by Rivas et al<sup>108</sup> and Segmulle et al<sup>109</sup>. Olson<sup>110</sup> et al used metal colloids to rapidly detect polycyclic aromatic hydrocarbons (PAH) at 5 ppb level in water. Lee et al<sup>111</sup> deposited silver film on the inner walls of glass sample vials and used this for multi-pesticide determination with a portable Raman system. SERS sensors developed with gold were reported<sup>112</sup> to detect nerve agent simulants at 50 ppb concentration and diethanol sulphide (a mustard simulant) and cyanide, each at the ppm level.

It was realised that the key to success in SERS for ultra-sensitive detection was to establish a strong analyte-surface compatibility. The laser wavelength was generally chosen either to coincide with the wavelength of absorption of the analyte or that of the surface plasmon<sup>9,13,49</sup>. Where both absorption bands were close, the choice was simple, but if these were far apart, the laser wavelength had to be chosen closer to either one of

the absorption bands. The SER spectrum was found to be susceptible to misinterpretation as some impurities adsorb preferentially on the SER-active surfaces, giving a much stronger signal. The photodecomposition effect was also found to contribute to the complexity by altering or desorbing the adsorbed surface species<sup>5</sup>.

SER's higher sensitivity has led to its use in explosive detection where there is a dire need for an extremely sensitive system<sup>1,8</sup>. Although many efforts are at hand, no field deployable system has been developed yet. Some of the work does not get published because of the nature of the confidentiality. Nevertheless, SciFinder Scholar 2004 gives reference to 15 publications directly related to explosive detection with SERS<sup>113</sup>, out of which only half are regarding the recent progress in this field. The works described in appendix B follow the goal of achieving lower LOD for different materials.

Explosives in general have comparatively low vapour pressure. Concentration of its vapour especially when sealed is likely to be extremely small. Therefore, materials with relatively higher vapour pressure found both in typical explosives and in other compounds, like peroxides and ammonium nitrate, increase the possibility of false alarm. Most of the work done so far has concentrated on nitro based explosives in general and TNT in particular. McHugh et al<sup>114,115</sup> have achieved very low detection limit for functionalised TNT, RDX and PETN using SERRS. Sylvia and co workers<sup>116-118</sup> in a series of papers have reproducibly detected the chemical signature of TNT explosive in the vapour phase from a buried landmine down to 5 ppb using SERS with roughened gold surfaces. Similar work was reported by Spencer et al<sup>119</sup> who, apart from buried landmines, also detected chemical and biological agents.

James et al<sup>120</sup> have recorded SER measurements of Tri-amino-trinitro-benzene (TATB) in the gas and liquid phase. Research on SERS reported by Kneipp et al<sup>121</sup> for TNT adsorbed on colloidal gold and silver in aqueous solution using an 830 nm laser wavelength claimed detection limits down to less than a picogram, making ultra-trace detection possible. Studies are being done in developing more sophisticated surfaces to further improve the detection capability. Montoya<sup>122</sup> has tried titanium-based surfaces to detect TNT, DNT and RDX with different lasers with results not yet comparable with

those observed with silver or gold. Spencer et al <sup>123</sup> have claimed a 5 ppb detection limit for TNT, and for HMX, RDX and PETN at 1 to 5 pg level from the headspace vapour. They have used electrochemically roughened gold and silver substrates and have claimed to have developed a ‘fieldable fibre optic SERS sensor’. The same group <sup>124</sup> have also reported the detection limits of 1 ppb for nerve-agent and 10 ppm for an explosive simulant in less than 30 seconds with a 785 nm wavelength laser source. Self assembling silica spheres of 450 nm diameter coated with 200 nm thickness of gold film were used as SER-active surfaces.

As stated above, critical progress in the field of Raman spectroscopy has been achieved with many encouraging developments occurring within the last decade. However, if SERS is to be used as an explosive detection technique, careful consideration of the chemical and the physical properties of the surface enhancement is required. From the review of the existing literature it is quite clear that with further understanding of the nanotechnology and using the technique within its limitations, ultra-trace detection is certainly possible.

## 2.6 Conclusions

Despite a large number of publications and extensive ongoing experimental and theoretical efforts to elucidate the physical basis of signal enhancement, the practicability of SERS for explosive detection is still elusive <sup>101</sup>. This is mainly due to the inability to reproduce the preparation of well-defined, reliable, and stable SER-active surfaces with a high concentration of ‘hot spots’. Additionally, problems of poor control over the particle aggregation state and of irreversible precipitation of metal colloids in solution have to be addressed according to a general consensus within the research community in the field.

For routine, on-line trace analysis, the literature shows that a SER-active surface is required to be stable, reproducible, inexpensive, and easy to fabricate. In simple terms, silver surfaces which give uniformly distributed roughness with height of the structures in the 50 to 400 nm range combined with ~700 to 800 nm laser excitation wavelength have been generally regarded as the most suitable SERS configuration for a field

system. The nanosphere lithographic (NSL) technique was found to be relatively more workable for SER-active surface fabrication within normal laboratory conditions, with high reproducibility and cost effectiveness.

### 3. THEORETICAL CONSIDERATIONS

#### 3.1 Raman Scattering and Resonance Raman Scattering

Raman theory, by now, is quite well established and has been developed by many researchers<sup>9,13,48,66</sup> over the last few decades. The theory deals with the molecular vibrational spectroscopy and the process has been fully explained using quantum theoretical procedures in the interaction of EM radiation with molecules<sup>13</sup>. Normal Raman scattering involves excitation to higher vibrational states via a virtual state as shown schematically in the energy diagram in figure 1.2 (chapter 1). Although quantum theory is needed for the explanation of all Raman phenomena, particularly the dependence of its strength on the wavelength of the excitation radiation, an insight can be obtained from first principles using classical procedures<sup>9,48</sup>.

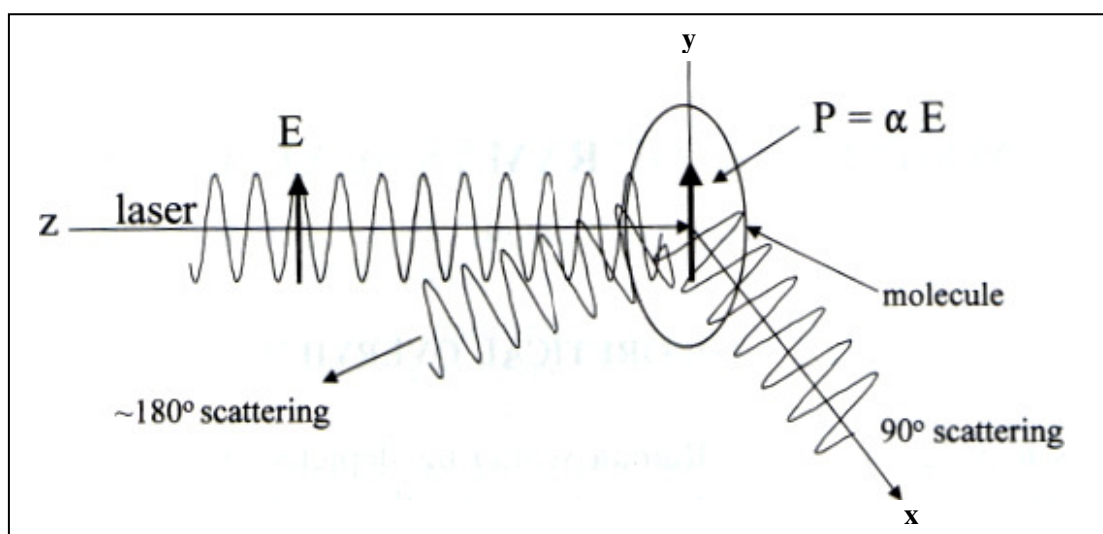


Figure 3.1 Dipole moment 'P' induced in the electronic cloud of the molecule by the incident field 'E' of the laser that results in scatterings. (Reference 9).

Consider a molecule that is subjected to an incident electric field so that it becomes polarised, i.e. the electron orbitals assume a preferential shape. The dipole moment induced in the molecule, 'P', (shown in figure 3.1) is related to the incident electric field strength 'E' by <sup>9</sup>:

$$P = \alpha E \quad \text{-----} \quad 3.1$$

where 'α' is polarisability of the material i.e. the ease with which the electronic cloud can be distorted. For a sinusoidal varying electric field, the dipole moment will also vary at the same frequency. In such a case the field strength in time 't' will be given by:

$$E = E_0 \cos 2\pi\nu_0 t \quad \text{-----} \quad 3.2$$

where  $E_0$  is the equilibrium field strength and  $\nu_0$  is the frequency of the incident light (laser). The fluctuating dipole with frequency  $\nu_0$  will scatter radiation at the same frequency  $\nu_0$ , which is called Rayleigh scatterings. The molecular vibrations are composed of specific vibrational modes. A non-linear molecule (like H<sub>2</sub>O) having N atoms will have 3N-6 modes and a linear molecule (like CO<sub>2</sub>) will have 3N-5 modes. Now if a molecule having 'j' modes vibrating with  $\nu_j$  at time 't', mode  $Q_j$  will be given by:

$$Q_j = Q_j^0 \cos 2\pi\nu_j t \quad \text{-----} \quad 3.3$$

where  $Q_j^0$  is the state without the laser radiation. If the polarisability of the electrons changes with the changes in the molecular vibrations then:

$$\alpha = \alpha_0 + \frac{\delta\alpha}{\delta Q_j} Q_j \quad \text{-----} \quad 3.4$$

Now with combination of equations 3.1 and 3.2:

$$P = \alpha E_0 \cos 2\pi\nu_0 t \quad \text{-----} \quad 3.5$$

Combining equations 3.3 and 3.4 we get:

$$\alpha = \alpha_0 + \left( \frac{\delta\alpha}{\delta Q_j} \right) Q_j^0 \cos 2\pi\nu_j t \quad \text{-----} \quad 3.6$$

Substituting the value of polarisability from equation 3.6 into equation 3.5, we get:

$$P = \alpha_0 E_0 \cos 2\pi\nu_0 t + \frac{\delta\alpha}{\delta Q_j} Q_j^0 E_0 (\cos 2\pi\nu_0 t) (\cos 2\pi\nu_j t) \quad \text{-----} \quad 3.7$$

The above equation, after trigonometric manipulation, can be written as follows:

$$P = \alpha_0 E_0 \cos 2\pi\nu_0 t + \frac{E_0 Q_j^0}{2} \frac{\delta\alpha}{\delta Q_j} [\cos 2\pi t(\nu_0 + \nu_j) + \cos 2\pi t(\nu_0 - \nu_j)] \quad \text{-----} \quad 3.8$$

This accounts for the fact that, in the interaction process, there are three components of scattered radiation. Rayleigh scattered component  $\nu_0$  having the same frequency as the incident radiation field, anti Stoke Raman scattered component having frequency  $(\nu_0 + \nu_j)$  which is higher than that of the incident radiation field and the Stokes Raman component having frequency  $(\nu_0 - \nu_j)$  which is lower than that of the incident frequency. The Raman shift  $\Delta\nu \text{ cm}^{-1}$  (wavenumber unit) is defined in terms of the incident wavelength  $\lambda_0 = c/\nu_0$  and the Raman scattered wavelength,  $\lambda_j = c/\nu_j$  as:

$$\left( \frac{1}{\lambda_0} - \frac{1}{\lambda_j} \right) = \Delta\nu \text{ (cm}^{-1}\text{)}$$



The Raman shift corresponds to the specific line of an IR absorption spectrum (vibrational mode). These scatterings processes are shown in simplified graphical form in figure 1.2 and 3.2. Equation 3.8 also highlights:

1. Polarisation and scattering intensities are proportional to incident radiation field.
2. Raman scattering is produced by the vibrations that result in the change in the polarisability of the molecules.
3. Raman shift is positive for Stokes scatterings and negative for anti-Stokes scatterings.
4. For anti-Stokes scatterings to occur, the molecule has to be in a vibrational excited state and at normal temperatures is much weaker than Stokes scatterings.
5. Raman intensity depends upon the polarisability and therefore it varies greatly for different molecules and for different vibrational modes within the molecule.

The extension of the theory provides <sup>9</sup> a relationship between the Raman intensity ‘ $I_R$ ’ and the frequency of the incident radiation:

$$I_R \cong \mu(v_0 \pm v_j)^4 \alpha_j^2 Q_j^2 \quad \text{-----} \quad 3.9$$

where ‘ $\mu$ ’ is the constant of proportionality and is assumed to be independent of the Raman frequency. For normal Raman scattering,  $v_0 \gg v_j$  and therefore, the latter can be ignored for all intent and purposes. Under these conditions the equation highlights that the normal Raman intensity is proportioned to the fourth power of the incident frequency <sup>125</sup>. Considering  $v_0 = c/\lambda_0$ , where  $c$  is the speed of light and ‘ $\lambda_0$ ’ is the wavelength of the incident laser, the Raman intensity is therefore proportional to the inverse fourth power of wavelength of the incident laser;

$$I_R \propto \frac{1}{\lambda_0^4} \quad \text{-----} \quad 3.10$$

Although this dependence is valid at excitation far removed from any real allowed electronic states of the molecules, it is not valid at near resonance excitation. Only

quantum theoretical considerations allow one to account for overtones and combination modes in Raman spectra and the complete wavelength dependence of its intensity. The derivations of such a theory are complex<sup>9,13</sup> and are beyond the scope of this thesis.

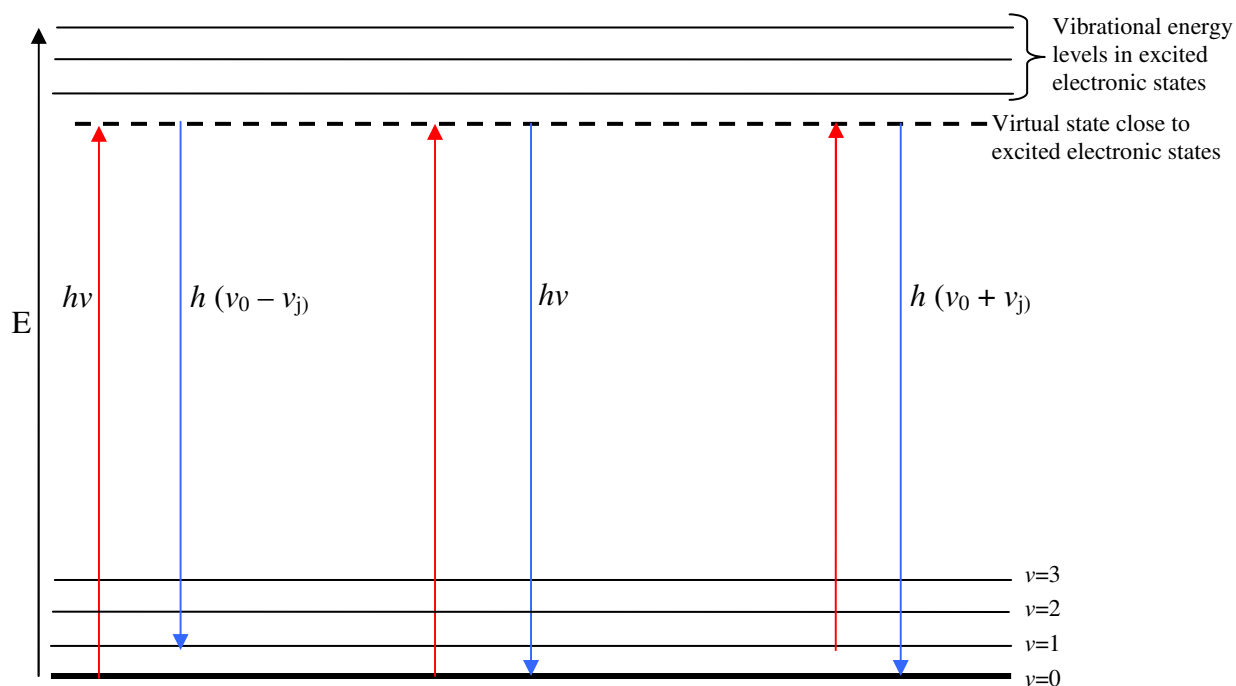


Figure 3.2 Simplified graphical representation of Resonance Raman Process.

In simple terms, at near resonance excitation (figure 3.2), the Raman intensity becomes higher giving rise to resonance enhancement. Another important aspect of RRS is the selectivity of the Raman band enhancement. There are Raman bands which undergo more enhancements while others are not enhanced at all. Such selectivity is governed by the coupling of the energy states involved in the interaction process.

Full effect of resonance can be demonstrated in the form of a Raman excitation profile (REP). A tuneable laser is required so that Raman spectra can be recorded for excitations at different laser frequencies. The Raman intensity of selected bands is then plotted against the frequency of the laser. Theoretically, the highest intensity will be at the resonance frequency but due to strong absorption and thermal dissipation of the energy, it becomes impossible to observe a Raman signal. Different vibrations will have

varying profiles as per the resonance effect. Although this technique is extremely sensitive to minor structural changes and the selective determination of an individual chromophore is possible, even traces of fluorescence can prevent acquisition of Raman spectra and vibrations with weak resonance enhancement may not be observed. It is not necessary to use the laser line exactly in the highest absorbance region of the material, rather resonance enhancement is normally recorded with the laser line close to it.

As already mentioned in chapter 1, the application of Raman spectroscopy is limited by fluorescence and low sensitivity. Fluorescence is a material property and in an open environment many types of molecule are likely to fluoresce. With selection of laser operating at a long wavelength region and a modern spectrometer, the fluorescence can be largely avoided. But the longer the excitation wavelength the lower the Raman intensity (for a given setup), which means poor detection limits. Apart from fluorescence, background noise has a major contribution to low sensitivity i.e. signal to noise ratio (S/N) <sup>12</sup>. Efforts to improve S/N have pushed the limits of existing technology and for a given sample it has improved many folds. Introduction of multi-channel techniques, use of longer wavelengths and low noise detectors have helped to reduce unwanted signals. The S/N has been described <sup>9</sup> as the ratio of average peak height of the specific Raman band, ‘S’ and the standard deviation of the peak height ‘ $\delta y$ ’:

$$S/N = \frac{S}{\delta y} \quad \text{-----} \quad 3.11$$

$\delta y$  decreases with the number of measurements. It is the combined effect given as:

$$\delta y = \sqrt{\delta_S^2 + \delta_B^2 + \delta_D^2 + \delta_F^2 + \delta_R^2} \quad \text{-----} \quad 3.12$$

$\delta_S$      Signal shot noise occurring during photon counting by poisson statistics.

$\delta_B$      Background shot noise; photons other than Raman scatterings arising from stray laser, reflections and fluorescence.

- $\delta_D$  Detector dark noise; thermal generation of electrons from within the detector.
- $\delta_F$  Flicker noise; variation in laser intensity.
- $\delta_R$  Readout; arising during the constant process of converting electrons from the detector to useful form.

In practice, a spectrometer is designed so as to minimize most of these effects, except mainly from sample and from the environment.

### 3.2 Surface enhanced Raman spectroscopy (SERS)

Attempts have been made to explain the theory of SERS by Smith<sup>13</sup>, McCreery<sup>9</sup>, Hicks<sup>40</sup>, Tian<sup>36</sup>, Chang et al<sup>41</sup>, Moskovits<sup>42,46</sup>, Campion et al<sup>44</sup>, Roy et al<sup>54</sup>, Wu et al<sup>126</sup>, Kneipp et al<sup>50</sup> Smith and Dent<sup>13</sup>, Weatherby<sup>90</sup> and the most recent by Aroca<sup>49</sup>. These theories are still under development and do not fully account for the observed phenomenon. The understanding of SERS process is needed for its effective application by optimising experimental parameters for achieving maximum sensitivity. Here only the salient points are presented for enabling a comprehension of the likely mechanism of the effect and complete derivations of the theories propounded by different authors is beyond the scope of the present study. A phenomenological explanation of SERS is presented below.

Two effects known to produce enhancement in surface Raman measurements are: *electromagnetic* (EM) enhancement and *charge transfer* (CT) or chemical/electronic enhancement. The exact contributions of electromagnetic and chemical enhancements are not completely clear. However, the former is known to contribute much more towards the enhancement of Raman scatterings than the latter. It is commonly agreed<sup>42,49</sup> that the enhancement depends largely on the optical properties of the metal-molecule complex, the vibrational modes of molecule under study and the orientation of the adsorbed molecule.

The simplified approximation<sup>127</sup> used to explain the combined enhancement factor ‘G’ was:

$$G_{\text{vibration}} = G_{\text{EM}} \times G_{\text{electronic}}$$

The effect of each is briefly discussed here.

### 3.2.1 Electromagnetic (EM) Enhancement

Aroca<sup>49</sup> has used Moskovits's explanation to define the EM enhancement mechanism as follows:

*'As it is currently understood, SERS is primarily a phenomenon associated with the enhancement of the electromagnetic field surrounding small metal objects optically excited near an intense and sharp dipolar resonance such as a surface-plasmon polarisation. The re-radiated dipolar fields excite the adsorbate, and, if the resulting molecular radiation remains at or near resonance with the enhancing object, the scattered radiation will again be enhanced (hence the most intense SERS is the frequency-shifted elastic scattering by the metal). Under appropriate circumstances the field enhancement will scale as  $E^4$ , where  $E$  is the local optical field.'*

The conduction electrons on the surface of a metal like silver, gold or copper are in the form of a cloud. The electron density, being negatively charged, is held in place at a distance from the surface due to the presence of positive charge from the metal centres as shown in figure 3.3 (A). With the interaction of light, these clouds begin to oscillate as a group across the surface. The collective oscillation of this electron cloud near the surface of the metal, when excited, is called a *surface-plasmon*<sup>13</sup> and is described schematically in figure 3.3 (B). Therefore the creation of surface plasmon is a necessary requirement for SER scatterings to be observed. On a flat non-adsorbing metal surface only Raman or resonance Raman scatterings can be observed for that molecule-surface interface (figure 3.3 (A)). The SER scattering occurs when the plane of the oscillation of the surface plasmon is perpendicular to the metal plane. This is provided by the surface roughness that can be in the form of protrusions on the solid metal surface or in the form of small aggregated metal particles in suspension. If the molecules are adsorbed at these metal protrusions within the surface plasmon (figure 3.3, C), the Raman scatterings are greatly enhanced. The excitation of surface plasmon provides the theoretical basis for the development of the EM enhancement mechanism.

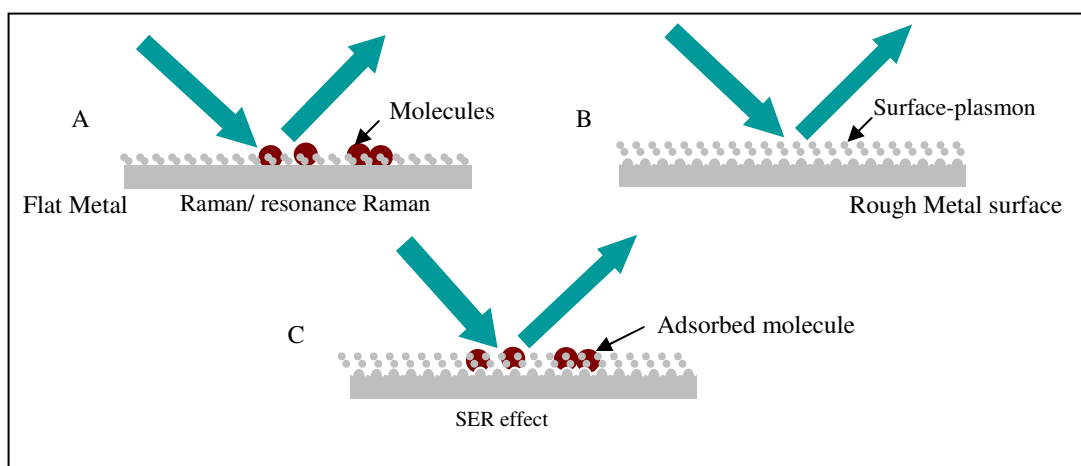


Figure 3.3 Schematic representation of Raman, resonance Raman and SER effect.

The EM mechanism is considered<sup>9,49</sup> to contribute more towards enhancement of SER scatterings and has been explained by considering a spherical particle being irradiated by an electric field as shown in figure 3.4. If a molecule placed near the surface of the metal particle is irradiated with the light having a wavelength longer than the particle diameter, it polarises the electron cloud and they start to oscillate (surface plasmon) with the frequency of the light. This polarisation generates a local electric field which is in resonance with the optical field but is much larger<sup>13,50</sup>. Now if the molecule is within the surface plasmon, as in figures 3.3 and 3.4, it will experience the effect of a much higher local field as compared to that of the light in the absence of the surface plasmon. This will enhance the scattering and the whole process is called EM enhancement.

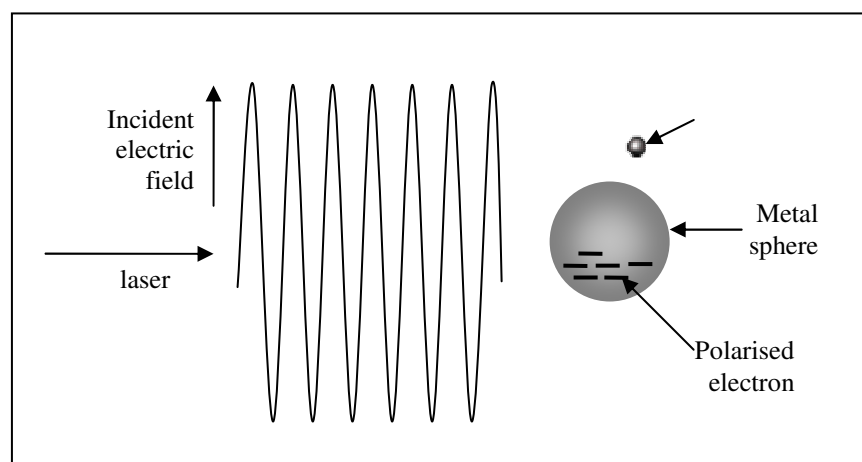


Figure 3.4 Graphical representation of SERS effect on metal sphere. (reference 9).

In the system shown in figure 3.4, the model considered <sup>42</sup> was a small metal sphere with dimensions smaller than the wavelength of illuminating light sustaining oscillating surface plasmon. Systems with free or almost free electrons sustain such dipolar plasmon resonance. When the exciting laser light is resonant with the dipolar plasmon the metal particle will radiate light characteristic of dipolar radiation. This radiation is a coherent process with the exciting field in which light intensity from a certain portion of space surrounding the particle is depleted while the intensity at certain portions near the metal particle is enhanced. Moskovits <sup>42</sup> defines the field enhancement factor averaged over the surface of the particle as ‘g’. The metal particle radiates field having an average magnitude, ‘E<sub>S</sub>’, <sup>9,42</sup>:

$$E_S = g E_0 \quad \text{-----} \quad 3.13$$

where ‘E<sub>0</sub>’ is the magnitude of the incident field. On the average, molecules adsorbed at the surface of the metal particle, therefore, will be excited by a field whose magnitude is ‘E<sub>S</sub>’, and the field strength of the Raman-scattered light, ‘E<sub>R</sub>’, produced by the molecule will be:

$$E_R \propto \alpha_R E_S \propto \alpha_R g E_0 \quad \text{-----} \quad 3.14$$

Here ‘α<sub>R</sub>’ is the combination of Raman components of polarisability. The metal particle will further enhance the Raman-scattered fields in the same manner as it enhanced the incident field, i.e. the metal particle can scatter light at the *Raman shifted* wavelength enhanced by a factor g’. SER-scattered field will therefore have the field strength, ‘E<sub>SERS</sub>’, given by:

$$E_{SERS} \propto \alpha_R g g' E_0 \quad \text{-----} \quad 3.15$$

And the average SERS intensity ‘I<sub>SERS</sub>’ will be proportional to the square modulus of E<sub>SERS</sub>:

$$I_{\text{SERS}} \propto |\alpha_{\text{R}}|^2 |gg'|^2 I_0 \quad \text{-----} \quad 3.16$$

Where  $I_0$  is the intensity of the incident field. For low-wavenumber bands when  $g \approx g'$ , the SER intensity will be enhanced by a factor proportional to the fourth power of the enhancement of the local incident near-field 'E<sub>L</sub>':

$$|E_{\text{L}}|^4 = |g|^4 \quad \text{-----} \quad 3.17$$

The SER scatterings component due to EM enhancement,  $G_{\text{EM}}$ , can be defined as the ratio of the Raman-scattered intensity in the presence of the metal particle to its value in the absence of the metal particle:

$$G_{\text{EM}} = \frac{|\alpha_{\text{R}}|}{|\alpha_{\text{R}_0}|} |gg'|^2 \quad \text{-----} \quad 3.18$$

Where 'α<sub>R<sub>0</sub></sub>' is the Raman polarisability of the isolated molecule.

Several points that can be noted are <sup>36,42,50</sup>:

- SERS excitation is a near-field phenomenon. The near-field, especially near a metal surface, will have spatial components that decay more rapidly with distance than the spatial variation in the far-field. It is maximum at the interface and then minimises as it extends to about 10 nm away from the surface.
- The surface-plasmon largely depends on the optical properties of the material (metal), the shape of the roughness (nano-structures) in addition to some other system specific variables.
- Although α<sub>R</sub> is referred to as the Raman polarisability of the molecule, in fact it is the Raman polarisability of the metal-molecule complex and may, as a result, be greatly altered in its magnitude, symmetry and resonant properties from the Raman polarisability of the isolated molecule.



- Although the SERS intensity varies as the fourth power of the local field, the effect is a linear optical effect that depends on the first power of  $I_0$ . But the extraordinary enhancement of SERS emanates from the fourth power dependence on  $g$ .
- In comparison, the major contribution to SER scattering is by the metal rather than the adsorbate.

### 3.2.2 Charge transfer (CT) or chemical enhancement

This, also sometimes referred to as electronic enhancement, is considered<sup>13,46</sup> to contribute less than that due to EM enhancement towards total SER scatterings. This results from an interaction of the molecule-metal system in which molecular energy levels partially overlap with the metal conduction bands or surface plasmon. In other words the molecule bonds to the surface of the metal and the excitation occurs from electrons of the metal to the molecule and back to the metal again<sup>9,44,50</sup>. This is a virtual excitation process in which the charge-transfer state can be partially resonant with the exciting radiation<sup>126</sup>. This gives a large contribution to the Raman scattering cross section of the molecule-metal complex. The enhancement is normally by a factor of 10-100.

In most experimental systems a weak interaction is involved in the surface-molecule system and the molecular energy level partially overlaps with the metal conduction band resulting in the enhancement of the Raman intensity. Otto<sup>127</sup> found contributions of chemical enhancement in SER scatterings, through experimental evidence, of up to about  $3 \times 10^3$  folds. In the absence of EM enhancement there would be no signal but the observation of the signal was determined by the chemical mechanism. Quantitative analysis and the prediction of the appearance of vibrational modes of adsorbed molecules can only be done through the understanding of the chemical effect. The chemical mechanism gains a little more importance in the detection field. In the case where the molecule is present but its contact with the metal surface has been broken, the possibility of its characteristic peaks appearing in the spectrum becomes negligible. Such a situation might occur when the specimen is forced away by a more strongly bonding molecule or when it might accumulate on the surface to the extent of blocking

the whole metal-molecule complex. In this case the chemical mechanism needs to be incorporated in the overall SER effect.

Generally, the process of charge transfer can be described in four steps<sup>49,126</sup>:

- A photon is consumed in exciting an electron from the substrate into a excited electronic state.
- The excited electron is transferred to the adsorbed molecule.
- The excited electron comes back to the donor from the acceptor and at the same time a Raman photon is radiated.
- The metal-molecules complexes are excited to the special vibrationally excited level of the initial electronic state.

Although the exact mechanism of charge transfer contribution to SER intensity is still a controversial issue<sup>55</sup>, it seems to depend strongly on the adsorption site occupied by the adsorbate and also on the adsorption orientation of the molecule. When the adsorption orientation of the molecule is changed on the surface, the charge transfer mechanism may be changed due to the change in interaction between the surface and adsorbate. SERS is also sensitive to the surface coverage and the components of the solution in the electrochemical systems<sup>126</sup>. The theory for chemical contributions to the SER enhancement is still developing. One of the major reasons for its comparatively slow development is that it is much more complex than the EM mechanism<sup>127</sup>.

### 3.3 Summary

It is very difficult to quantify the contributions of the electromagnetic and the chemical mechanisms to the SER scattering, especially for the strong adsorption of molecules on the surface. Although some studies have considered both effects<sup>9,13,46</sup>, it is still open to exploration as to whether or not there are some co-operative effects between the two mechanisms. In the field of detection, where the presence of the target molecule cannot be ignored just on the pretext of the lack of ability to interpret the SER spectrum, the knowledge of all aspects of SERS becomes apparent.

## **4. SAMPLES AND CHARACTERISTICS**

### **4.1 Introduction**

The research was mainly focussed on the detection of peroxide explosives and pentaerythritol tetranitrate (PETN). Peroxide explosives; triacetone triperoxide (TATP) and hexamethylene triperoxide diamine (HMTD), are being used in improvised explosive devices (IEDs) and are not detected by most of the conventional detection systems designed for the detection of nitro-based compounds. PETN is a nitro-based explosive and is also used in homemade IEDs. Its extremely low vapour pressure demands the use of a very sensitive system for the detection of its vapour.

In addition to the main target analytes mentioned above, some well characterised Raman active samples namely; acetone, nitrobenzene and pyridine were also selected for experiments with Raman, resonance Raman and surface enhanced Raman spectroscopy. These samples also facilitated the setup phase and the optimisation of SER-active surfaces. Here, a few of the important characteristics of the analyte samples are presented. Further details can be found in the corresponding references.

All the samples were obtained from the chemical laboratories and were either from Alfa Aesar, UK or from Fisher Scientific, UK. Peroxide explosives were synthesised within the laboratory by Dr T Bellamy. PETN was obtained from the existing stock. These samples were either used as received, diluted or in vapour state. Bulk samples were used to obtain reference Raman spectra for comparison during low concentration SERS analysis. Solvents used for making low concentration solutions will be discussed with

each experiment in subsequent chapters. In all SERS experiments, the solvent was allowed to evaporate before the Raman spectra were recorded.

The ultra-sensitive analysis was done by exposing the SER-active surfaces to the headspace vapour from the sample (liquid or solid). The sample presentation is diagrammatically shown in figure 4.1. A known quantity of sample was contained in 12 ml glass vials (figure 4.1, a) and SER-active surface was placed over the mouth of the vial with SER-active surface facing down as shown in figure 4.1 (b). For volatile liquid samples the time of exposure was restricted to a few seconds and the exact exposure time will be mentioned where the experiments are discussed. For solid samples the, exposure time was ~2 hours at normal laboratory conditions to allow vapour saturation within the vial. No external heating was done to expedite the evaporation of explosives.

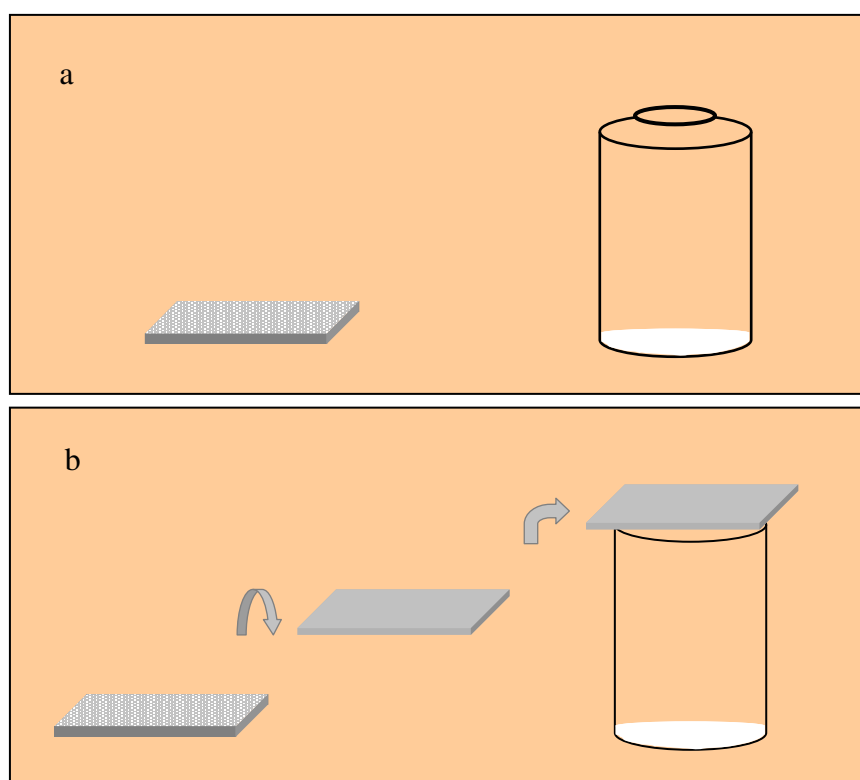
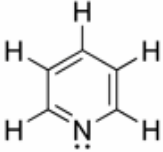


Figure 4.1 Diagram showing the sample presentation setup for the vapour detection. The SER-active surface is fabricated and analyte is put in the vial (a) and surface is put face down on the vial where it is exposed to vapour from the analyte (b).

## 4.2 Pyridine

Pyridine is an aromatic compound resembling benzene. It is used as a solvent and for the demonstration of SERS for its good adsorption ability on metal surfaces. It is also an atmospheric pollutant and exists as a constituent of cigarette smokes. Basic properties<sup>128</sup> are given in table 4.1.

Table 4.1 Basic properties of pyridine.

Molecular Formula	C <sub>5</sub> H <sub>5</sub> N
Molecular structure	
Appearance	Colorless liquid
Odour	Putrid
Density	0.9819 g/cm <sup>3</sup>
Boiling point	115.2 °C
Solubility	It is polar aprotic, Versatile solvent
Vapour pressure	2 x 10 <sup>3</sup> Pa at 20 °C or 2.1 parts per hundred

Pyridine has maximum UV absorbance between 330 to 350 nm. The Raman spectrum of liquid pyridine was recorded with an excitation wavelength of 785 nm by placing the pure sample in a cuvette and is shown figure 4.2. Table 4.2 gives the assignment of characteristic Raman vibrational modes of pyridine.

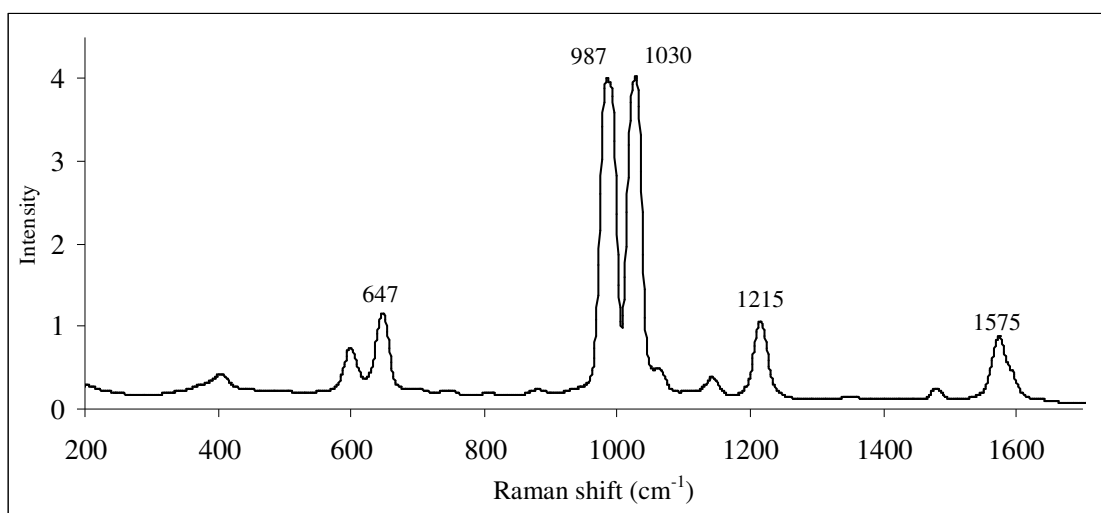


Figure 4.2 Raman spectrum of pyridine recorded with a 785 nm excitation wavelength.

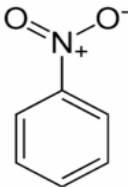
Table 4.2 Characteristic Raman modes of pyridine.

Raman shift (cm <sup>-1</sup> )	Characteristic mode
647	Ring deformation
987	Ring breathing
1030	Trigonal ring breathing
1215	Ring vibration
1575	C=C stretch

### 4.3 Nitrobenzene

Nitrobenzene is an organic compound found in both liquid and crystalline form. It is used as a mild solvent and as an oxidising agent and is known to be carcinogenic. It is found in shoe polish and may be used as an ingredient in the IEDs. Its basic properties<sup>129</sup> are given in table 4.3.

Table 4.3 Basic properties of nitrobenzene.

Molecular Formula	C <sub>6</sub> H <sub>5</sub> NO <sub>2</sub>
Molecular structure	
Appearance	Oily liquid
Odour	Almond like
Density	1.19 g/cm <sup>3</sup>
Boiling point	210.9 °C
Soluble in	Benzene
Vapour pressure	1.6 x 10 <sup>4</sup> Pa at 20 °C or 16 parts per hundred

The Raman spectrum of liquid nitrobenzene was recorded with an excitation wavelength of 785 nm by placing the pure sample in a cuvette and is shown in figure 4.3. Table 4.4 gives the assignment of characteristic Raman vibrational modes of nitrobenzene.

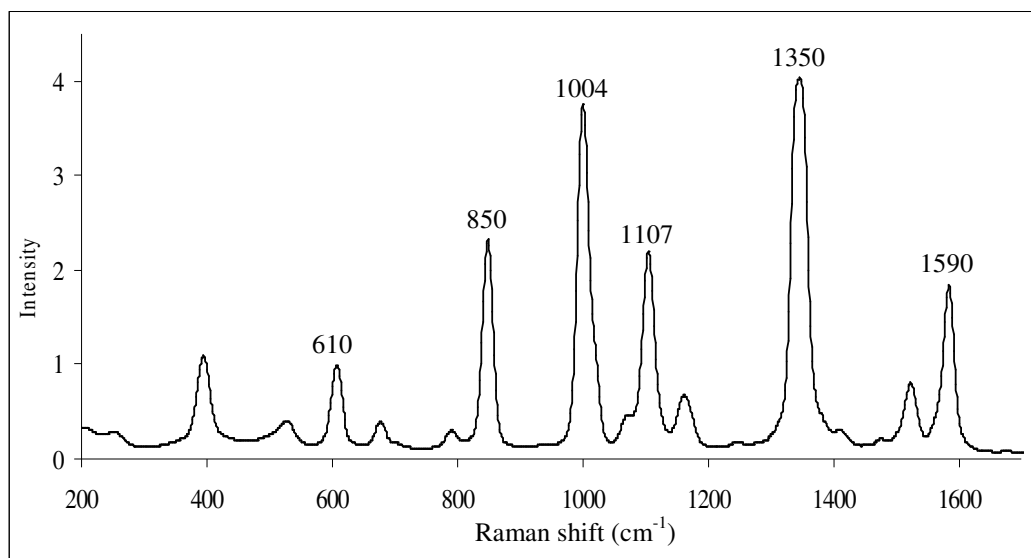


Figure 4.3 Raman spectrum of nitrobenzene recorded with 785 nm laser wavelength.

Table 4.4 Characteristic Raman modes of nitrobenzene.

Raman shift (cm <sup>-1</sup> )	Characteristic mode
610	Ring deformation
850	Ring breathing
1004	Ring breathing
1107	Ring breathing
1350	NO <sub>2</sub> symmetric stretch
1590	C=C stretch

#### 4.4 Acetone

Acetone is a ketone and also known as propanone. It is flammable and is a good solvent. It is also used in synthesis of peroxide explosives. Its basic properties<sup>130</sup> are given in table 4.5.

Table 4.5 Basic properties of acetone.

Molecular Formula	C <sub>3</sub> H <sub>6</sub> O
Molecular structure	$\begin{array}{c} \text{O} \\    \\ \text{CH}_3 - \text{C} - \text{CH}_3 \end{array}$
Appearance	Colourless liquid
Odour	Characteristic
Density	0.79 g/cm <sup>3</sup>
Boiling point	56.3 °C
Soluble in	Water, ethanol, ether
Vapour pressure	3.1 x 10 <sup>4</sup> Pa at 20 °C or 30 parts per hundred

The UV-vis spectrum show that acetone has absorbance maximum at 280 nm. The Raman spectrum of liquid acetone was recorded with an excitation wavelength of 785 nm by placing pure sample in a cuvette and is shown in figure 4.4. Table 4.6 gives the assignment of characteristic Raman vibrational modes of acetone.

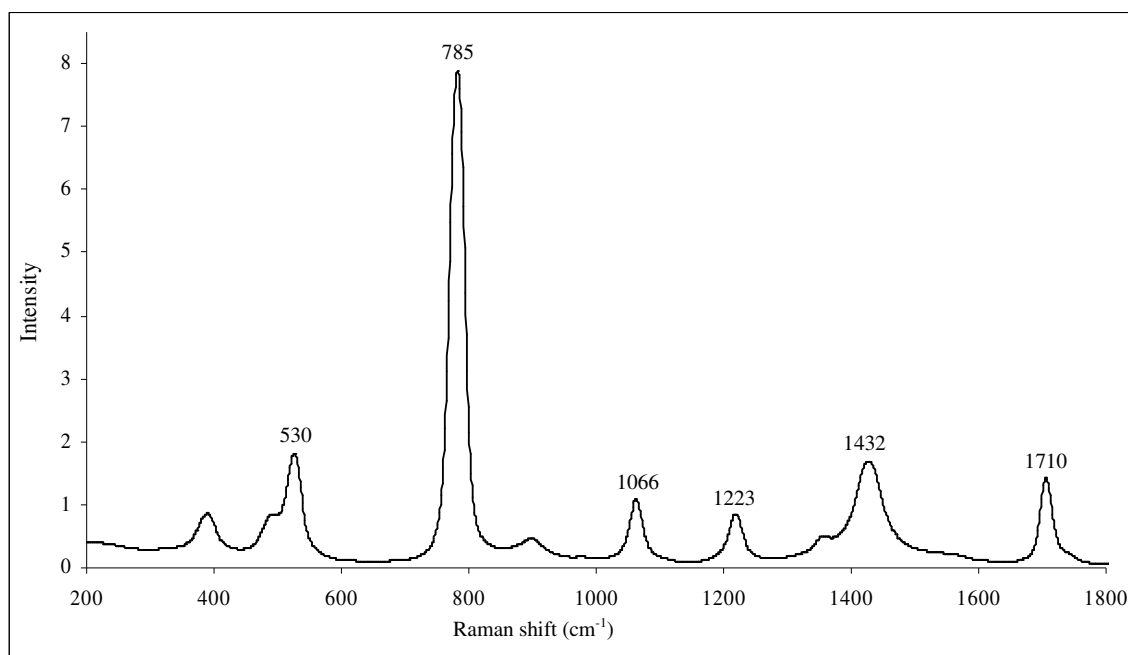


Figure 4.4 Raman spectrum of acetone taken with an excitation wavelength of 785 nm.

Table 4.6 Characteristic Raman modes of acetone.

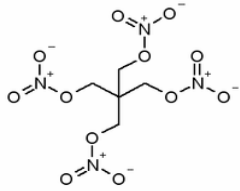
Raman shift (cm <sup>-1</sup> )	Characteristic mode
785	C <sub>3</sub> O skeletal
1066	C-C stretch
1223	C-H deformation
1432	CH <sub>3</sub> deformations
1710	C=O stretch

#### 4.5 PETN

PETN is a crystalline solid and is also called 'Penta'. It is used in detonators, blasting caps, detonating cords, plastic explosives and also in IEDs. It is also used in medicine as a vasodilator. It is sensitive to impact. Basic properties<sup>131,132</sup> are given in table 4.7.



Table 4.7 Basic properties of PETN.

Molecular Formula	$C_5H_8N_4O_{12}$
Molecular structure	
Appearance	White crystalline
Density	$1.77 \text{ g/cm}^3$
Melting point	$141.3 \text{ }^\circ\text{C}$
Soluble in	Acetone, benzene, ethanol
Vapour pressure	$1.8 \times 10^{-6} \text{ Pa}$ at $25 \text{ }^\circ\text{C}$ or 18 ppt

PETN show an absorbance maximum at 330 nm in a UV-vis spectrum. Raman spectra of solid PETN were recorded with excitation wavelengths of 514 nm and 785 nm and are shown in figures 4.5 and 4.6 respectively. Table 4.8 gives the assignment of characteristic Raman vibrational modes of PETN<sup>133</sup>.

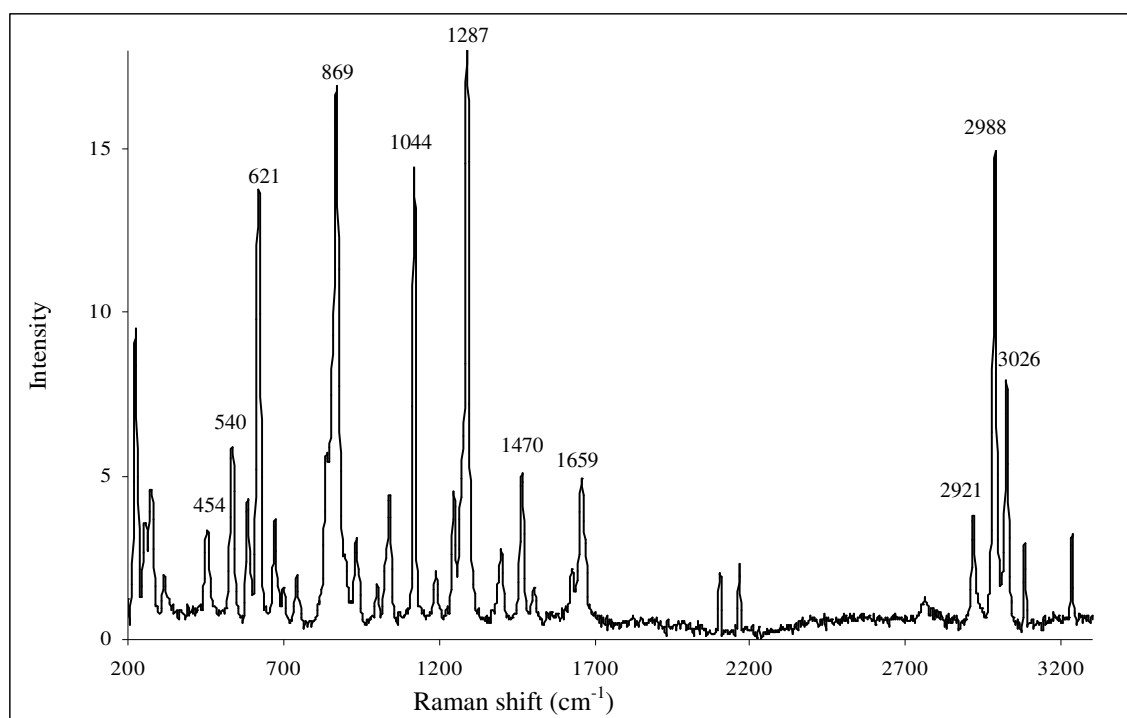


Figure 4.5 Raman spectrum of PETN recorded with an excitation wavelength of 514 nm.

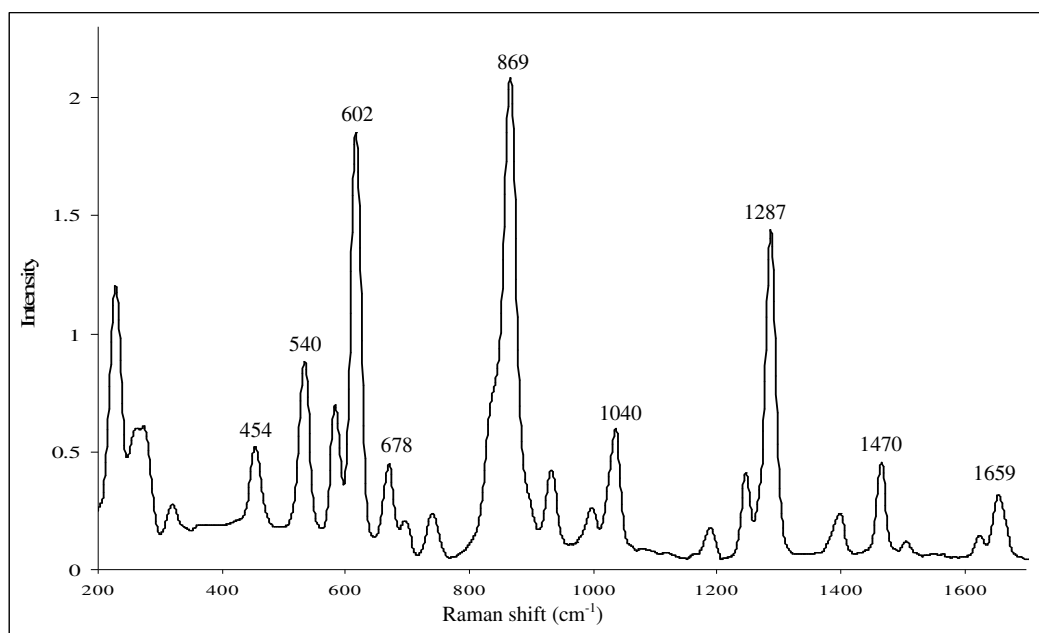


Figure 4.6 Raman spectrum of PETN recorded with an excitation wavelength of 785 nm.

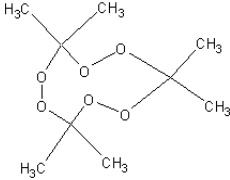
Table 4.8 Characteristic Raman modes of PETN. (reference 133).

Raman Shift	Characteristic modes
454	CH <sub>2</sub> Wag, CCC deformation
540	CH <sub>2</sub> Wag, O-NO <sub>2</sub> rocking vibration
621	CCC deformation, O-NO <sub>2</sub> in plane
678	O-N stretch, CC stretch
744	CCC deformation, O-N stretch
869	O-N stretch
938	CCC deformation, CH <sub>2</sub> torsion
1044	CH <sub>2</sub> torsion, CC bend
1121	NO <sub>2</sub> symmetric stretch
1194	CCC deformation, CH <sub>2</sub> Wag
1251	CH bend
1287	NO <sub>2</sub> symmetric stretch, CH bend
1402	CH <sub>2</sub> Wag, CC stretch
1470	CH <sub>2</sub> scissors
1659	NO <sub>2</sub> asymmetric stretch
2921	CH <sub>2</sub> asymmetric stretch
2988	CH <sub>2</sub> asymmetric stretch
3026	CH <sub>2</sub> asymmetric stretch
3085	Asymmetric CH <sub>2</sub> stretch

#### 4.6 TATP

TATP is an organic peroxide in crystalline powder form. It is very sensitive to impact and heat and regarded as unstable. It is used as primary high explosive mainly in IEDs. Three peroxide functionalities give it explosive potential. TATP has about 88% of TNT blast strength. TATP is one of the most sensitive explosives known. Unlike most explosives in use by the military and civilian entities, it contains neither nitro groups nor metallic elements. This makes its detection by standard methods difficult. Its basic properties are given in table 4.9<sup>136-138</sup>.

Table 4.9 Basic properties of TATP.

Molecular Formula	$C_9H_{18}O_6$
Molecular structure	
Appearance	White powder
Density	$1.18 \text{ g/cm}^3$
Odour	Acrid
Melting point	$91^\circ\text{C}$
Soluble in	Acetone, Butanone
Vapour pressure	$7 \text{ Pa}$ at $25^\circ\text{C}$ or $70 \text{ ppm}$

It has no significant absorption within the UV and visible range and has no fluorescence characteristics<sup>134,135</sup>. The Raman spectrum of solid TATP was recorded with an excitation wavelength of 785 nm and is shown in figure 4.7. Table 4.10 gives the assignment of characteristic Raman vibrational modes of TATP<sup>139-141</sup>.

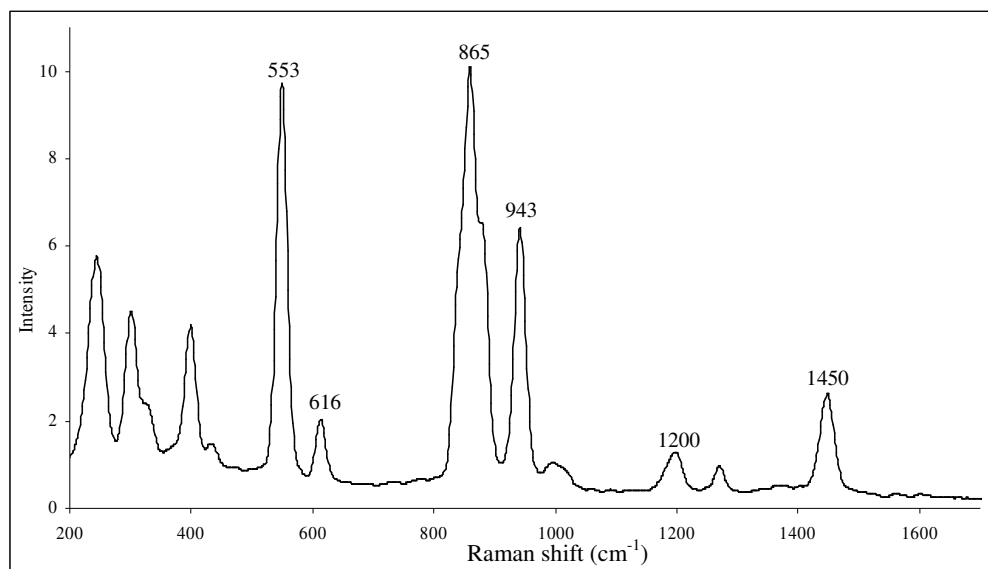


Figure 4.7 Raman spectrum of TATP recorded with a 785 nm excitation wavelength.

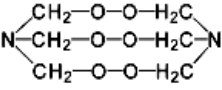
Table 4.10 Characteristic Raman modes of TATP.

Raman Shift (cm <sup>-1</sup> )	Characteristic modes
553	O-C-O stretch
616	O-C-O stretch
865	O-O symmetric stretch
943	O-O asymmetric stretch
1200	C-O stretch
1277	Ring stretch
1450	CH <sub>3</sub> deformation

#### 4.7 HMTD

HMTD is an organic peroxide in crystalline powder form. It has about 60% of TNT blast strength. It is not as sensitive to impact as TATP, but is liable to spontaneous explosions under impact, friction, and temperature changes. There is no significant absorption within the UV and visible range and it has no fluorescence characteristics<sup>134,135</sup>. It is used as primary high explosive and is also used in IEDs. Its basic properties<sup>137,142, 143</sup> are given in table 4.11.

Table 4.11 Basic properties of HMTD.

Molecular Formula	$C_6H_{12}N_2O_6$
Molecular structure	
Appearance	White powder
Density	$0.88 \text{ g/cm}^3$
Melting point	$75^\circ\text{C}$ (decomposes)
Soluble in	Acetone, Butanone
Vapour pressure	$0.03 \text{ Pa}$ at $25^\circ\text{C}$ or $0.29 \text{ ppm}$

The Raman spectrum of solid HMTD was recorded with an excitation wavelength of 785 nm and is shown in figure 4.8. Table 4.12 gives the assignment of characteristic Raman vibrational modes of HMTD<sup>139,141</sup>.

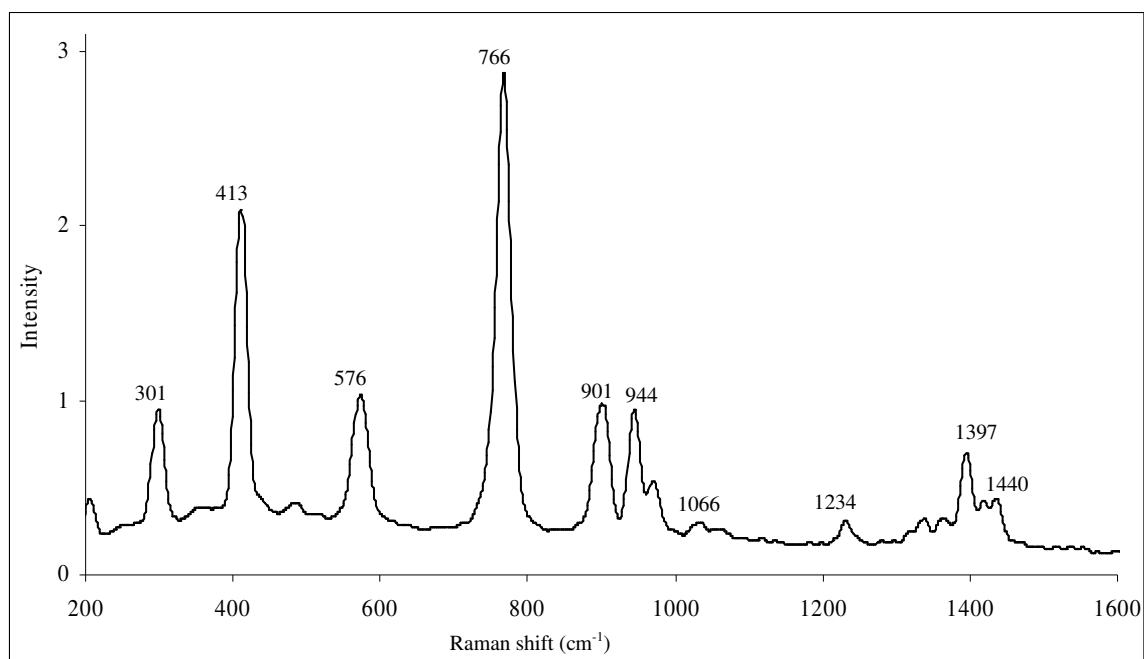


Figure 4.8 Raman spectrum of HMTD recorded with 785 nm laser wavelength.

Table 4.12 Characteristic Raman modes of HMTD.

<b>Raman Shift (cm<sup>-1</sup>)</b>	<b>Characteristic modes</b>
413	Not identified
576	Not identified
766	O-O symmetric stretch
901	O-O asymmetric stretch
944	O-O asymmetric stretch
1066	N-C stretch
1450	CH <sub>2</sub> deformation

## **5. EXPERIMENTAL - INITIAL WORK**

### **5.1 Introduction**

A series of experiments was conducted to gain expertise in the Raman spectroscopy of some energetic and relevant materials. These proved to be the stepping-stones in designing and conducting experiments based on RRS, SERS and SERRS. Each of the phases, for which evidences in the literature has been discussed earlier, will be discussed in the following order:

- a. Preliminary Raman spectroscopy with a non-laser source.
- b. Excitation laser wavelength dependence in Raman Spectroscopy.
- c. SERS with colloidal surfaces.
- d. SERS with fabricated solid surfaces.

### **5.2 Specifications of Equipment**

#### **5.2.1 Modified Spectrofluorometer**

A modified Spectrofluorometer, SPEX FluroMax, was used in emission mode to record Raman spectra. It had a Xenon lamp as the light source, a single monochromator as a filter and photomultiplier tube (PMT) as a detector. Raman scatterings were collected at  $90^{\circ}$  from the excitation beam direction. It had wavelength resolution of 0.3 nm. Further details are given in appendix C.

### 5.2.2 UV-Vis-NIR Spectrometers

The emission spectra over the UV-vis-NIR wavelength bands of some selected materials were recorded using a Perkin Elmer Spectrometer (Lambda 9) which was fitted with a deuterium lamp for the UV range and a Tungsten/Halogen lamp for the visible/NIR range. The system's configurations are given in appendix D.

The UV absorption spectra of all colloidal solutions were obtained with a UV-vis Spectrometer; Cintra 5 double-beam spectrophotometer with Visionite Scan-Version 1.0 software. The colloidal suspensions were diluted to 10% in water and placed in a 1cm optical cuvette for analysis. Appendix E

### 5.2.3 Spex 1404 Raman spectrometer

The setup had a Spex 1404 (0.85 focal length) double monochromator and an Intensified Diode Array detector assembly (E G & G - type 1460). This was controlled by a matched (E G & G) Optical Multi-channel Analyser (OMA III). A Spectra Physics 165 argon ion laser emitting in six wavelength bands; 514.5, 496.5, 488, 476.5, 465.8 and 457.9 nm was used. Specifications are given in appendix F.

### 5.2.4 Renishaw RM2000 Raman Microscope

For SER scattering measurements with colloidal solutions, a Renishaw Raman system at the Institute of Material Structures, Madrid, Spain was used. Raman spectra from solid SER-active surfaces were recorded with the Raman system at Biophotonics research group, Gloucester Royal Hospital, Gloucester using a similar Renishaw Raman Imaging Microscope System RM2000, fitted with a Leica microscope and an electrically cooled CCD camera. The system in Spain was coupled with two lasers operating at 514 nm and 785 nm from argon and diode lasers respectively whereas, only a 832 nm diode laser was available with the system at Gloucester. The spectra were obtained using a 100 x objective. The laser power at the sample was ~2.0 mW. The spectral resolution was set at  $2\text{ cm}^{-1}$ . Appendix G



### 5.2.5 The commercial Raman system at our laboratory

The Ocean Optics Raman Systems (R-3000), a fully integrated Raman Spectrometer at our laboratory was used to record the Raman spectra. The all-in-one system included a diode laser, a CCD-array spectrometer, a fiber optic probe and operating software and offered a wavelength resolution of  $15\text{ cm}^{-1}$ . It had thermoelectrically cooled CCD array detector, that allowed integration times of up to 4 minutes. It was coupled with a 200 mW, 785 nm (red) solid-state diode laser giving a spectral wavelength range of  $\sim 200$  to  $2700\text{ cm}^{-1}$ . Appendix H.

### 5.2.6 Digital surface profiler

For surface characterisation, MicroXam Surface Mapping Microscope was used with Map Vue Ex surface mapping software. Appendix I.

### 5.2.7 Microscopes

Very rough surfaces were checked by either a Polyver Met Microscope fitted with CeberTek camera or a Richter Jung Optical microscope with CeberTek camera was used to capture surface images with  $\sim x100$  magnifications.

### 5.2.8 Scanning electron microscopes

For surface characterisation, two Scanning electron microscopes (SEM) JEOL JSM-840A and LEO 435 VP SEM at variable pressure mode were used to take surface micrographs. The details are given in appendix J.

### 5.2.9 Magnetron sputtering equipment

Reactive DC-Magnetron Sputtering was used to coat silver films in an argon or argon–oxygen environment at a pressure of  $\sim 2 \times 10^{-3}$  mbar. A 75mm diameter silver disc of 3mm thickness was purchased from *Goodfellow, Cambridge* for use as a sputtering target. The temperature of the substrate could be controlled from ambient to  $500^{\circ}\text{C}$ . Its details are given in appendix K.

### 5.3 Results and Analysis

#### 5.3.1 Preliminary Raman Spectroscopy with a non laser source

A few basic experiments were conducted in order to test and set the wavelength calibration of the spectrometer system using known Raman lines of various samples. These experiments were intended to establish a best practice protocol for sample preparation and presentation as well as a practice for data acquisition and handling.

#### Excitation profile of Acetone

The modified FluroMax system was calibrated using the spectrum of acetone. The spectrum of acetone is shown in figure 5.1 measured with laser wavelength  $\lambda_i = 350$  nm and integration time  $t_i = 0.1$  second.

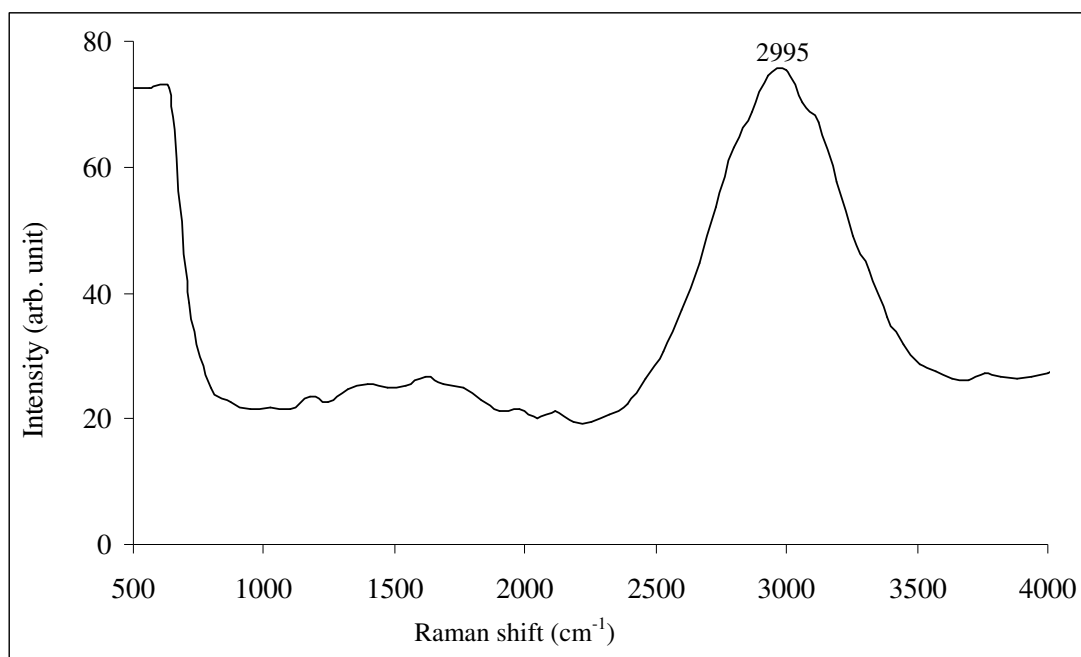


Figure 5.1: Raman spectrum of liquid acetone at  $\lambda_i = 350$  nm.

The excitation profile for acetone was recorded for  $2995\text{cm}^{-1}$ , the  $\text{CH}_3$  symmetric stretching mode over the excitation wavelength from 350 to 450 nm at 50 nm intervals, keeping the band pass at 5 nm and  $t_i = 0.1$  second. The logarithmic plot between Raman intensity  $I_R$  and  $\lambda_i$  was drawn and is shown in figure 5.2. The trend line has been drawn showing 1.1% error bars. The relationship between Raman intensity and the excitation wavelength (represented by the trend line) was as defined in equation 3.5. This meant

that the Raman intensity varied with the inverse fourth power of the change in excitation wavelength in the absence of any effect of resonance.

The spectral resolution of the system was very low and the excitation source had low power for sensitive Raman analysis, therefore, further experiments were conducted with a laser source and a high resolution Raman spectrometer.

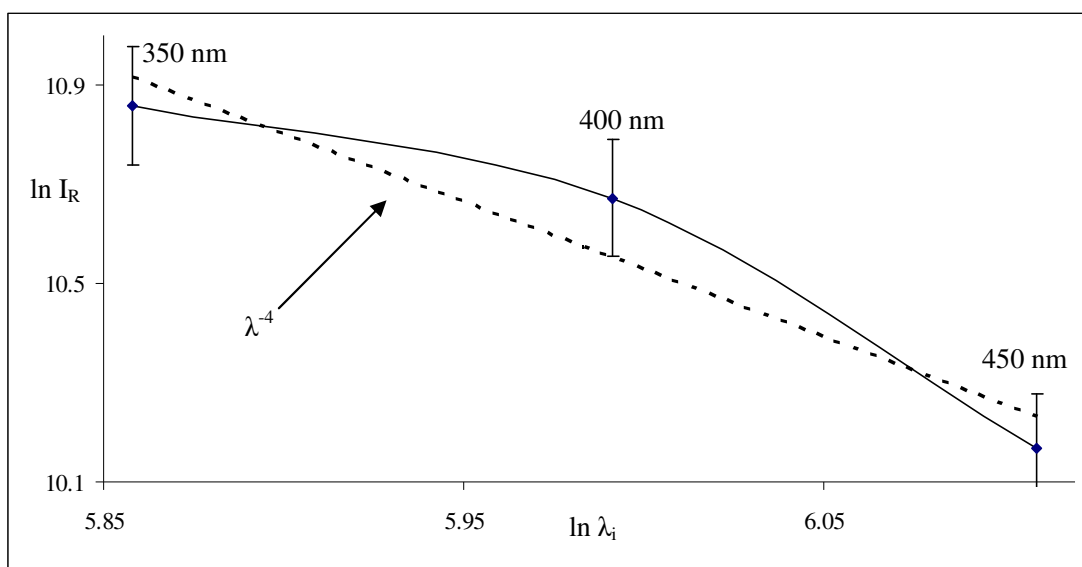


Figure 5.2 REP of  $\text{CH}_3$  asymmetric stretch at  $2995 \text{ cm}^{-1}$  of acetone within  $\lambda_i = 350$  to  $450 \text{ nm}$ .

### 5.3.2 Excitation laser wavelength dependence

The Raman intensity depends on the inverse fourth of the incident laser wavelength as was observed in the above experiment. This is true for a non-resonant (non-absorbing) region for the sample molecule. However, in the spectral region where the sample molecule starts to absorb, this dependence is no more valid and the effect of resonance becomes evident in the Raman spectrum and the mechanism is known as resonance Raman spectroscopy (RRS). As already discussed in chapter 2, it results in the large enhancements in the Raman scatterings. The material chosen for the preliminary study of RRS was a high explosive, pentaerythritol tetranitrate (PETN). Its details are given in section 4.5. The choice was based on its widespread use as a component of explosives and its well-characterised Raman lines.

The Spex 1404 double monochromator with OMA III system was used to record the Raman spectrum (section 5.2.3 above). A 514.5 nm output line from an argon ion laser was used for the experiment and a blocking filter was used to cut off excitation laser light from entering monochromator. The schematic of the experimental layout is shown in figure 5.3. The details of equipment and setup are given in appendix F. Power was set to 600 mW, with a slit size of 700  $\mu\text{m}$  and exposure time of 1 second and the spectrum was recorded with 100 accumulations. The spectral data were normalised for the system's wavelength response. The data were baseline corrected using Microcal Origin 5.0 software. The spectrum recorded was similar to the one shown in Figure 4.5, and conform to the ones reported earlier<sup>133</sup>.

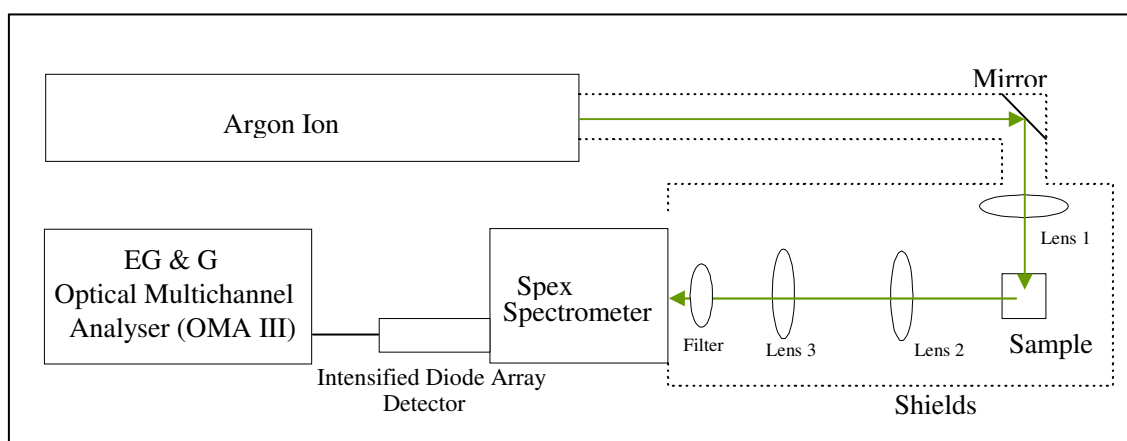


Figure 5.3 Schematic layout of equipment setup for collection of Raman scatterings at  $90^{\circ}$ .

Suggested vibrational mode assignments for PETN molecule were discussed in chapter 4 section 4.5 and are given in Table 4.8. The absorption spectrum of solid PETN over the UV-vis wavelength band is presented in figure 5.4. It was recorded using the solid sample attachment of Lambda 9, UV-vis-NIR spectrometer. The spectrum showed the maximum absorption at around 330 nm and the gradual reduction until around 650 nm.

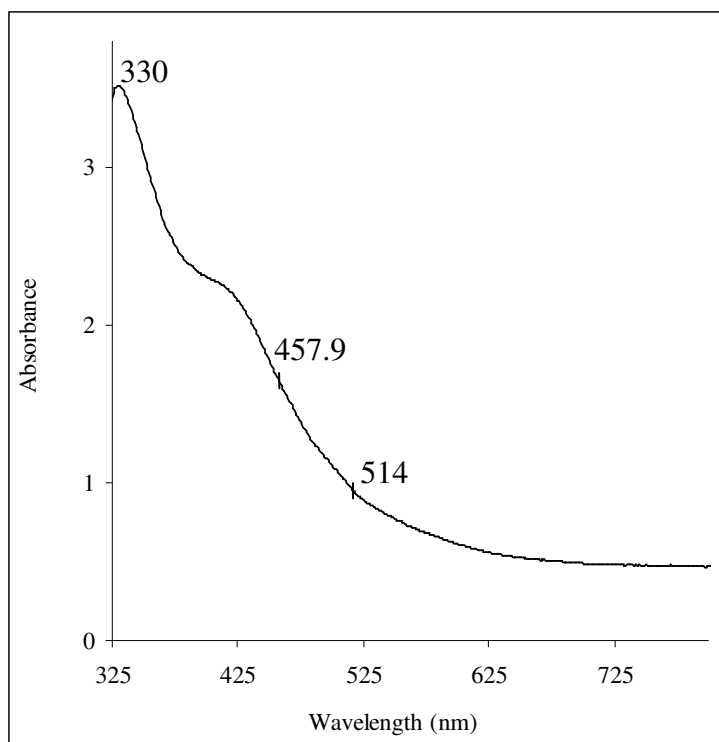


Figure 5.4 Absorption spectrum of PETN over the UV-vis-NIR wavelength showing the maximum absorption at ~330 nm.

The Raman spectra were collected with six different wavelengths without using the blocking filter and keeping the slit size at 400  $\mu\text{m}$ , an exposure time of 1 second and 100 accumulations for each spectrum. No variations in settings were made during the experiment, except changing the laser wavelength. The spectra are shown in figure 5.5. The increase in Raman intensity with the decrease in the laser wavelength can be observed from the spectral comparison. The Raman intensity increased with laser wavelength closer to the resonance (absorption) wavelength. The lowest wavelength of 457.9 nm was in a higher absorbance region as marked in figure 5.4.

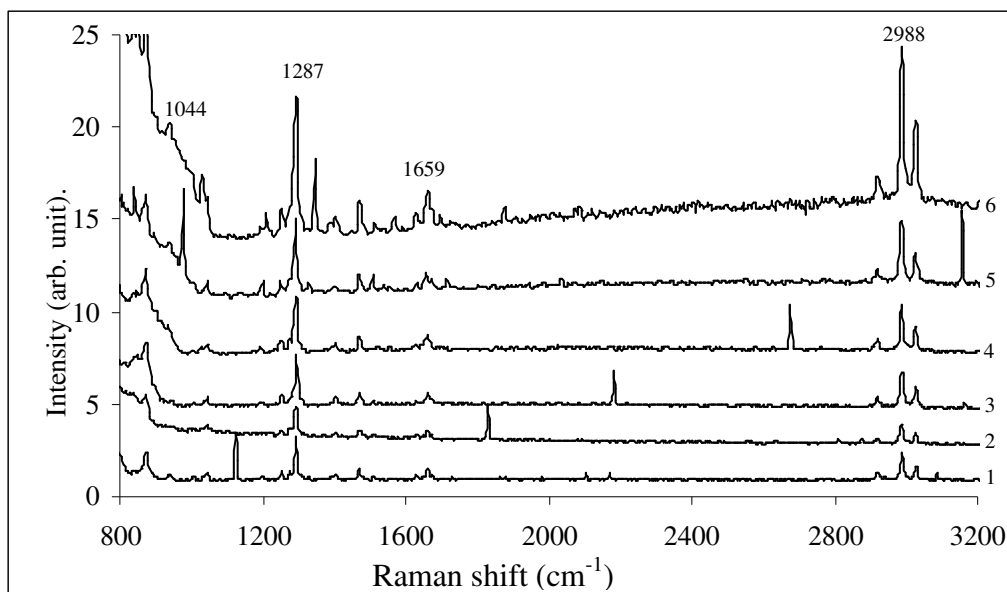


Figure 5.5 Raman spectra of PETN recorded with six different wavelengths; 514.5, 496.5, 488, 476.5, 465.8 and 457.9 nm marked from 1 to 6 in the same order. Normalised for laser intensities.

The complete Raman spectrum is shown in figure 4.5 and the characteristics Raman frequencies are given in table 4.8. The  $\text{NO}_2$  symmetric stretch at  $1287\text{cm}^{-1}$  is shown in figure 5.6, showing higher Raman scatterings intensity with a laser wavelength of 457.9 nm than of 514.5 nm. Better comparison can be visualised by plotting the laser wavelength against the Raman intensity of the same vibrational group as shown in figure 5.7. The dotted line represents the trend line for the excitation wavelengths, excluding the lowest wavelength at 457.9 nm. A large anomalous enhancement in Raman intensity, as the excitation wavelength approaches a resonance condition beyond 457.9 nm, was observed. A drastic enhancement was expected at a lower wavelength (UV-excitations) but it was not possible to investigate this in the present work due to the non availability of the shorter wavelength laser sources in the absorbing region of the explosive.

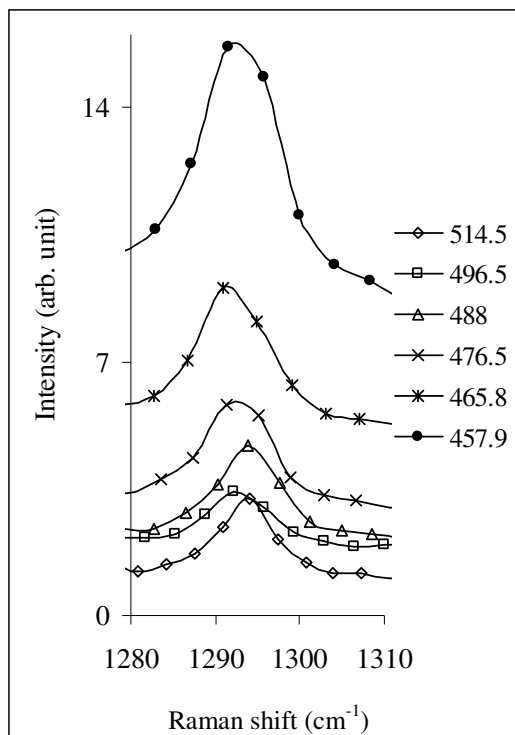


Figure 5.6 Raman spectra of PETN recorded with six different wavelengths showing increase in Raman intensity of peak at  $1287\text{ cm}^{-1}$  with the decrease in laser wavelength.

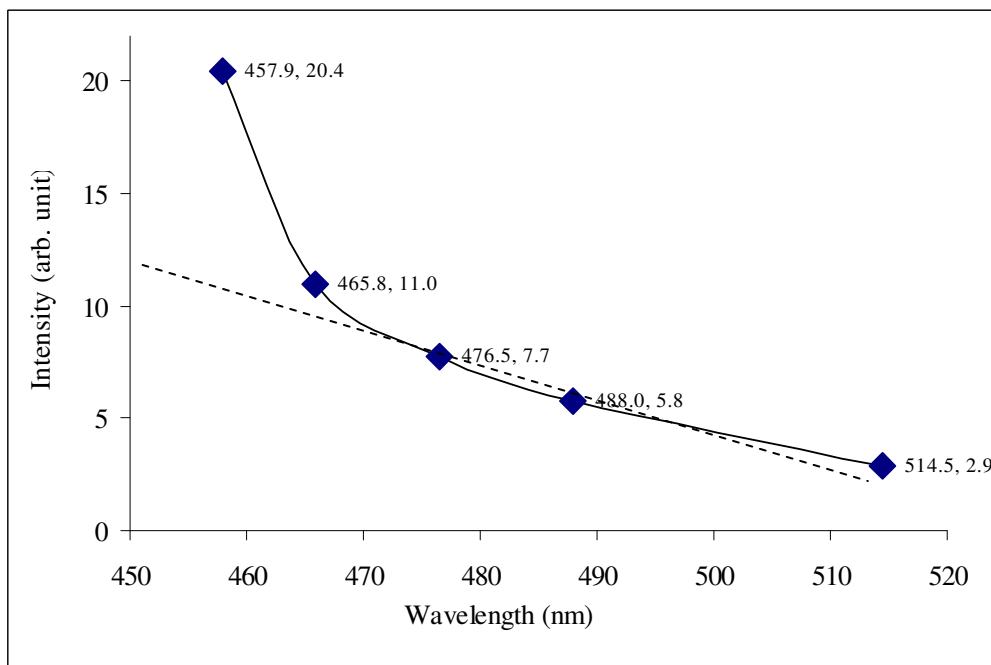


Figure 5.7 Graph showing the effect of changing  $\lambda_i$  on  $I_R$  for the PETN peak at  $1287\text{ cm}^{-1}$ . There is an increase in  $I_R$  with the decrease in  $\lambda_i$ . Trend line for the excitation wavelengths from 465.8 nm to 514.5 nm is shown by the dotted line.

To evaluate the extent of resonance coupling, the excitation wavelength dependence of the Raman cross-section (REP) was constructed. In the non-resonance region, the relation between the excitation wavelength and the Raman intensity is given by equations 3.9 and 3.10. For this experiment the wavelength dependence of the five Raman vibrational modes (1044, 1287, 1659, 2988 and 3026  $\text{cm}^{-1}$ ) of the PETN molecule were evaluated with five values of  $\lambda_i$ ; (514.5, 488, 476.5, 465.8 and 457.9 nm) from an argon-ion laser.

The REP was constructed on a natural log scale of both  $I_R$  and the Raman shift (wavenumber). The results showed that the profile followed equation 3.10 for the five longer wavelengths but the intensity was enhanced considerably for the shorter wavelength ( $\lambda_i = 457.9$  nm). This was considered to be due to the onset of resonance, where PETN started to absorb at around this wavelength, as shown in figure 5.4. The REP was plotted on a logarithmic scale as per equation 3.10 and is shown in figure 5.8 for a few of the band peaks. The trend line for the higher wavelengths is shown as dotted and the trend line between the excitation wavelengths 457.9 nm and 465.8 nm is shown as hashed. The dotted lines showed near fourth power dependence in most cases, that held good for the non-resonant region. However, the sudden relative increase in the intensity shown by the hashed line was considered to be due to the resonance enhancement at shorter excitation wavelengths.

The increase in intensity varied for different Raman bands, which may be due to the variation in response of the vibrational mode to the excitation wavelength. For bands showing resonance enhancement, some were more intense than others. The increase in Raman intensity of five different bands, given in orders of magnitude, with the decrease in excitation wavelength is shown in table 5.1. The increase in Raman intensity at the short wavelength (near resonance) was much higher than at longer wavelengths (far resonance). This was believed to be due to the onset of the resonance in this region. The average enhancement was around 4 times the magnitude of the normal scattering intensities with a few bands showing higher enhancement values.



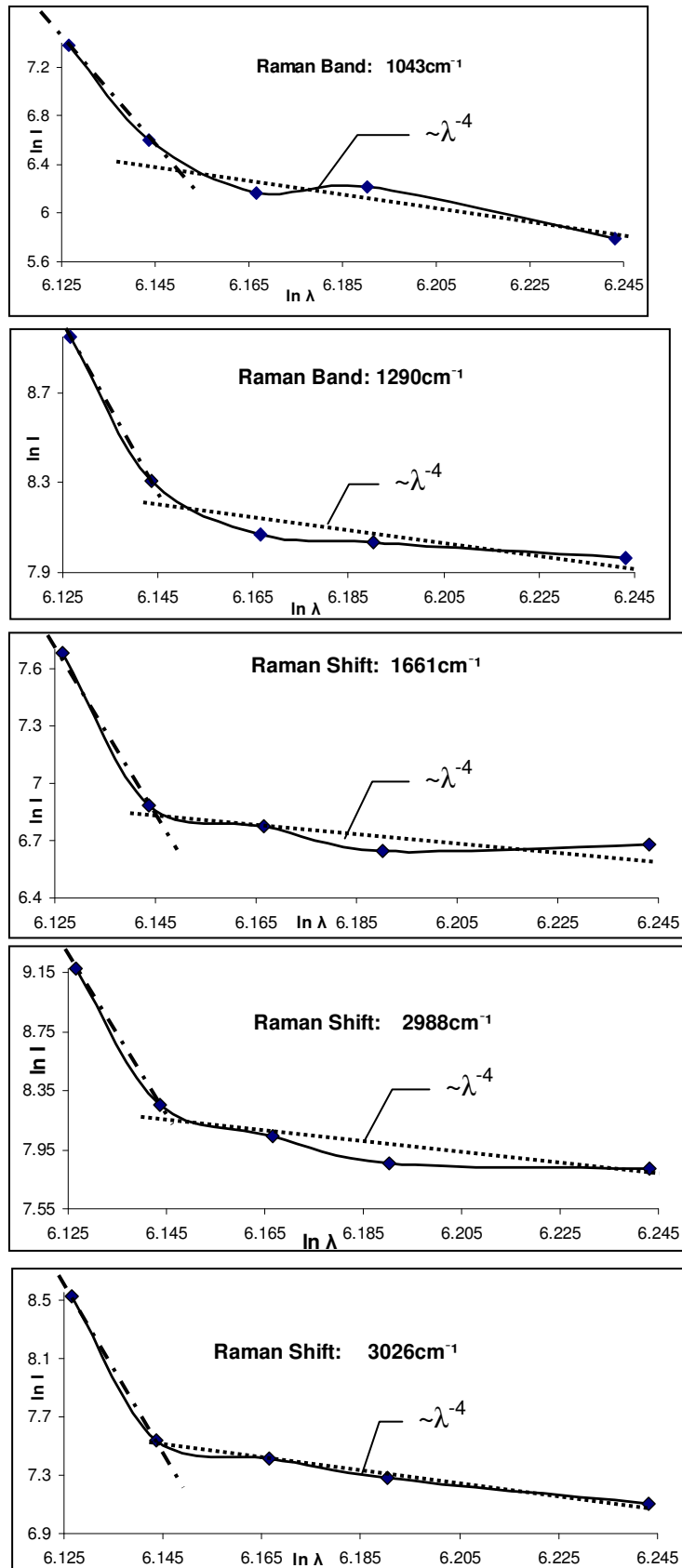


Figure 5.8 REP for five different Raman bands of PETN showing resonance enhancement of Raman scattering.

Table 5.1 Increase in Raman intensity in order of magnitude of five different PETN bands with excitation wavelengths approaching resonance region.

Peak at	Rise in intensity between excitation wavelengths by factors		
	465.8 - 457.9 nm (near resonance)	488 - 514.5 nm (far resonance)	514.5 - 457.9 nm (maximum)
1044 $\text{cm}^{-1}$	1.9	1.6	7.1
1287 $\text{cm}^{-1}$	1.8	1.3	4.1
1659 $\text{cm}^{-1}$	1.7	1.5	5.4
2988 $\text{cm}^{-1}$	2.1	1.2	5.2
3026 $\text{cm}^{-1}$	2.0	1.4	5.8

Further experiments are needed to explore the full potential of the RRS. However, the results have shown that the normal Raman technique becomes comparatively more sensitive by merely choosing the near resonance excitation laser wavelength to achieve enhancement. The possibility of combining the resonance enhancement with the surface enhancement (SERRS) offers a sensitive analytical method.

### 5.3.3 Surface Enhanced Raman Spectroscopy with metal colloids

Metal colloids have been prepared by many methods for various applications over the last few decades. The preparation of colloids for application in SERS is directly related to the type of target molecule, system of analysis and the availability of equipment to prepare them. Even once the colloids are prepared keeping in view the analytical parameters, the performance of colloids remain variable due to other reasons, such as slight changes in preparation protocol, presence of impurities, laboratory/preparation environment, purity of starting material etc. Changes in preparation method cause changes in morphology of colloids which is the controlling factor of molecular adsorption as well as surface plasmon generation. The presence of even very small quantities of impurities may overwhelm the signal from the desired molecular species. The basics of this nanotechnology were experimented on during a short term scientific mission to the Institute of Material Structures at Madrid (Spain).

#### Sample Preparation

Both silver (Ag) and gold (Au) colloids were prepared. The aqueous solutions were prepared using tri-distilled water (TDW). All the glass materials were cleaned using

chromic acid solution and then rinsed many times with TDW before use. The methods of preparation used were by *Citrate Reduction*, *Hydroxylamine Reduction* and *Borohydride Reduction*, which have been referred to in chapter 2. Methods are briefly described here.

Following the Lee and Meisel<sup>53</sup> method, 50 ml of a  $10^{-3}$  M  $\text{AgNO}_3$  aqueous solution was heated to boiling. 1 ml of a 1% Trisodium Citrate ( $\text{C}_6\text{H}_5\text{O}_7\text{Na}_3$ ) solution was then added to it. The mixture was kept boiling for 1 hour and then was allowed to cool down. The resultant colloidal mixture was of a dark grey colour. Gold colloids can be prepared in a similar manner. The silver colloids were prepared by the Leopold and Lendl<sup>70</sup> method in which Hydroxylamine Hydrochloride ( $\text{NH}_2\text{OH.HCl}$ ) was used as a reducing agent. Firstly, 0.017 gm of Silver Nitrate ( $\text{AgNO}_3$ ) was dissolved in 90 ml water. 0.021 gm of Hydroxylamine Hydrochloride ( $\text{NH}_2\text{OH.HCl}$ ) was dissolved in 5 ml water and 4.5 ml of 0.1 M Sodium Hydroxide was added to it. The mixture was rapidly added to the  $\text{AgNO}_3$  solution under vigorous stirring and in a few seconds a grey-brown solution was obtained. Silver colloids were also prepared by the Creighton<sup>82</sup> method using Sodium Borohydride as reducing agent. Aqueous solutions of 10 ml of a  $10^{-3}$  M  $\text{AgNO}_3$  and 30 ml of a  $10^{-3}$  M  $\text{NaBH}_4$  were prepared and ice-cooled separately. The  $\text{AgNO}_3$  solution was added drop by drop to the  $\text{NaBH}_4$  solution with vigorous stirring. The mixture was kept still for 1 hour and then vigorously stirred again for 10 minutes.

### **Characterisation of metal colloids**

The colloids were characterised by UV-vis spectroscopy. The concentration was kept at 1  $\mu\text{l}$  of colloid solution in 3 ml water and the spectra were recorded from 200 nm to 1100 nm. The UV-vis spectra taken after one day of preparation of three silver colloids are shown in figure 5.9, and that of gold colloid in figure 5.10. Silver colloids prepared by the three different methods show differences in their spectral absorption characteristics, which was mainly attributed to the morphological differences. The absorption maximum of the colloidal solution provides information on the average particle size, whereas its full-width at half-maximum (fwhm) gives an estimation of particle size distribution. Colloids prepared repeatedly with the same methods gave more or less the same results. In some cases, they either aggregated during preparation or froze during

storage. Strict adherence to the preparation protocol and the use of clean apparatus is therefore vital.

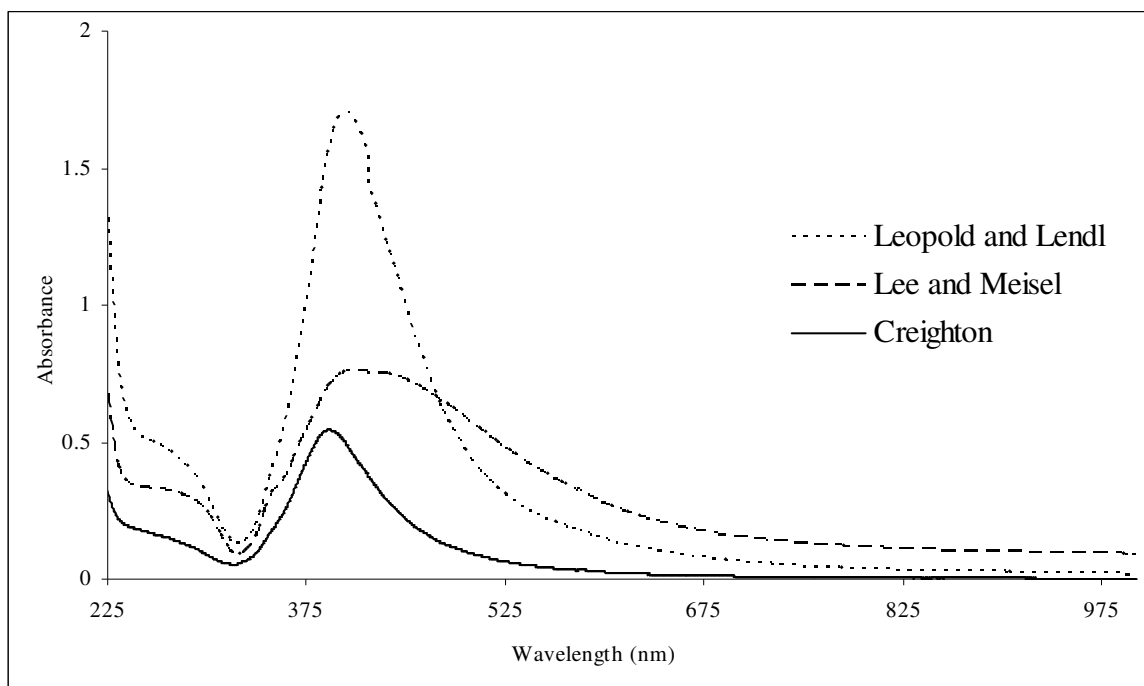


Figure 5.9 UV-vis absorption spectra of silver colloids prepared by three different methods.

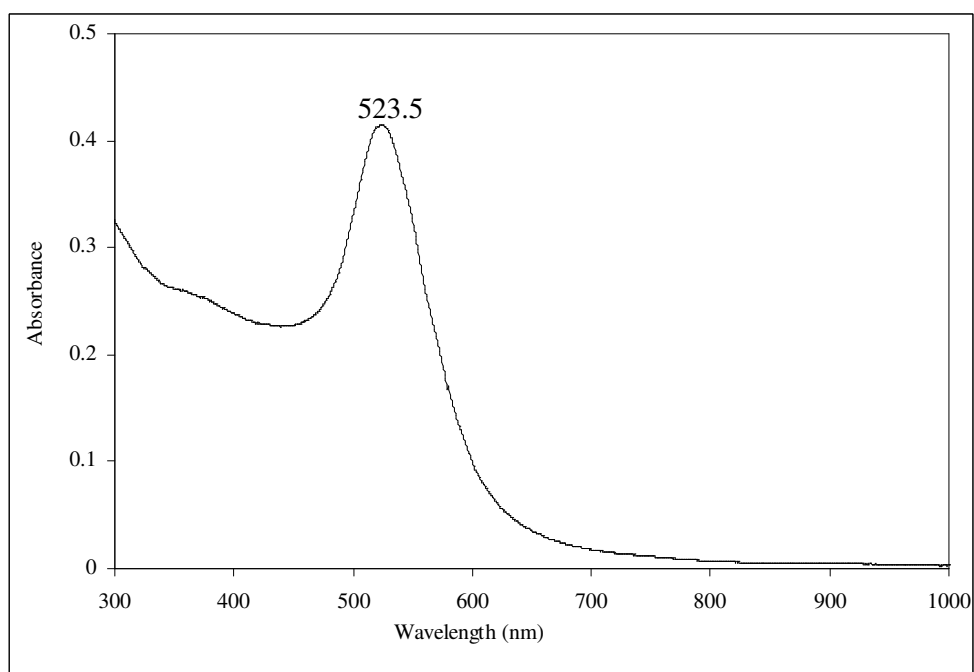


Figure 5.10 UV-vis absorption spectrum of gold colloid prepared by the Lee and Meisel method.

The silver colloids prepared using Hydroxylamine, Borohydride and Citrate as reducing agents had absorption maxima at 404 ( $\pm 2$ ) nm, 394 ( $\pm 3$ ) nm and 414 ( $\pm 6$ ) nm respectively as shown in Figure 5.9. A little difference in average particle sizes was observed. However, the fwhm of the same colloids were 149.5 nm, 81 nm and 196 nm respectively, showing a range of particle dispersion. Silver citrate colloids showed absorption at longer wavelength indicating the presence of larger particle sizes due to partial aggregation.

Absorption spectra of gold colloids prepared by the citrate reduction method (figure 5.10) showed an absorption maximum at 523.5 ( $\pm 2$ ) nm which was normal for gold colloids<sup>82</sup>. The full width at half maximum (fwhm) was at 96 nm, indicating a small particle dispersion, and the absorption was negligible at longer wavelength, showing the absence of bigger particles.

### **SERS Results**

SER spectra from colloidal solutions were recorded with a Renishaw Raman Imaging microscope fitted with CCD detector and lasers operating at 514 nm and 785 nm wavelengths were provided by argon and diode lasers respectively. Raman spectra of the colloids before adding the target molecule provided information regarding the background for subsequent SER scattering measurements as well as the presence of impurities, if any. It was also essential to check colloids after adding the aggregating agent because some impurities did not appear otherwise. Pyridine was selected as an analyte molecule, representing a pollutant species, with a nitrogen component and is a known Raman-active. The sample was diluted with triply-distilled water (TDW) to achieve various concentrations. SER spectra were recorded using a 1 cm quartz cuvette.

Raman measurements were recorded using both 514 nm and 785 nm lines. A fairly strong signal from Pyridine was obtained at  $10^{-11}$  M concentration using gold colloid with  $\text{KNO}_3$  as the aggregating agent and a 785 nm diode laser. Figure 5.11 shows the Raman spectrum of pure pyridine and its SER spectra of  $10^{-5}$ ,  $10^{-8}$  and  $10^{-11}$  M concentrations. A slight shift in peak wavelength (red shift) between the Raman spectrum of pyridine (figure 5.11a) and its SER spectra (figure 5.11 b, c & d) was

observed. This has been reported by others and was mentioned in chapter 2<sup>9,41,42,49</sup>. Similar results were observed with silver colloids using  $\lambda_i = 785$  nm.

With an argon-ion laser, using silver colloids prepared with hydroxylamine as reducing agent, pyridine could not be detected even at  $10^{-3}$  M concentration. Instead an altogether different band closely resembling the Rhodamine 6G molecule was detected (figure 5.12) which was also reported to have appeared in previous studies as anomalous or spurious bands and discussed in chapter 2<sup>57,108</sup>. This was only observed when using 514 nm laser wavelength.

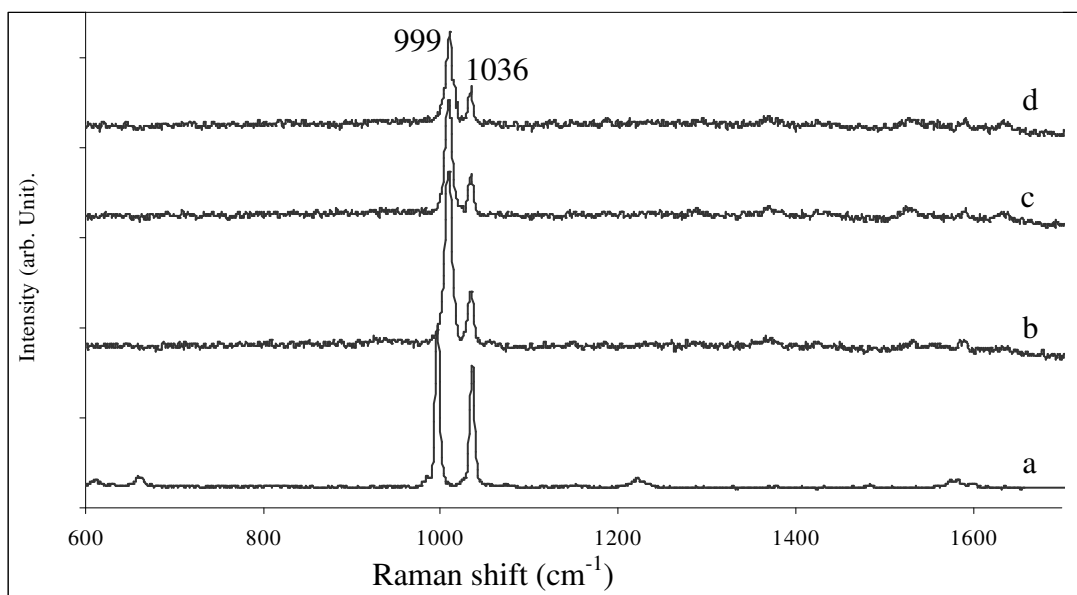


Figure 5.11 SER spectra of pyridine from gold colloidal solution recorded with  $\lambda_i = 785$  nm; pure pyridine Raman spectra (a), at  $10^{-5}$  M (b), at  $10^{-8}$  M (c) and at  $10^{-11}$  M (d) concentrations.

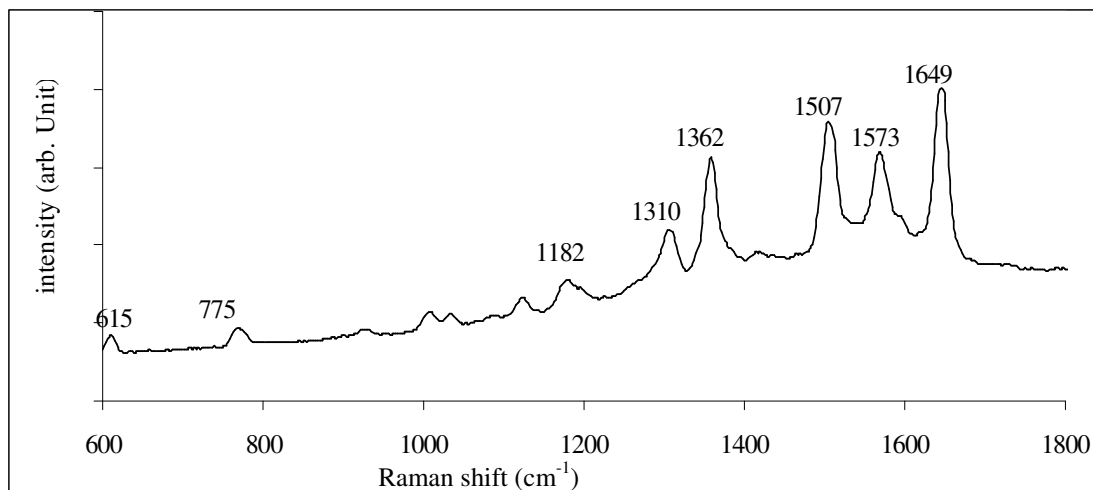


Figure 5.12 SER spectrum of  $10^{-3}$  M pyridine in silver colloidal solution recorded with  $\lambda_i = 514.5$  nm showing spurious band (see text in chapter 2 for explanation).

pH dependency of Raman signal from colloids was also observed. It has been established that decrease in pH value results in enhancement of Raman intensity, decrease in bandwidth and changes in relative intensities of the bands. This is due to the progressive transition from a highly covered surface SER spectrum to a less covered one. The colloids having lower pH value showed more enhancement in Raman scatterings; like the unmodified gold colloids having 5.5 pH showed better results as compared to silver colloids having pH of 7-8.

The positive results indicated that the SERS technique using metal colloids as SER-active surfaces can be used for almost all the chemical analytical applications. It provides user with the flexibility to modify components to achieve optimum results. At the same time, a slight alteration in any of the aspect (such as colloid preparation, sample presentation or equipment settings) may give different results. Nevertheless, specificity as well as high sensitivity can be achieved using SERS for which various combinations of surfaces, lasers and sample presentation techniques can be adopted.

#### 5.3.4 SERS with fabricated solid surfaces

SER-active surfaces can be prepared by many techniques as discussed in chapter 2. Some of these were experimentally evaluated, mainly with a view to justify the:

- Use of metal type for SER-active surfaces
- Surface roughness (morphology) that support highly sensitive SERS
- Protocol for fabricating such a surface

### Flat copper surfaces

Copper discs of 20 mm diameter and 2 mm thickness were cleaned in acetone and then washed thoroughly in TDW. The top surface of the disc was physically removed and washed again with acetone and TDW. The PETN explosive weighing  $\sim 10 \mu\text{g}$ , was placed on the surface and then pressed with a clean metal to form a very thin layer over  $\sim 1\text{mm}^2$  area. R3000 Raman system (section 5.2.5) was used to record Raman spectrum by focussing the laser directly over the area where explosive was placed and keeping  $t_i$  as 30 seconds. The Raman spectrum in figure 5.13 showed the characteristic Raman peaks of PETN against a high background. The high background was considered to be due to the specular reflections from the copper surface (the system uses  $180^\circ$  backscatter geometry as shown in appendix H) and could be reduced by baseline subtraction.

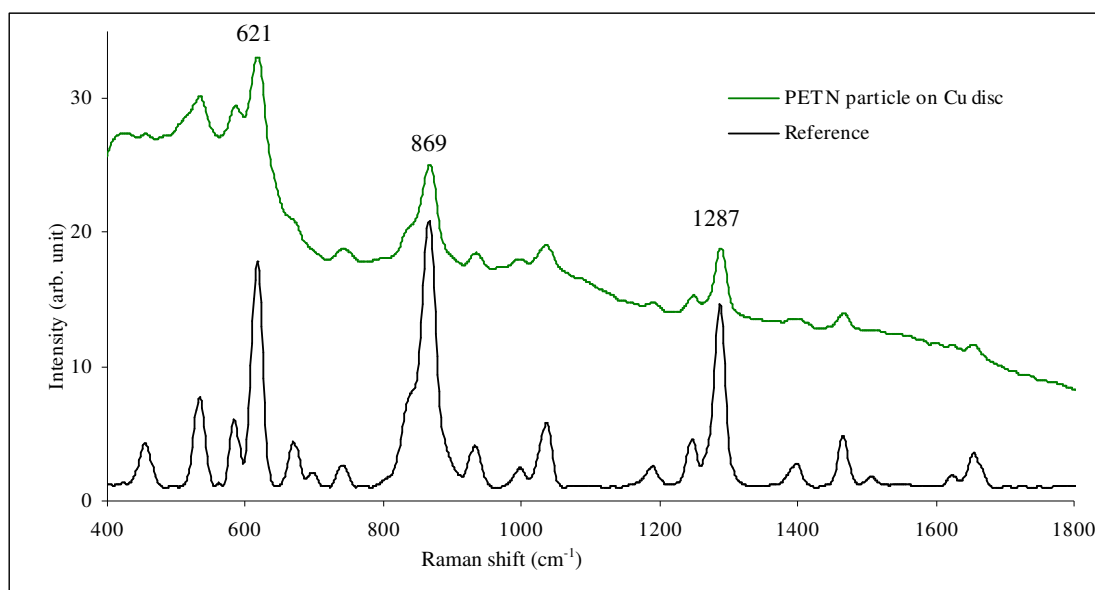


Figure 5.13 Raman spectra of PETN in bulk and on copper disc recorded with  $\lambda_i = 785$  from a diode laser.  $t_i = 30$  seconds.

The copper surface being non-Raman-active, had no contributions to the Raman signal and allowed the signal from a very small quantity of PETN to be analysed by this method that was otherwise difficult in both solid and dissolved forms. The experiment was repeated for RDX with the same sample conditions and the result, shown in figure



5.14, was recorded with  $t_i = 20$  seconds. The explosive was then dissolved in the acetone at  $\sim 10\%$  (w/v) and  $10\mu\text{l}$  was drop/dried on the similar copper surface. No Raman signal could be observed from the explosive material due to the low concentration of molecules on the surface in the absence of any surface enhancement effect.

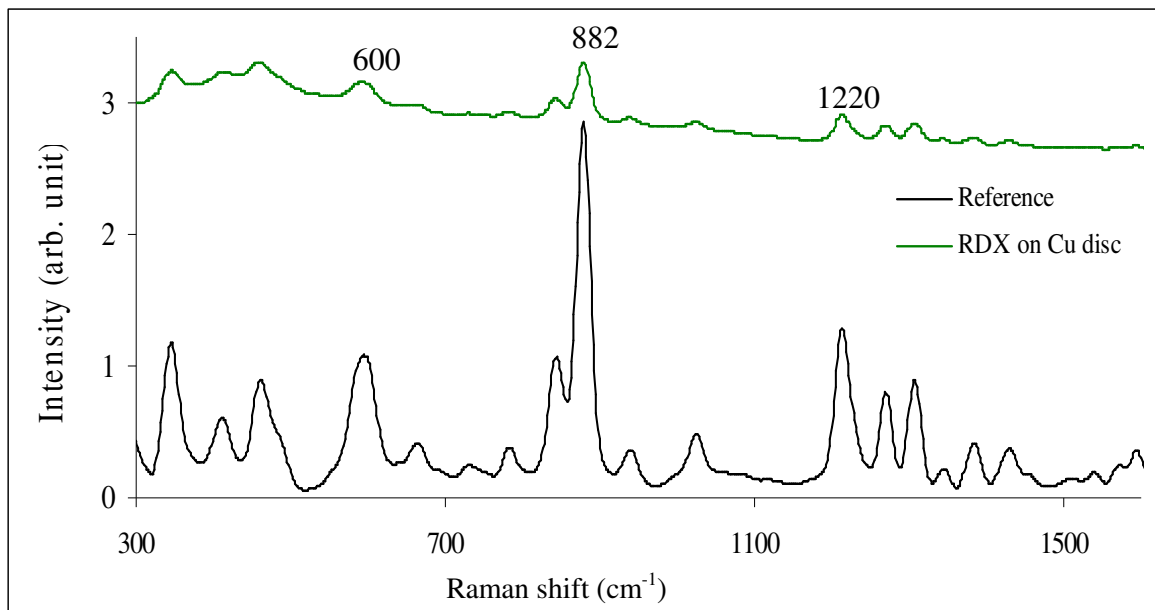


Figure 5.14 Raman spectrum of RDX in bulk and on Cu disc recorded with  $\lambda_i = 785$  nm.  $t_i = 20$  seconds.

### Laser ablated gold surfaces

Laser ablated metal surfaces have been used as SER-active surfaces<sup>84</sup>. In our experiment glass discs of 2.5 cm diameter coated with  $\sim 0.5\ \mu\text{m}$  gold layer were used. These were exposed to shots from an Nd:YAG laser 1064 nm wavelength of 10 nanoseconds pulse duration of various power levels to produce nano-scale roughness on the surface. The details of surface preparation and results are summarised in appendix L. The surfaces were studied under a microscope and images are also shown in appendix L.

The effect of laser was not uniform primarily due to the non-uniform power density across the cross-sectional area of the laser pulse and presence of time varying hot spots

in the beam area. It was concluded that gold layer was too thin for the laser to produce effective roughness. Whenever the laser was higher or focused, it burned a hole through the layer and melted the edges. However, when the laser power was kept low or out of focus, there was no or very little effect on the surface and no surface roughness was observed. Raman Spectra were recorded by putting 10  $\mu\text{l}$  from 1.5% (w/v) PETN solution (in acetone) on the surface but no measurable SER signal was observed. The surface could not be roughened with laser to suite the requirement of SERS. Fabrication of thicker gold surfaces is considered to be too costly. A laser with constant power density across the laser spot is expected to improve results.

### **Etched Silver Surfaces**

Silver was economical to use as compared to gold. Therefore, silver slabs of 2 mm thick and 25x25 mm area having quoted purity of 99.95% were obtained from Goodfellow, Cambridge Limited. Slabs were cleaned thoroughly with alcohol and then with TDW. Silver slab was etched in 1:2 nitric acid : TDW solution for 2 minutes, thoroughly rinsed with water and then air dried. It was expected that acid solution would have cleaned the surface of any contamination. A droplet of 5  $\mu\text{l}$  of 1% PETN solution (in acetone) was put on the surface and was allowed to evaporate. After drying, it was rinsed thoroughly with TDW several times to remove any deposited material and then air-dried. This was done to remove the residual layer of solution left on the surface which otherwise could obstruct Raman spectrum of PETN molecules adsorbed on the rough silver edges. This also precluded any chance of residual PETN left on the surface.

The figure 5.15 shows SEM images of raw silver slab (a) and then etched disc at various magnification (b-f). The surface was roughened with the 2 minutes etch creating metal edges across the surface.

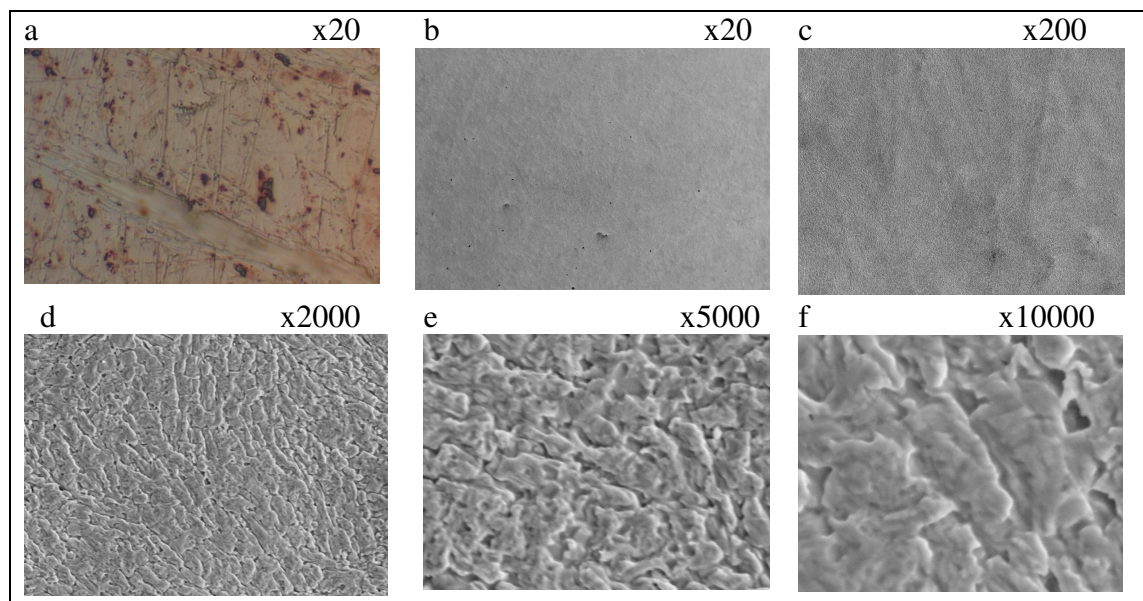


Figure 5.15 SEM images of silver slab before etching at 20 magnifications (a) same slab after etching in nitric acid solution at different magnifications (b-f).

The surface morphology was also observed using surface profiler (section 5.2.6) and some of the images are shown in Figure 5.16. The roughness in terms of shape of the structures was not uniform that resulted in the reduced area of sharp metal edges. The surface was found to be etched in valleys with sharp ridges at the edges. A wide distribution was observed in the height of the edges and the sharp needle like protrusions on the surface were ranging in height from 300 to 1000 nm with 2-3  $\mu\text{m}$  wide gap (valley) between them.

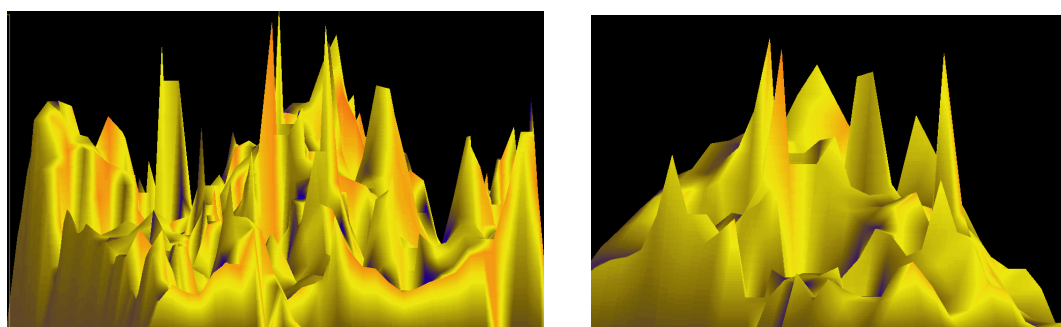


Figure 5.16 Surface profiles of etched silver slab showing 300 to 1000 nm high needle like structures.

Raman spectra were recorded before etching, after etching, after putting the droplet of PETN solution and lastly after washing away the residues from the surface. The results obtained with  $t_i = 50$  seconds are shown in figure 5.17. The etched surface gave low

metal background and no SER scatterings were observed after putting the small amount of PETN solution (10  $\mu\text{l}$ ) on the surface. This was expected to be due to the surface coverage by residue from solution after drying that did not allow the laser to interact with the molecules adsorbed at the metal edges.

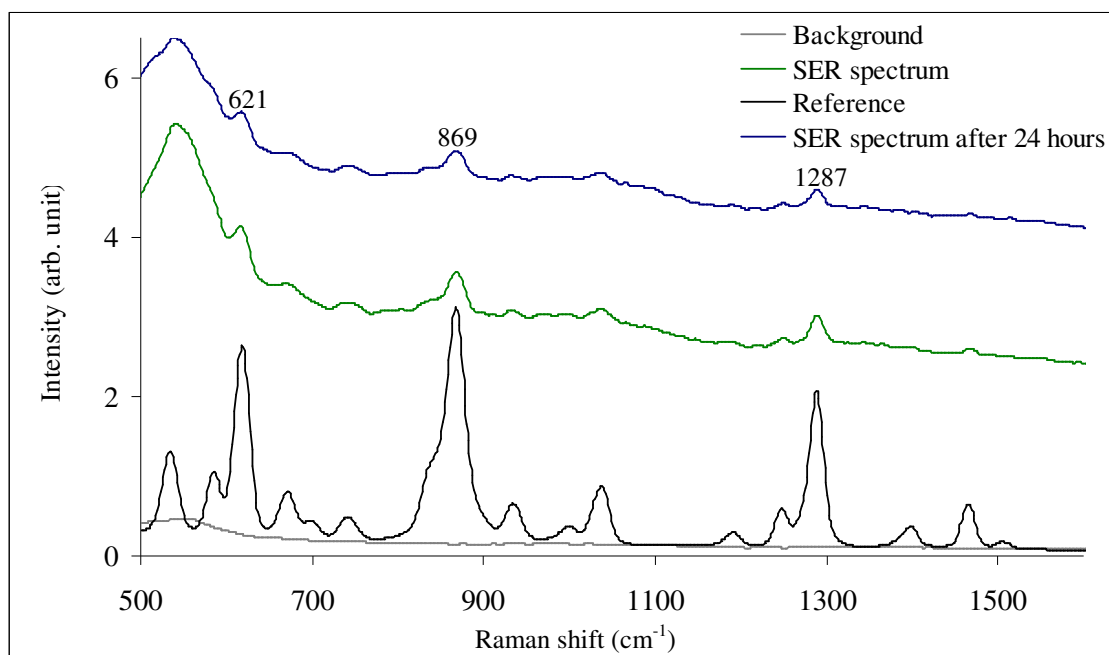


Figure 5.17 Raman spectra from etched silver slab before PETN droplet as background and of bulk for reference. SER spectra after putting small droplet of PETN solution, washing and drying and after 24 hours.  $\lambda_i = 785 \text{ nm}$ .  $t_i = 50 \text{ seconds}$ .

SER scatterings recorded after washing the surface (for any residue) showed characteristic Raman peaks of PETN molecule. The appearance of Raman spectra after washing off the residue indicated surface enhancement from the adsorbed PETN molecules within the surface plasmon. The number of molecules responsible for the Raman scatterings could not be estimated. Although the quantity of molecules in the PETN solution was high the solution was spread over much larger area ( $\sim 4 \text{ cm}^2$ ) than the laser diameter ( $\sim 0.1 \text{ mm}^2$ ) reducing the number of molecules settling in target area. The number of molecules that produced Raman signal would be much less than those settling within the laser diameter considering their further reduction during the evaporation of acetone and repeated washing of the surface with TDW. In addition, among the molecules adsorbed on the surface the enhancement in Raman intensity was

expected to have occurred from only those molecules that were actually adsorbed on the metal edges (hot spots).

The SER spectrum was also observed after 24 hours as shown in figure 5.17. The silver surface oxidises in air, therefore, such a surface can remain useful for longer period if unexposed to atmosphere.

In another experiment silver slab was etched for 2.5 minutes following the same procedure as in the experiment described above. Figure 5.18 shows the SEM images before and after etching at various magnifications. Surface roughness increased and became less uniform as compared to that of the earlier experiment due to the longer etching time. Surface morphology was checked by digital profiler but since the roughness was more than ~2000 nm no worthwhile images could be recorded (instrument limitation).

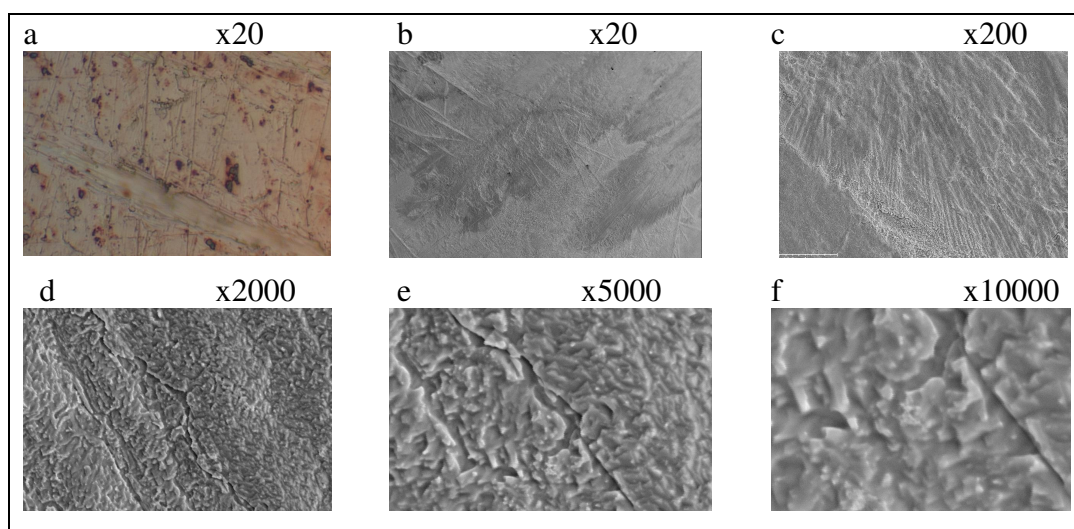


Figure 5.18 SEM images of Silver slab before etching at 20 magnifications (a) same slab after etching for 2.5 minutes at different magnifications as indicated (b-f).

The difference in the surface roughness could easily be observed at 20 times magnification. The formation of ridges across the surface were clearly visible from where the acid solution had etched the surface. Apart from the distinguished ridges the surface was generally devoid of sharp edges. The surface not only had comparatively

less number of metal edges but also the height of most of the structures was beyond the nano-scale dimensions.

After fabrication was complete, a  $\sim 10 \mu\text{l}$  droplet from 0.5% (w/v) PETN solution in acetone was put on the surface. SER spectrum was also recorded in the similar manner keeping  $t_i$  as 100 seconds and is shown in Figure 5.19. Although SER spectrum indicated presence of PETN, its very low intensity was indicative of combination of two factors: firstly, the concentration of PETN had been reduced to half which presented lesser number of adsorbed molecules for detection and secondly, the surface roughness had reduced in number and increased in height beyond the required scale for effective SER activity.

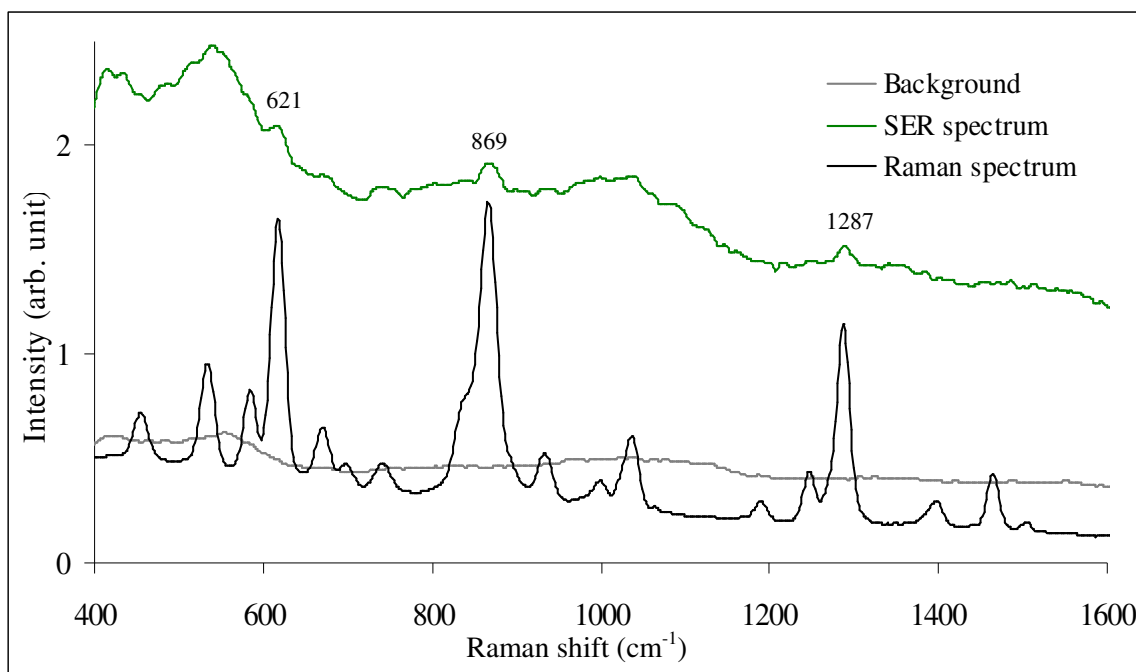


Figure 5.19 Raman spectra of PETN (reference) and of etched silver slab after fabrication. SER spectrum of adsorbed PETN molecules.

In these experiments, the enhancement in Raman intensity was not theoretically calculated but keeping in view the sample presentation and the adsorption phenomenon of molecules at the metal edges, it was expected to be at trace level. The technique for fabrication of SER-active surface was limited by the non-uniformity of the roughness that considerably reduced the number of useful adsorbing sites and thus the sensitivity. It also required thick metal surfaces as the starting substrate.

### Silver-Coated Surfaces

Ultra-sensitive detection with SERS depends mainly on producing the right type of surfaces. The need to produce uniformly rough SER-active surfaces that are reproducible and economical, have led to experimentations with metal coated surfaces. Realising the suitability of silver for SERS from the literature and confirmed by initial experiments, it was selected as the metal for further experiments. Although etched silver slabs gave excellent results but reusing the same after removing the used layer was found to be difficult and was found to render the surfaces unreliable. It was also important to preserve the surfaces for future references and that would have been too costly. Therefore, it was decided to fabricate surfaces by coating silver films over substrates that could then be roughened to achieve SER activity. For coating, high vacuum magnetron sputtering technique was chosen where the coating parameters could be effectively controlled.

Two main techniques were evaluated to get the desired roughness on the coated surfaces, as discussed in chapter 2; rough films over smooth substrates or by using rough substrates for coating. An attempt was made to optimise the surface roughness to achieve the traditional SER enhancement. Experiments conducted are summarised in table 5.2.

Table 5.2 Fabrication of SER surfaces using silver films deposition.

Serial	Substrate	Film thickness (nm)	Rate of coating (nm/second)	Percentage of oxygen in chamber	Substrate temperature ( $^{\circ}$ C)	Roughness* (rms in nm)
1	Glass slide	20	0.2	Nil	25	2
	Rough Cu disc	20	0.2	Nil	25	1400
	Rough Al disc	20	0.2	Nil	25	~2000
	Au disc	20	0.2	Nil	25	3
2	Glass slide	20	2	Nil	200	10
3	Glass slide cover	100	0.2	Nil	400	25
4	Slide cover with silicon oil film	100	0.2	Nil	300	25
5	Glass slide cover	100	1	Nil	450	13
	Frosted glass					>1000
6	Glass slide	100	2	Nil	400	20
7	Glass slide	100	1	20	200	25

\* defined as the rms height of the spikes.



The surface at serial 1 in table 5.2 was fabricated with glass slide cleaned in piranha solution for 30 minutes and washed in TDW and then sputtered with 20 nm silver layer. The glass surface was almost flat with very small and smooth undulations. Figure 5.20 shows the glass surface profile with the 20 nm silver layer showing ~2 nm roughness features and no sharp edges. Such a surface was not expected to be SER-active.

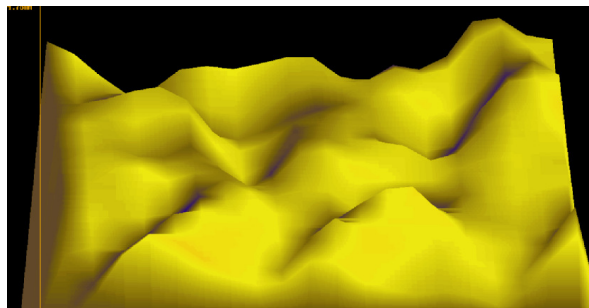


Figure 5.20 Surface profile of glass substrate with 20 nm silver layer.

The aluminium and copper substrates mentioned at serial 1 (table 5.2) were roughened by polishing to micron grade. The surfaces protrusions were  $\sim 2\mu\text{m}$  and therefore a very thin layer of 20 nm silver could not reduce the roughness to a level that supported SERS. On the other hand increase in silver layer reduced the sharpness (edges) of the structures and therefore desired level of roughness could not be achieved. In the experiment mentioned at serial 2 of the table 5.2, the substrate's temperature was increased to  $200\text{ }^{\circ}\text{C}$  during sputtering. This technique has shown to give fairly rough surfaces<sup>88</sup>. It was expected to result in cluster formation over substrate presenting rough surface. In our experiments, the effect of thermal deposition increased the roughness features to  $\sim 10\text{ nm}$  but the shape of the features remained unchanged from the previous result shown in figure 5.20.

With the further increase in temperature to  $400\text{ }^{\circ}\text{C}$  (serial 3 in table 5.2), the roughness was increased to the range of  $\sim 20\text{ to }30\text{ nm}$  (rms of 25 nm) with only slight change in the roughness features. The experiment at serial 4 was conducted by depositing silver layer on heated substrate at  $300\text{ }^{\circ}\text{C}$  previously coated with thin layer ( $\sim 1\text{ }\mu\text{m}$ ) of silicon oil. It was expected to increase the roughness<sup>85</sup>. The oil acted as a medium in which the depositing molecules could arrange themselves in a uniform crystalline patterns giving roughness at nano-scale with enough hot spots to give SER signal. The roughness of



features measured with digital profiler was between 20 to 25 nm with no sharp edges or crystalline structures. Experiment done with frosted glass having roughness in excess of 1000 nm was also not successful. With thin film deposition the structures remained fairly sharp but the height of structures increased further. The thicker films did reduce the structure height but it resulted in the reduction of sharp edges.

Thicker silver layers as mentioned at serial 6 and 7 of table 5.2 presented similar results. The sputtering in 20% oxygen atmosphere also did not increase the roughness as predicted<sup>89</sup>. In the presence of oxygen the sputtered molecules were expected to form largely Ag<sub>2</sub>O molecules and therefore were considered to settle on the substrate as bigger particles giving higher roughness. The roughness remained in the range of 20 nm. Two points were realised; the silver coating on smooth surfaces did not make the surfaces rough enough for a reliable SERS analysis and secondly the substrate should be roughened to a desired structural height before silver coating.

Enhancement in Raman scattering was not observed for any of the surfaces prepared in these experiment due mainly to the lack of sharp edges or the structures not having the right height. The SER spectrum was obtained for these surfaces when the PETN solution in acetone was drop dried on the surface. The solution tends to distort the surface morphology during drying and the resulting surface presented sharp edges of structural heights in hundreds of nanometers. These experiments were conducted with the surfaces mentioned at serial 2, 3 and 6 in table 5.2.

PETN solution in acetone at 0.08% (w/v) was prepared and 10 µl drop was placed on the surface which immediately spread and evaporated. This surface composed of a glass slide as substrate and coated with 100 nm of silver at 400 °C. The 3D images recorded by digital profiler after drying of PETN solution are shown in figure 5.21. It was observed that the surface had been modified by the evaporating solution forming crystalline structures on the surface. The ridges were closely located with uniform structural height of 400 to 600 nm. The ridges had sharp needle like ends. No change was noticed in the morphology of the surface after rinsing with TDW and heating at 40 °C for 10 minutes.

Similarly, 1% PETN solution (in acetone) was spotted on a surface fabricated with glass substrate and coated with 100 nm silver layer at 450 °C. Again, at the place where the solution was spotted, there appeared crystal like patterns on the surface. The roughness features were 300 to 500 nm in height, visibly similar to figure 5.21 and are shown in figure 5.22.

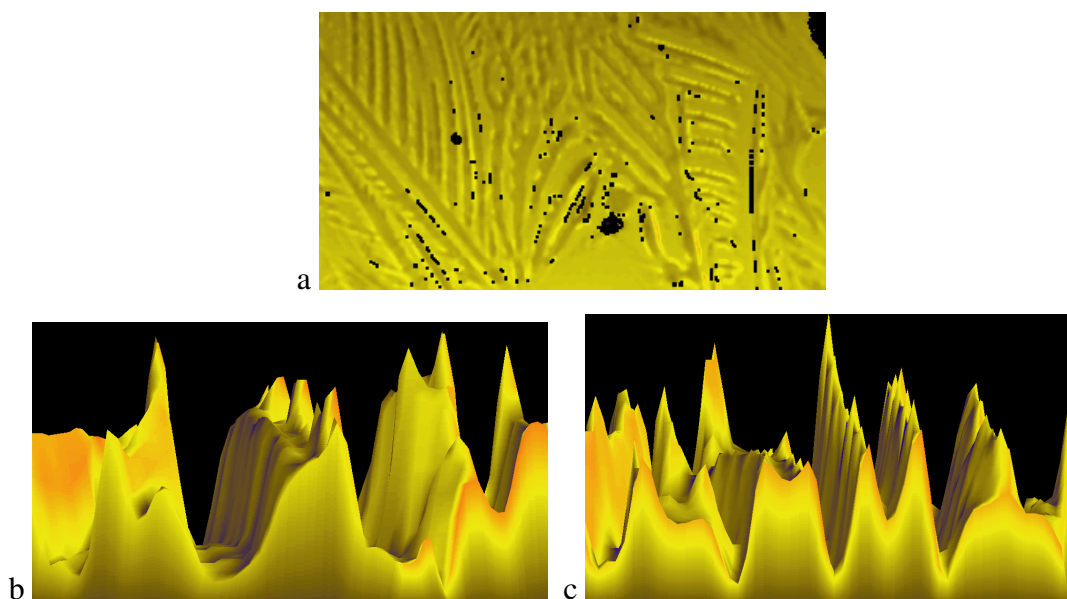


Figure 5.21 Profile images of 100 nm silver film spotted with 10  $\mu\text{l}$  of 0.08% PETN solution, showing uniform crystal like pattern giving roughness 400 to 600 nm (a) and digital profile images of the features (b and c).

The SER spectrum in figure 5.23 was taken with R3000 system keeping  $t_i = 100$  seconds after spotting the surface with the PETN solution, air drying, rinsing it thoroughly with TDW and drying again. Some of the peaks were completely missing while others have undergone slight change in the Raman shift. Referring to table 4.8, peaks at  $454\text{ cm}^{-1}$  and  $869\text{ cm}^{-1}$  were clearly visible. Additionally, a peak at the  $593\text{ cm}^{-1}$  O-N stretch could also be observed. Note that the SER measurements as well as profile images were taken after thoroughly removing any residual layer from the silver film by TDW wash.

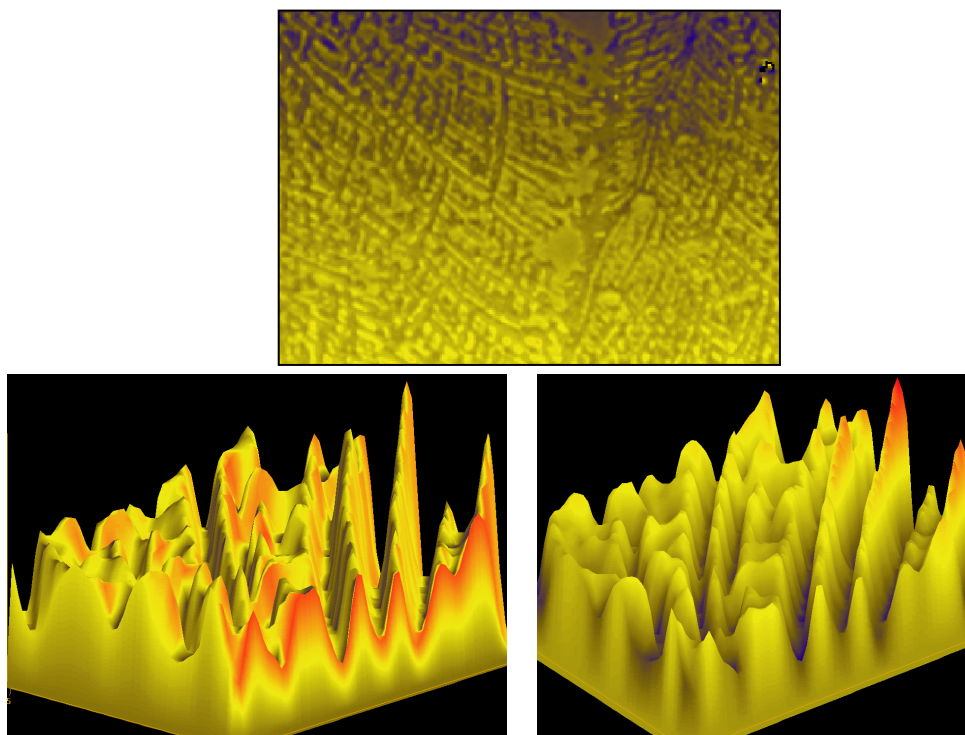


Figure 5.22: Profile images of 100 nm silver layer spotted with 10  $\mu\text{l}$  spot of 1% PETN solution, showing crystal like structures having roughness of 400 to 600 nm.

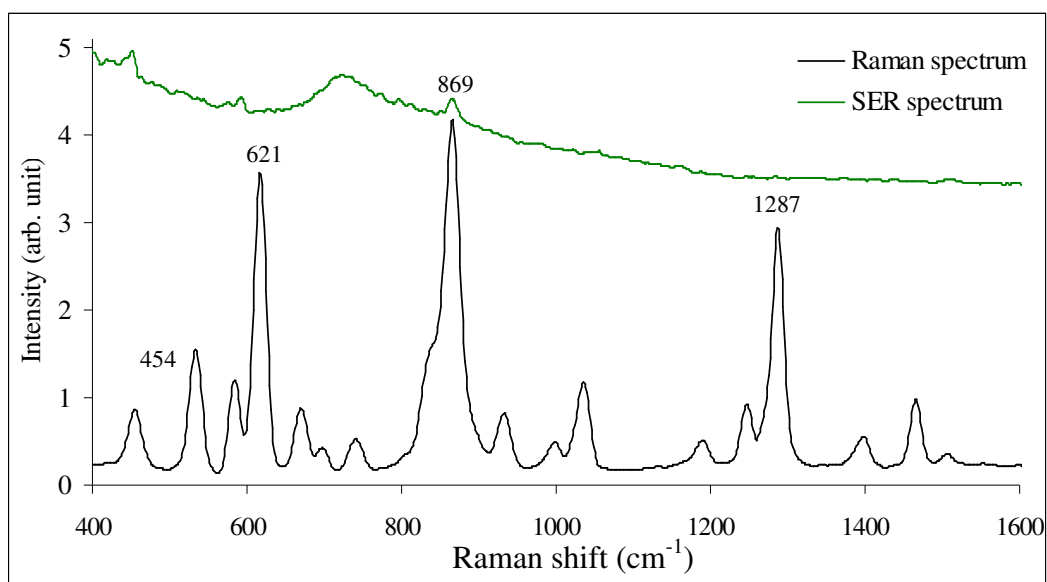


Figure 5.23 Raman spectrum of PETN and SER spectra from 100 nm silver film sputtered on glass slide at 400  $^{\circ}\text{C}$ , spotted with 0.08% PETN.  $\lambda_i = 785$  nm.  $t_i = 100$  seconds.

For the surface shown in figure 5.22, the SER spectrum is shown in figure 5.24. The spectrum was collected with  $t_i = 40$  seconds and the peaks at  $621\text{ cm}^{-1}$ ,  $869\text{ cm}^{-1}$  and at  $1287\text{ cm}^{-1}$  were observed. Note that the enhancement of Raman scattering was due to the roughness produced by the crystal like structure formation on the silver surface which did not have sharp structures before spotting with PETN solution.

To check the effect of solvent on the structure formation, PETN was dissolved in butanone to make 1% (w/v) solution and it was spotted on a 100 nm silver film on glass substrate in the similar manner as described above. The effect of PETN-butanone solution on the surface presented relatively less pronounced crystal patterns along the edge of the spot and almost no roughness in the centre. The images are shown in figure 5.25. The silver surface before the analyte spot was fairly smooth with  $\sim 20$  nm roughness features (figure 5.25 a) In the centre of the spotted area instead of patterns, there were numerous holes deep into the silver layer with sharp needle like structures at the edges (figure 5.25, d and e). It seemed that the silver layer had been corroded at these places.

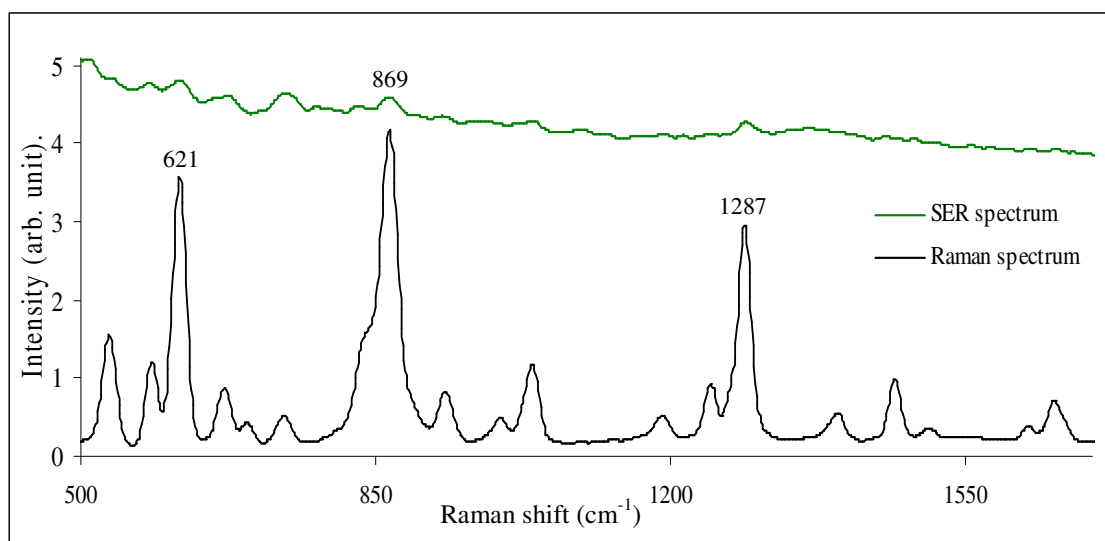


Figure 5.24: Raman spectrum of PETN and SER spectrum of 1% PETN in acetone spotted on 100 nm silver film sputtered on glass slide at  $450\text{ }^{\circ}\text{C}$ .  $\lambda_i = 785$  nm.  $t_i = 40$  seconds.

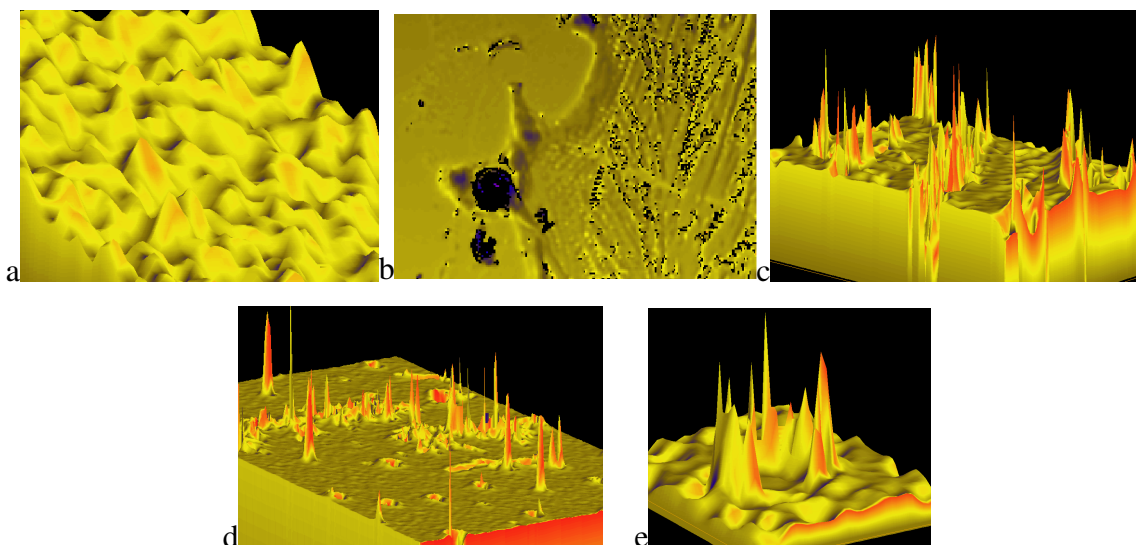


Figure 5.25: Profile images of 100 nm silver film over glass slide before spotting (a), rough patterns after PETN spot (b), magnification of ‘b’ at the edge (c), and the area in centre of spot (d and e).

In another experiment Raman spectrum of substrate spotted with 1% PETN in acetone after washing away the residual layer was recorded with  $t_i = 60$  seconds. It showed peaks at  $621\text{ cm}^{-1}$ ,  $869\text{ cm}^{-1}$  and at  $1287\text{ cm}^{-1}$  of C-C-C deformation, O-N stretch and N-O<sub>2</sub> symmetric stretch respectively and is given in figure 5.26. In case of PETN-butanone solution, the Raman peaks of PETN had very low intensity and could not be positively identified. The spectrum is also shown in figure 5.26.

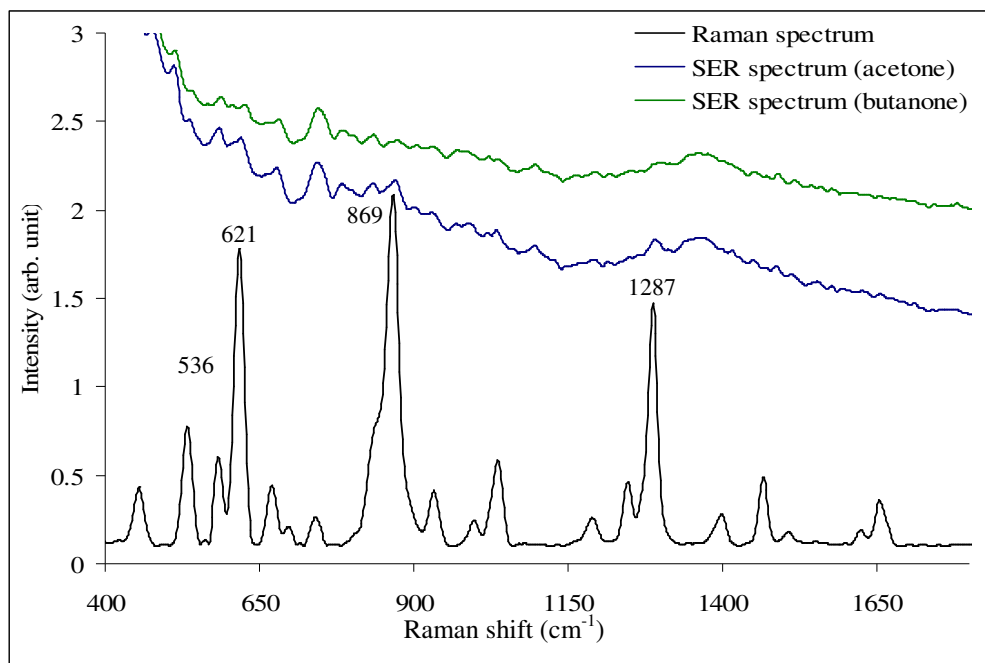


Figure 5.26 Raman spectrum of PETN and its SER spectra of 1% PETN in acetone and in butanone. The surfaces were fabricated with 100 nm silver film deposited on glass slides at 450 °C.  $t_i = 60$  seconds.

The surface morphology observed in figures 5.21 and 5.22 may be near optimum for a SER scatterings but it only appeared after the analyte was spotted on the surface. These roughness patterns also decreased with increasing or decreasing PETN concentration in the solution. The same surface was spotted with various concentrations of H<sub>2</sub>O<sub>2</sub> aqueous solution (10<sup>-2</sup> to 10<sup>-5</sup> M) and 10<sup>-2</sup> M solution of pyridine, but neither SER signal nor formation of crystal patterns were observed. The substrates used in these experiments were placed in vacuum oven at 60 °C for six hours. The prominent crystal pattern disappeared but the spot stain did remain on the layer surface. The surface was again analysed for SER scatterings but no signal was observed.

The surfaces fabricated with 100 nm sputtered silver layer in the presence of oxygen (20%) on glass slide at 200 °C were roughened by nitric acid etch for making SER-active surfaces. Surfaces were etched in HNO<sub>3</sub> solution for different durations to achieve surface roughness on the same lines as was observed with etched silver slabs described earlier. It was also envisaged that the etching process would liberate the oxygen from the surface particles leaving a very rough surface. The experimental

parameters and results are given in table 5.3. Too much time in the acid solution and the silver layer was removed and too less time would not create sufficient roughness on the surface. The workable concentration of  $\text{HNO}_3$  was found to be 7:22 with 2 to 3 minutes of etch and the surfaces had roughness  $\sim 50$  nm. The roughness features were not sharp, widely placed and non uniform in height. These surfaces resembled etched silver discs in appearance shown in figure 5.16.

Table 5.3 Parameters and results of 100 nm silver film etched in  $\text{HNO}_3$  solution to produce rough SER-active surface.

Concentration ( $\text{HNO}_3$ : TDW)	Etch Time (minutes)	Result
7 : 19 & higher	1 - 2	Layer corroded
7 : 22	1	No Signal
7 : 22	2	SER spectrum recorded
7 : 22	3	SER spectrum recorded
7 : 22	4	Layer corroded

Pyridine at  $10^{-2}$  M solution was used as an analyte and enhancement in Raman scatterings was observed for 2 minutes etch time with 7:22  $\text{HNO}_3$ :TDW. Figure 5.27 shows the Raman spectrum of pure pyridine as well as SER spectrum from  $10^{-2}$  M pyridine solution.

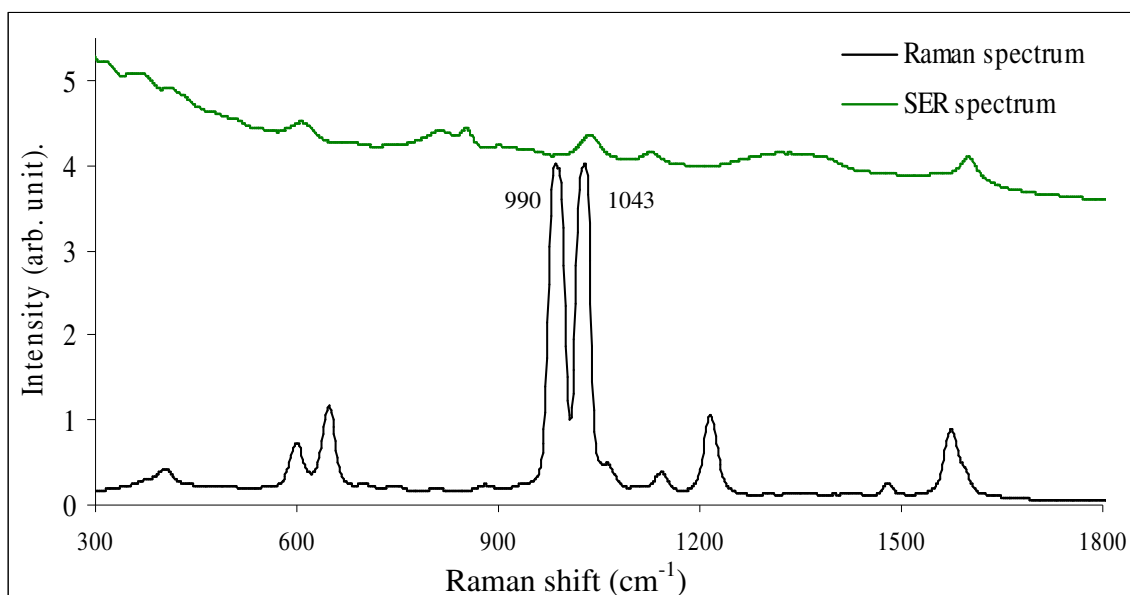


Figure 5.27 Raman spectrum of pyridine and SER spectrum after a drop of  $10^{-2}$  M pyridine solution was put on 100 nm silver film that was etched for 2 minute in  $\text{HNO}_3$  solution.  $t_i = 5$  seconds.

## 5.4 Conclusions

The experiments outlined in this chapter were aimed at establishing an experimental protocol to optimize surface roughness for maximum surface enhancement of Raman scatterings. It was recognised that the preparation of SER-active surface is one of the most important aspects of whole process. All four stages of research have contributed towards better understanding of applied Raman spectroscopy and its advanced techniques. To this end, the following major conclusions are drawn:

1. In the non-resonant region, the relation of Raman intensity with excitation wavelength is governed by the inverse fourth power. The onset of the resonance wavelength enhances the Raman intensity with the magnitude dependent mostly on the material properties. Tuneable lasers providing output of the resonant wavelength would enhance the SERS analysis.
2. The selection of laser excitation wavelength is important for not only RRS and SERRS but also for SERS.
3. In most cases, much higher enhancement is possible with the colloidal system than the larger metal surfaces. However, the coated metal surfaces seem to be simpler to prepare, economical, reproducible and more suitable for field use. These may be relatively more durable if specifically prepared for the purpose.
4. The technique of fabricating SER-active surfaces only by controlling the deposition parameters of silver films on the plane substrates can simplify the process.
5. It may be easier to deposit silver films over the rough substrates to make uniform SER-active surfaces. It may be relatively easy to prepare the substrate of appropriate roughness before metal coating. This would ensure reproducibility as well as simplicity.
6. As the deposited silver films are sensitive to corrosive materials, such molecules (as peroxide based) should be used in lower concentration in SER experiments.
7. For ultra-sensitive detection work, especially involving vapour detection, SER-active surfaces would have to be fabricated with high concentration of nano-structures of optimum heights. This was experimentally demonstrated.



## **6. EXPERIMENTAL – SURFACE ENHANCED RAMAN ACTIVE SURFACE FABRICATION**

### **6.1 General**

The optimum SER effect relies primarily upon the surface morphology of the substrate in addition to a host of other factors. Although high enhancement was achieved using silver-coated surfaces (as discussed in Chapter 5), two major limitations were also noted:

- a. Roughness achieved with sputtered silver layers was not of the dimension usually regarded to be the optimum for SER activity.
- b. These surfaces were not capable of achieving sufficient enhancement of Raman scattering so that the vapour deposited from solid samples at the normal laboratory temperature and pressure could be observed.

Most of the techniques discussed earlier in Chapter 2 are capable of producing surface morphology to support SERS. However, not all were found to be suitable for vapour phase analysis, and accounts of a few important ones which have undergone tests have been included in Chapter 5. The technique based on Nanosphere Lithography (NSL) discussed in detail in Chapter 2 is considered to be most suitable for the present research. Surfaces fabricated with this technique were found to be efficient for adsorbing target molecules emanating from the liquids as well as from the solids having very low vapour pressure. Such surfaces do not require further modification to exhibit SER activity even for a very low concentration of molecules at the surface.

In this chapter, the details of substrate fabrication based on the NSL technique is discussed. The concept and basic design have been adopted from the published work by Van Duyne<sup>80,97-99</sup> and modified to suit our experimental setup and conditions of sample presentation. Two different types of substrates were used: *glass* and *fused quartz*. The justifications for the choice of substrates and their respective techniques of fabrication will be discussed in detail in this chapter and in Chapter 7. Nevertheless, it is important to simply highlight the reasons for this choice of substrate at this stage. Glass gives a very high background fluorescence/scatterings noise due to its chemical composition that make it impossible to get any useful SER signal without either effective background subtraction or long time data averaging, both of which are contrary to the concept of real time monitoring. Therefore, it became imperative either to use a glass substrate with modification prior to SER analysis or to use optical fused quartz to reduce high background noise to obtain acceptable signal to noise ratio (S/N).

Since the techniques for the preparation of surfaces with the glass and the quartz substrates are different, they are described separately in the subsequent sections. It is noted that both types of substrates support SER activity and we have used the former for the presentation of molecules onto the surface via solution and the latter (for showing better SER capability) for the adsorption of molecules from vapour (from solid samples at standard temperature and pressure (STP)).

## **6.2 Instrumentation**

The equipment used for these experiments has been described in Chapter 5 (appendices C-K).

## **6.3 Glass-based substrate**

The SER-active surfaces based on glass substrates were fabricated with three different techniques that resulted in surfaces with different specifications. The fabrication procedure is described here and variations for modified SER-active surfaces are highlighted separately.

### **6.3.1 Materials**

Polystyrene latex micro-spheres (2.5 wt% dispersion in water,  $2 \times 10^{11}$  particles per ml) of 500 nm diameter were purchased from Alfa Aesar. A silver sputtering target of 2 mm thickness and 75 mm diameter having quoted purity of 99.9% was obtained from Goodfellow, Cambridge Limited. For glass based substrate preparation, super premium microscope slides of 1 mm thickness were purchased from Fisher Scientific, UK. The data sheet is included as appendix M. All other chemicals used were common laboratory grade materials. Tri-distilled water (TDW) was prepared in the laboratory and was used throughout the experiments.

### **6.3.2 Surface fabrication procedure**

The glass slides were cut into small sizes (25 mm x 25 mm or 15 mm x 25mm) and were cleaned in Piranha solution (3:1,  $\text{H}_2\text{SO}_4$  : 30%  $\text{H}_2\text{O}_2$ ) for 30 minutes at 80 °C and rinsed thoroughly with TDW. These were etched in an ultra sonication bath in 1:1:5,  $\text{NH}_4\text{OH}$  : 30%  $\text{H}_2\text{O}_2$  :  $\text{H}_2\text{O}$  for 1 hour to make the glass surface hydrophilic. These were rinsed thoroughly with TDW and kept in it until used.

### **6.3.3 Nanosphere lithography**

The polystyrene nanospheres (PNS) were used in various concentrations to optimise the monolayer coverage. The nanosphere's surface consists of negatively charged carboxyl-terminated polymer molecules that have a strong hydrophobic nature. The detailed account of polymer charge behaviour in aqueous solution is discussed by Chen et al <sup>144</sup>. The glass surface becomes hydrophilic on sonication in ammonia solution, it helps in strong adherence of nanospheres onto the surface. Suspensions between  $1-2 \times 10^{11}$  particles per ml were used. The substrates were placed at various slopes between 0 and 12° and ~10 µl solution of polystyrene nanospheres solution was dropped onto the surface. The nanosphere solution was allowed to flow under gravity leaving a monolayer over the area covered. The surface was then allowed to dry at room temperature. The process is shown schematically in figure 6.1.

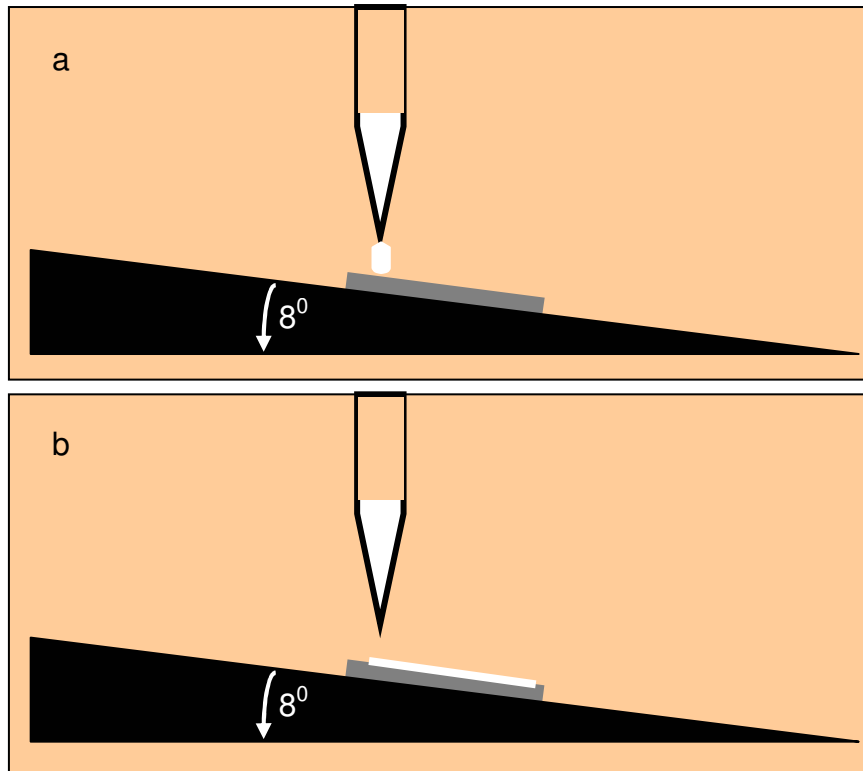


Figure 6.1 Schematic of NSL process. The measured quantity of nanosphere solution is placed on inclined substrate (a) and the solution spread and flow to form mono-layer on evaporation of solvent (b).

### 6.3.4 Silver Deposition

The substrates with PNS monolayer were then placed in the chamber of a Reactive DC-Magnetron Sputtering equipment. The chamber was evacuated down to  $\sim 2 \times 10^{-5}$  mbar before injecting argon gas, raising the pressure to  $2 \times 10^{-3}$  mbar. At normal laboratory temperature, the substrates were then sputtered with a silver layer varying between 40-300 nm thickness at the rate of 1 nm per second while being rotated at a slow speed of  $\sim 10$  rpm. The images in appendix K show the equipment and figure 6.2 show the samples placed on sample plate inside the chamber.

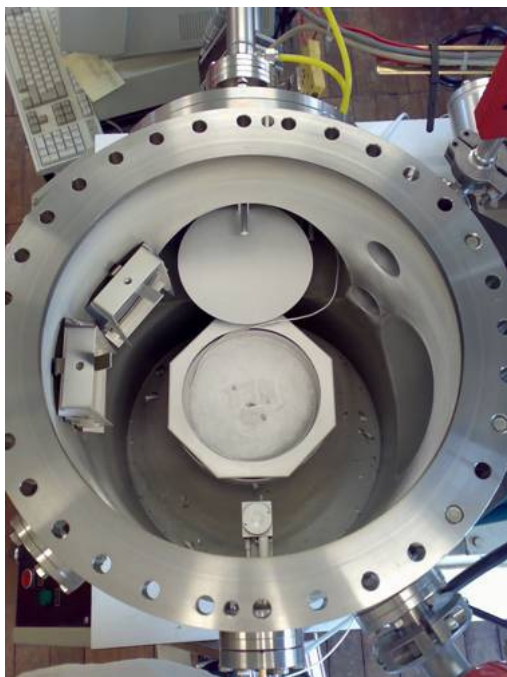


Figure 6.2 Photograph of the substrates coated with monolayer of nanospheres placed in the chamber of magnetron sputtering equipment.

### 6.3.5 Nanosphere removal

The substrates were sonicated in absolute ethanol at 40 °C for approximately 2 minutes to remove the layer of deposited nanospheres. The substrate were then washed thoroughly with TDW and used as soon as they were dry to avoid contamination.



Figure 6.3 Removal of nanospheres by ultra-sonication in ethanol.

It is important to note some of the experimental considerations which had effected the properties of substrate fabricated by the method described above and shown schematically in figure 6.4(a). In the SER surfaces prepared using the above-mentioned technique, most of the exposed surface was found not to be covered with the silver structures. The S/N in the Raman spectrum due to the impurities within the exposed glass surface was far too low for useful analysis without an extensive background subtraction. This led to the evolution of two variants from the original method. It was decided to introduce a thin silver layer on to the glass surface either before the NSL process or after the removal of PNS, with the aim to stop the laser interacting directly with the glass surface. The variations are shown graphically in figure 6.4 (b and c). In either case, the laser does not come in contact with the raw surface of the glass substrate due to the additional silver layer and therefore the background florescence noise is largely eliminated.

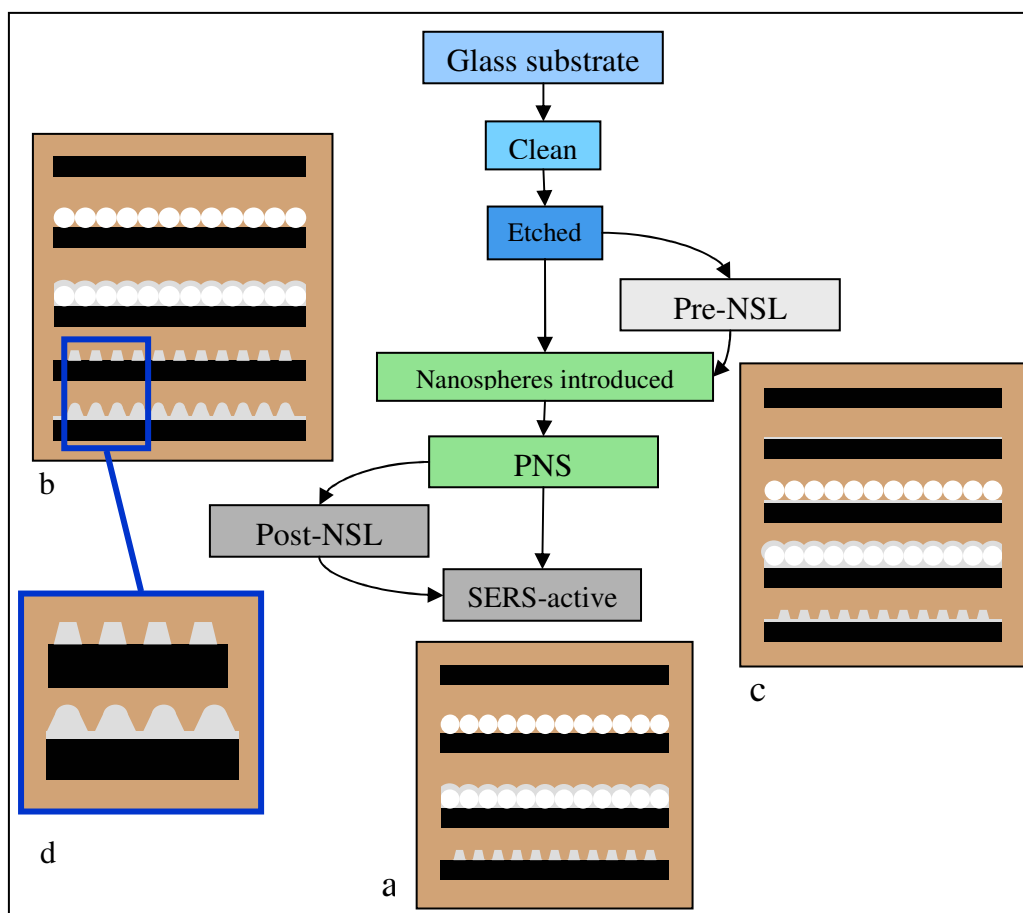


Figure 6.4 The basic NSL method (a) and the two variants for preparation of SER-active glass-based substrates (b) and (c). Enlargement of part of (b) is shown as (d).

### **6.3.6 Variation 1 - Deposition of Pre-NSL Silver layer.**

A schematic layout of this variation is shown in figure 6.4 (c). After cleaning with Piranha solution and etching in ammonia solution in an ultrasonic bath (discussed in section 6.3.2), the substrates were taken out of TDW, dried and placed in the chamber of the Reactive DC-Magnetron Sputtering equipment. They were sputtered with a silver layer of 10 or 15 nm thickness at the rate of 1 nm per second at the normal room temperature under the same pressure conditions discussed in section 6.3.4. The rest of the process of NSL, silver deposition and PNS removal remains the same. This variation in NSL procedure makes the technique difficult due to the reduced hydrophilic effect on a thin silver surface as compared to the glass surface. The flow rate of nanosphere increases and therefore the angle of substrate during the NSL process had to be reduced as discussed (vide afro).

### **6.3.7 Variation 2 – Deposition of Post-NSL Silver layer.**

The substrate was fabricated as per the process discussed in sections 6.3.2 to 6.3.5. These were then put in the Magnetron Sputtering chamber and coated with a second layer of silver of 10-15 nm, keeping the chamber conditions the same as mentioned in section 6.3.4. A diagrammatic layout of such a surface is presented in figure 6.4 (b). Note the enlarged portion, figure 6.4 (d), showing the smooth finished surface as compared to the sharp edges achieved by the other two methods.

## **6.4 Quartz-based substrates**

### **6.4.1 Materials.**

Optical fused glass (quartz) microscope slides were purchased from UQG Ltd that had ~94% transmittance at 785nm wavelength. The UV-vis-NIR and Raman spectra will be discussed in Chapter 7 and the data sheet is attached as appendix M. The slides were cut into smaller sizes of 25 mm x 25 mm or 15 mm x 25 mm. The rest of the materials were the same as mentioned in section 6.3.1 above.

### **6.4.2 Surface Fabrication Procedure**

The nano-structured surface fabrication must be preceded by the preparation of a suitable substrate. The substrate fabrication process is explained diagrammatically in figure 6.5. The quartz substrates were cleaned in Piranha solution (3:1, H<sub>2</sub>SO<sub>4</sub> : 30%

H<sub>2</sub>O<sub>2</sub>) for 30 minutes at 80<sup>0</sup>C and rinsed thoroughly with TDW. These were sonicated in 1:1:5, NH<sub>4</sub>OH : 30% H<sub>2</sub>O<sub>2</sub> : H<sub>2</sub>O for 2 hours to make the surface hydrophilic. These were rinsed thoroughly with TDW and kept in it until used.

The remaining procedures for the NSL treatment, silver deposition and nanosphere removal was similar to that for preparing surfaces based on glass substrates (sections 6.3.3-5). The process of NSL becomes a little difficult due to the reduction in hydrophilic effect on the optical fused glass as compared to ordinary glass. Again, a little reduction in the angle of substrate during the NSL treatment (discussed later) substantially compensated for this reduced hydrophilic effect.

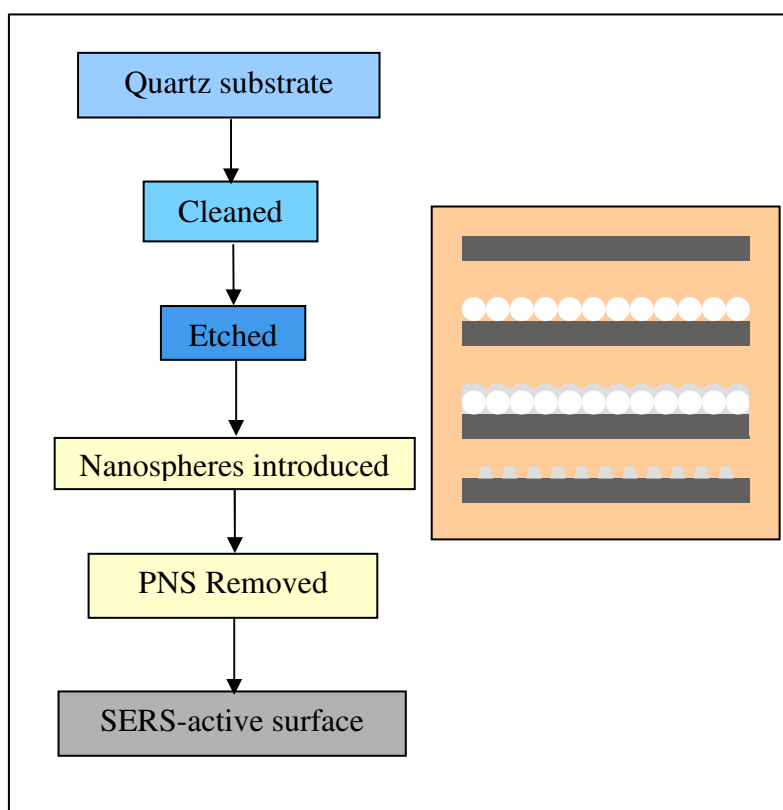


Figure 6.5 The diagrammatic layout of the method for preparation of SERS-active quartz-based substrates.



## 6.5 NSL structure characterisation

### 6.5.1 Glass based substrates.

As stated earlier, the SER-active surfaces were initially prepared with glass substrate. It took a series of experiments to achieve the correct protocol of substrate fabrication. The mono-layer formation of packed nanospheres is vital to achieve a uniform structural array that would ensure the maximum number of silver structures (or hotspots) suitable for higher enhancement of Raman intensities over the area of the substrate. Schematic surface models of substrates during different stages of fabrication are presented schematically in figure 6.6 for clarity. The surface at three stages of fabrication is shown in figure 6.7. The glass substrate coated with nanospheres to achieve a monolayer assembly is shown in figure 6.7 (b) and its model in figure 6.6 (b). It is then sputtered with a layer of silver [figure 6.6 (c)]. Finally, the silver structural array after removal of the nanospheres is shown in figure 6.7 (c), the height of which corresponds to the thickness of the sputtered silver layer and its schematic is shown in figure 6.6 (d).

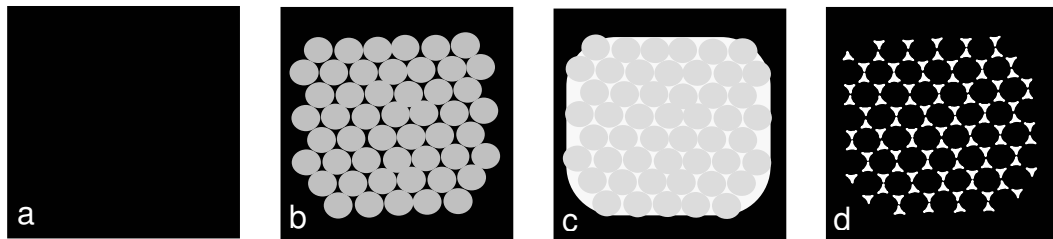


Figure 6.6 Schematic representation of the surface fabrication stages in a lithographic method. Glass substrate (a), with nanospheres (b), with silver layer (c) and after the nanospheres are removed (d).

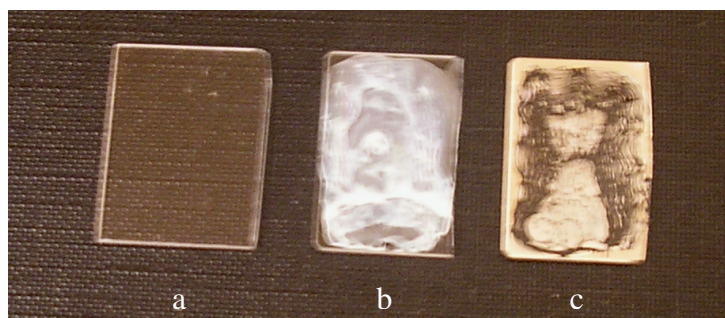


Figure 6.7 Surface fabrication stages by NSL technique. Glass substrate (a), with nanospheres (b), and after silver layer and the removal of the nanospheres (c).

This configuration of a single array formed by the assembly of seven nanospheres, is given in figure 6.8. This structure array geometry has been described. It is deduced that the nanospheres of diameter 500 nm will have the distance between any two adjacent structures ‘D’ (centre to centre distance of two adjacent structures) of ~288 nm and the average size of the structure ‘d’ (the length of the perpendicular bisector of largest inscribed equilateral triangle) of ~116 nm. The detailed calculations are given in appendix N.

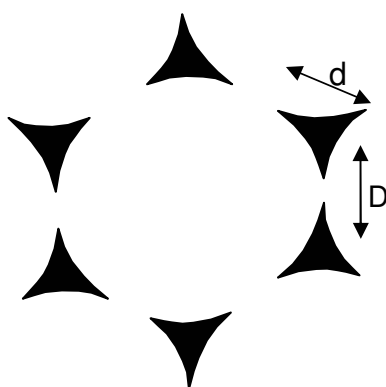


Figure 6.8 Configuration of a single silver structural array formed by the assembly of seven nanospheres.

Such an array of nano-structures would provide around  $10^6$  structures in an area of  $0.1 \text{ mm}^2$  which is approximately the size of the laser spot (at the target) in Raman scattering experiments using the Ocean Optic spectrometer (R3000). This meant that only about 8% of the area was covered by the structures and the remaining 92% was that of exposed substrate which accounts for a very high background noise from the glass substrate (discussed later in Chapter 7). The structure concentration did not change with the changes in height of the structures as it was entirely dependent upon the diameter of the nanospheres and their arrangement on the substrate. The shape also remained approximately the same for the thickness of silver layer between 40 and 300 nm. Therefore the structural arrangement, their uniformity and their concentration were almost entirely dependent upon the nanosphere arrangement (for a specific diameter of nanosphere), thereby making nanosphere coating the most important stage of SERS.

As mentioned before, the cleaned and etched substrates were kept in TDW until used. No observable difference was found due to the time of the storage and all the substrates were used within a four week period. The laboratory temperature remained between 21 and 25 °C and both the PNS as well as the substrate were at the normal temperature before coating. The arrangement of nanospheres on the substrate was mostly governed by two variables; *concentration of PNS* and *inclination of substrate* during coating. By changing these preparation variables, the effects on the PNS monolayer were recorded and are summarised in table 6.1.

Hydrophilic ability also plays an important role in the NSL process, but the variations could be effectively overcome by modifying the two main variables mentioned above. Other factors having a minor effect on the PNS monolayer like cleanliness of substrate, sputtering conditions, the nanosphere removal process and other laboratory conditions were kept controlled and whenever any flaw was detected, the preparation was discarded.

The initial experiments were conducted on the glass substrates with ‘as-received’ samples ( $2 \times 10^{11}$  particles. $\text{ml}^{-1}$ ) and by increasing the inclination of the substrate from  $0^\circ$  to  $12^\circ$  from horizontal. At a  $0^\circ$  to  $4^\circ$  slope the nanospheres tend to make a multilayer as shown in the SEM image in figure 6.9. Due to the hydrophilic nature of the treated glass, the nanospheres tend to stick to the surface and as the concentration of the nanospheres is high they bunch up in layers. For the nanospheres to be able to spread into a single layer, either the concentration of nanospheres needed to be reduced or the slope of the substrate required to be increased so that after the initial layer has stuck to the glass surface, the rest could flow over to the lower end.

Table 6.1 Effects on substrate’s morphology with the changes in PNS concentration and angle of coating.

Substrate	Concentration of PNS (particles.ml <sup>-1</sup> )	Angle of substrate	Effect on substrate morphology
Glass	2x10 <sup>11</sup>	0 <sup>0</sup>	Multilayer formation
Glass	2x10 <sup>11</sup>	4 <sup>0</sup>	Multilayer formation
Glass	2x10 <sup>11</sup>	6 <sup>0</sup>	Double layer formation with patches of mono-layer
Glass	2x10 <sup>11</sup>	8 <sup>0</sup>	Mono-layer pronounced *
Glass	2x10 <sup>11</sup>	10 <sup>0</sup>	Monolayer patches with most area covered with dispersed nanospheres
Glass	2x10 <sup>11</sup>	12 <sup>0</sup>	Most area covered with dispersed nanospheres with multilayer at lower half
Glass	1.5x10 <sup>11</sup>	6 <sup>0</sup>	Monolayer formation with patches of dispersed nanospheres
Glass	1.5x10 <sup>11</sup>	8 <sup>0</sup>	Monolayer formation in patches with more areas of dispersed nanospheres and multilayer
Glass	1.5x10 <sup>11</sup>	10 <sup>0</sup>	Most area covered with dispersed nanospheres
Glass	1x10 <sup>11</sup>	4 <sup>0</sup>	Monolayer formation in patches with more areas of dispersed nanospheres and multilayer
Glass	1x10 <sup>11</sup>	6 <sup>0</sup>	Most area covered with widely dispersed nanospheres clusters
Glass	1x10 <sup>11</sup>	8 <sup>0</sup>	Most area covered with widely dispersed nanospheres clusters
Glass with 10nm Ag under-layer	2x10 <sup>11</sup>	8 <sup>0</sup>	Patches of monolayer and multilayer formations with widely dispersed nanospheres at places
Glass with 10nm Ag under-layer	2x10 <sup>11</sup>	6 <sup>0</sup>	Patches of monolayer and multilayer formations with widely dispersed nanospheres at places
Glass with 15nm Ag under-layer	2x10 <sup>11</sup>	8 <sup>0</sup>	Monolayer patches with most area covered with dispersed nanospheres
Glass with 15nm Ag under-layer	2x10 <sup>11</sup>	6 <sup>0</sup>	Mono-layer pronounced *
Glass with 15nm Ag over layer	2x10 <sup>11</sup>	8 <sup>0</sup>	Pronounced monolayer. Over-layer does not change the surface morphology *

\* Optimum results. See text

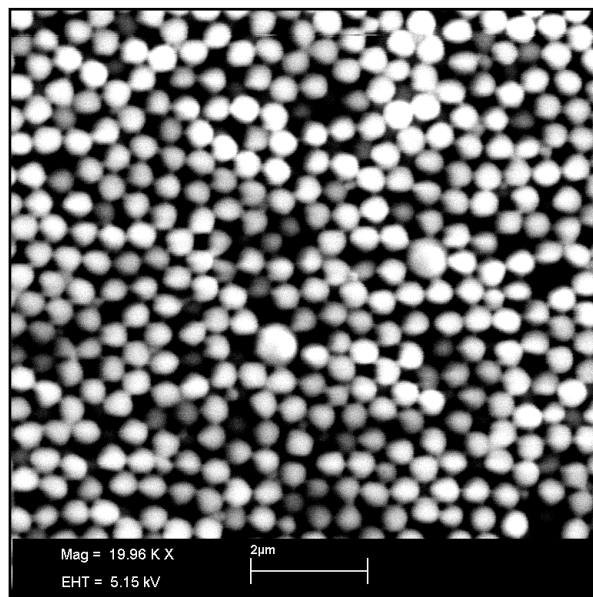


Figure 6.9 SEM image of multilayer of polystyrene nanospheres over treated glass surface.

At a  $6^\circ$  inclination, few patches of monolayer were observed in the higher half of the substrate while the rest of the surface had multilayer. Figure 6.10 shows the edge of one such patch where the monolayer converts into a multilayer for a substrate kept at  $6^\circ$  slope and coated with ‘as-received’ nanospheres ( $2 \times 10^{11}$  particles. $\text{ml}^{-1}$ ).

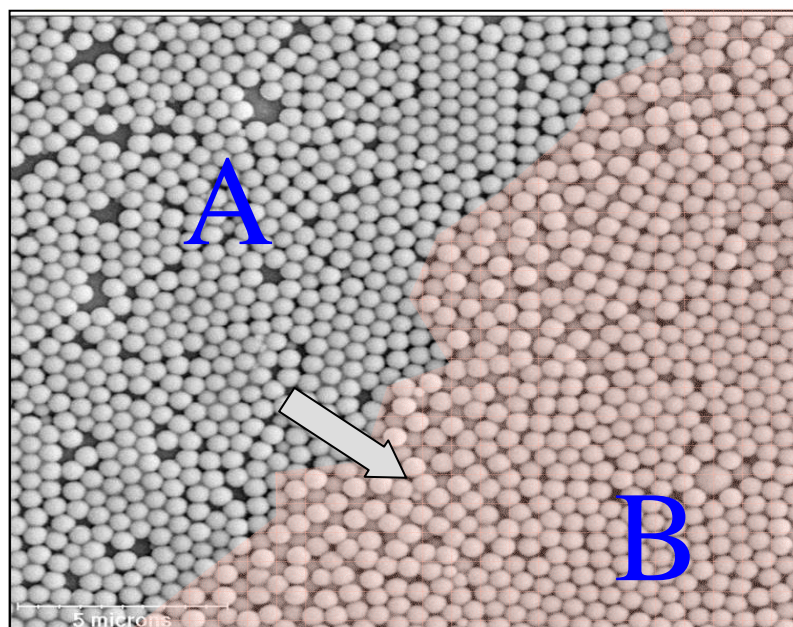


Figure 6.10 SEM image of nanosphere monolayer formed at a  $6^\circ$  slope (A) converts to multilayer at the lower end (B).

A uniform monolayer was observed when the substrate was kept at an angle of  $8^{\circ}$  and coated with undiluted PNS. The nanosphere layer was observed to be uniform and without gaps, however, some gaps were observed at the higher end of the substrate which were due to the movement of much of the spheres to the lower end under gravity. An SEM image of the higher end is shown in figure 6.11 and provides a better picture of the distribution of nanospheres coated under an  $8^{\circ}$  slope.

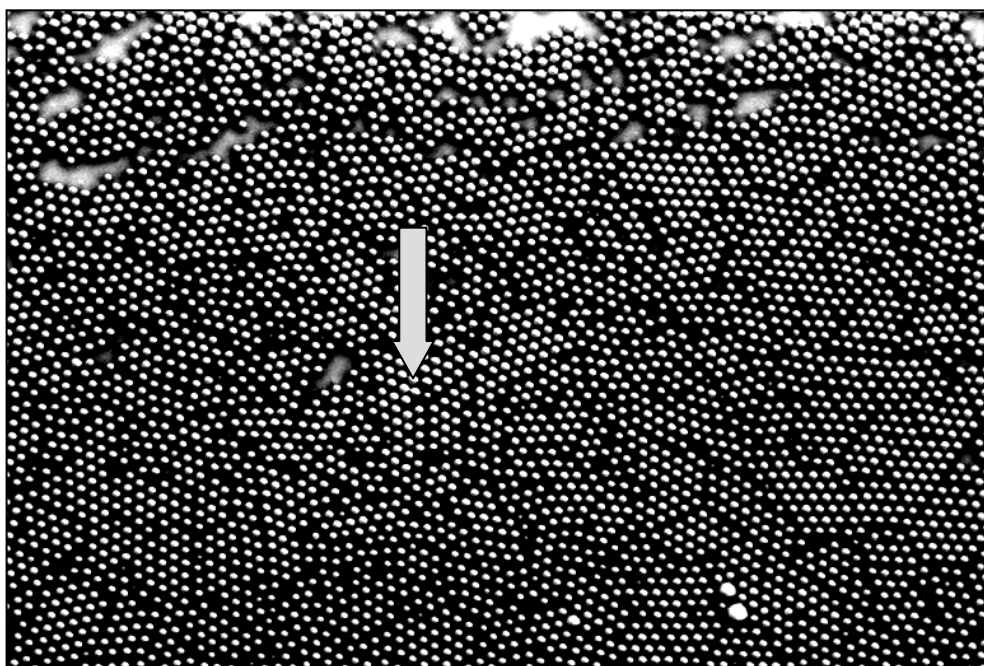


Figure 6.11 SEM image showing uniform monolayer assembly of substrate kept at an  $8^{\circ}$  slope from the horizontal.

Figure 6.12 shows a further magnified SEM image of a nanosphere assembly in a single layer that was not fully packed as expected. The breakages in geometrical arrangement is usual <sup>79,100</sup> in a self-assembly process and in this case it was also due to the variation in particle size. But even if the particle size distribution is ideally uniform, the uniformity of packing does not occur except for a rather smaller patch (domain size) within the coated area. This phenomenon does obviously result in a reduction of structural concentration (hot spots) but minor defects, as visible in figure 6.11, are not likely to cause any significant reduction in the effectiveness of the SER-active surfaces, keeping in view their very large number within the laser spot (around one million in  $0.1 \text{ mm}^2$ ).

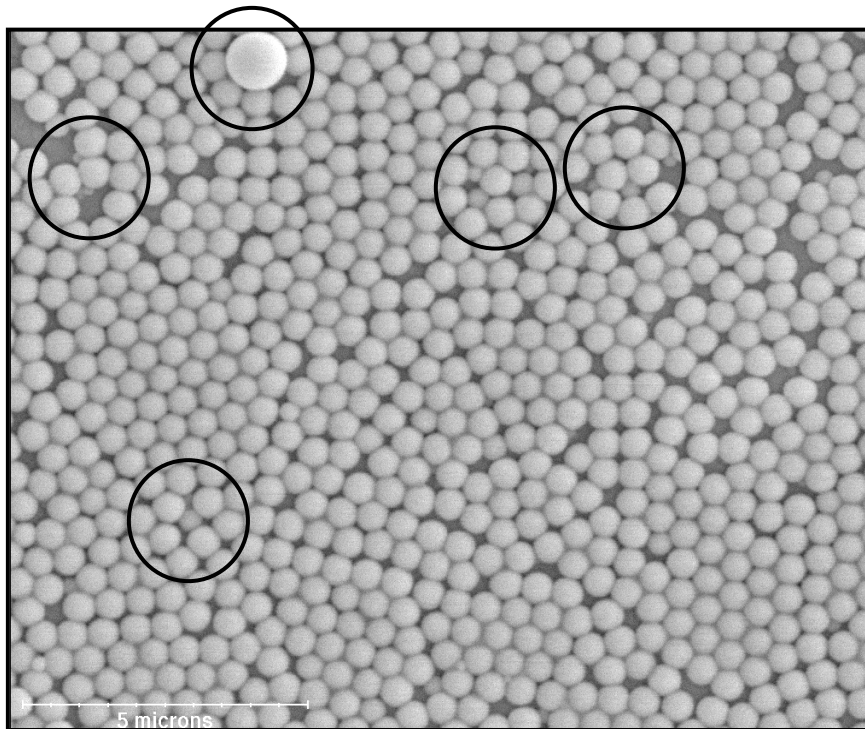


Figure 6.12 SEM image of a typical assembly of nanosphere in a monolayer. The circled areas show defects occurring due to the variations in particle size.

A seriously defective area, however, can have a much lower concentration of structures. Such areas are not uncommon in laboratory-fabricated surfaces, but remains scarce if carefully prepared by strictly following the protocol in an industrial/commercial system. An illustration of a highly defective patch on a surface prepared with substrate at a  $6^\circ$  slope coated with the ‘as-received’ nanosphere solution and sputtered with a 100 nm silver layer is shown in figure 6.13. Figure 6.13 (a) shows the SEM image of a broken monolayer and figure 6.13 (b) shows the SEM image of the similar kind of patch after removal of the nanospheres. A gap left in the monolayer appears as an island on silver coating indicated by ‘A’, whereas ‘B’ indicates an ideal cluster formation.



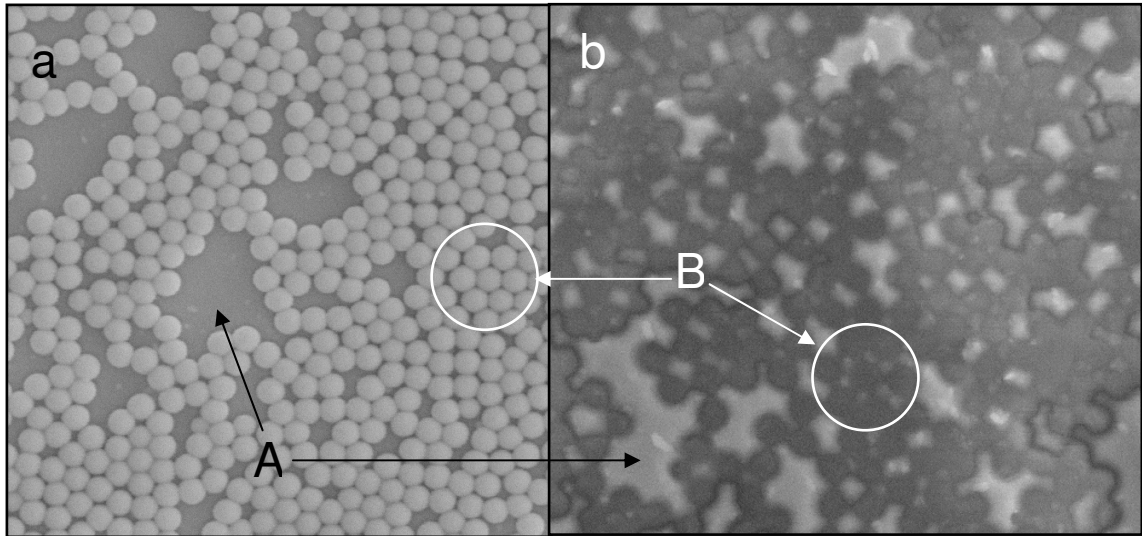


Figure 6.13 SEM image of a defective patch on a substrate kept at a  $6^{\circ}$  slope from the horizontal (a) and the similar patch after removing PNS (b).

SEM images of a substrate prepared under similar conditions to that shown in figure 6.14 and sputtered with 250nm layer of silver are shown in figure 6.14. These images of a mono-layer in figure 6.14 (a), the resulting structural cluster in figure 6.14 (b), the 3D image recorded with the digital surface profiler in figure 6.14 (d) and a single cluster in figure 6.14 (c) can be directly compared with the schematics in figure 6.6 and photographs in figure 6.7. The nanosphere arrangement in a uniformly packed area was as discussed earlier (also given in appendix N). A group of seven nanospheres form a silver structural cluster of six nanostructures having the predicted morphology.

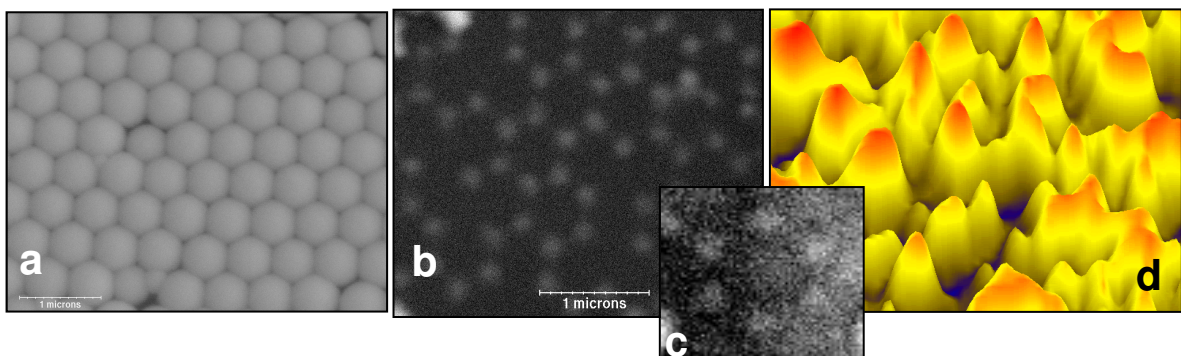


Figure 6.14 SEM images of PNS monolayer over glass substrate kept at an  $8^{\circ}$  slope coated with a 150 nm silver layer (a), after removal of nanospheres (b), single cluster (c) and a 3D digital profile image (d).



With a further increase in the slope of the substrate, a deterioration in the uniformity of the mono-layer in most of the area of the substrate was observed. As described in table 6.1, the nanospheres dispersed rapidly under gravity and did not form a monolayer. The inter-sphere distance increased as the slope was increased. Consequently, the bulk of spheres bunched up in a layer towards the bottom half and formed a multilayer. Figure 6.15 show a surface prepared with undiluted nanospheres while the substrate was kept at  $10^0$  inclination from the horizontal.

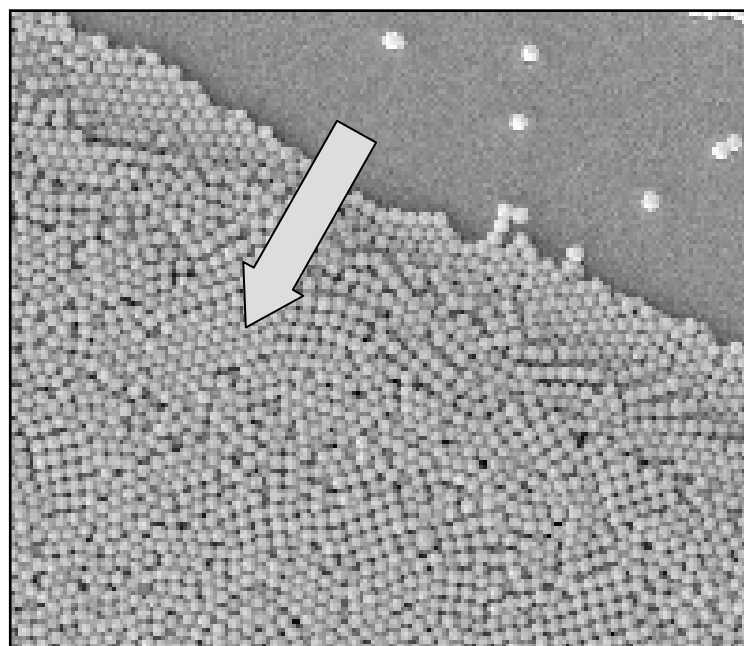


Figure 6.15 Surface prepared with undiluted nanospheres while the glass was kept at  $10^0$  from the horizontal.

With the increase in the inclination to  $12^0$  the dispersion increased further. The SEM images in figure 6.16 (a and b) show widely dispersed nanospheres over most of the two similarly prepared substrate's surface. After removal of PNS, most of the area was covered by silver with holes from where the nanospheres were removed. Microscopic image of such a surface is given in figure 6.17 (a), showing widely dispersed nanospheres, and its SEM image in figure 6.17 (b), showing that most of the area was still covered with silver while the places from where the nanospheres had been removed by sonication were scarce. Such a surface, due to the lack of uniform structural concentration, is not likely to be reliable for SER analysis.

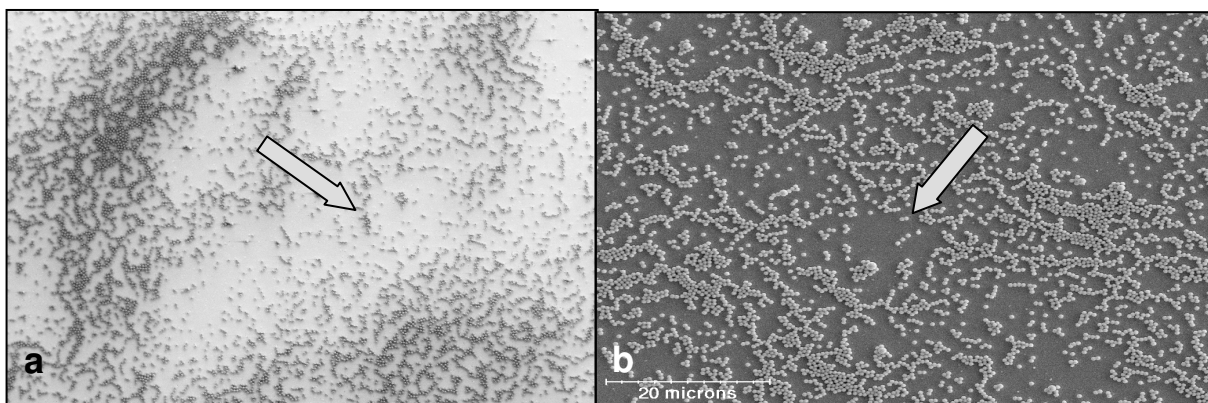


Figure 6.16 Surface prepared with undiluted nanospheres while the glass was kept at  $12^{\circ}$  slope, show the widely dispersed nanospheres over the entire surface.

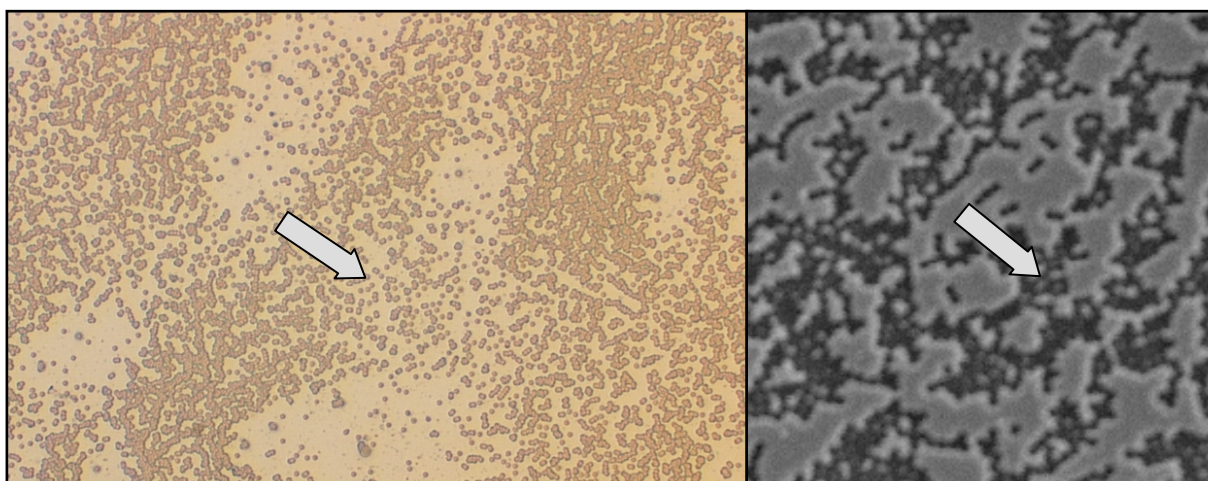


Figure 6.17 Microscopic image of surface prepared similar to the one in figure 6.16 with nanosphere removed (a) and further enhanced SEM image showing large silver islands (b).

### 6.5.1.1 Surface fabricated with Pre-NSL layer

A thin silver layer was sputtered onto the glass substrate before coating it with nanospheres. With a 10 nm layer, the monolayer did not assemble as desired, instead the nanospheres were clustered together leaving wide gaps in between. The SEM image in figure 6.18 shows the PNS coating resulting from an undiluted suspension with a 10 nm silver pre-layer during which the substrate was kept at  $6^{\circ}$  from the horizontal, expecting a reduced hydrophilic effect due to the silver under layer. The 10 nm silver layer was too thin to achieve a uniform layer and resulted in the gaps/islands across the surface.

The gaps in the silver layer retarded the free flow of nanospheres and they clustered together instead of forming a mono-layer.

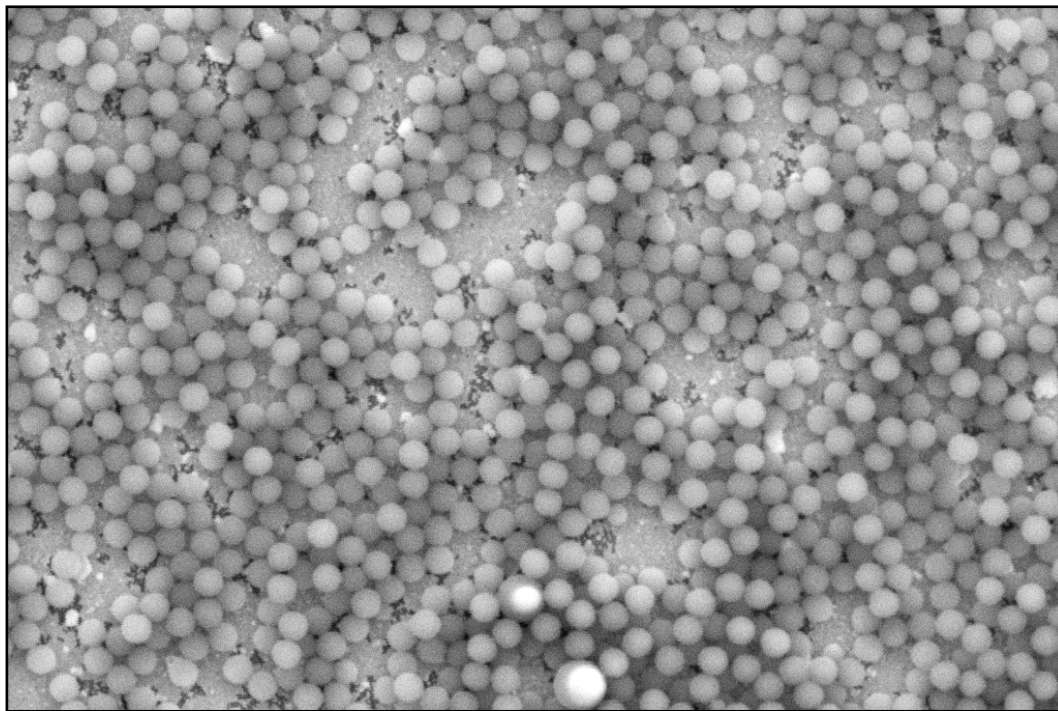


Figure 6.18 Glass substrate with 10nm silver layer coated at a  $6^{\circ}$  slope showing partial silver coverage and PNS could not form monolayer.

Although full coverage of the substrate was achieved with 15 nm pre-NSL layer, the formation of a mono-layer was not as uniform as without the silver layer (figures 6.11 and 6.12), mainly due to further reduction of hydrophilic effect of the glass substrate. Figure 6.19 presents an SEM image of the surface with 15 nm under-layer, coated with undiluted nanospheres at  $6^{\circ}$  slope. The various stages of fabrications of surface are shown in figure 6.20. The method of introducing the underlayer did solve the problem of excessive glass exposure, but the fabrication protocol became more complex. The uniform (and mono-layer) nanosphere coating over silver became difficult to achieve and a slight error in the procedure resulted in non-uniform spreading of nanospheres, primarily due to much reduced hydrophilic properties of the silver coated glass. A slight error can result in defective patches appearing within the surface similar to the one shown in figure 6.21 prepared with 15 nm underlayer and then coated with ‘as received’ nanospheres on substrate kept at  $8^{\circ}$  inclination.



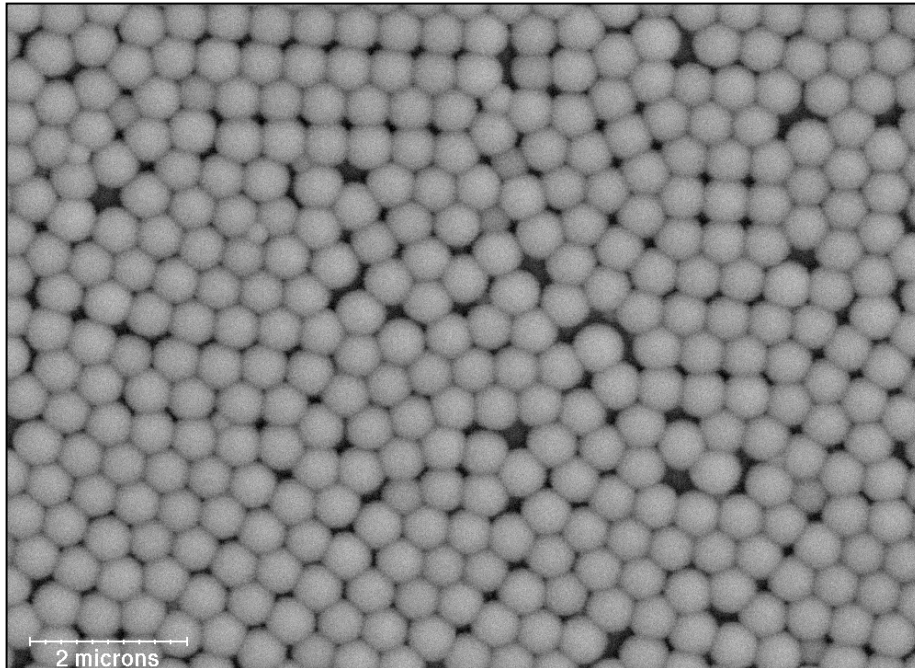


Figure 6.19 Glass substrate with 15nm silver underlayer coated at  $6^\circ$  slope with undiluted nanospheres, showing PNS monolayer in less than an ideal geometrical packing.

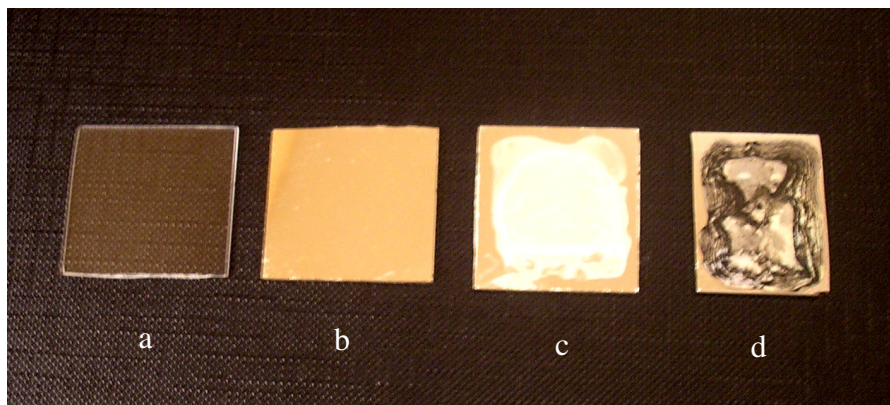


Figure 6.20 Surface fabrication process of a glass-based surface with 15 nm silver under-layer coated at a  $6^\circ$  slope. Glass surface (a) with a 15 nm silver layer (b) with a monolayer of the nanospheres (c) and with the nanospheres removed (d).

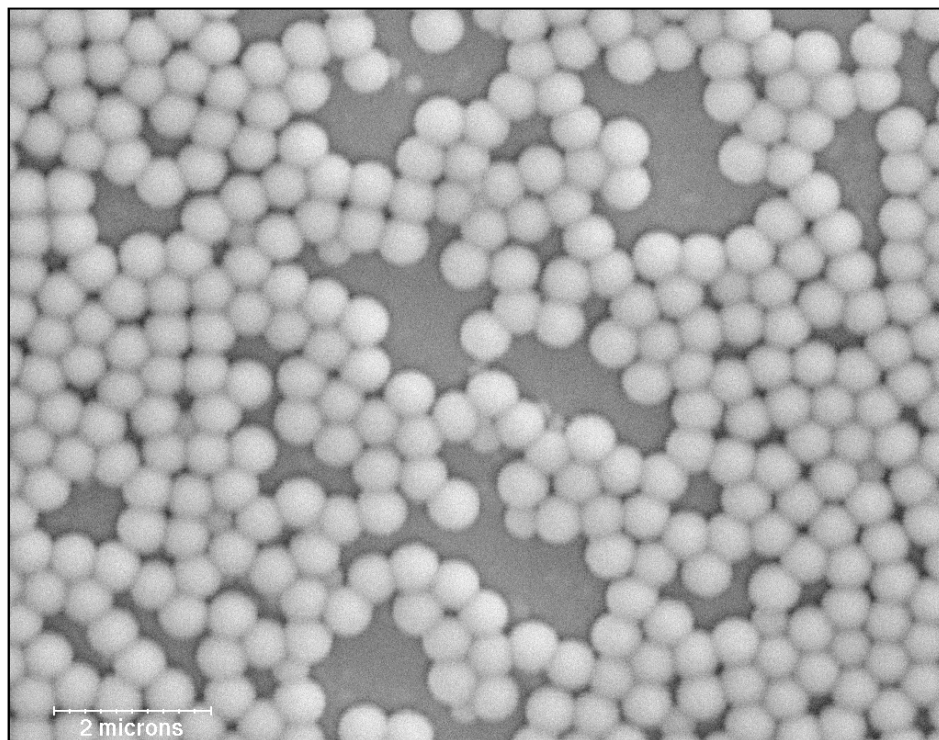


Figure 6.21 Glass substrate with 15nm (non-uniform) silver underlayer coated at  $8^{\circ}$  slope with undiluted nanospheres, showing a highly defective domain.

#### 6.5.1.2 Surface fabricated with post NSL layer

To avoid the complex/difficult process of substrate fabrication with silver underlayer, experiments were undertaken to sputter the silver layer after the removal of PNS with the aim of covering the glass substrate exposed to the laser (92.7% of surface). It was considered that the over-layer would sufficiently cover the exposed glass and at the same time would not affect the SERS capacity by changing the structural morphology. This procedure was therefore a trade off between easily depositing a highly uniform layer of nanospheres directly on to the glass surface and reducing the SER scattering capability. The reduction was considered to be from the additional silver deposited over the structures which could make the sharp structural edges (hot spots are considered to exist at sharp edges) slightly rounded off.

A silver overlayer of 15 nm thickness (the thickness already observed to give complete coverage) was coated on to the prepared glass based SER-surface. The morphological effects of the additional layer could not be observed in the electron micrograph due to the very small film thickness as was explained schematically in figure 6.4 (b) and (d)

(section 6.3.7). Note the slight enlargement of structural size (not to scale) that result in smooth edges (exaggerated for presentation purpose). In the actual case the enlargement /rounding off the edges was likely to be considerably less.

The SEM image of a substrate fabricated with undiluted nanospheres coated at an  $8^\circ$  slope and sputtered to give a 250 nm thick layer as shown in figure 6.22 and was found to be similar to those in figures 6.11, 6.12 and 6.19. The microscope image of a similar surface prepared with 40 nm silver layer is shown in figure 6.23. Good geometrical packing of a nanosphere and monolayer formation over the large areas (visible in both the images) resulted in equally large domains of uniform silver structural clusters. Such surfaces are highly SER-active. The SER results are discussed in Chapter 7.

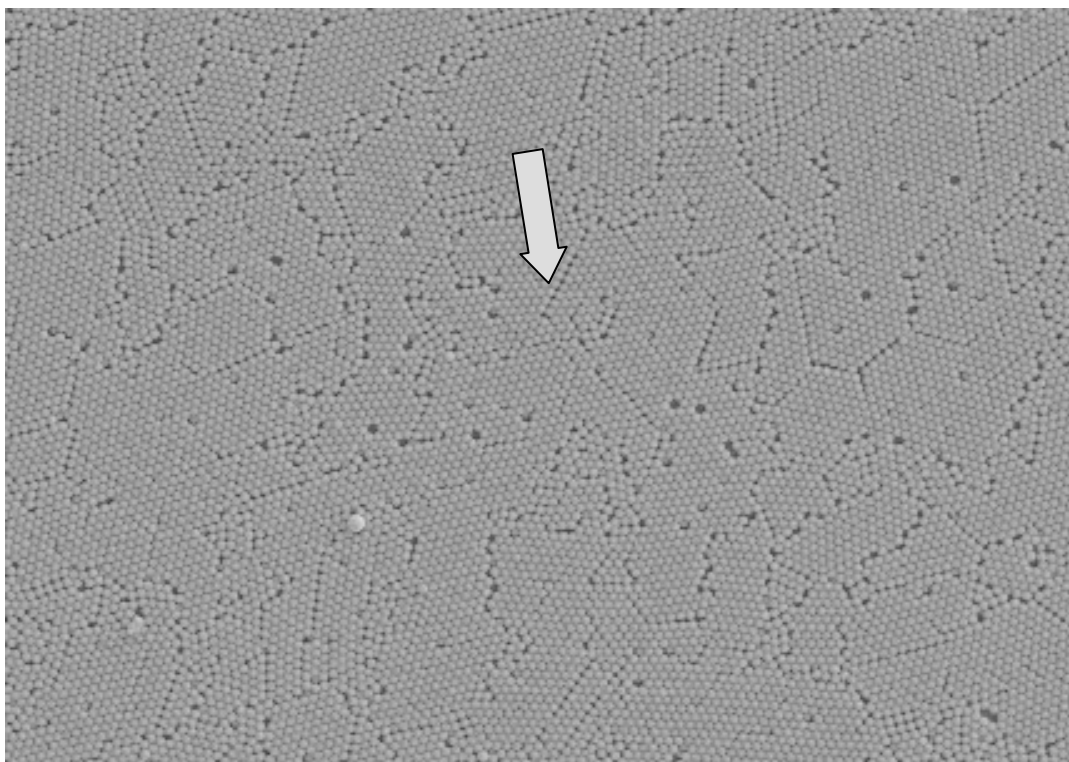


Figure 6.22 Electron micrograph of glass substrate coated at an  $8^\circ$  slope with undiluted nanospheres and sputtered with a 250 nm thick silver layer.

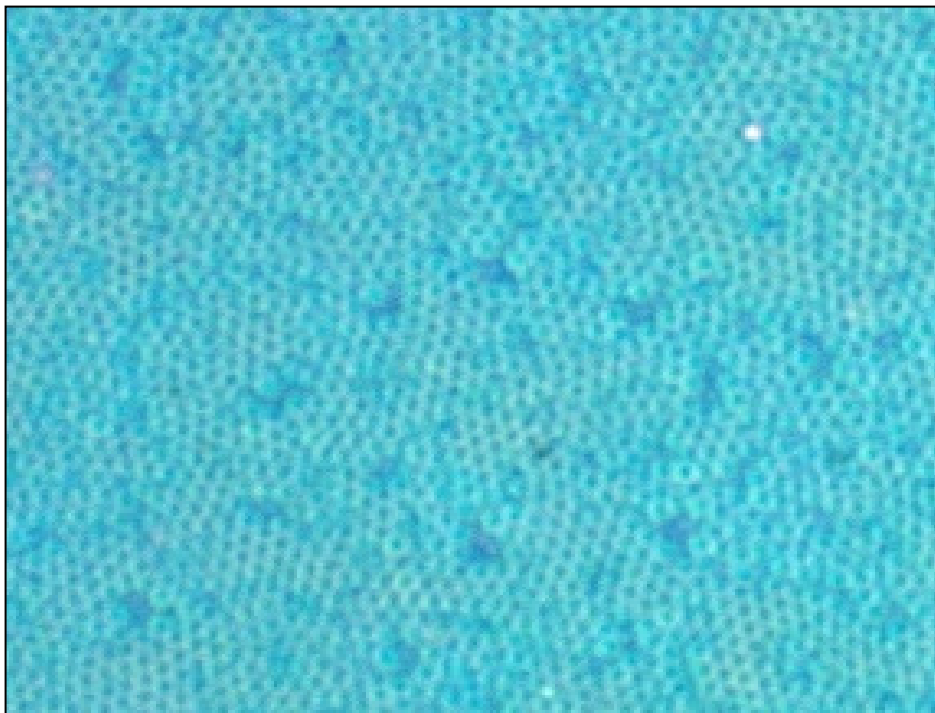


Figure 6.23 Microscope image of glass substrate coated at an  $8^{\circ}$  inclination with undiluted nanospheres and sputtered with a 40 nm thick silver layer.

### **6.5.2 Quartz based substrates**

The quartz substrates were tested to eliminate the need for applying silver under or over-layers. The substrate fabrication was carried out in a similar manner to the glass based substrates described earlier and is schematically shown in figure 6.5. The quartz cannot be made as hydrophilic as glass due to their different chemical composition that, in turn, makes NSL using quartz a slightly difficult process. The nanospheres, due to less attraction to the surface, tend to accumulate in clusters, leaving gaps in between while drying. The nanosphere coating becomes similar to that on glass substrates, with a 15 nm silver under-layer resulting in surfaces similar to the one shown in figure 6.21. With the increase in time of ultra-sonication, etch in ammonia solution the substrate showed improvement in hydrophilic ability. Also the decrease in slope of the substrate during PNS coating allowed more time for the nanospheres to get settled in a monolayer rather than flowing off rapidly towards the lower end of the substrate.

Therefore, to arrive at a final preparation protocol for the quartz-based surfaces it was decided to use the ‘as-received’ nanosphere solution and adjust the slope of the

substrate for a coating that gave the best uniform monolayer. Table 2 shows the summary of a series of experiments conducted to achieve reproducibility in monolayer formation.

Table 6.2 Effects of angle of coating on assembly of nanospheres.

Angle of substrate	Result
4 <sup>0</sup>	Double layer formation with patches of monolayer
6 <sup>0</sup>	Monolayer pronounced
8 <sup>0</sup>	Monolayer patches with most area covered with dispersed nanospheres

Quartz substrates were coated with undiluted nanospheres as a further reduction in the concentration caused the nanospheres to flow rapidly over this surface even on slopes of less than 6<sup>0</sup>. The substrate etched for 2 hours and kept at an 8<sup>0</sup> slope was coated with undiluted PNS. A poorly formed layer was observed having widely spaced bunches of nanospheres. The SEM image in figure 6.24 shows one such surface in which nanospheres can be seen grouping together in layers due to the reduced hydrophilic effect supplemented by the higher slope with larger islands of silver at places devoid of nanospheres. This surface was sputtered with 50 nm thick silver layer. The partial PNS removal was due to the less sonication time which, though not intentional, facilitated the study of surface morphological layout.

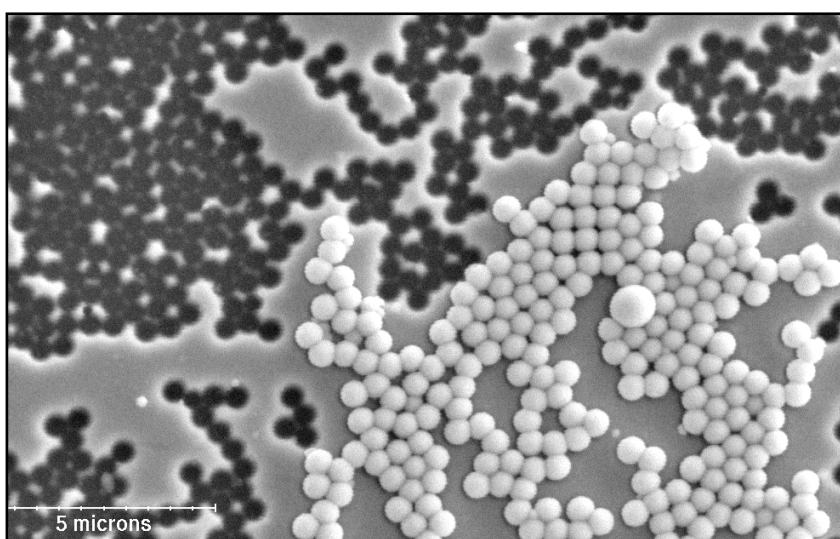


Figure 6.24 SEM image of partially removed PNS from quartz-based surface coated with nanospheres at 8<sup>0</sup> slope and sputtered with 50 nm silver layer.



The results observed with the quartz etched for more than 2 hours and placed at  $8^{\circ}$  from horizontal were not much different. The formation of a monolayer was observed but with many defective patches and silver islands. The surface could not be used for reliable SERS analysis. Much better results were observed when the substrate was kept at a  $6^{\circ}$  slope for coating. Such surfaces could be safely regarded as similar to well-fabricated glass-based surfaces without silver under or over-layers. The surface at three stages of fabrication is shown in figure 6.25.



Figure 6.25 Surface fabrication process of a quartz-based surface with 60 nm silver layer coated at a  $6^{\circ}$  slope. Quartz substrate (a) with a monolayer of the nanospheres (b) and after silver coating and the nanospheres removed (c).

Figure 6.26 shows a quartz-based substrate etched for 2 hours and fabricated using undiluted nanospheres applied at a  $6^{\circ}$  slope and sputtered with a 60 nm silver layer before PNS removal. The microscope and profile images of another substrate fabricated with a 70 nm silver layer showing a uniform nano-structural layout are presented in figure 6.27. Note the large domains of silver structures with fewer defects in both the surfaces. The bright spots are silver islands formed where the defects appear during the NSL process. In the microscope image, these silver islands appear larger than their original size due to their bright appearance and dominate an additional area around them. Such surfaces are expected to give very high enhancement of Raman scattering due to a high concentration of silver structures for the 500 nm diameter PNS. The SER results are discussed in Chapter 7.

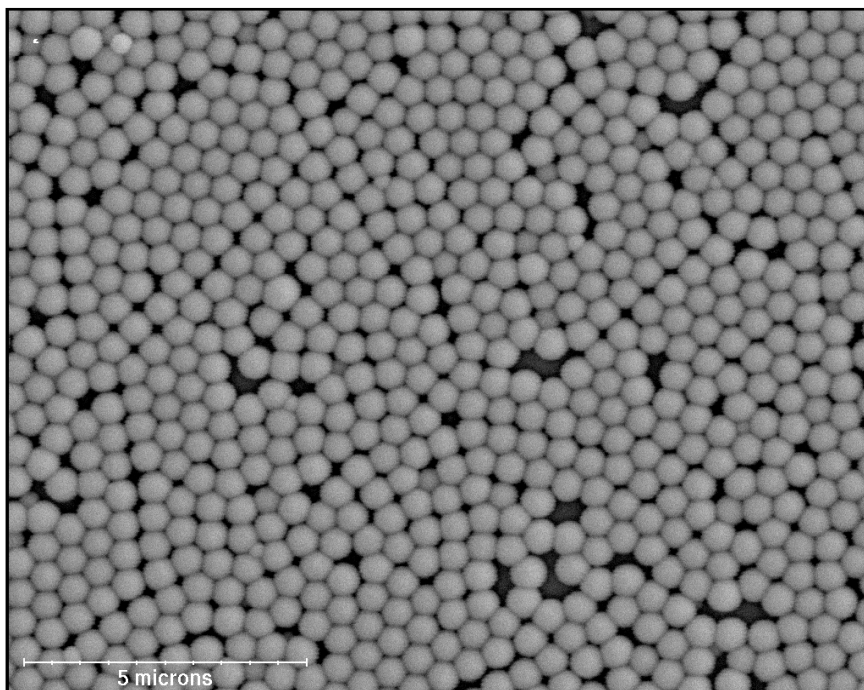


Figure 6.26 SEM image of a quartz-based surface having a 60 nm silver layer showing good mono-layer assembly.

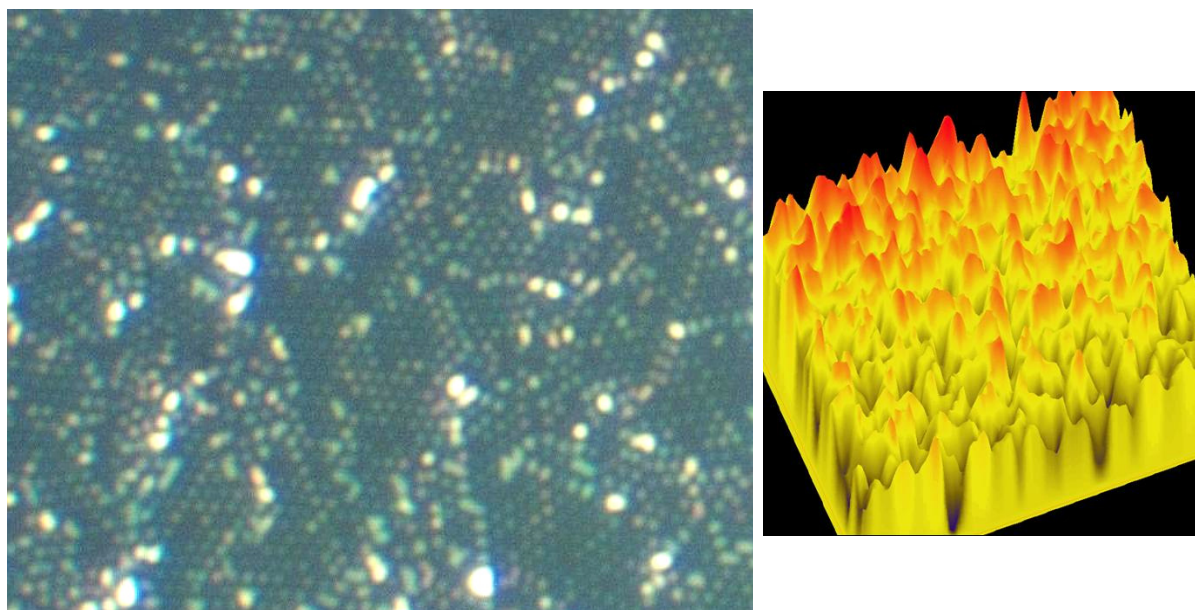


Figure 6.27 Microscope image of a quartz-based surface having a 70 nm silver layer (left) and a profile image of the same surface (right).

## 6.6 Characterisation of surface plasmon resonance (SPR) of the SER-active surfaces

Tuneability of nanostructures with different nanosphere sizes and varying thickness as of the silver layer has been discussed (vide infra)<sup>58,98</sup>. With the change in the shape,

size or height of the nanostructures the optical properties of the substrate change. A SER-active surface of specific structural dimension absorbs more at a certain wavelength known as its resonance wavelength,  $\lambda_{\max}$  (or frequency  $\nu_f = c/\lambda_{\max}$ ) of the surface plasmon. It is also referred to as surface plasmon resonance (SPR) or, more precisely, local surface plasmon resonance (LSPR). A UV-vis-NIR (UVN) spectrometer can be used to determine the LSPR frequency of the surfaces.

The use of single nanosphere size (500 nm diameter) restricted the structural size to ~116 nm as shown earlier. No noticeable change was found in the structural shape with changes in the silver thickness between 40 and 300 nm, therefore no effect on the absorbance/transmittance was considered to occur due to shape/size. Any effect on the absorption property of the surfaces could be attributed to the height of the silver structures. Therefore, only the determination of changes in the LSPR with the changing sputtered silver thickness from 40 to 300 nm (only changing the structure height) was considered.

Unfortunately, the available UVN spectrometer was not suitable for the LSPR study. It had a fixed light spot of 10 x 2 mm size that was considered to be much larger than the normal domain size of geometrically packed nanostructures. Unless the size of the light spot is equal or smaller than the uniformly packed domain size, the results would vary considerably. This is because of the inclusion of defected patches within the scanned area that would have larger silver islands due to disordered structural arrays. It has been reported<sup>99,102</sup> that a small change in either shape or height of the nanostructure results in a large shift in LSPR. For example<sup>58</sup> surface prepared with nanospheres of 540 nm diameter, with a 60 nm structural height and a 145 nm structural width (shape dependent) showed  $\lambda_{\max} \cong 720$  nm. But the same surface with a 150 nm structural width (shape change with annealing) showed  $\lambda_{\max} \cong 497$  nm. There was, therefore, a change of approximately 220 nm in LSPR with the change in shape that increased the structural width by only 5 nm.

Due to the large light spot size of the UVN spectrometer (10 mm x 2 mm) and comparatively smaller domain sizes (maximum ~50 x 50  $\mu\text{m}$ ) our results could not

show a definite absorption region in UVN spectra. The beam spot size was large enough to cover geometrical defects that resulted in the non-uniform structure size distribution. This effect can be better realised by observing the absorption measurements discussed in Chapter 5, recorded with the metal colloids. Figures 5.9 and 5.10 show results of UV-vis absorption of silver and gold colloids respectively. The peak width is the representation of the particle size distribution and the narrower the particle size distribution the narrower the peak width. In the case of surfaces prepared in our laboratory, structure size varied widely and resulted in a very wide band with no noticeable peaks.

Nevertheless, the UVN spectra of surfaces fabricated with 40, 50, 60, 150 and 250 nm silver thick layers (structure height) are shown in figure 6.28. Although the resonance effect is evident from the increase in the absorbance with the decrease in the silver layer thickness,  $\lambda_{\max}$  cannot be deduced from these spectra. As discussed above, wide bands show a wide distribution of structure sizes. The analysis of fabricated surfaces (by SEM, microscope and 3D surface profiler) showed that the structures were geometrically arranged in clusters of the same shape and height (vide infra). The possible explanation for the wide distribution of size of structure observed in the UVN spectra is the inclusion of a large area under the beam spot that included defect regions in addition to the uniform clusters.

The increase in absorbance value with the decrease in height of the structures can be related to the increasing resonance value. By drawing a parallel to the reported work<sup>99,102</sup>, the  $\lambda_{\max}$  should be near 785 nm wavelength when the silver structural height is in 40-50 nm region keeping the shape of the structures the same. Present results also show an increase in the absorbance that was considered to be due to the absorption effect. Table 6.3 shows the increasing absorbance at a wavelength of 785 nm for the corresponding decrease in the heights of the nano-structures. The same effect is graphically presented in figure 6.29. It is considered that the LSPR frequency is likely to be highest for the SER-surfaces fabricated with ~40-50 nm thick silver layers. These surfaces are likely to further enhance SER scattering intensity as compared to those

from the non resonant region (structure height > 50 nm). The SER results will be discussed in Chapter 7.

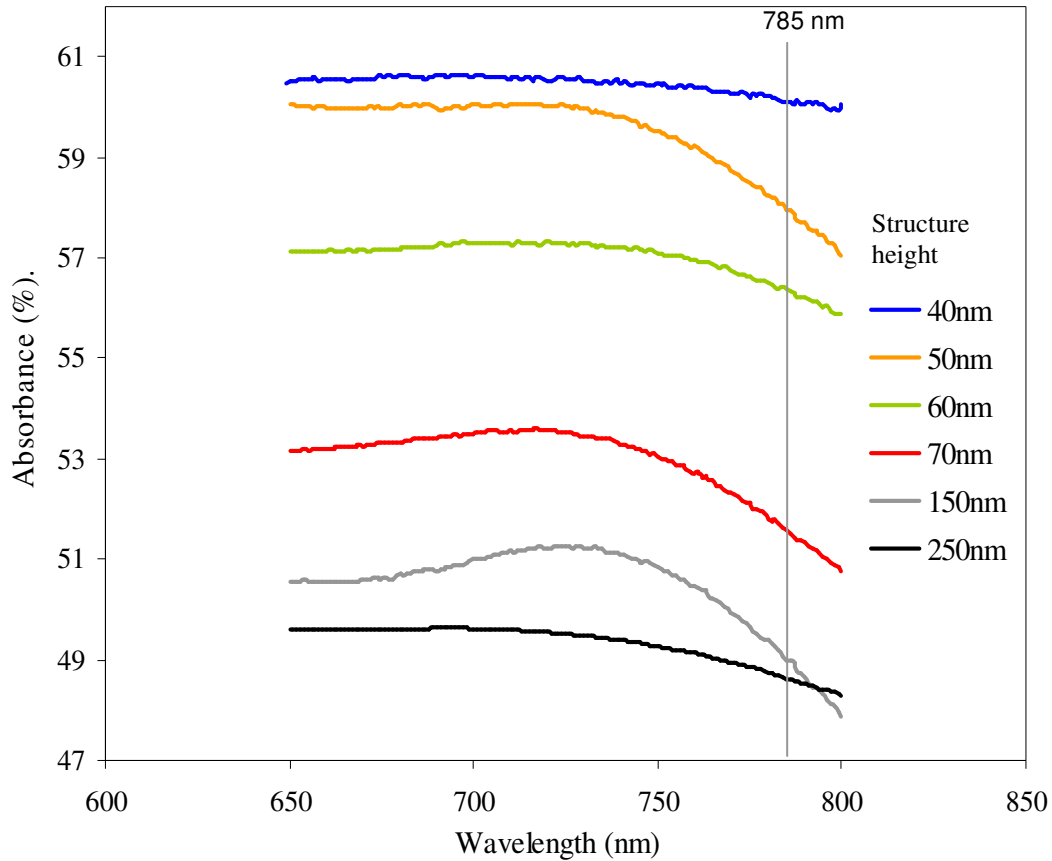


Figure 6.28 UVN spectra of SER-active surfaces fabricated with different heights of nano-structures.

Table 6.3 UVN spectral readings of SER surfaces fabricated with different heights of nano-structures with corresponding absorbance at 785 nm wavelength.

Height of nano-structures (nm)	Absorbance at 785 nm wavelength (%)
250	48.7
150	49.1
70	51.8
60	56.4
50	58.1
40	60.1

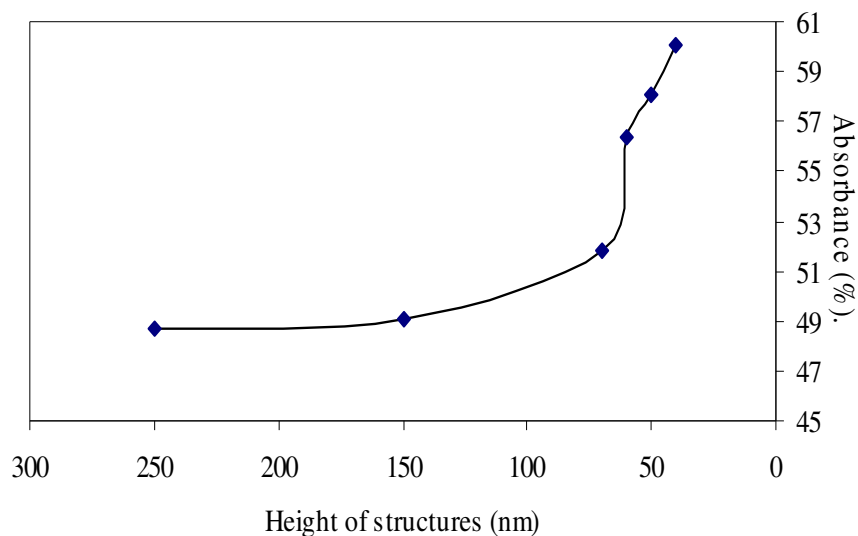


Figure 6.29 UVN spectral values showing increasing absorbance at a wavelength of 785 nm for the corresponding decrease in the heights of nano-structures.

## 6.7 Summary

A preparation protocol for the fabrication of SER active surfaces based on the NSL technique has been discussed. Glass based surfaces could not be used for reliable SER analysis due to the very poor S/N. Since the objective of the present research was to evaluate the possibility of avoiding long analysis times and background subtraction by long time data averaging, the S/N from the SER-active surfaces needed to be very high. The S/N had to be at a level where inherently weak signals from a few molecules adsorbed on the surfaces could be observed above the background noise.

Glass based surfaces were therefore modified to cut off the entire background from the substrate constituents by introducing an additional silver layer. This was either coated on the raw substrate before the NSL process or after the surface was completely fabricated. A reduction in SER ability was visualised by observing the effects of the additional silver layer. This is evaluated in Chapter 7.

Quartz-based surface, on the other hand, were difficult to perfect but, after the protocol was finally developed, they presented much better qualities as SER active surfaces. These surfaces had maximum possible structure concentrations with reasonably large

uniform cluster domain sizes. With optical fused quartz giving much less background compared to normal glass, these surfaces are likely to be appropriate for adsorbed molecules from analytes in vapour.

The LSPR characterisation did not go as planned due to the unavailability of a suitable UVN spectrometer and the existing equipment could not be modified to analyse the surfaces. Nevertheless, some useful conclusions could be drawn from the UVN spectra recorded. The changes in the absorption properties of surfaces with the varying height of the structures was studied and compared with some of the published work. It can be concluded that the surfaces prepared with 500 nm diameter nanospheres having 40-50 nm height of the structures would be in the resonance region of the surface plasmon. This would also be evaluated in Chapter 7. Actual characterisation of surfaces to determine  $\lambda_{\max}$  (LSPR) would be an important feature for future studies in the field.

This technique of surface fabrication allowed us to prepare surfaces with considerable simplicity and reproducibility that facilitated SERS for a variety of analytes. The protocol adopted was found well suited to normal laboratory facilities apart from a few specialised items of equipment required for silver coating and surface characterisation.

The full potential advantages of these surfaces as SER-active could only be evaluated after rigorous SERS analysis. Nevertheless, the observations made during the characterisation of these surfaces and their comparison with the published practical and theoretical work showed promising results.



## 7. EXPERIMENTAL – SERS RESULTS

### 7.1 Introduction

The experiments described in Chapter 5 have shown that the use of the SERS technique can greatly enhance the Raman intensity thus making it possible to analyse a very low concentration of sample that is otherwise not possible using the normal Raman spectroscopy. These experiments were conducted with solid samples dissolved in a solvent at trace concentrations to measure their limits of detection after their adsorption on specially prepared surfaces. Due to special properties of the explosive compounds, strong solvents were needed to be used and these affected the Raman measurements. It was found that the dissolved explosives (in acetone or butanone) caused changes in the surface morphology during the interaction/drying process on silver coated surfaces. This effect was likely to affect the NSL fabricated surfaces having the periodical arrays of nano-scale silver structures and gaps.

The analyte solution (analyte in solvent) leaves behind a residue on the substrate on drying, which also gave a high Raman scattering and fluorescence as background noise. While such noise could be subtracted or eliminated with a laboratory-based high-resolution, high-throughput spectrometer having a high background rejection factor this is not possible with the present experimental configuration using a portable low-resolution Raman spectrometer. Sample presentation in the dissolved form was, therefore, not considered to be a suitable option for the detection of samples at low concentrations, especially when using a commercial (R3000) Raman system having a low resolution and a low background rejection capability. Nanosphere Lithography was



selected to achieve a desired surface morphology for ultra sensitive SERS analysis. In this Chapter, the results of experiments conducted using the surfaces fabricated with the NSL technique are presented. The analytes used were Pyridine, Nitrobenzene, TATP, HMTD and PETN. Their basic characteristics have already been discussed in Chapter 4.

The vapour phase detection was carried out by putting a known quantity of explosive sample in a vial of known volume and then laying the fabricated SER-active surface onto its mouth such that the surface was exposed to the vapour rising from the solid explosive inside the vial. Raman spectra were recorded immediately afterwards. Details of the samples and the sample presentation process (figure 4.1) for detection of explosive vapour are given in Chapter 4. To establish a general idea of the quantification for the limit of detection (LOD), the headspace concentration of molecules that may encounter the SER-active surfaces during exposure are also given in Chapter 4.

Fabrication of SER-active surfaces required extreme caution and care, as slight deviation from the preparation protocol would result in faulty surfaces incapable of achieving the desired sensitivities. Equally important and delicate were the processes of surface presentation and the recording of Raman spectra. On the whole, half the surfaces prepared were faulty (especially during the initial experimentations) and many of those that were well-fabricated got contaminated before or during the SER analysis. The faulty surfaces (as discussed in Chapter 6) were discarded after characterisation. The surfaces found to be contaminated (most of them with pyridine) in the SER analysis were disregarded and will not be discussed here. Therefore, the results mentioned are those considered to have some analytical value. Also, the results being discussed were reproducible, both in terms of surface fabrication as well as for detection by SERS.

## 7.2 The limitations of glass substrates.

The possibility of using ordinary glass as substrates was explored. The Raman spectra obtained with these substrates were overwhelmed by a very large background signal from the glass constituents like oxides of silicon, sodium, calcium etc present in high concentrations. The composition of the glass used in the present experiments (Fisher

brand, super premium, borosilicate) had a very high absorbance in the IR region of interest, and therefore, gave a very high signature during the Raman analysis. The Raman spectrum of a glass substrate recorded with only three seconds integration time ( $t_i = 3$  seconds), shown in figure 7.1, exhibits a very high intensity signal that was referred to as background noise for our experiments in the absence of any coating of silver or analyte. The R3000 Raman spectrometer had a dark noise subtraction facility but did not have the in-built option for the background subtraction. For effective background reduction from the glass substrate, the data had to be processed further, which would mean longer analysis time, thus losing the much required real time detectability.

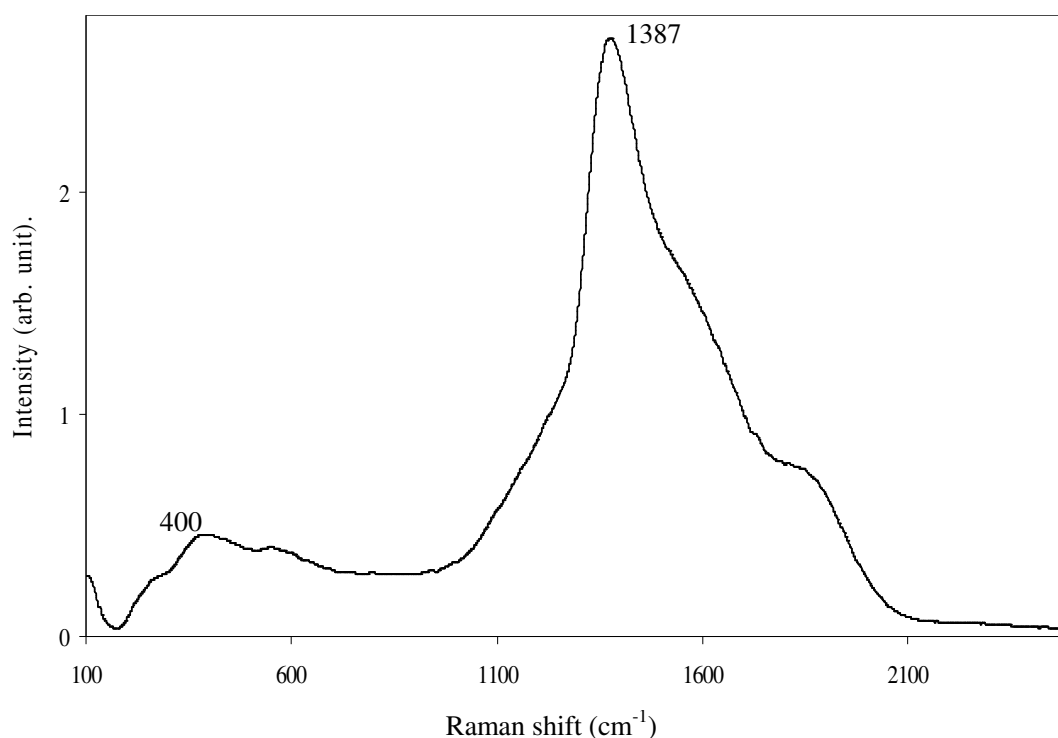


Figure 7.1 Typical spectrum of a glass substrate showing a characteristic background, ( $t_i = 3$  seconds).

For instance, in one of the initial experiments, done with glass substrate prepared by NSL and coated with 200 nm thick silver, 10  $\mu\text{l}$  of a  $10^{-2}$  M Pyridine solution (aqueous) was drop coated onto the substrate and allowed to dry. The SER spectrum of the Pyridine sample was compared to that of a spectrum of a pyridine sample in a cuvette in figure 7.2. The Raman lines of pyridine at  $990\text{ cm}^{-1}$  and  $1030\text{ cm}^{-1}$  belonged to ring

breathing modes and were barely visible in the SER spectrum. This was primarily due to the large noise background from the glass surface. The spectrum shown in figure 7.1 is also included for comparison. It was obvious that most of the noise associated with glass was present in the SER spectrum with a very poor S/N. In figure 7.2, for the 987  $\text{cm}^{-1}$  peak of pyridine, the S/N is 379 as compared to 6.4 for the same peak in the SER spectrum. The two ring breathing modes at 990  $\text{cm}^{-1}$  and 1030  $\text{cm}^{-1}$  could not be resolved and were only visible as a combined wide peak. Also note that the  $t_i$  for glass was only 3 seconds as compared to 8 seconds for the SER spectrum, but the noise level is similar due to the reduction in exposed glass surface to 92.3% and also because of the high enhancement of the Raman signal from the molecules adsorbed on the metal edges.

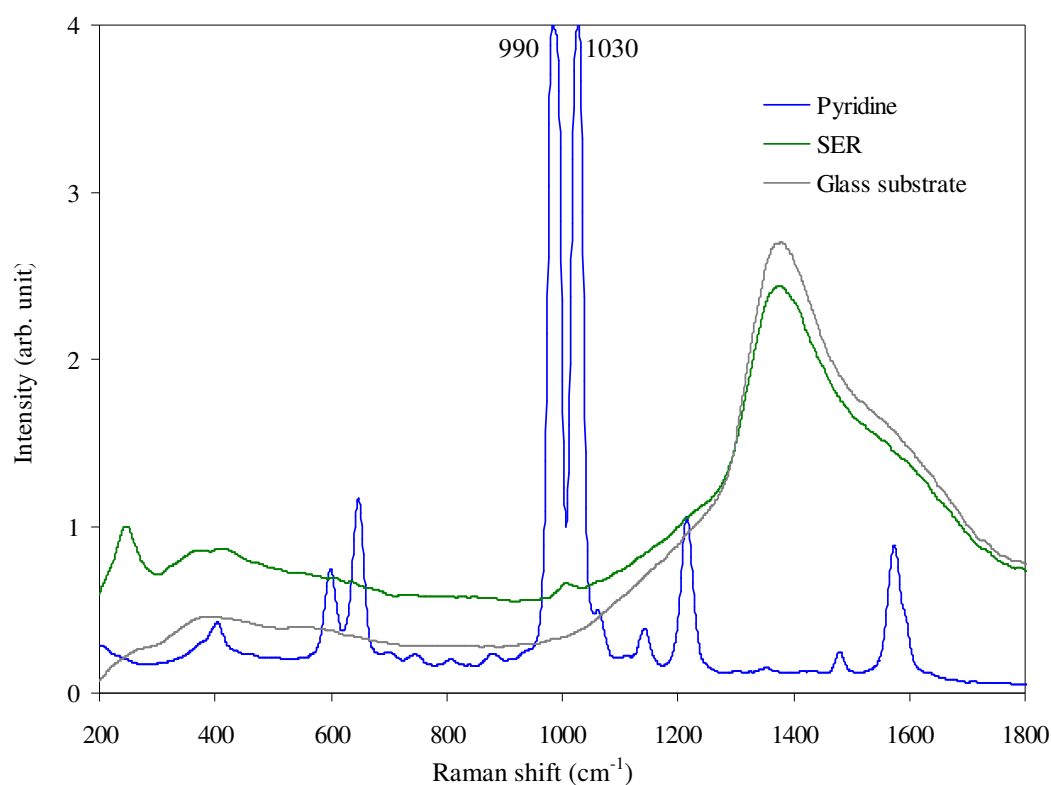


Figure 7.2 SER spectrum of a 10  $\mu\text{l}$  drop coating of Pyridine ( $10^{-2}$  M solution) on a glass-based surface ( $t_i = 3$  seconds). Raman spectra of bulk pyridine ( $t_i = 5$  seconds) and of glass surface ( $t_i = 3$  seconds) are also included for reference.

In order to lower this background and improve S/N, special glass with better transmittance in the IR region was considered. Optical fused quartz used for as our substrate had quoted transmittance of  $\sim 94\%$  in the NIR region (UQG Ltd; see appendix

13 for details) and had very small quantities of optical noise producing constituents. The Raman spectrum of the quartz substrate with  $t_i = 3$  seconds is shown in figure 7.3.

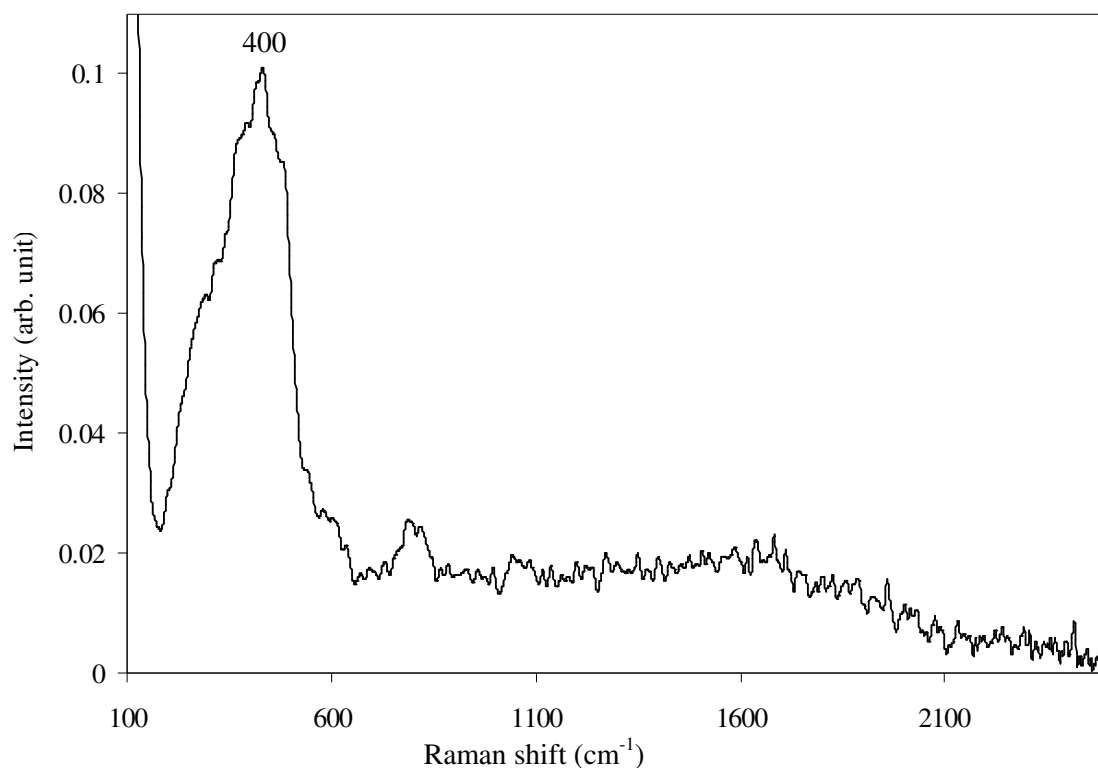


Figure 7.3 The Raman spectrum of the clean quartz substrate with  $t_i = 3$  seconds.

This substrate offered a better choice for an effective SER-active surface than the glass. The background fluorescence was much lower in this case as compared to that of the glass. A weaker broad peak at  $\sim 400$  cm<sup>-1</sup> appeared mainly from a SiO<sub>2</sub> vibration mode<sup>145</sup>. Note that the intensity units are the same for figure 7.2 and 7.3 and the peak at 1387 cm<sup>-1</sup> in the Raman spectrum of glass had the intensity of 2.6 (arb. unit) as compared to 0.1 for the peak at 400 cm<sup>-1</sup> in the Raman spectrum of quartz. There was almost a 96% decrease in background noise level. Additionally, the background from the glass covers the entire useful fingerprint region (peaking at 1387 cm<sup>-1</sup>) whereas the optical fused quartz gave negligible noise at 400 cm<sup>-1</sup> and almost none beyond that point. For direct comparison, typical spectra of glass and quartz are shown in figure 7.4. Note that the fluorescence background having a sharp peak at 1387 cm<sup>-1</sup> in glass did not appear in quartz whereas the noise at  $\sim 400$  cm<sup>-1</sup> in quartz is also much higher in glass.

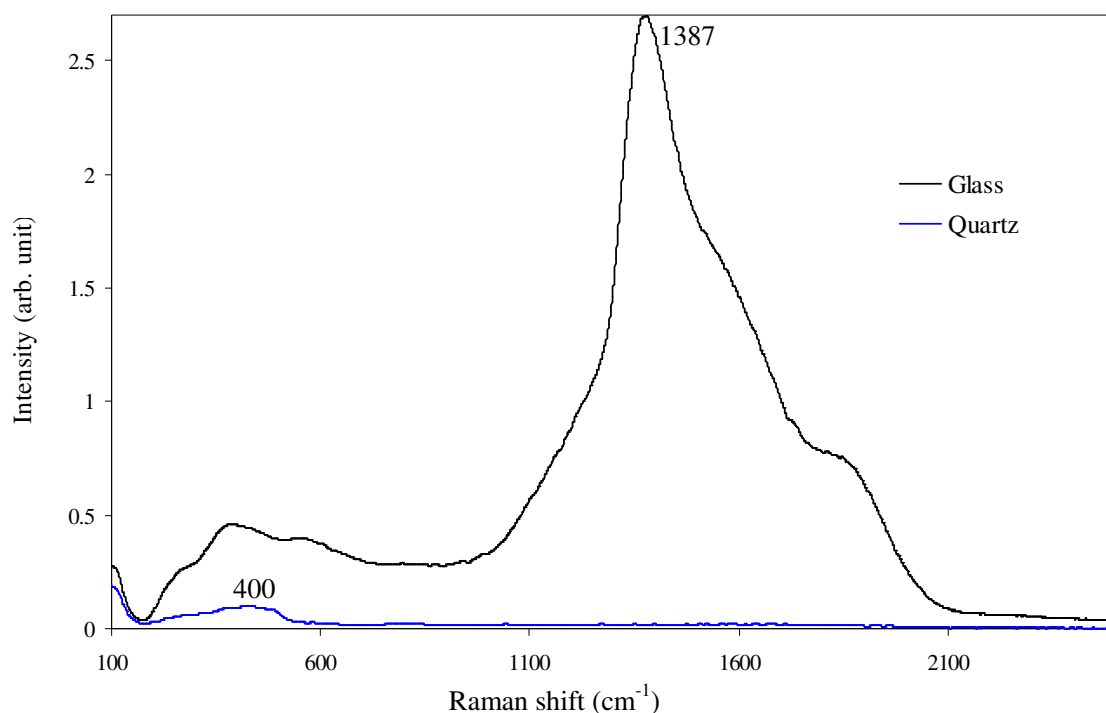


Figure 7.4 The Raman spectra of the glass and quartz substrates recorded with  $t_i = 3$  seconds each.

The background noise in the case of quartz-based SER-active surfaces was expected to further decrease with the decrease in exposed substrate area of the fabricated surfaces in a similar manner to that shown in figure 7.2 for a glass-based surface. For a nanosphere diameter of 500 nm, the estimated number of the resulting silver structures is around one million within a focussed laser spot dimension (appendix 14). This would reduce to around 8% of the substrate area in the ideally fabricated surfaces and more in geometrically defected regions. Therefore, quartz was preferred as substrate over the glass substrates. Glass substrates were only used with the modifications to the NSL method as discussed in detail in Chapter 6.

### 7.3 SERS results as per the types of SER-active surfaces

The SERS experiments conducted can be broadly divided into three major parts based on the substrate fabrication techniques used. These have been discussed in detail in Chapter 6 and are presented in this chapter under the following headings:

- a. Glass-based substrates with pre-NSL silver layer
- b. Glass-based substrates with post-NSL silver layer

## c. Optical fused quartz-based substrates

**7.4 Glass-based substrates with pre-NSL silver layer**

As already described in Chapter 5, a 20 nm thick silver underlayer was sufficient for complete coverage of a glass substrate, allowing uniform NSL monolayer formation. Such a surface, although requiring extra care during monolayer coating, was found to give an enhancement high enough for useful SERS analysis using the R3000 Raman spectrometer. A large number of experiments were conducted with two different silver underlayer thicknesses of 20 and 30 nm and by varying the final silver layer from 40 to 300 nm. The summary of a few of the selected SERS experiments conducted is presented in table 7.1.

Table 7.1 Summary of experiments conducted with glass-based substrate with pre-NSL silver layer.

Substrate Configuration		Analyte			Detection ; S/N of Characteristic breathing mode	Remarks
Underlayer Thickness (nm)	Structure Height (nm)	Type	Surface adsorption as	Concentration or time of exposure to vapour		
20	300	Pyridine pure	Solution (drop)	$10^{-2}$ M	18.1 of $990\text{ cm}^{-1}$	Figure 7.5
30	60	Pyridine $10^{-2}$ M	Vapour	20 seconds	27.1 of $990\text{ cm}^{-1}$	Figure 7.6
20	50	Pyridine	2.1 parts per hundred	10 seconds	25 of $990\text{ cm}^{-1}$	Figure 7.7
30	100	Nitrobenzene	16 parts per hundred	20 seconds	7 of $1004\text{ cm}^{-1}$	Figure 7.8

In figure 7.5, the SER spectrum shown was recorded after a  $10\ \mu\text{l}$  of  $10^{-2}$  M pyridine (in water) drop was put on the surface and allowed to evaporate. The surface was prepared by coating a 20 nm thick pre-NSL layer and a 300 nm thick final layer. The Raman spectrum of a  $10^{-2}$  M pyridine solution in a cuvette is also included as a reference. The strong ring breathing modes at  $990\text{ cm}^{-1}$  and  $1030\text{ cm}^{-1}$  were observed clearly with  $t_i = 5$  seconds only. The S/N for the  $990\text{ cm}^{-1}$  ring breathing mode was found to be 18.1. It was noted that the ring deformation and ring breathing modes at  $650\text{ cm}^{-1}$  and  $1215\text{ cm}^{-1}$  respectively were missing in the SER spectrum. The changes in the SER spectrum both in terms of the shift in the peak wavenumber as well as the variation in the relative intensities is governed by the differences in selection rules for the SERS (discussed in

Chapter 2). Also, note that the signal from the glass substrate peak at  $1387\text{ cm}^{-1}$  was completely removed.

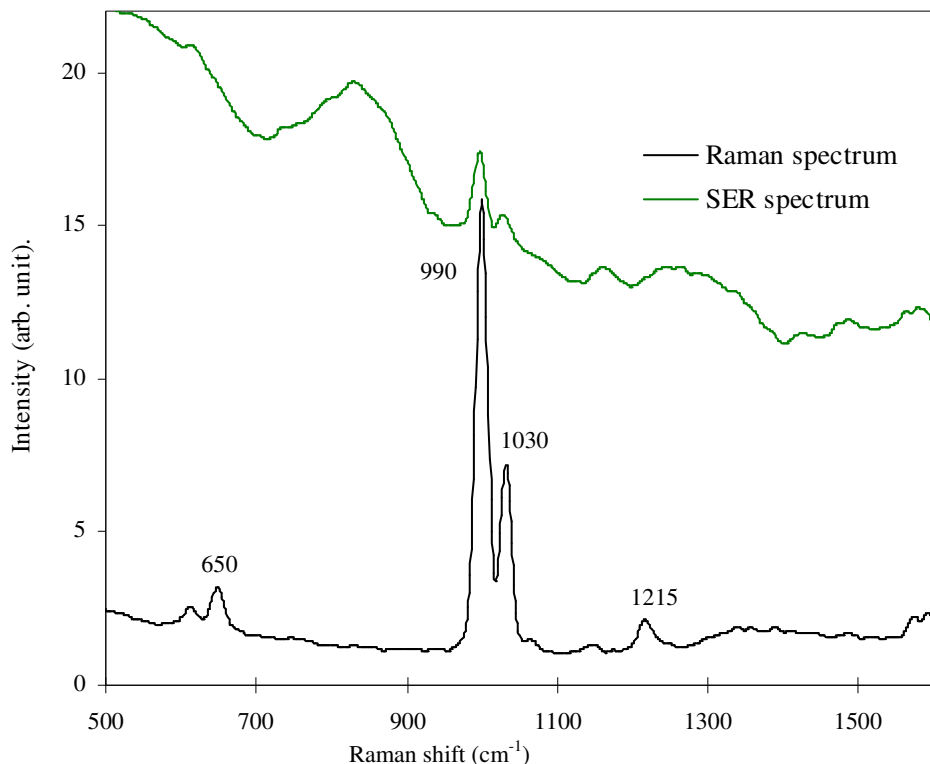


Figure 7.5 Normal Raman spectra of  $10^{-2}$  M solution of pyridine in a cuvette (a) and the SER spectrum of the adsorbed molecules on a SER-active glass-based surface.  $t_i = 5$  seconds.

As can be seen from the table 7.1, nano-structured surfaces were also prepared with 20 and 30 nm thick underlayers. The height of the structures varied from 50 to 300 nm. Within these conditions, it was observed that at the higher thickness of the silver underlayer the formation of the monolayer became erratic and non-uniform. Additionally, such surfaces did not exhibit any better quality or performance. In most cases, the monolayer was not formed due to the comparatively hydrophobic nature of the silver layer. Reproducibility decreased considerably with the increase in the thickness of the silver layer but the surfaces were found to remain SER-active irrespective of the thickness of the silver layer (40-300 nm).

One of the surfaces with 30 nm silver underlayer and a monolayer formation of PNS was later sputtered with 60 nm of a final silver layer. The surface was then exposed to headspace vapours from a  $10^{-2}$  M pyridine solution for 20 seconds. The SER spectra shown in figure 7.6 were recorded with  $t_i = 5$  and 10 seconds as indicated. The two ring breathing modes appeared having S/N for the  $990\text{ cm}^{-1}$  peak of  $\sim 18.35$  and  $27.1$  for  $t_i = 5$  and 10 seconds respectively. As mentioned earlier, there was no direct effect of the increase in the thickness of the underlayer on the enhancement in the Raman intensity. It only affected the formation of the monolayer and therefore the reproducibility of the surface. Once the monolayer was formed, the rest of the fabrication process was not affected and the SER-effect of the resulting surfaces were independent of the variation in underlayer thickness.

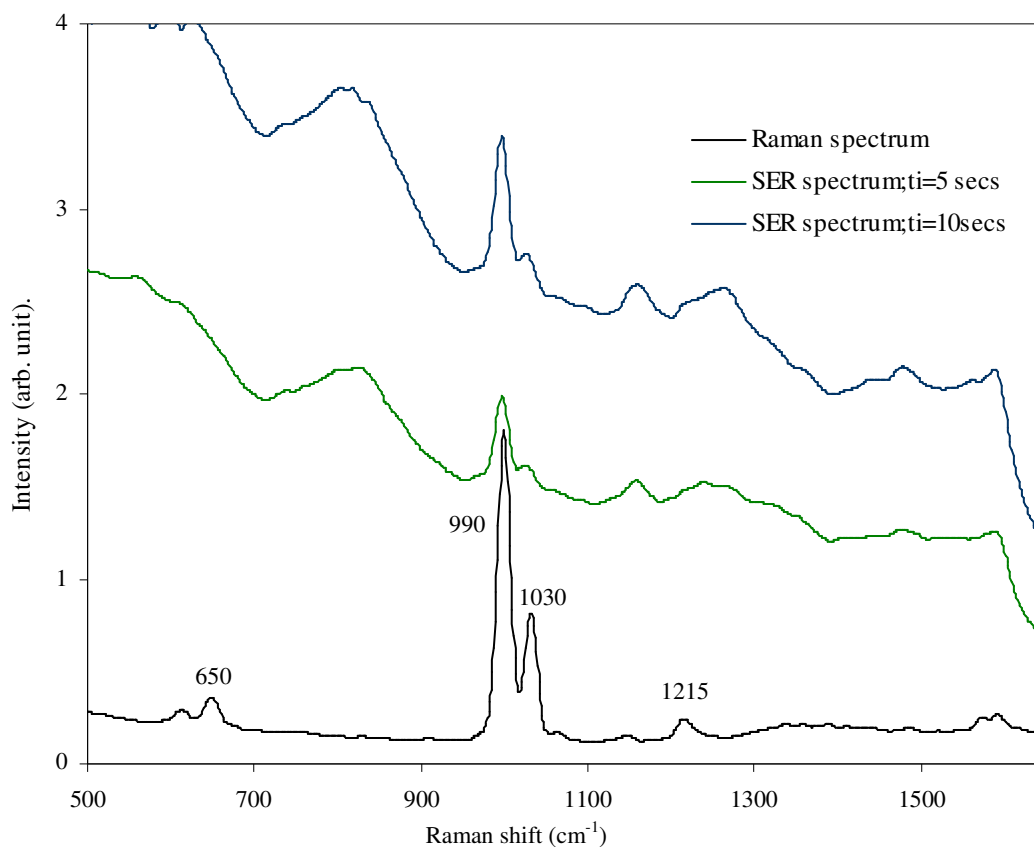


Figure 7.6 Raman spectrum of  $10^{-2}$  M pyridine in cuvette and SER spectra of pyridine exposed surface with  $t_i = 5$  and 10 seconds.

The substrate with a 20 nm thick underlayer gave best results for a monolayer formation and hence for the SERS analysis. The result of another test is shown in figure 7.7. The glass substrate was fabricated with 20 nm thick underlayer and a 50 nm thick final layer



of silver. It was exposed to the headspace vapours of pure pyridine for ~10 seconds. A Raman spectrum was recorded both before and after exposing the surface to pyridine. The spectrum of the surface before exposure to the analyte shows negligible background, as compared to that of a glass background. The SER spectra of pyridine molecules adsorbed on silver nano-structures are shown in figures 7.7 recorded with,  $t_i = 3$  and 5 seconds respectively.

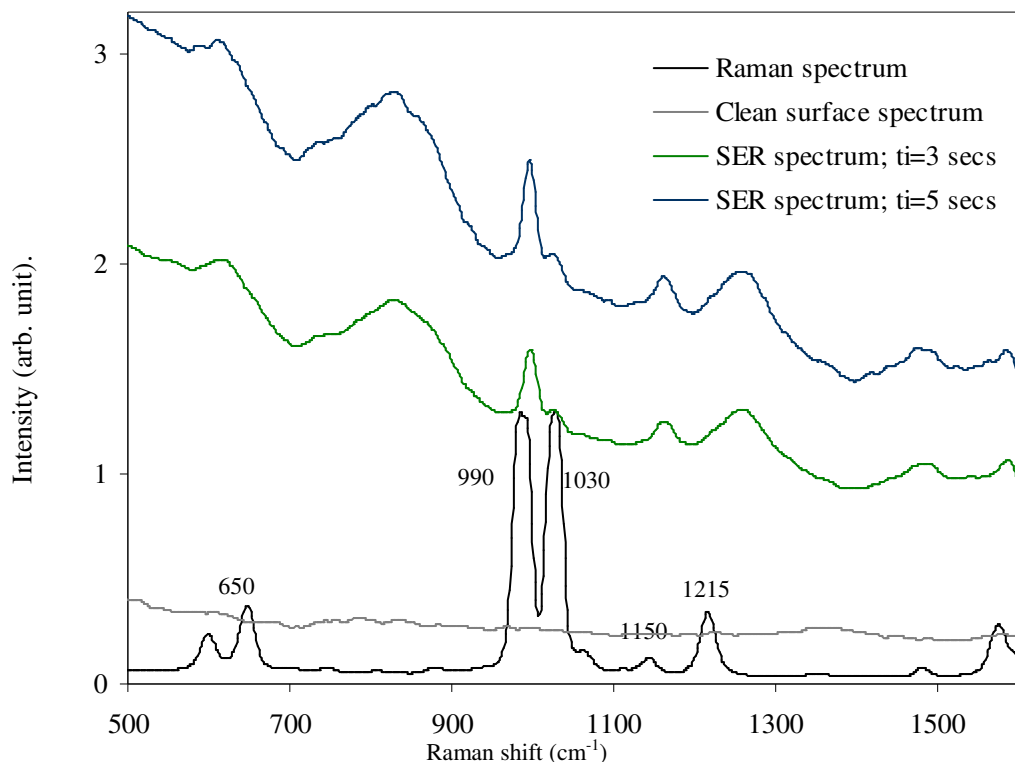


Figure 7.7 Raman spectrum of pure pyridine in cuvette, SER spectrum of surface before Pyridine exposure and after surface was exposed to pyridine vapour for 10 seconds with  $t_i = 3$  and 5 seconds as indicated.

The two ring breathing modes at  $990\text{ cm}^{-1}$  and  $1030\text{ cm}^{-1}$  appeared strong as usual, with a S/N for the  $990\text{ cm}^{-1}$  of ~ 19 and 25 for  $t_i = 3$  and 5 seconds respectively. This S/N value was considered better compared to the result discussed above (figure 7.6). Although the latter surface was exposed to pure pyridine instead of a  $10^{-2}\text{ M}$  solution the exposure time to pyridine vapour was reduced to 10 seconds and that the integration time was also reduced to 5 seconds. This meant that the latter surface was exposed to pyridine vapour for a shorter period and data accumulated over less time. The resulting S/N were found to be almost equal. This was considered to be due to the higher

enhancement in the Raman scattering in the latter case. The higher Raman intensity was considered to have a contribution from LSPR enhancement due to the 50 nm height of the nano-structures.

Nitrobenzene was also used as a target analyte with a surface fabricated with a 30 nm silver underlayer and was later sputtered with 100 nm of final silver layer. The surface was then exposed to headspace vapours from pure nitrobenzene for 20 seconds. The Raman and SER spectra, recorded with  $t_i = 5$  and 10 seconds respectively are shown in figure 7.8. The ring breathing mode at  $1004\text{ cm}^{-1}$  appeared strongest. The  $\text{NO}_2$  symmetric stretch at  $1350\text{ cm}^{-1}$ , the ring vibration mode at  $850\text{ cm}^{-1}$  and the C=C stretch at  $1590\text{ cm}^{-1}$  were also identified. The S/N for the ring breathing mode at  $1004\text{ cm}^{-1}$  was  $\sim 7$ .

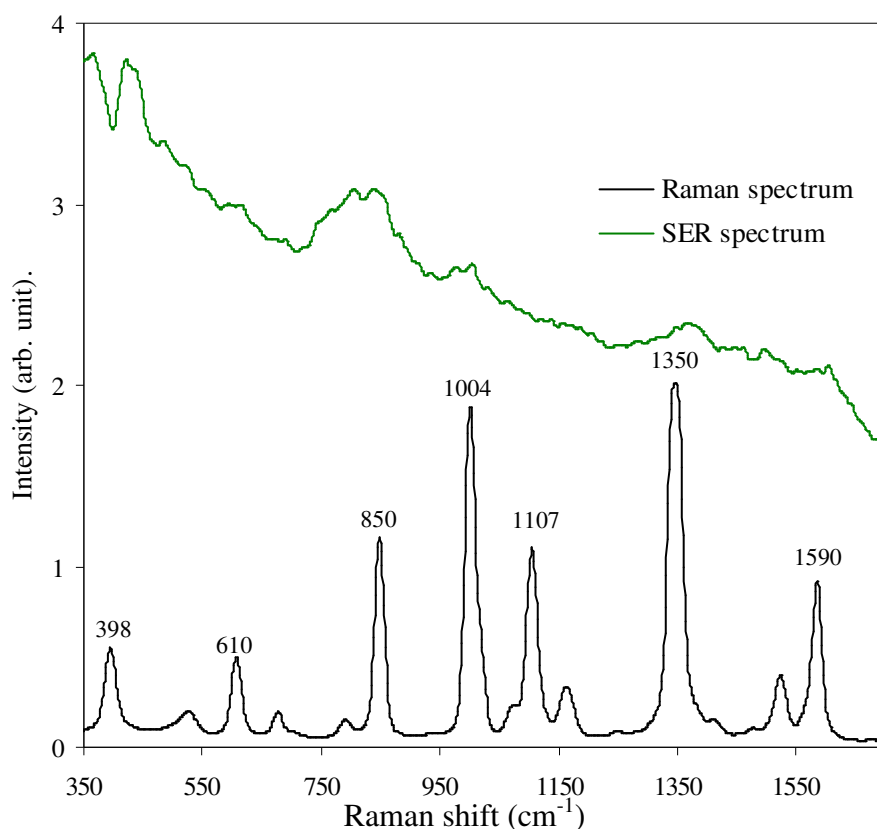


Figure 7.8 Raman spectrum of nitrobenzene in a cuvette ( $t_i = 5$  seconds) and the SER spectrum of a surface exposed to its vapours for 20 seconds ( $t_i = 10$  seconds) as indicated.

The benefit of the silver underlayer in reducing the background noise from the glass-based surface was positively realised. It was noted that the negligible background noise,

observed in a glass-based surface even with 20 nm thick silver underlayer, opened up the possibility of real time detection of species in trace concentrations with a portable Raman system.

The intensity of a particular Raman peak, in the normal Raman analysis, was linearly proportional to the quantity of the target molecules being sampled if all the other experimental parameters were assumed constant. The Raman intensities in the experiments discussed above could not be compared directly from the spectra. Even if all the equipment settings, including the integration time, were kept the same, the SER spectra from two different points on the same SER-active surface could not be directly compared with respect to their Raman peak intensities. The reasons for such discrepancies are discussed below:

#### **Nano-structural configuration**

No matter how well the self-assembling monolayer was laid, the flawless domains were restricted to very small areas (a few square microns), therefore the number of defective lines within the area of the laser diameter ( $0.1 \text{ mm}^2$ ) would always differ. This would, to some extent, vary the peak intensities among similarly prepared substrates and therefore would not allow straightforward comparison.

#### **Target molecule concentration**

The adsorption of molecules on to hot spots within the silver nano-structures could not be predicted with certainty. As the experiments were performed in normal laboratory environments, the distribution of molecules across the substrate was not considered to be even. Especially in the vapour phase analysis, the exposure time of (say) 10 seconds might not ensure the number of molecules being transferred to the SER-active surface were similar and uniform across the surface.

#### **Height of nano-structures**

The silver underlayer did not affect the surface morphology till the time the PNS monolayer was achieved. The effect of the height of the structures, on the other hand, could have been pronounced, as discussed in the earlier chapters. The enhancement in Raman intensities in the LSPR region (surfaces having 40-50 nm height of structures)

was likely to be much higher. However, variations like these would result from a variety of factors that influence the SER analysis, as discussed in Chapter 2.

The reasons mentioned above are only three of the many factors affecting the SERS experiments. However, the ultimate aim of our research is not quantitative analysis but to investigate the ultra-sensitive detection potential of substrates fabricated with different experimental parameters and protocols. To this end, *the identification of the target molecule at the lowest possible concentration and by the shortest possible time* was being investigated.

### **7.5 SERS analysis with glass-based substrates with thin silver overlayer**

The effects of the silver layer on the metal nano-structures have been discussed in Chapter 6, with the likely morphological changes schematically shown in figure 6.1 (b) and (d). Theoretically, the hot spots existed at the sharp edges of the structures<sup>49</sup> and when these sharp edges got flattened out (lost sharpness at edges) the SER enhancement factor was expected to decrease. Although the overlayer applied was thin (20 nm) compared to the height of the structures (40-300 nm), it was, nevertheless, found to reduce the effectiveness of the surfaces, as was observed during the experiments.

The process was not believed to be workable for the surfaces having smaller nano-structures because the smaller the structure height the more effect the overlayer had on the structure. For example, a 20 nm overlayer would have less effect on the surface having a structure height of 300 nm than a surface with 40 nm high structures. That meant the additional advantages of LSPR of the SER-active surfaces could not be gained. When an overlayer (20-30 nm) was added to a surface having a lower height of structures, say 50 nm, it caused larger changes in morphology compared to those with higher structures (200-300 nm). This meant that glass-based surfaces could preferably be fabricated with initial silver layers of 200-300 nm thickness.

Therefore, due to the combined effect of loss of metal edges and the non resonant region of surface plasmon, the probability of a molecule being detected decreased and in some of the experiments performed on the surfaces prepared with this method, the presence of

target molecules (in the vapour phase) could not be detected. However, for surfaces with initial silver layer in the range of 200-300 nm, the SER enhancement achieved was high enough to detect the target molecules. Some of the results have been summarised in table 7.2.

A surface prepared with a 20 nm silver overlayer on 250 nm high nano-structures was exposed to the headspace vapour of pyridine for 15 seconds. The Raman spectrum was recorded before and after the exposure to pyridine vapour, keeping  $t_i = 10$  seconds. The result is shown in figure 7.9. The S/N for the  $990\text{ cm}^{-1}$  ring breathing mode was  $\sim 27$ . The Raman spectrum of a clean surface was essentially of silver, which did not give much background.

Table 7.2 Summary of experiments conducted with glass-based substrate with silver overlayer.

Substrate Configuration		Analyte			Detection ; S/N of peak identified	Remark
Structure Height (nm)	Over layer (nm)	Type	Surface adsorption as	Concentration or time of exposure to vapour		
250	20	Pyridine	Vapour	15 seconds	27 of $990\text{cm}^{-1}$	Figure 7.9
225	20	Pyridine	Vapour	10 seconds	22 of $990\text{cm}^{-1}$	Figure 7.10
250	20	PETN	Vapour	18 ppt	9 of $869\text{cm}^{-1}$	Figure 1 Appendix 15
225	20	PETN	Vapour	18 ppt	13 of $869\text{cm}^{-1}$	Figure 7.11
250	20	HMTD	Vapour	0.29 ppm	15 of $766\text{ cm}^{-1}$	Figure 7.12
225	20	HMTD	Vapour	0.29 ppm	11 of $766\text{ cm}^{-1}$	Figure 2 Appendix 15

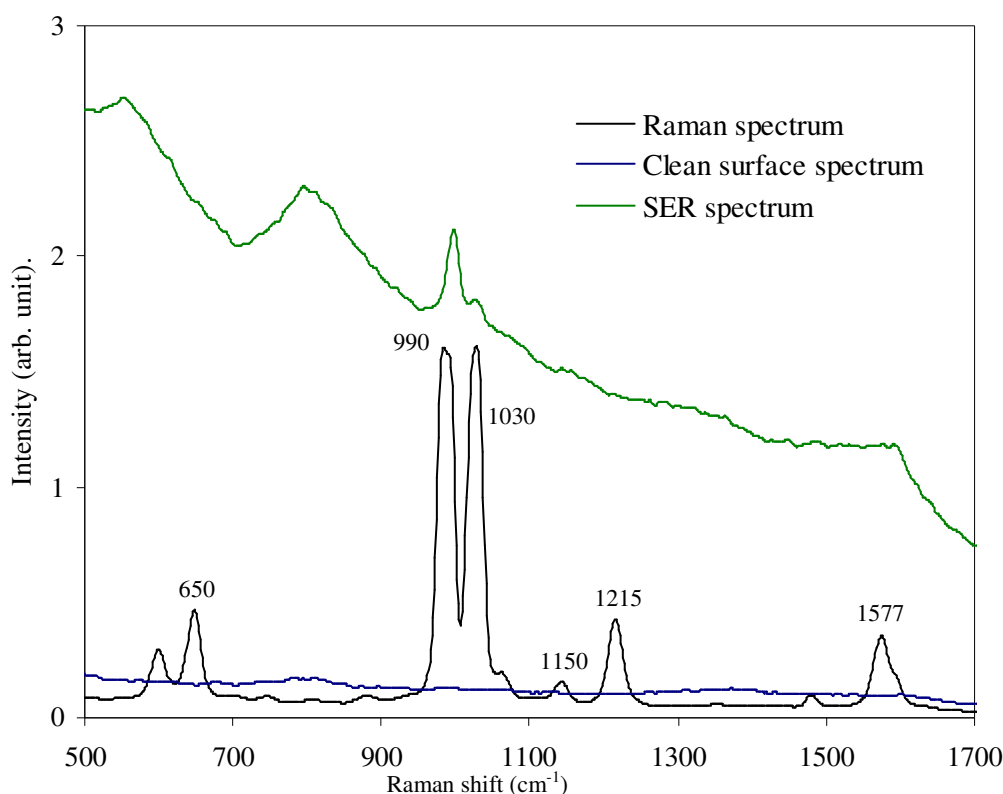


Figure 7.9 SER spectrum recorded with  $t_i = 10$  seconds, from surface exposed to pyridine vapour for 15 seconds. Raman spectra of pyridine in cuvette and of background from substrate without exposure to analyte are also shown.

In another experiment a glass-based surface having a silver structure thickness of 225 nm and a sputtered overlayer of 20 nm after removal of nanospheres, was exposed to the headspace from pyridine for 10 seconds. Figure 7.10 presents the Raman spectrum of pyridine in a cuvette and the SER spectrum of adsorbed pyridine molecules. The ring breathing modes at  $990\text{ cm}^{-1}$  and  $1029\text{ cm}^{-1}$  were observed clearly with  $t_i = 10$  seconds. The S/N for the  $990\text{ cm}^{-1}$  ring breathing mode was found to be  $\sim 22$ . All other prominent characteristic modes were too weak to be positively identified. In comparison with the result shown in figure 7.9, the low S/N could be due to the shorter time of exposure to pyridine vapour, assuming all other factors remained constant.

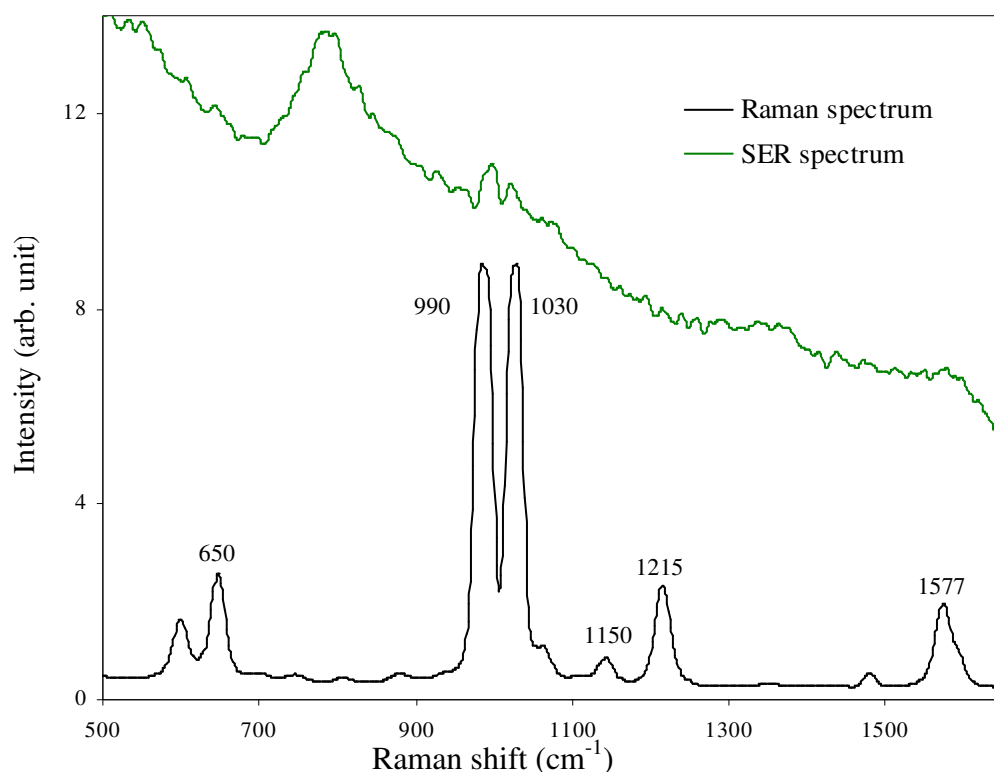


Figure 7.10 SER spectrum ( $t_i = 10$  seconds) from a glass-based surface exposed to pyridine vapour for 10 seconds showing ring breathing modes.

The surfaces prepared with silver overlayer were also used to detect the solid explosives. This was achieved by exposing the fabricated surface to the headspace vapour from the explosive. Very small quantities of explosives were used for the experiments and due to their extremely low vapour pressures, the SER-active surfaces were exposed to the explosive vapour for a period long enough for the equilibrium/saturated vapour pressure to be reached. At this condition it was possible to calculate the concentration of molecules in the headspace so that an approximate limit of detection could be established. The details of the vapour concentrations have been discussed in Chapter 4 for each analyte separately.

A SER-active surface, fabricated with a 225 nm sputtered silver layer and an additional 20 nm of silver overlayer was exposed to the headspace vapour from the PETN explosive. The normal Raman spectrum and its SER spectrum recorded with  $t_i = 10$  seconds are shown in figure 7.11. The C-C stretch mode at  $869\text{ cm}^{-1}$  was identified and had a S/N of  $\sim 13.3$ . The O-NO<sub>2</sub> symmetric stretching mode at  $1287\text{ cm}^{-1}$  and the O-

$\text{CH}_2$  vibration at  $1466\text{ cm}^{-1}$  could not be positively identified. The  $\text{O-NO}_2$  rocking vibration at  $536\text{ cm}^{-1}$  was also visible but the  $\text{C-C-C}$  deformation mode at  $621\text{ cm}^{-1}$  was not observed.

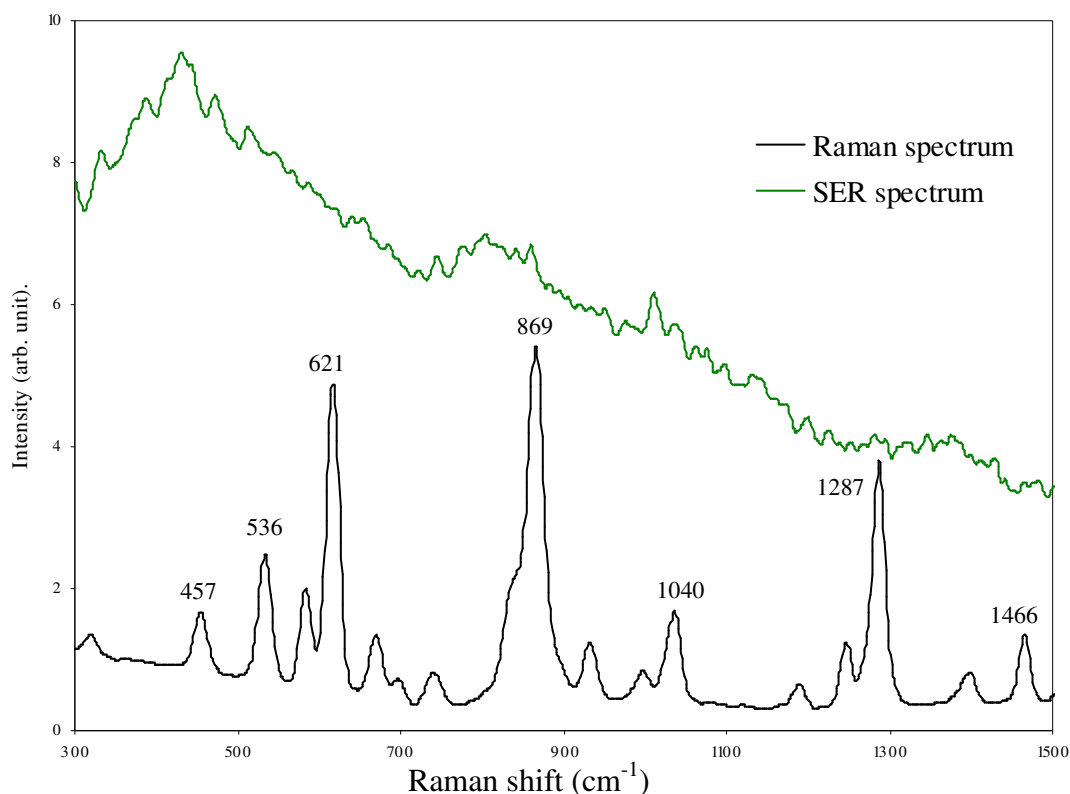


Figure 7.11 SER spectrum ( $t_i = 10$  seconds) from a glass-based surface having a 225 nm height of nano-structures with a 20 nm silver overlayer when exposed to headspace vapour from PETN.

HMTD was also detected by the surface fabricated with a 250 nm silver layer and an additional 20 nm silver overlayer. The surface was exposed to the headspace vapour from the HMTD. The Raman and SER spectra were recorded with  $t_i = 10$  seconds and are shown in figure 7.12. The peroxide symmetric stretch at  $766\text{ cm}^{-1}$  appeared strong, having a S/N of  $\sim 15$ . The asymmetric stretching modes of peroxide at  $900\text{ cm}^{-1}$  and  $944\text{ cm}^{-1}$  were too weak to be identified.



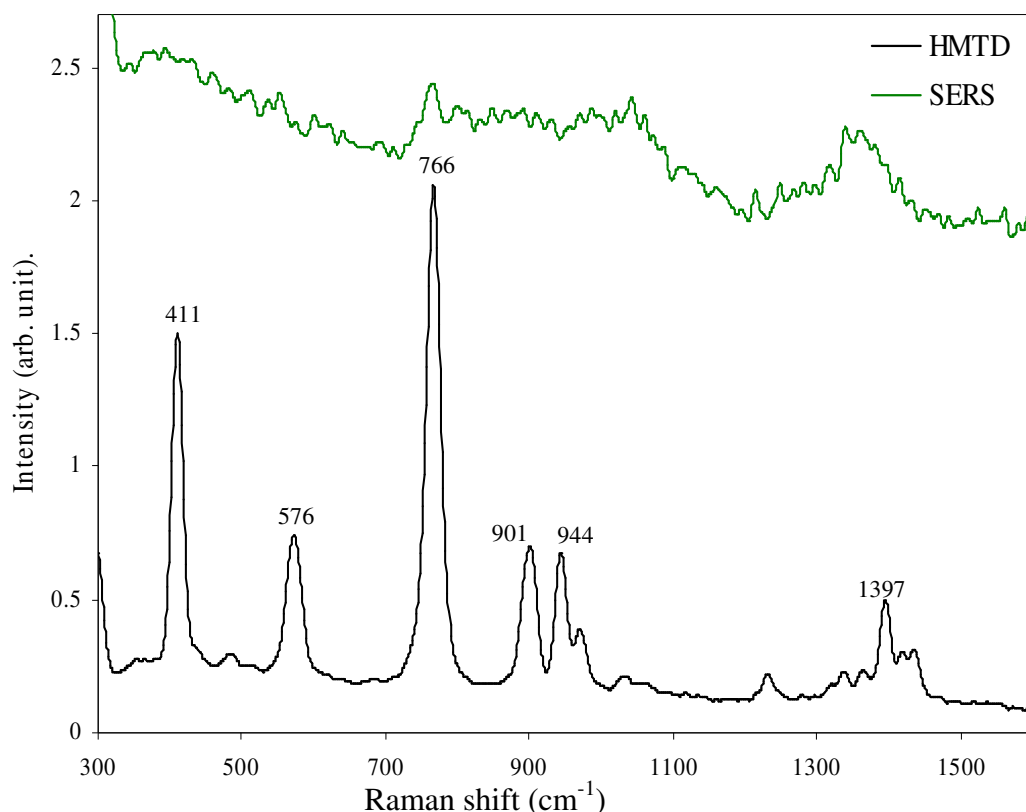


Figure 7.12 Raman (reference) and SER spectra ( $t_i = 10$  seconds) from a glass-based surface having 250 nm height of nano-structures with 20 nm silver overlayer when exposed to headspace vapour from HMTD.

The enhancement factor for these surfaces was found to be lower than the surfaces without the overlayer because of the slight smoothing of the otherwise sharp metal edges and no additional enhancement from the LSPR. Nevertheless, the detection of molecules from solution as well as from the solid analyte was successful. The major problem was the poor S/N that made detection of the explosives difficult.

Not every time the surface was exposed were the characteristic peaks observed. It was found that the detection of adsorbed molecules was only possible when the entire process of surface fabrication, sample presentation and Raman analysis was ideally followed. Though reproducibility was not good, the capability of SERS was undoubtedly confirmed, which was the main aim of our research.

## 7.6 SERS analysis with quartz-based substrates

Quartz-based surfaces provided a better opportunity for sensitive analysis than the glass-based ones. Although detection of explosive vapours was successful with modified glass-based surfaces, much better results were observed with surfaces fabricated with quartz substrates. These SER-active surfaces were prepared with sputtered silver layers of thicknesses varying between 40 and 300 nm.

The sensitivity of the SER process was found to depend mainly upon the analyte properties. This was true when the conditions of surface fabrication, sample presentation and Raman spectroscopic measurement were kept similar. The analyte's vapour pressure, surface adsorption and light absorption properties ultimately made them easier or difficult to detect. The SER-activity of each analyte is discussed separately below.

### 7.6.1 SER spectroscopy of pyridine

Pyridine being a well-characterised and widely tested sample for SER analysis, was used to investigate the SERS properties of the quartz-based nano-structured surfaces in our laboratories. It was found to have good adsorption ability for our silver-based surfaces and therefore could be detected under most of the experimental conditions. The results are summarised in table 7.3 for surfaces having different height of silver structures.

Table 7.3 Summary of experiments conducted using pyridine with quartz-based surfaces.

Structure height (nm)	Analyte state/ exposure	Detection ; S/N of peak identified	Remarks
300	Vapour-10sec	16 of $990\text{cm}^{-1}$	Figure 7.13
250	Vapour-20sec	27 of $990\text{cm}^{-1}$	Figure 7.14
200	Vapour-20sec	14 of $990\text{cm}^{-1}$	Figure 7.15
150	Vapour-20sec	11 of $990\text{cm}^{-1}$	Figure 3 Appendix 15
80	Vapour-10sec	16 of $990\text{cm}^{-1}$	Figure 4 Appendix 15
50	Vapour-10sec	23 of $990\text{cm}^{-1}$	Figure 7.16

The identification of pyridine molecules was based on the two ring breathing modes at  $990\text{ cm}^{-1}$  and at  $1030\text{ cm}^{-1}$ . In the Raman spectrum, both these modes have equally strong peak intensity but in the SER spectrum the former appeared much stronger than the latter. In figure 7.13, Raman and SER spectra are shown. This surface was prepared with structures of 300 nm height. Raman spectrum were recorded with  $t_i = 10$  seconds. The surface was exposed to headspace vapour from the pyridine liquid for 10 seconds. The SER spectrum was recorded with the Renishaw Raman system at GRH (appendix 7) using  $t_i = 2$  seconds with 20 accumulations. The substrate were prepared in our laboratory and transported to GRH in an air-tight container for analysis. The S/N for the  $990\text{ cm}^{-1}$  ring breathing mode was 16 compared to  $\sim 300$  for the same peak in the normal Raman spectrum. A slight shift in the peak position was observed; from  $990\text{ cm}^{-1}$  in the normal Raman spectrum to  $999\text{ cm}^{-1}$  in the SER spectrum.

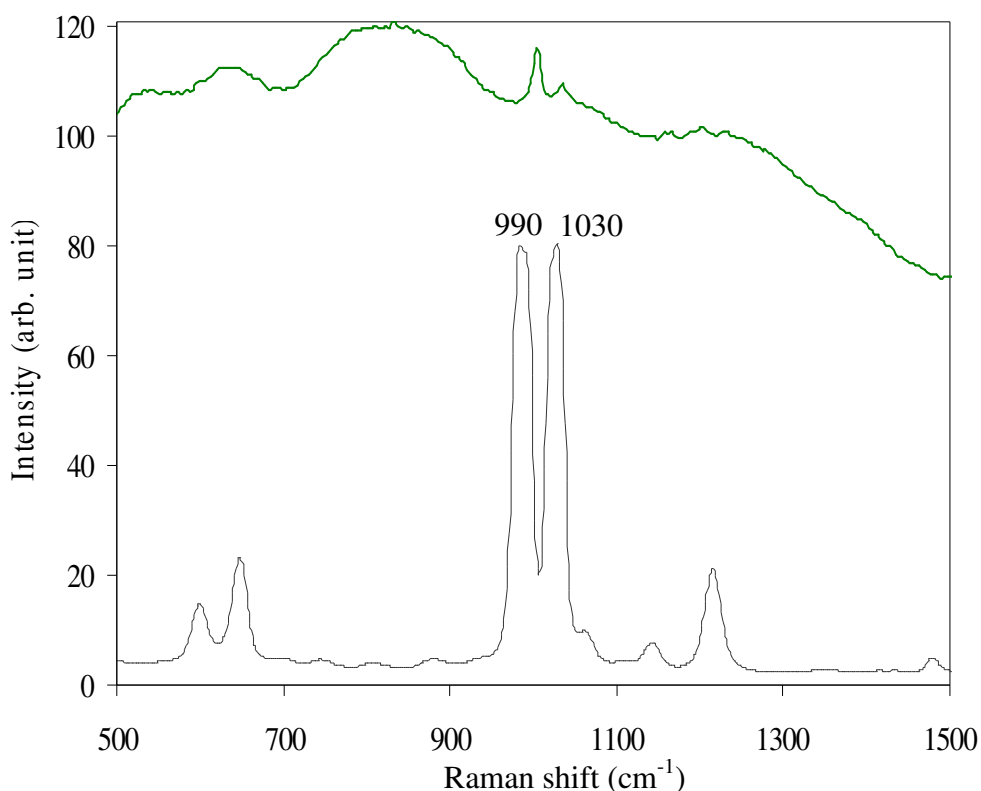


Figure 7.13 Normal Raman spectrum of pyridine and SER spectrum recorded from a surface having 300 nm high silver structures exposed to the vapour from pyridine for 10 seconds.

In another experiment at GRH using the Renishaw system, a surface having an average of 250 nm high structures was used, keeping  $t_i = 2$  seconds with 20 accumulations. This

was exposed to headspace vapour from pyridine liquid for 20 seconds. Figure 7.14 shows the SER spectrum of adsorbed pyridine. The shift in the peak position was the same as in figure 7.13. The S/N of the  $990\text{ cm}^{-1}$  ring breathing mode was  $\sim 27$ . A slight improvement in S/N may be due to the increased exposure time of the surface to the pyridine vapour or to the better enhancement effect of the surface with 250 nm high structures than the one having 300 nm high structures or the combination of the two factors.

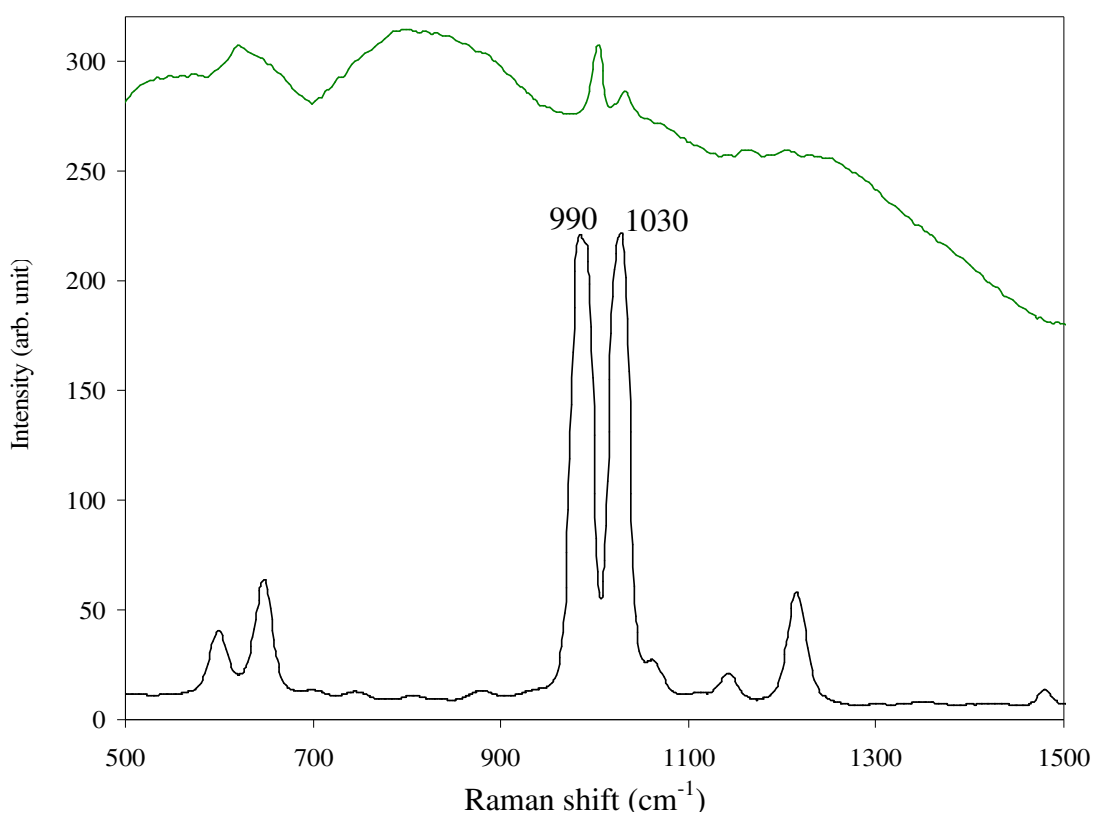


Figure 7.14 Normal Raman spectrum of pyridine and SER spectrum recorded from a surface exposed to the vapour from pyridine for 20 seconds having 250 nm high structures.

After establishing the SER ability of the quartz-based surfaces using high resolution equipment (Renishaw), similar experiments were conducted with the portable low resolution Raman system. A quartz based surface was prepared by sputtering a 200 nm silver layer and later exposed to headspace vapour from liquid pyridine for 20 seconds. Both Raman and SER spectra were recorded using  $t_i = 10$  seconds. The spectra are

shown in figure 7.15 and the S/N for the  $990\text{ cm}^{-1}$  ring breathing mode was 14. The shift in peak position was the same as observed previously.

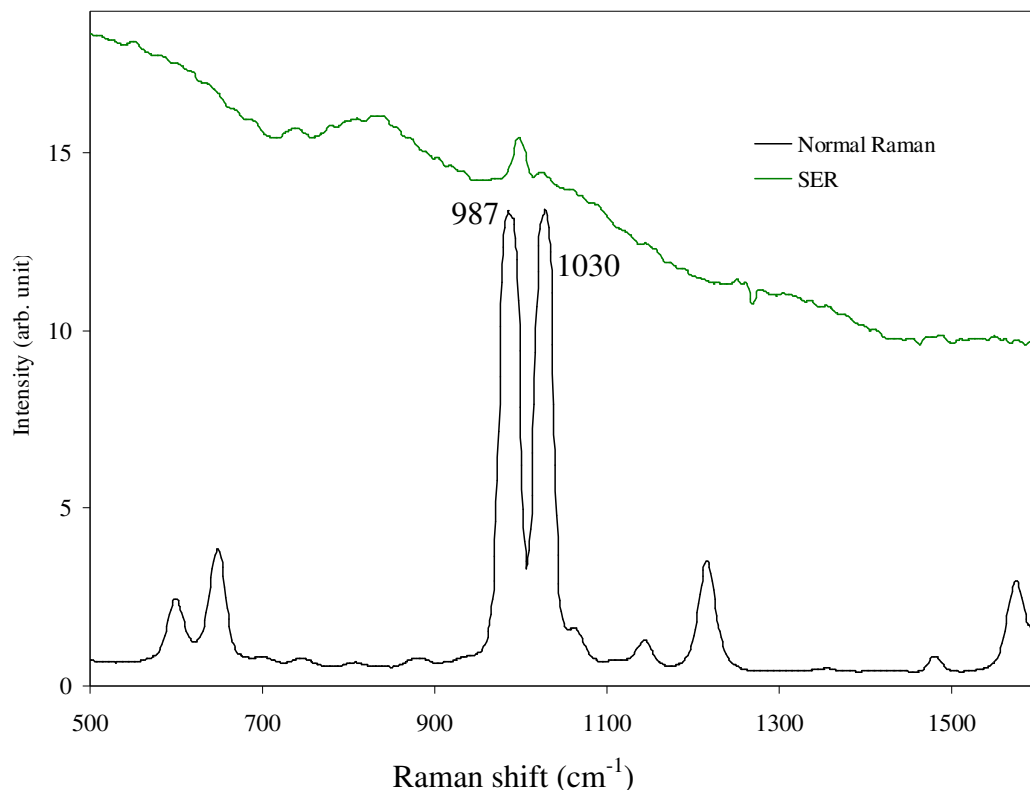


Figure 7.15 Normal Raman spectrum of pyridine and SER spectrum recorded from a surface exposed to the vapour from pyridine for 20 seconds having 200 nm high structures.

The surfaces were gradually improved and, based on the study of the LSPR discussed in Chapter 6, the surfaces with structural heights in 40-50 nm region were expected to give higher enhancement than the surfaces believed to be in non resonant regions (structures higher than 60 nm). The SER results for pyridine generally supported the LSPR results. The S/N was found to improve when the surfaces had heights of 40-50 nm. Figure 7.16 shows the SER spectrum of the adsorbed pyridine on the surface prepared with a 50 nm sputtered silver layer. The surface was exposed to headspace vapour from liquid pyridine for 10 seconds and the S/N was found to be 23 for the  $990\text{ cm}^{-1}$  ring breathing mode.

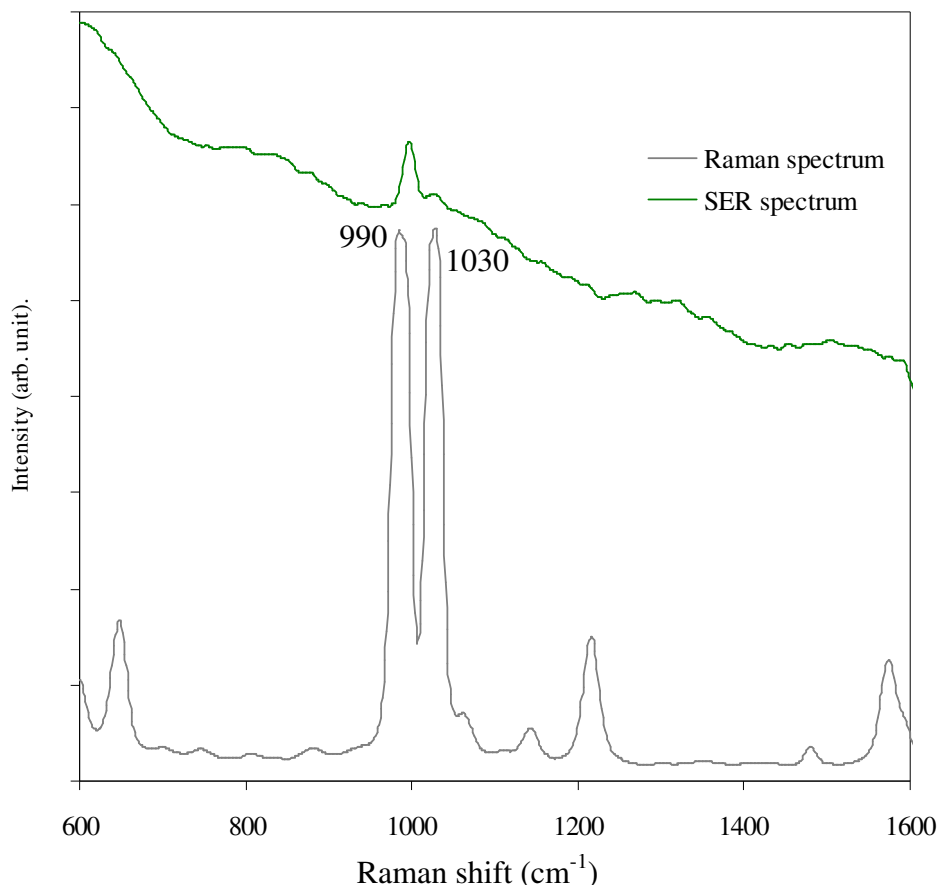


Figure 7.16 Normal Raman spectrum of pyridine and SER spectrum recorded from a surface exposed to the vapour from Pyridine for 10 seconds having 50 nm high structures.

### 7.6.2 SER spectroscopy of Nitrobenzene

Nitrobenzene, having a nitro group ( $\text{NO}_2$ ) on the side of the benzene ring, resembles some of the molecular structures of typical explosives. The positive charge on the nitrogen in the nitro group gives it good adsorption properties. It has a higher vapour pressure than solid explosives and therefore it was useful for preliminary experiments before solid explosives having comparatively lower vapour pressures were used. Some results are listed in table 7.4.

Table 7.4 Summary of experiments conducted using nitrobenzene with quartz-based surfaces.

Height of structure (nm)	Analyte state/ exposure time	Detection ; S/N of peak identified	Remarks
300	Vapour-60sec	5 of 1350 $\text{cm}^{-1}$	Figure 5, Appendix 15
250	Vapour-20sec	12 of 1350 $\text{cm}^{-1}$	Figure 7.17
50	Vapour-20sec	9 of 850 $\text{cm}^{-1}$	Figure 6, Appendix 15

Nitrobenzene was also detected by exposing the SER-active surface to its headspace vapour. The quartz-based surface was fabricated with a silver structure of average height  $\cong 250$  nm and was exposed to the headspace vapour of nitrobenzene for 20 seconds under normal laboratory conditions. The SER spectrum of this sample was recorded with a Renishaw Raman system at GRH from a surface (quartz-based substrate) prepared in our laboratory and transported to GRH in an airtight container for analysis. The data was collected for  $t_i = 2$  seconds and was averaged for 20 accumulations. Figure 7.17 shows the normal Raman spectrum (in cuvette) of nitrobenzene and the SER spectrum from the adsorbed molecules. The  $\text{NO}_2$  symmetric stretch at  $1350 \text{ cm}^{-1}$  appeared strongest. The ring breathing mode at  $1004 \text{ cm}^{-1}$  and the ring vibration mode at  $850 \text{ cm}^{-1}$  were also identified. The S/N for ring breathing mode  $1004 \text{ cm}^{-1}$  and the  $\text{NO}_2$  symmetric stretch at  $1350 \text{ cm}^{-1}$  were  $\sim 11$  and  $12$  respectively. The spectra were base line corrected.

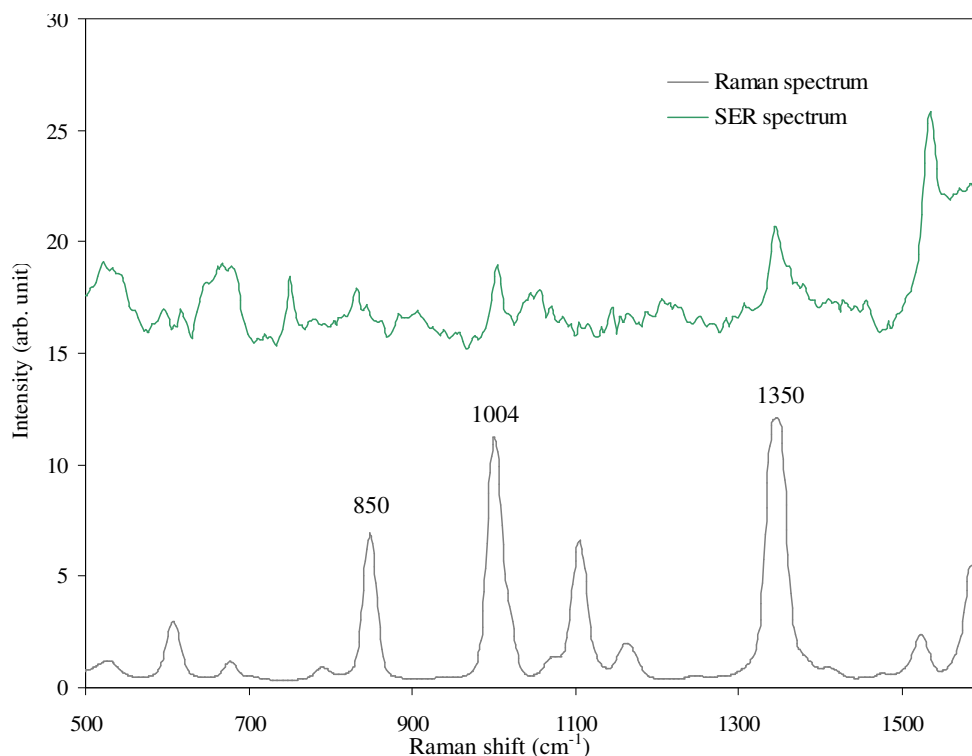


Figure 7.17 SER spectrum of nitrobenzene (vapour) adsorbed on a SER-active surface with 250 nm structure height recorded with a Renishaw Raman Microscope.

### 7.6.3 SER spectroscopy of TATP

TATP molecules do not have any nitrogen atom like other explosive/non-explosive molecules studied for SERS. The presence of nitrogen is known to provide an adsorption capability for such molecules on the nano-structured surfaces that is a prerequisite for effective SER activity. The peroxide group, O-O, in TATP molecules creates a positive charge on the adjacent carbon atoms. It is by one or more of these carbon atoms joining the two O-O groups and the two-methyl groups that TATP is likely to attach itself to the surface.

Some of the results showing detection of TATP are presented in table 7.5. These experiments were conducted by exposing the SER-active surface to the headspace vapour from TATP. The headspace vapour concentration was around 70 ppm.



Table 7.5 Summary of SERS results recorded with quartz-based surfaces showing detection of headspace vapour from TATP at 70 ppm concentration.

Structure height (nm)	Detection ; S/N of peak identified	Remarks
250	13 of 945 $\text{cm}^{-1}$	Figure 7.18
225	9 of 945 $\text{cm}^{-1}$	Figure 7.19
200	6 of 945 $\text{cm}^{-1}$	Figure 7, Appendix 15
80	16 of 945 $\text{cm}^{-1}$	Figure 7.20
70	9 of 945 $\text{cm}^{-1}$	Figure 8, Appendix 15
50	12 of 945 $\text{cm}^{-1}$	Figure 9, Appendix 15

Figure 7.18 presents the SER spectrum of TATP vapours adsorbed onto a quartz substrate having 250 nm high silver structures. The substrate was exposed to the headspace vapour of the explosive under normal laboratory conditions and a Raman measurement was taken with  $t_i = 10$  seconds. The asymmetric O-O stretch mode at around 945  $\text{cm}^{-1}$  was found to be stronger than the otherwise strong peroxide symmetric stretch and the O-C-O vibration at 865  $\text{cm}^{-1}$  and 550  $\text{cm}^{-1}$  respectively. The characteristic asymmetric stretch at 945  $\text{cm}^{-1}$  had a S/N of  $\sim 13$ .

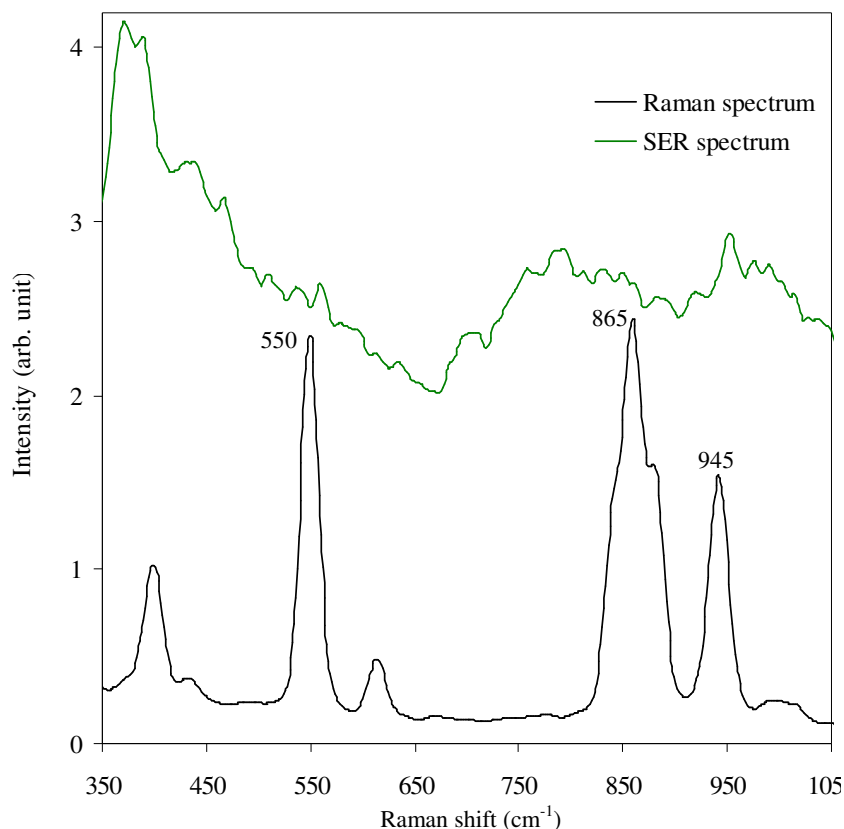


Figure 7.18 Normal Raman spectrum of TATP and its SER spectrum recorded from a surface (quartz-based) exposed to the headspace vapour, prepared with 250 nm thick sputtered silver layer.

A SER-active surface fabricated with 225 nm high silver structures was exposed to the headspace vapour of TATP. The result is shown in figure 7.19 recorded with  $t_i = 10$  seconds. The S/N for the asymmetric stretch at  $945\text{ cm}^{-1}$  was  $\sim 9$ .

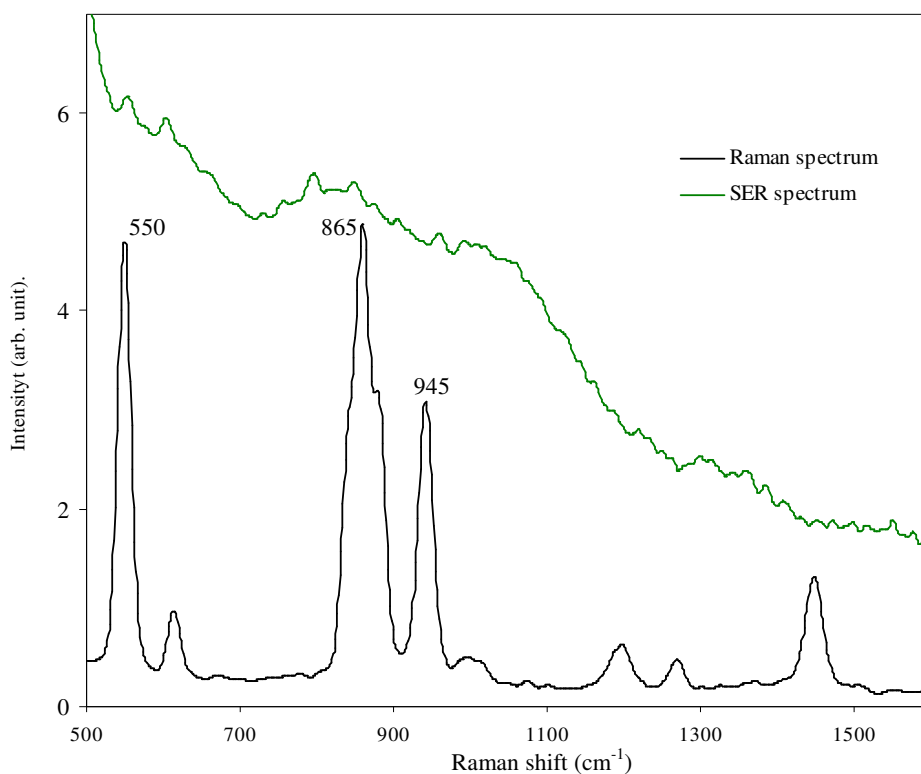


Figure 7.19 Normal Raman spectrum of TATP and its SER spectrum recorded from a surface (quartz-based) exposed to the headspace vapour, prepared with 225 nm thick sputtered silver layer.

The SER spectrum recorded on a surface fabricated with a 50 nm sputtered silver layer show similar results with a S/N of  $\sim 12$  for the asymmetric stretch at  $945\text{ cm}^{-1}$  with  $t_i = 10$  seconds. Therefore the TATP was detected with surfaces having structural height varying from 300 to 50 nm. No drastic increase in Raman intensity was observed for surfaces having a structure height of 50 nm that are thought to be in the LSPR region.

The SER spectrum shown in figure 7.20 was obtained with a quartz-based surface having 80 nm structural height. It was exposed to TATP headspace vapour and the SER spectrum was recorded with  $t_i = 10$  seconds. The O-O asymmetric stretch at  $945\text{ cm}^{-1}$  had S/N of 16.

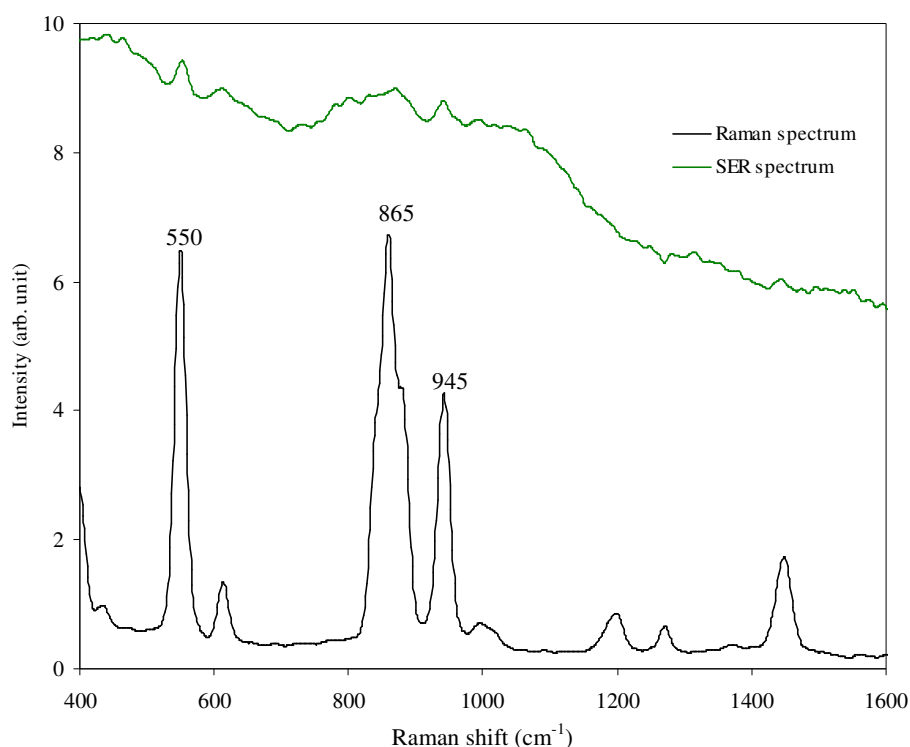


Figure 7.20 Normal Raman spectrum of TATP and its SER spectrum recorded from a surface (quartz-based) exposed to the headspace vapour, prepared with 80 nm thick sputtered silver layer.

#### 7.6.4 SER spectroscopy of HMTD

Unlike TATP, the HMTD molecule has no single ring configuration and also has two nitrogen atoms within the complex molecular structure. The N-C bond provides a likely adsorption orientation at these nitrogen junctions. Like TATP, HMTD was also detected by exposing SER-active surfaces to headspace vapour from the explosive. The headspace vapour concentration was around 0.29 ppm. The results of some of the typical spectral analyses are listed in table 7.6.

Table 7.6 Summary of SERS results of quartz-based surfaces showing detection of headspace vapour from HMTD having a concentration of 0.29 ppm.

Structure height (nm)	Detection ; S/N of peak identified	Remarks
250	10 of 766cm <sup>-1</sup>	Figure 7.21
250	19 of 766cm <sup>-1</sup>	Figure 10, Appendix 15
225	8 of 766cm <sup>-1</sup>	Figure 11, Appendix 15
100	6 of 766cm <sup>-1</sup>	Figure 12, Appendix 15
70	15 of 766cm <sup>-1</sup>	Figure 13, Appendix 15
60	10.5 of 766cm <sup>-1</sup>	Figure 7.22

The SER spectrum of HMTD molecules adsorbed on a quartz-based surface fabricated with a 250 nm thick silver layer exposed to its headspace vapour is shown in figure 7.21. The Raman spectrum of solid HMTD is also shown as reference. The spectra were recorded with  $t_i = 10$  seconds. The peroxide symmetric stretch at  $766\text{ cm}^{-1}$  appeared as a wide peak in the SER spectrum having S/N of  $\sim 10$ . The wide peak may be due to the complex nature of the molecular structure of HMTD and the restriction imposed on the molecular vibrations on adsorption or to the noise associated with quartz that appears around  $800\text{ cm}^{-1}$ . The asymmetric stretching modes of peroxide at  $901\text{ cm}^{-1}$  and  $944\text{ cm}^{-1}$  did not appear convincingly but a peak did appear at  $975\text{ cm}^{-1}$  where there is usually a weak shoulder of a peak at  $944\text{ cm}^{-1}$ .

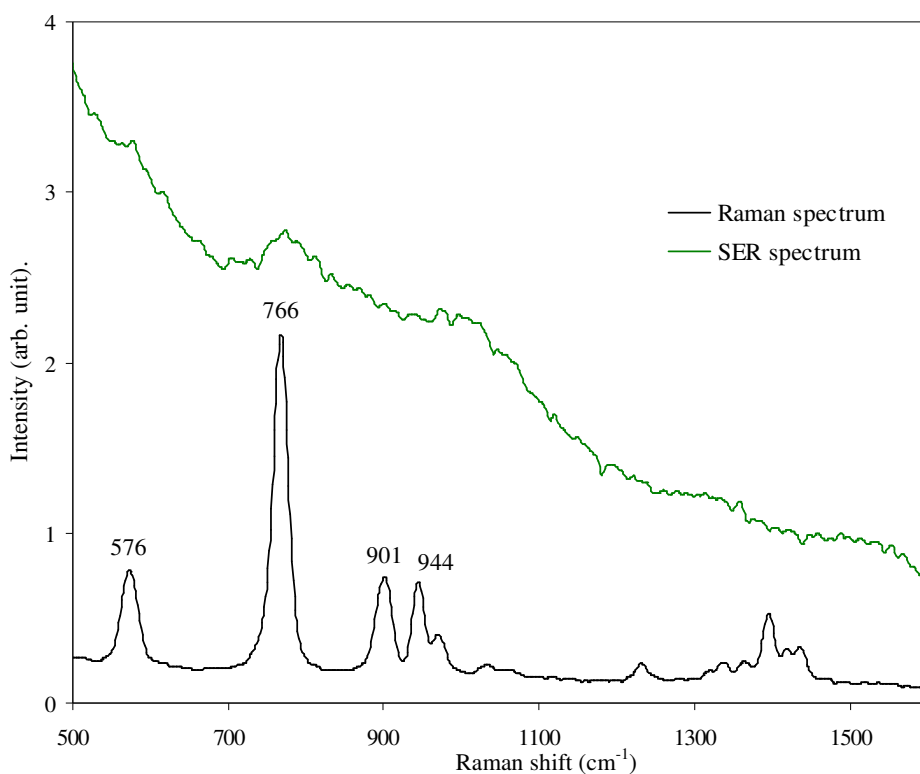


Figure 7.21 Normal Raman and SER spectra recorded from a quartz-based surface with 250 nm high silver structure exposed to the headspace vapour of HMTD.

The detection of HMTD in the LSPR region presented similar results to those observed with much larger structural heights. Figure 7.22 shows the Raman and SER spectra obtained from the surface having 60 nm high structures when exposed to the headspace

vapour from HMTD. With  $t_i = 10$  seconds, the S/N for the symmetric O-O stretch at  $766\text{ cm}^{-1}$  was  $\sim 10.5$  and it also appeared as a wide peak.

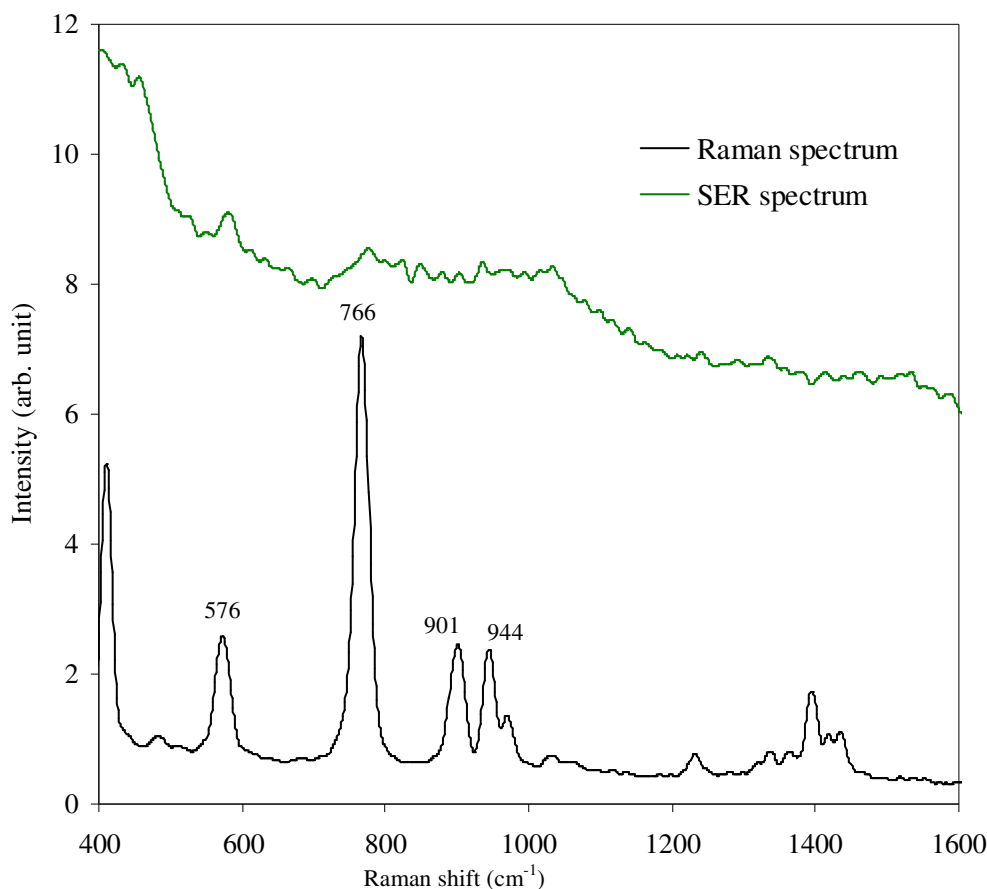


Figure 7.22 Normal Raman and SER spectra recorded from a quartz-based surface with a 60 nm silver structure exposed to the headspace vapour of HMTD.

### 7.6.5 SER spectroscopy of PETN

PETN, has a structure typical of most explosives with four nitro groups giving it good adsorption properties, but its detection becomes challenging in the vapour phase because of its much lower vapour pressure compared to the peroxide explosives and other analytes discussed above. The headspace vapour concentration was around 18 ppt. The PETN molecule is considered to attach to the silver surface through the positive charge on the nitrogen atoms. PETN was detected using quartz based SER-active surfaces and the the results are presented in table 7.7.

Table 7.7 Summary of SERS results of quartz-based surfaces showing detection of headspace vapour from PETN having a concentration of 18 ppt.

Structure height (nm)	Detection ; S/N of peak identified	Remarks
250	15 of 1287cm <sup>-1</sup>	Figure 7.23
250	5 of 1287cm <sup>-1</sup>	Figure 14, Appendix 15
225	6 of 1287cm <sup>-1</sup>	Figure 15, Appendix 15
200	11 of 1287cm <sup>-1</sup>	Figure 7.24
80	13 of 1287cm <sup>-1</sup>	Figure 16, Appendix 15
60	22 of 1287cm <sup>-1</sup>	Figure 7.25
40	18 of 1287cm <sup>-1</sup>	Figure 7.26

The spectrum in figure 7.23 was recorded with a quartz-based surface fabricated with a 250 nm thick sputtered silver layer which was exposed to the headspace vapour from the explosive. Raman spectra were recorded with  $t_i = 10$  seconds. The O-NO<sub>2</sub> symmetric stretching mode at 1287 cm<sup>-1</sup> (S/N was ~ 15) and the O-CH<sub>2</sub> vibration at 1466 cm<sup>-1</sup> could be identified. The C-C-C deformation mode at 621 cm<sup>-1</sup> and the O-NO<sub>2</sub> rocking vibration at 536 cm<sup>-1</sup> were also visible. The normally strong C-C stretch at 869 cm<sup>-1</sup> was hidden in the background noise and could not be clearly identified.

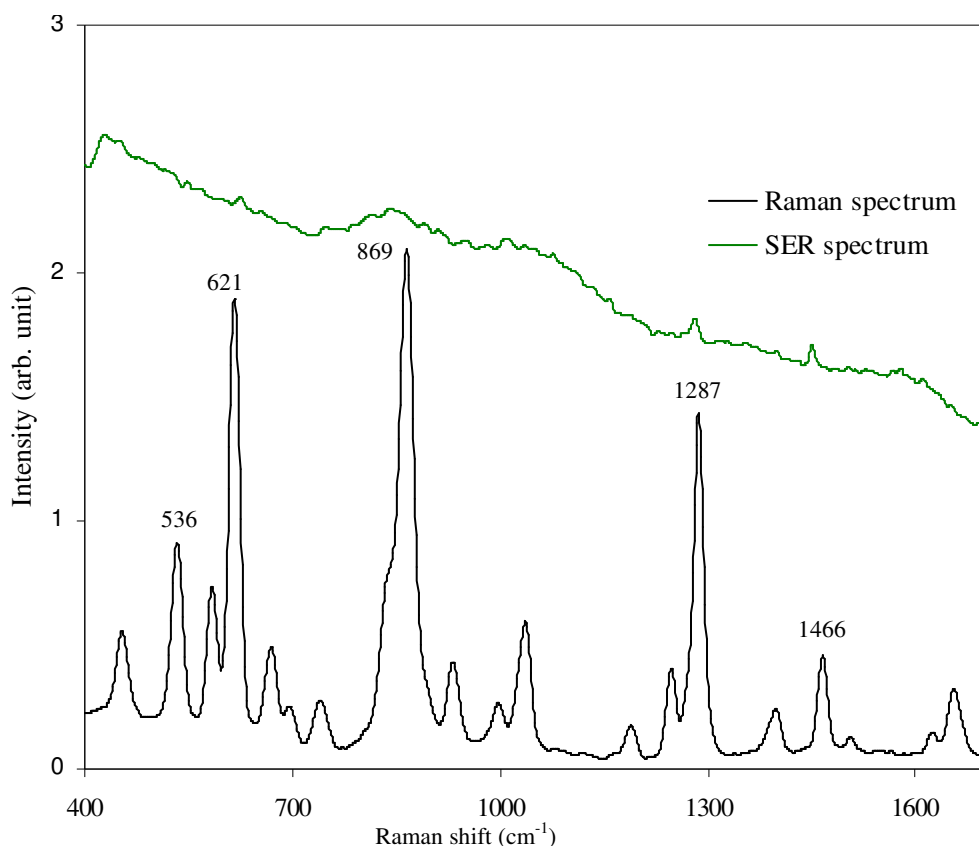


Figure 7.23 Normal Raman spectrum of solid PETN and its SER spectrum recorded from a quartz-based surface having 250 nm high silver structures, exposed to the headspace vapour.

With a surface having a silver structure height of 200 nm, the result of detection is shown in figure 7.24. All conditions of sample presentation and Raman measurements were kept the same as above. The characteristic O-NO<sub>2</sub> symmetric stretching mode at 1287 cm<sup>-1</sup> had S/N of 11. The C-C stretch at 869 cm<sup>-1</sup> was also observed.

In the LSPR region, the S/N slightly improved. Figure 7.25 shows the SER spectrum from a surface having 60 nm high silver structures recorded with  $t_i = 10$  seconds. Sample presentation condition were kept the same. The characteristic O-NO<sub>2</sub> symmetric stretching mode at 1287 cm<sup>-1</sup> had a S/N of ~ 22. The C-C stretch at 869 cm<sup>-1</sup> and the C-C-C deformation at 621 cm<sup>-1</sup> were also present.

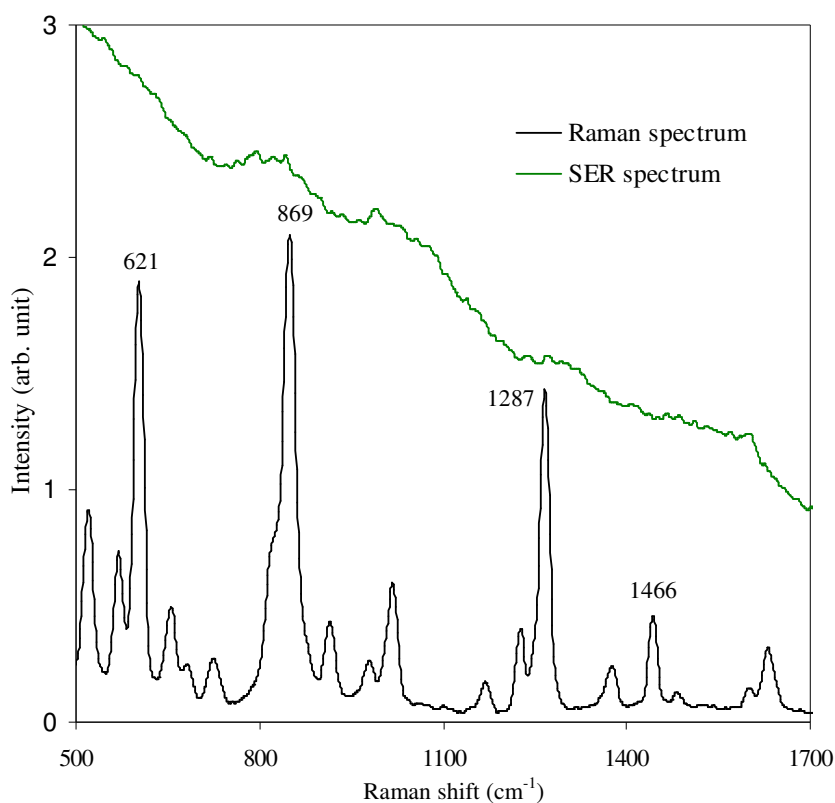


Figure 7.24 Normal Raman spectrum of solid PETN and its SER spectrum of surface having 200 nm high silver structures, exposed to the headspace vapour.

A surface with 40 nm high structures and the same conditions of sample presentation and Raman measurements showed similar results (figure 7.26). The S/N reduced to 18 for the characteristic O-NO<sub>2</sub> symmetric stretching mode at 1287 cm<sup>-1</sup> but the C-C stretch at 869 cm<sup>-1</sup> and C-C-C deformation at 621 cm<sup>-1</sup> appeared stronger in the SER spectrum.

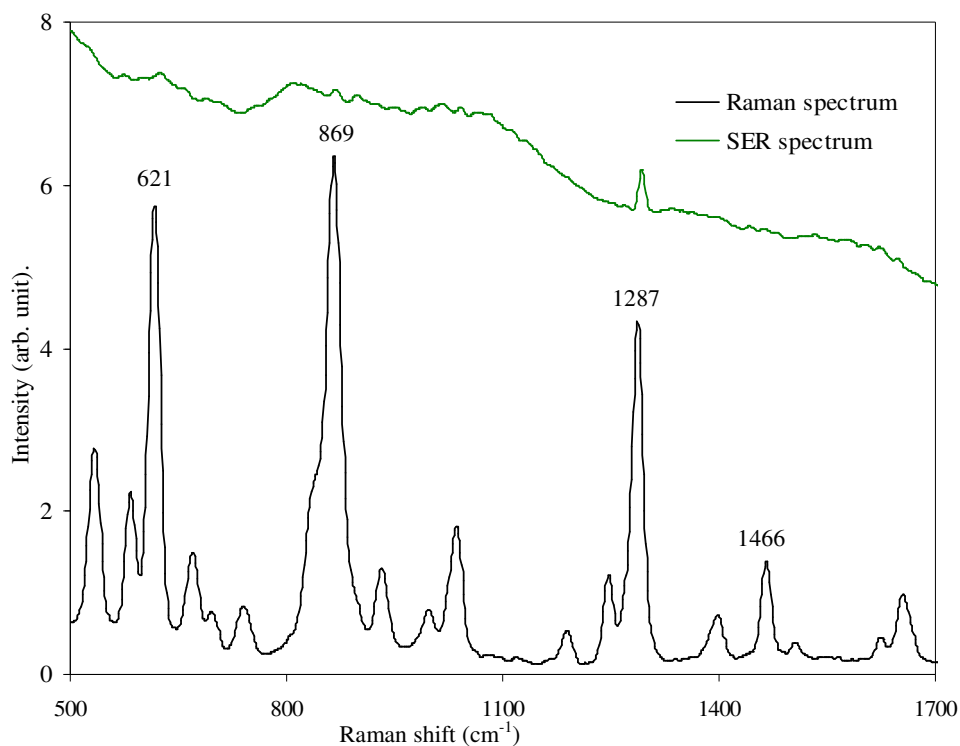


Figure 7.25 Normal Raman spectrum of solid PETN and its SER spectrum of headspace vapour from a surface having 60 nm high silver structures.

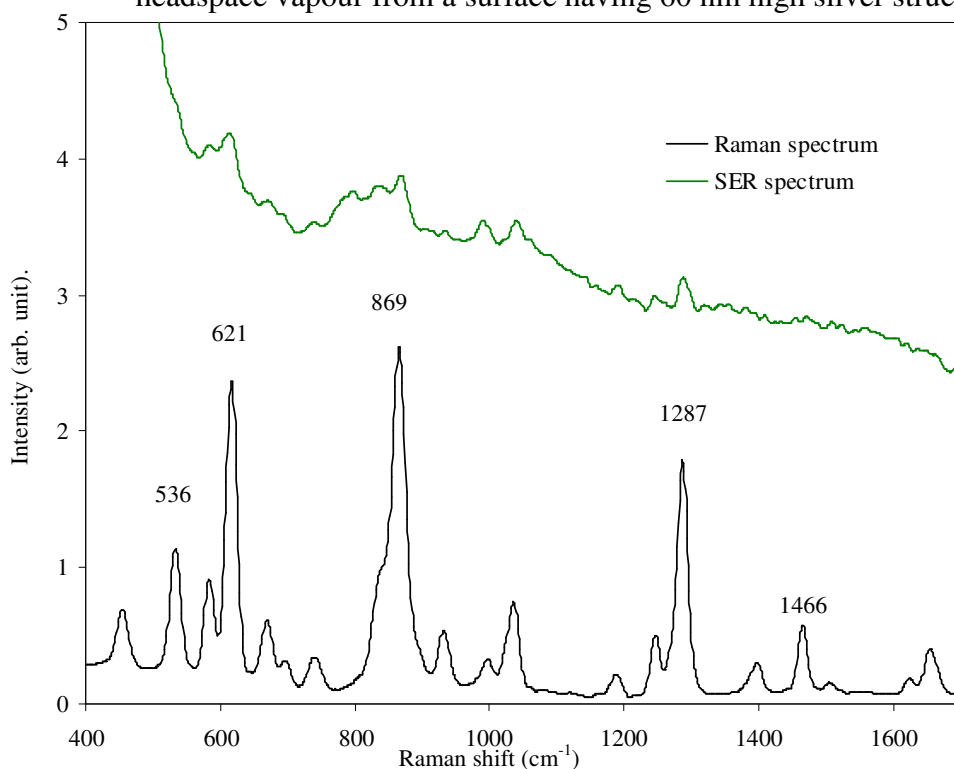


Figure 7.26 Normal Raman spectrum of solid PETN and its SER spectrum from headspace vapour from a surface having 40 nm high silver structures.



## 7.7 Photo-desorption

The adsorbed molecules on the SER-active surfaces may be dislodged from the surface if the photon energy of the laser is more than the binding energy of the molecules to the surface. The process is known as photo-desorption<sup>49</sup> and was discussed in Chapter 2. Experimentally, the process of desorption is very difficult to monitor during the SERS analysis, especially if a high power laser is being used (as in our case; 200 mW). The process depends not only upon the adsorption efficiency of the surface for the target molecule but also upon the molecular adsorption properties and the concentration of molecules adsorbed. At high laser power levels, the rate of desorption may become too high and cause the molecules to evaporate off the surface before any meaningful measurements can be made. Therefore, the study of the photo-desorption process may be possible when the desorption is a gradual process rather than being completed on the first interaction with the laser. In the gradual process Raman signals can be monitored by recording consecutive spectra without changing the sample and equipment parameters. Each consecutive spectrum will then show the changes in concentration of adsorbed molecules as all the other variables remain the same.

The photo-desorption process was experimented on using a quartz based substrate prepared with a 250 nm high silver structure ( $h$ ), exposed to  $10^{-2}$  M pyridine solution for 10 seconds. SER spectra were recorded with  $t_i = 10$  seconds with 10 seconds gap in between the two consecutive spectra (for dark spectrum recording). Total of 52 spectra were obtained and analysed for the  $990\text{ cm}^{-1}$  ring breathing mode peak intensity. The results showed that initially the peak intensity increased for up to 13 readings and then started to decrease to reading number 52. The twelve results of initial increase are shown in figure 7.27, where the lowest spectrum is the 1<sup>st</sup> and the 13<sup>th</sup> is the top most with the highest intensity.

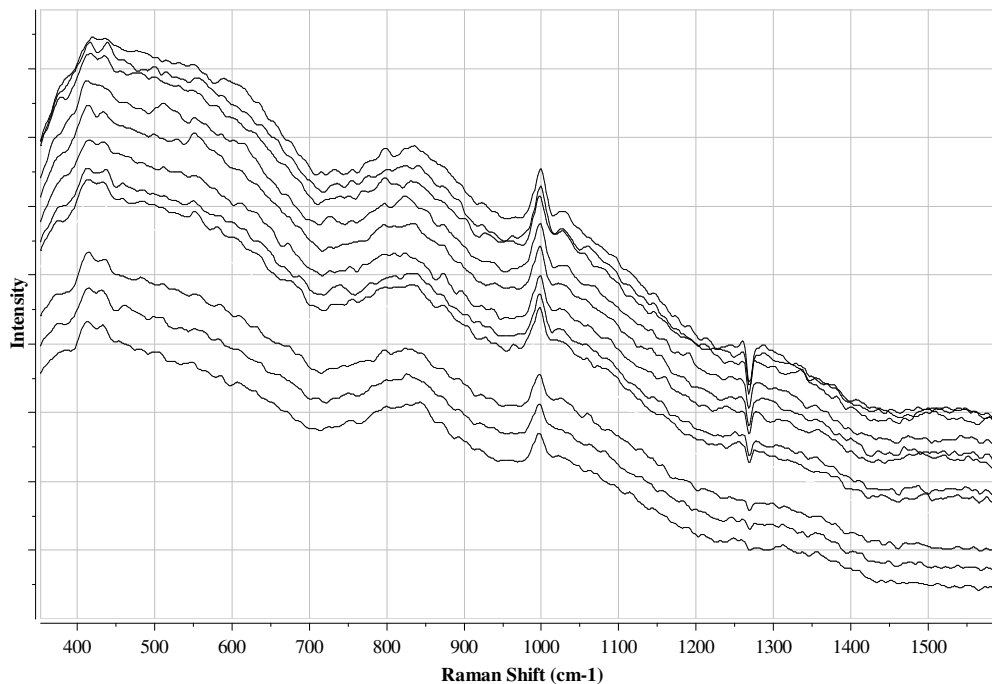


Figure 7.27 SER spectra showing an initial increase in the peak intensity of the pyridine with the decrease in the quantity of adsorbed molecules.

Likewise the desorption phase is shown in figure 7.28, in which the topmost is the 13<sup>th</sup> spectrum having the highest peak intensity and the subsequent spectra show decreasing intensity down to the 52<sup>nd</sup> reading at the bottom.

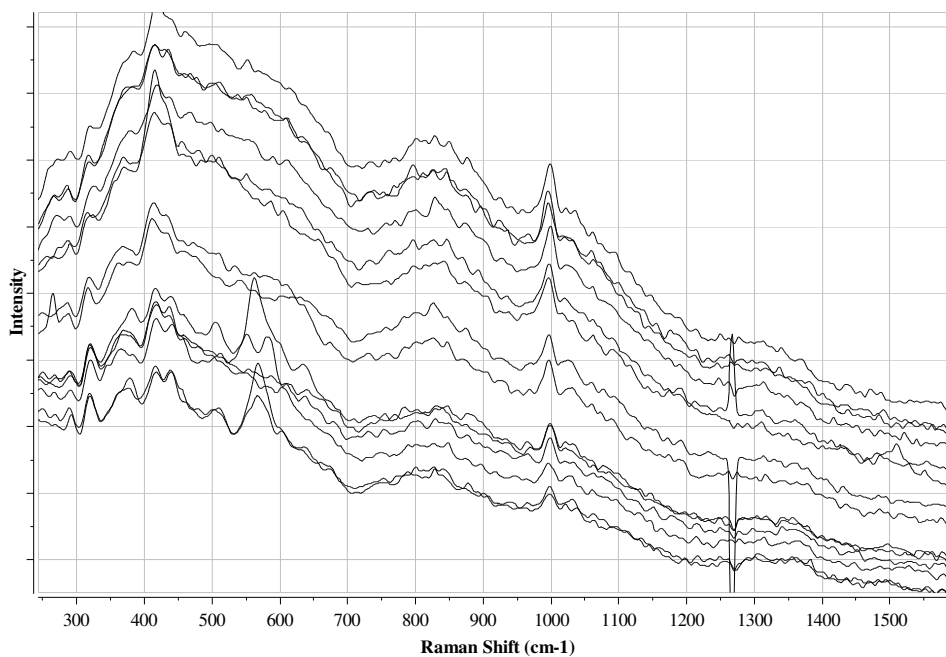


Figure 7.28 SER spectra showing a decrease in the peak intensity of the pyridine with the decrease in the quantity of adsorbed molecules.

The results present a better picture when these spectra are observed together. Therefore, spectrum number 1, 6, 13, 21, 31, 41 and 52 are shown in figure 7.29 and are marked from 1 to 7 respectively. Note that the peak intensity of the ring breathing mode at  $990\text{ cm}^{-1}$  increases from spectrum 1 to 3 and then decreases until it is a minimum in spectrum 7. The differences in peak intensity are the measure of the molecular concentration adsorbed on the surface. Table 7.8 gives the peak intensity differences for the ring breathing mode at  $990\text{ cm}^{-1}$  among the spectra shown in figure 7.29. These changes are directly related to the time of the laser exposure.

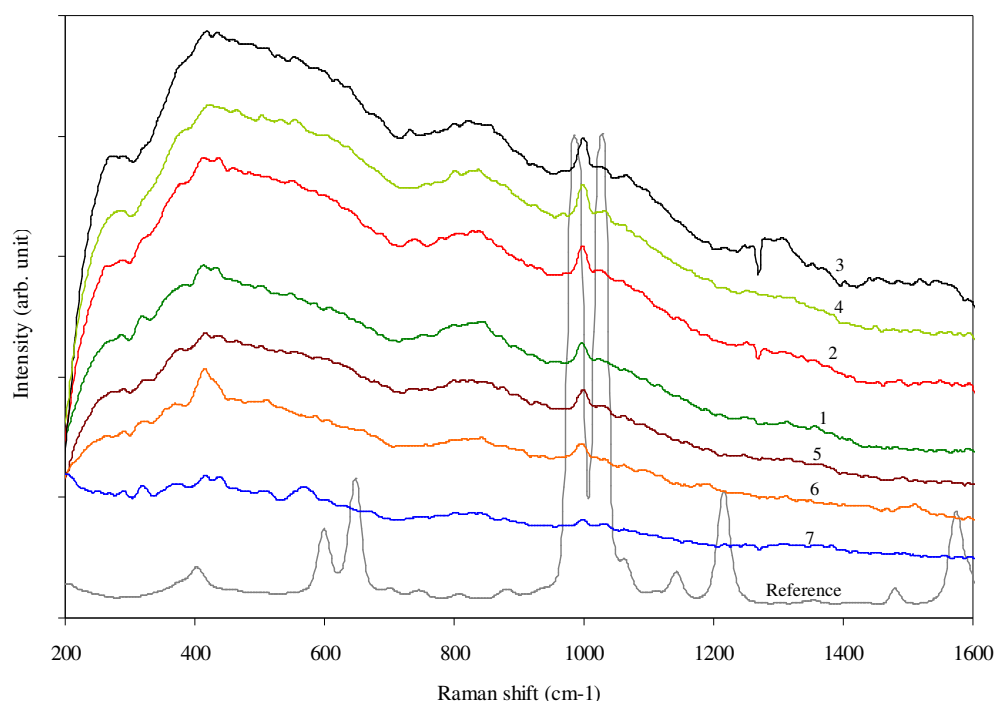


Figure 7.29 Consecutive SERS spectra of pyridine showing initial increase and subsequent decrease in the peak intensity due to desorption effect.

Table 7.8 Some of the peak intensity changes due to the desorption of pyridine molecules from the SER surface.

Index	Spectrum #	Laser exposure (seconds)	Peak intensity (cps)	Peak Intensity/ exposure time (cps/sec)
1	1	10	80.5	8.05
2	6	60	116.9	1.96
3	13	130	135.9	1.05
4	21	210	129.7	0.62
5	31	310	77.4	0.25
6	41	410	52.4	0.13
7	52	520	28.7	0.06

The table indicates that the intensity increases for a laser exposure of up to 130 seconds and then it starts to decrease for further increase of exposure up to 520 seconds. The trend is graphically shown in figure 7.30. With the experimental condition kept constant, these changes in the peak intensity are mainly related to the concentration of molecules adsorbed on the substrate. The initial increase might be due to the desorption of pyridine molecules that had saturated the surface, denying direct access to the molecules within the surface plasmon. After 130 second exposure the number of molecules adsorbed on the surface is likely to be the maximum possible that could give the best Raman intensity. Thereafter, the number of molecules started to decrease with every laser exposure until very few molecules remain adsorbed on the surface after 520 seconds of exposure. Complete removal of molecules was not achieved even after 520 seconds of a 200mW laser exposure.

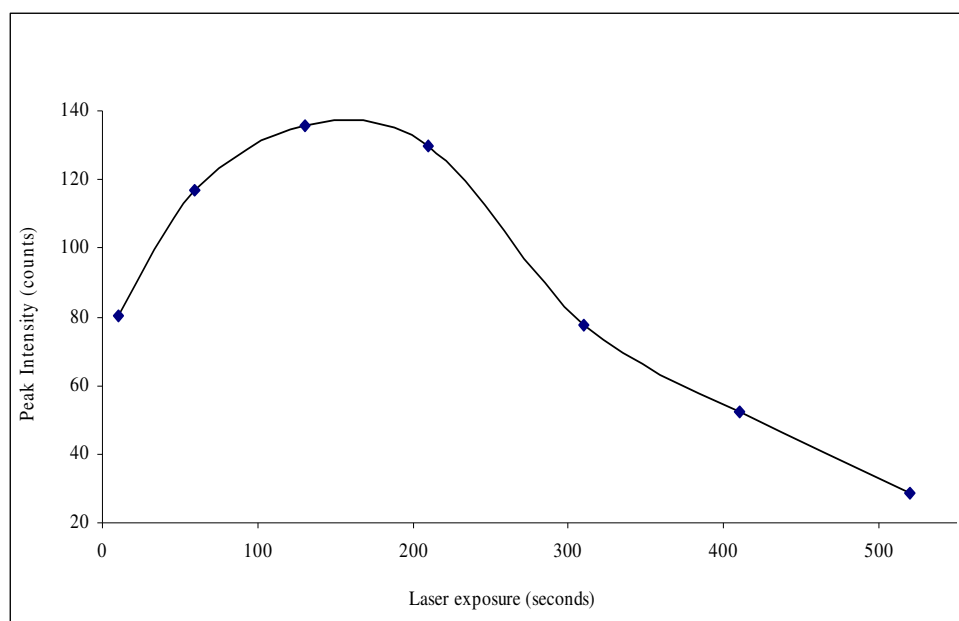


Figure 7.30 The initial increase and subsequent decrease in the peak intensity of the pyridine vapour adsorbed on a SER surface (quartz-based substrate) with the increase in duration of laser exposure.

The desorption process is likely to follow the trend shown in the last column of table 7.8. There is a change in the Raman intensity with the exposure of the surface to the laser. Figure 7.31 shows the desorption of molecules adsorbed on the surface (in terms of the decreasing Raman intensity) with the increasing laser exposure. The results show

that the desorption process slowed down with the decrease in the number of adsorbed molecules on the surface. It is likely that the first layer molecules have greater force of adsorption than the subsequent layers and became difficult to dislodge.

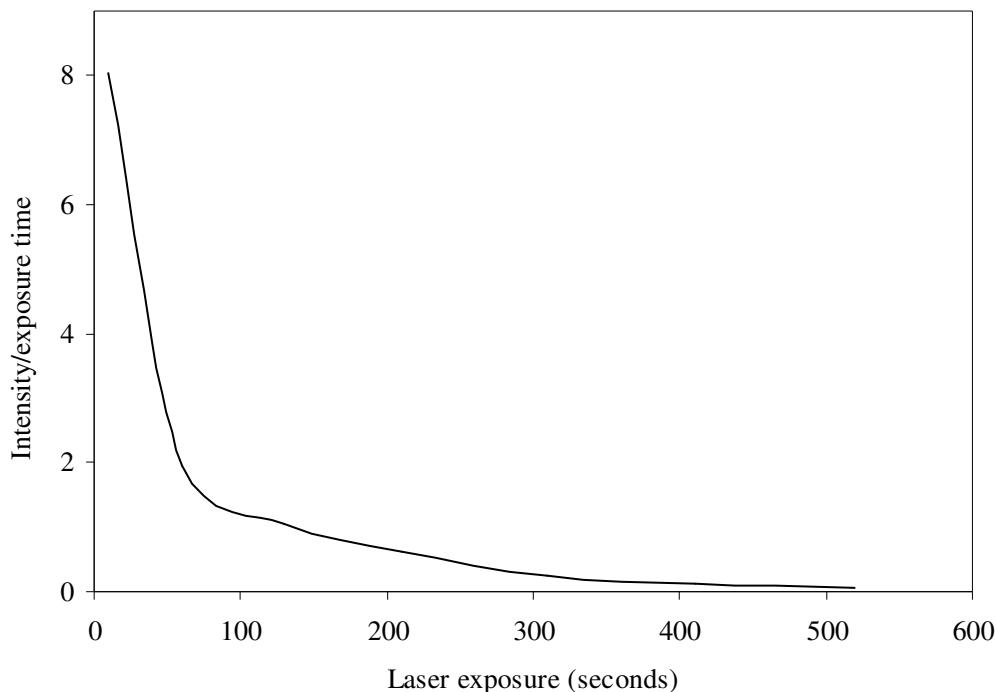


Figure 7.31 The removal of pyridine molecules from the quartz-base surface shown in term of decreasing Raman intensity with the increasing exposure to the laser radiation.

## 7.8 Heat desorption

Desorption of the analyte molecules adsorbed on the SER-active surfaces is an important property, especially for the reusability of the fabricated surfaces. Our experiments to observe desorption of molecules from the SER-active surfaces remained inconclusive. The major factor is that the progress of desorption could only be recorded by taking periodical Raman measurements, each of which required laser irradiation of the surface. Laser irradiation of the surface itself generated heat that might wholly or partially become responsible for the desorption of analyte molecules from the surface. The whole process becomes very complex where, at least, all the major factors that may contribute towards the desorption of molecules had to be separately evaluated and only the effect of heat could be measured. The desorption is an important aspect of SERS,

especially when considering the reusability of the fabricated surface. Therefore, it would remain an important research direction for any future endeavour.

## 7.9 Summary

The substrate preparation protocol used with ordinary glass substrates was found to be also suitable for quartz substrates with minor modifications. Larger domain sizes of arrays of silver nano-structures were comparatively easy to achieve with direct PNS assembly on a substrate than with those having silver underlayer. Surfaces produced by NSL on quartz-based substrates provide a high quality of SER-active surfaces that showed reproducibility with a very high sensitivity for detection of vapours from explosives. Surfaces fabricated with the heights of silver nano-structures from 40 to 300 nm were found to have similar shape and size. Surfaces with the height of the nano-structures within the predicted region that support LSPR showed some evidence of further enhancement in a few cases.

Once the SER-active surface was fabricated, it could simply be exposed to the vapours from the explosive for detection. Such a system is favourable for detection of concealed explosives. The detection of explosives at trace level was possible with single scan of 10 seconds (or less) without the need for long time data averaging to increase the S/N. The concentration of PETN molecules in the headspace at equilibrium vapour pressure was around 18 ppt. The headspace concentration at equilibrium vapour pressure for both peroxide explosives; TATP and HMTD was around 70 ppm and 0.29 ppm respectively.

Experiments conducted to evaluate the possibility of desorption of molecules from the SER-active surface by laser irradiation showed that the Raman intensity from the adsorbed molecules decreased with the increasing laser exposure. With all parameters kept constant, the Raman intensity gave the direct measure of the number of molecules adsorbed on the surface. It also showed that the Raman intensity was lower than the maximum when the adsorbed molecules were more than an optimum number. Therefore, SER scatterings originating from the metal-molecule complex are maximum when first layer (or first few layers) of adsorbed molecules are being investigated.

## 8. CONCLUSIONS AND RECOMMENDATIONS

### 8.1 Conclusions

A protocol was conceived, developed and experimentally validated for the ultra-sensitive detection of explosives with surface enhanced Raman spectroscopy. The explosives were detected in the open laboratory environment with a portable Raman spectrometer in 10 seconds or less time at trace level concentrations. The protocol for the preparations of an effective nano-structured surfaces and its use for SERS is considered to be suitable for field use without the need for any special sample preparation. Detection of explosives, pentaerythritol tetranitrate (PETN), hexamethylene triperoxide diamine (HMTD) and triperoxide triacetone (TATP), from their headspace vapour emanating from the solid samples, albeit having very low vapour pressure and molecular concentrations, has been demonstrated.

In this research the focus has been on the fabrication of SER-active surfaces as in the case of a typical SERS work. The structures prepared with the nanosphere lithographic (NSL) process, on both glass and the quartz substrate, were found to give the desired enhancement in Raman scatterings. The characterisation of glass-based surfaces showed a very high background noise that prevented any useful analysis. But its modification with a thin silver layer before or after the PNS application was found to reduce the background noise to a workable S/N. Both modifications had their down sides, the former for difficulty in achieving monolayer of nanospheres due to the decreased hydrophilic nature of the silver coated surface and the latter for the reduction of sharp metal edges that are considered to be vital for sensitive SERS analysis.

Quartz-based surfaces, on the other hand were found to be free from these problems. After the initial difficulties of monolayer application of PNS were overcome, these surfaces were morphologically similar to the basic glass-based surfaces and much better in reproducibility, enhancement and ease of fabrication. These surfaces were finally used for the explosive vapour detection.

Both the glass and the quartz-based surfaces were found to show very high enhancement in Raman scatterings. Pyridine and nitrobenzene could be detected by exposing the surface to their headspace vapour for as short a time as 10 seconds in ambient conditions. Headspace vapours from explosives were also detected using both glass and quartz-based surfaces. PETN with a very low vapour pressure had a molecular concentration of 18 ppt in the headspace vapour, whereas, HMTD and TATP were detected with headspace concentrations of 0.29 ppm and 70 ppm respectively. The detection of these explosives in the vapour phase within 10 seconds of analysis was possible with a very high enhancement mechanism presented by SERS. Such a fast and sensitive detection of explosives by a portable system shows the immense potential of the technique in field applications.

The performance of SER-active surfaces prepared with the NSL method was far superior to the surfaces prepared with other techniques discussed in chapter 5. Acid etching of silver slabs also produced surface morphology that supported SERS. Such surfaces had structures with height ranging approximately from 300 nm to beyond 1000 nm depending upon the duration of etch. PETN was detected when a small amount of PETN solution (0.5% in acetone) was put on an etched slab. The SER spectrum of PETN was recorded on the slab's surface after the solvent evaporated and the surface was washed with tri-distilled water (TDW) for any residues on the surface. Thin silver films on glass surfaces remained smooth in all the roughening techniques used. However, when such a surface was drop coated with a small quantity of PETN solution (1% in acetone or butanone), the surface morphology showed extensive roughness in the 300-600 nm region, making the surface SER-active. PETN was detected from such a surface after the solvent had evaporated.



The work on the parallel surface fabrication technique using metal colloids was found to be very sensitive. Metal colloids were prepared with both silver and gold salts with three different techniques. Pyridine was detected at the concentration of  $10^{-11}$  M using the gold colloids. Although this technique was found to give very high enhancement with quantifiable parameters of detection, the long analysis time, extensive sample preparation and sensitive methods of fabrication precluded its use for field applications. Nevertheless its application in ultra sensitive chemical analysis within the laboratory cannot be ignored.

The high sensitivity of SERS for detection of explosives has been demonstrated and has also been supported by the published work. Further enhancement in the SERS was also found to be possible with the introduction of the resonance effect. The process becomes laser wavelength dependent and is possible when it coincides with either the surface plasmon of the metal surface or is near an isolated absorption line of the analyte or both. The technique of SERRS is expected to be more sensitive than the normal SERS but then a setup has to be either surface plasmon specific or the analyte specific.

Both the possibilities for above perspective were experimentally evaluated. The resonance Raman of PETN explosive showed the enhancement in the Raman intensity by using the incident laser wavelength in the near resonance region. The enhancement of up to a factor of 7 was observed in the Raman intensity for less than 60 nm change in the laser wavelength in the mid resonance region of PETN.

## 8.2 Recommendations for future work

The field of surface enhanced Raman spectroscopy is still an active research field with many of its aspects not clearly explained so far. Therefore, much can be done for further exploitation of this technique that is otherwise well known for its potentialities in sensitive chemical analysis.

- Local surface plasmon resonance (LSPR) excitation of the fabricated SER-surface is believed to play an important role in defining the limits of sensitivity.

The fabrication and characterisation of the surfaces configured to a specific laser wavelength to be used is likely to unleash the full potential of the SERRS technique.

- In any experiment with SER-active surfaces where the molecules from the headspace vapour are being used as analyte, the precise calculation of the number of molecules responsible for Raman scattering becomes very complex. If the whole process is calibrated to calculate the enhancement factor for Raman intensity of a given SERS setup, an approximate quantification system can then be developed to predict the molecular concentration.
- The reusability of the SER-active surface would eliminate the need for fabricating a large number of surfaces for replacement after each use and save the precious time needed for their replacement for a new analysis. Thermal or photo desorption processes are simple techniques that have shown the capability of dislodging an adsorbed species from the metal surface.
- The high sensitivity afforded by the SERS technique allows analysis of chemical compounds at very low concentrations. A further increase in sensitivity is possible by selecting a laser in the near resonance region of the adsorbed molecule. For a SERS system being designed for the detection of specific explosives, the sensitivity can be further improved using the SERRS process by carefully selecting the laser line.
- The inherent geometrical defects in the SER-active surfaces fabricated with the NSL process limits the size of the defect-free domains to a few square microns. The use of a standard background for subtraction is therefore not possible, especially when using the laser having a diameter of ~0.1 mm. The possibility of standardising the background by increasing the defect-free domain and by using Raman microscopes to target that region, might enable the S/N to be increased with further reduction in the time of analyses.

## REFERENCES

1. Shea DA, Morgan D. *Detection of Explosives on Airline Passengers: Recommendation of the 9/11 Commission and Related Issues*. CRS Report for Congress: RS21920, 2005.
2. U.S. Congress, Office of Technology Assessment, *Technology Against Terrorism: The Federal Effort, OTA-ISC-481* Washington, DC: U.S. Government Printing Office; 1991.
3. Davies R. Terrorist Prevention: Technology versus Terrorism. *Jane's International Defence Review*; 2001.
4. Syed AA. Explosive detection methods. *Explosive Ordnance Engineering MSc thesis. RMCS, Cranfield University*. 1994.
5. Rhykerd CL, Hannum DW, Murray DW, Parmeter JE. Guide for the Selection of Commercial Explosives Detection Systems for Law Enforcement Applications. *Report by US National Institute of Justice*. 1999; NIJ Guide 100-99.
6. Singh S, Singh M. Explosives detection systems (EDS) for aviation security. *Signal Processing*. 83, 1, 2003, 31-55.
7. Yinon J. Field detection and monitoring of explosives. *Trends in anal. Chem.* 2002; 21, 4, 292-301.
8. Report. *Committee on the Review of Existing and Potential Standoff Explosives Detection Techniques*. The National Academies Press Washington: DC, 2004.
9. McCreery RL. *Raman Spectroscopy for Chemical Analysis*. John Wiley & Sons Ltd:

- 2000.
10. Kawai NT, Spencer KM. Raman Spectroscopy for Homeland Defense Applications. *Raman Technology for today's Spectroscopics*. 2004; 54-58.
  11. Christesen SD, Lochner JM, Hyre AM, Emge DK. UV Raman spectra and cross sections of chemical agents. *Chemical and Biological Sensing. Proceedings of SPIE*; 6218: 2006.
  12. Ruffel A. Remote detection and identification of organic remains: An assessment of archaeological potential. *Archaeological Prospection*. 2002; 9: 115-122.
  13. Smith E and Dent G. *Modern Raman Spectroscopy: A Practical Approach*. John Wiley & Sons Ltd: 2005.
  14. Lewis ML, Lewis IR, Griffiths PR. Anti-Stokes Raman Spectrometry with 1064-nm Excitation: An Effective Instrumental Approach for Field Detection of Explosive. *Applied Spectroscopy*. 2004; 58: 4.
  15. Lewis IR, Daniel NW. Raman spectroscopic studies of explosive materials: towards a fieldable explosives detector. *Spectrochimica Acta Part A*. 1995; 51.
  16. Haywood I, Kirbride TE, Batchelder DN, Lacey RJ. Use of a Fiber Optic Probe for the Detection and Identification of Explosive Materials by Raman Spectroscopy. *J. of Forensic Science*. 1995; 40, 5: 883- 884.
  17. Carter JC, Angel SM, Snyder ML, Scaffidi J, Whipple RE, Reynolds JG. Standoff Detection of HE Materials in ambient light conditions using a small Raman instrument. *Applied Spectroscopy*. 2005; 59: 6.
  18. Nafie LA. Theory of resonance Raman optical cavity: the single electronic state limit. *Chemical Physics*; 1996, 205: 309-322.
  19. Greek SL, Schulze HG, Blades MW, Haynes CA, Klein KF, Turner RFB. Fiber-Optic Probes with Improved Excitation and Collection Efficiency for Deep-UV Raman and Resonance Raman Spectroscopy. *Applied Optics*. 1998; 37, 1: 170-180.
  20. Moore DS. Determination of energetic materials in soil using multivariate analysis of Raman spectra. *J. Anal Chem*. 2001; 369: 393-396.
  21. Lewis ML, Lewis IR, Griffiths PR. Evaluation of a dispersive Raman spectrometer with a Ge array detector and a 1064 nm laser for the study of explosives. *Vib Spectr*.

- 
- 2005; 38: 11-16.
22. Lewis ML, Lewis IR, Griffiths PR. Raman Spectroscopy of Explosive with no moving parts fiber coupled spectrometer; A comparison of excitation wavelength. *Vib. Spectr.* 2005; 38: 17-28.
  23. Zhang Y, Seitz WR, Grant CL. A Clear; amine-containing poly(vinyl chloride) membrane for in situ optical detection of 2,4,6- trinitrotoluene. *Anal. Chimica Acta.* 1989; 217: 217-227.
  24. Zhang Y, Seitz WR. Single Fiber Absorption Measurements For Remote Detection Of 2,4,6-Trinitrotoluene. *Anal Chimica Acta.* 1989; L-9: 221.
  25. Jian C, Seitz WR. Membrane For In Situ Optical Detection Of Organic Nitro Compounds Based On Fluorescence Quenching. *Anal Chimica Acta.* 1990; 231: 265-211.
  26. Medary RT. Inexpensive, Rapid Field Screening Test For 2,4,& Trinitrotoluene In Soil. *Anal. Chunica Acta.* 1992; 258: 341-346.
  27. Ewing RG, Miller CJ. Detection of Volatile Vapors emitted from Explosives with a hand held IMS. *F. Anal. Chem. Tech.* 2001; 5(5); 215-221.
  28. Sohn H, Sailor MJ, Madge D, Trogger WC. Detection of Explosive based on photoluminescent polymers containing Metalloles. *J. Am. Chem. Soc.* 2003; 125: 3821-3830.
  29. Keith JA, Walt DR. High-Speed Fluorescence Detection of Explosives-like Vapors. *Anal. Chem.* 2000; 72: 1947-1955.
  30. Renishaw. *Application note from the Spectroscopy Products Division.* SPD/AN/098 2004; Issue 1.
  31. Von-Dinh T, *Oak Ridge National Laboratory; Fact Sheet:* [www.ornl.gov. http://www.ornl.gov/sci/eere/PDFs/FactSheet\\_Ramits\\_ORNL.pdf.](http://www.ornl.gov/sci/eere/PDFs/FactSheet_Ramits_ORNL.pdf)
  32. Sharma SK, Misra AK, Sharma B. Portable remote Raman system for monitoring hydrocarbon, gas hydrates and explosives in the environment. *Spectrochimica Acta Part A.* 2005; 61: 2404–2412.
  33. Moore DS. Comparative IR and Raman spectroscopy of energetic polymers. *J. Mol. Struc.* 2003; 661-662: 561-566.
-

- 
34. Gupta N, Dahmani R. AOTF Raman spectrometer for remote detection of explosives. *Spectrochimica Acta A*. 2000; 56: 1453–1456.
  35. Cheng C, Kirbride TE, Batchelder DN, Lacey RJ, Sheldon TG. In situ trace detection of Explosives by Raman Spectroscopy. *J. forensic Science*. 1995; 40:1.
  36. Wu DY, Ren B, Tian ZQ. Progress in the theory of Surface Enhanced Raman Scattering. *Internet J. Vib. Spectros*. 2000; 4: 2.
  37. Suetaka W, Yates Jr JT. *Surface Infraed and Raman Spectroscopy; Methods and Application*. Plenum Press: NY, 1995.
  38. Tian ZQ. Surface-enhanced Raman spectroscopy: advancements and applications. *J. Raman Spectrosc*. 2005; 36: 466–470.
  39. Kniepp K. SERS; A new tool for single molecule detection and identification. *Bioimaging*. 1998; 6: 104-110.
  40. Hicks CJ. *Surface Enhanced Raman Spectroscopy*. MSU CEM 924; 2001.  
<http://www.cem.msu.edu/~cem924sg/ChristineHicks.pdf>.
  41. Chang RK, Furtak TE. *Surface Enhanced Raman Scattering*. Plenum; 1982.
  42. Moskovits M. Surface-enhanced Raman spectroscopy: a brief retrospective. *J. Raman Spectrosc*. 2005; 36: 485–496.
  43. Haynes CL, Yonzon CR, Zhang X, Van Duyne RP. Surface-enhanced Raman sensors: early history and the development of sensors for quantitative biowarfare agent and glucose detection. *J. Raman Spectrosc*. 2005; 36: 471–484.
  44. Champion A, Kambhampati P. Surface Enhanced Raman Scattering. *Chem. Soc. Rev*. 1998; 27.
  45. Grabhorn H, Otto A. What determines the selection rules of SERS. *Vacuum*. 1990; 41, 1-3: 473-475.
  46. Moskovits M. Surface-enhanced Spectroscopy. *Rev. of modern phys*. 1985; part 1, 57, 3.
  47. Garcia-Vidal FJ, Pendry JB. Collective theory of Surface Enhanced Raman Spectros. *Phys. Rev. Letter*. 1996; 77, 6, 1163-1167.
  48. D.J. Gardiner, P.R. Graves. *Practical Raman Spectros*. Springer – Verlag: 1989.
  49. Aroca R. *Surface-Enhanced Vib. Spec*. Wiley; 2006.
-

- 
50. Kneipp K, Kneipp H, Itzkan I, Dasari RR, Feld MS. Surface-enhanced Raman scattering and biophysics. *J. Phys. Condens. Matter.* 2002; 14: R597–R624.
  51. Kim, NH, Kwan K. Surface-enhanced resonance Raman scattering of rhodamine 6G on Pt nanoaggregates. *J. Raman Spectrosc.* 2005; 36(6/7): 623-628.
  52. Olubotko AM. Some anomalies of the SER spectra of symmetrical molecules adsorbed on transition metal substrates: Consideration by the dipole-quadrupole SERS theory. *J. Raman Spectrosc.* 2005; 36(6/7): 522-532.
  53. Klug O, Parlagh GY, Forsling W. Raman and surface-enhanced Raman spectroscopy of adsorbed phthalic acid on oxidized aluminum foil. *AIP Conf. Proc.* 1998; 430: 614-617.
  54. Roy D, Barber ZH, Clyne TW. Ag nanoparticle induced surface enhanced Raman spectroscopy of chemical vapor deposition diamond thin films prepared by hot filament chemical vapor deposition. *J. Appl. Phys.* 2002; 91: 9.
  55. Sanchez-Cortes S., Garcí'a-Ramos JV. Influence of coverage in SERS of cytosine. *Surface Science.* 2001; 473.
  56. Rivas L. Sanchez-Cortes S, Garcia-Ramos JV, Morcillo G. Growth of Silver colloidal particle obtained by Citrate Reduction to increase the Raman enhancement factor. *Langmuir.* 2001; 17: 574-577.
  57. Kunduy S, Hazray S, Banerjee S, Sanyaly MK, Mandalz SK, Chaudhuriz S, A K Palz. Morphology of thin silver film grown by dc sputtering on Si(001). *J. Phys. D: Appl. Phys.* 1998; 31: L73–77.
  58. Jenson TR, Malinsky MD, Hayes CL, Van Duyne RP. Nanosphere Lithography: Tunable Localised Surface Plasmon Resonance Spectra of Silver Nanoparticles. *J. phys. Chem. B.* 2000,104,10549-10556.
  59. Sanchez-Cortes S., Garcí'a-Ramos JV. Anomalous Raman Bands Appearing in Surface-Enhanced Raman Spectra. *Journal of Raman Spectroscopy. J.Raman Spectrosc.* 1998; 29: 365-371.
  60. Socrates G. *Infrared and Raman Characteristic Group Frequencies; Tables and Charts.* Wiley; 2004.
  61. Guo, Groza M, Burger A, Mu R, Morgan SH. Surface-Enhanced Raman
-

- 
- Spectroscopy Using Silver-Coated Porous Glass-Ceramic Substrates. *Appl. Spectrosc.* 2005; 59, 6: 782-786.
62. Viets C, Hill W. Fibre-optic SERS sensors. *Int. J. Vib. Spect.* 2000; 4, 2, 8.
63. Rivas L, Sanchez-Cortes S, Garcia-Ramos JV, Morcillo G. Mixed Silver/Gold Colloids: A Study of Their Formation, Morphology, and Surface-Enhanced Raman Activity. *Langmuir.* 2000; 16: 9722-9728.
64. Perez R, Ruperez A, Rodriguez-Castell E, Laserna JJ. Study of experimental parameters for improved adsorbate detectability in SERS using etched silver substrates. *Surf. Interface Anal.* 30, 592–596 (2000).
65. Bao LL, Mahurin SM, Liang CD, Dai S. Study of silver films over silica beads as a surface-enhanced Raman scattering (SERS) substrate for detection of benzoic acid. *J. Raman Spectrosc.* 2003; 34: 394–398.
66. Lewi IR, Edwards HGM. *Handbook of Raman Spectroscopy.* Marcel Dekker Inc. 2001.
67. Littleford RE, Cunningham D, Matousek P, Towrie M, Parker AW, Khan I, McComb DW, Smith E. Surface-enhanced resonance Raman scattering using pulsed and continuous-wave laser excitation. *J. Raman Spectrosc.* 2005; 36: 600–605.
68. Leyton P, Sanchez-Cortes S, Garcia-Ramos JV, Domingo C, Campos-Vallette M, Saitz C, Clavijo RE. Selective Molecular Recognition of Polycyclic Aromatic Hydrocarbons (PAHs) on Calix[4]arene-Functionalized Ag Nanoparticles by Surface-Enhanced Raman Scattering. *J. Phys. Chem. B.* 2004; 108: 17484-17490.
69. Millan JI, Ramos JVG, Sanchez-Cortes S, Rodriguez-Amaro R. Adsorption of lucigenin on Ag nanoparticles studied by surface-enhanced Raman spectroscopy: effect of different anions on the intensification of Raman spectra. *J. Raman Spectrosc.* 2003; 34: 227-233.
70. Leopold N, Lendl B. A New Method for Fast Preparation of Highly Surface-Enhanced Raman Scattering (SERS) Active Silver Colloids at Room Temperature by Reduction of Silver Nitrate with Hydroxylamine Hydrochloride. *J. Phys. Chem. B.* 2003; 107: 5723-5727.
71. Sasic S, Itoh T, Ozaki Y. Detailed analysis of single-molecule surface-enhanced
-



- resonance Raman scattering spectra of Rhodamine 6G obtained from isolated nano-aggregates of colloidal silver. *J. Raman Spectrosc.* 2005; 36: 593-599.
72. Wei G, Zhou H, Liu Z, Li Z. A simple method for the preparation of ultrahigh sensitivity surface enhanced Raman scattering (SERS) active substrate. *Applied Surface Science.* 2005; 240, 260-267.
73. Aroca RF, Goulet PG, Santos DSD, Alvarez-Puebla RA, Oliveira ON. Silver Nanowire Layer-by-Layer Films as Substrates for Surface-Enhanced Raman Scattering. *Anal. Chem.* 2005; 77: 378-382.
74. White DJ, Stoddart PR. Fibre-Optic SERS Sensors with Well-Defined Nanoscale Structures. *19th ICORS proceedings*, Australia; 2004.
75. Brolo AG, Christopher JA. Surface-enhanced Raman scattering from oxazine 720 adsorbed on scratched gold films. *J. Raman Spectrosc.* 2005; 36: 629-634.
76. Drachev VP, Thoreson MD, Nashine V, Khaliullin EN, Ben-Amotz D, Davisson VJ, Shalaev V. Adaptive silver films for surface-enhanced Raman spectroscopy of biomolecules. *J. Raman Spectrosc.* 2005; 36: 648-656.
77. Tominaga J. The application of silver oxide thin films to plasmon photonic devices. *J. Phys: Condens. Matter.* 2003; 15: R1101-R1122.
78. Carvalho AT, Silvaa MLP, Filhoa APN, Jesusb DP, Filho SGS. Improvement on organic compound adsorption and/or detection by using metallic thin films deposited onto highly rough silicon substrates. *Sensors and Actuators B*, 2005; 108, 947-954.
79. Moskovits M, Jeong DH. Engineering nanostructures for giant optical fields. *Chem. Phys. Letters.* 2004; 397, 91-95.
80. Haes AJ, Duyne V, Richard P. A highly sensitive and selective surface-enhanced nanobiosensor. *Materials Research Society Symposium Proceedings.* 2002; 723.
81. Lee PC, Meisel D. Adsorption and Surface enhanced Raman of Dyes on Silver and Gold Solutions. *J. Phys. Chem.* 1982; 86: 3391-3395.
82. Creighton JA, Blatchford CG, Albrecht MG. Raman scattering by Pyridine on AU and AG sols. *Faraday Trans.* 1979; 75: 790.
83. Maruyama Y, Futamata M. Elastic scattering and emission correlated with single-molecule SERS. *J. Raman Spectrosc.* 2005; 36: 581-592.

- 
84. Lee I, Han SW, Kim K. Simultaneous preparation of SERS-active metal colloids and plates by laser ablation. *J. Raman Spectrosc.* 2001; 32: 947-952.
  85. Feng CM, Ge HL, Tong MR, Ye GX, Jiao ZK. Growth behavior and surface morphology of Ag rough thin films deposited on silicone oil surfaces. *Thin Solid Films.* 1999; 342: 30-34.
  86. Re MD, Gouttebaron R, Dauchot JP, Leclère P, Lazzaroni R, Wautelet M, Hecq M. Growth and morphology of magnetron sputter deposited silver films. *Surface and Coatings Technology.* 2002; 86, 90: 151-152.
  87. Suzukia T, Abea Y, Kawamura M, Sasakia K, Shouzub T, Kawamata K. Optical and electrical properties of pure Ag and Ag-based alloy thin films prepared by RF magnetron sputtering. *Vacuum.* 2002; 66: 501-504.
  88. Piersona JF, Wiederkehra D, Billard A. Reactive magnetron sputtering of copper, silver, and gold. *Thin Solid Films.* 2005; 478: 196-205.
  89. Buchel D, Mihalcea C, Fukaya T, Atoda N, Tominaga J. Sputtered silver oxide layers for surface-enhanced Raman spectroscopy. *Appl. Phys. Letters.* 2001; 79, 5.
  90. Weatherby S. Surface Enhanced Raman Spectroscopy. *Faraday Discussions.* 132; 2006.
  91. Kumar CSSR, Hormes J, Leuschner C. *Nanofabrication; Towards Biomedical Applications.* Wiley- VCH, Weinheim. 2005.
  92. Schmid G. *Nanoparticles.* Wiley-VCH, Weinheim. 2004.
  93. Arshak K, Mihov M, Arshak A, McDonagh D, Sutton D. Focused Ion Beam Lithography- Overview and New Approaches. *Proc. 24th International Conference on Microelectronics.* 2004; Vol 2, 459-462.
  94. Guo LJ. Recent progress in nanoimprint technology and its applications. *J. Phys. D: Appl. Phys.* 2004; 37, 123-141.
  95. Sun ZQ, Chen X, Zhang JH, Chen ZM, Zhang K, Yan X, Wang YF, Yu WZ, and Yang B. Nonspherical Colloidal Crystals Fabricated by the Thermal Pressing of Colloidal Crystal Chips. *Langmuir.* 2005; 21: 8987-8991.
  96. Aistilean S. fabrication of periodic metallic nanostructures by using nanosphere lithography. *Romanian reports in Physics.* 2002; 56,
-

- 
97. Hulteen JC, Duynes RPV. Nanosphere lithography: A materials general fabrication process for periodic particle array surfaces. *J. Vac. Sci. Technol A*. 1995; 13, 3. 1553-1558.
  98. Hulteen JC, Treichel DA, Smith MT, Duval ML, Jensen TR, Van Duynes RP. Nanosphere Lithography: Size-Tunable Silver Nanoparticle and Surface Cluster Arrays. *J. Phys. Chem. B*. 1999; 103, 3854-3863.
  99. Ormonde AD, Hicks ECM, Castillo J, Van Duynes RP. Nanosphere Lithography: Fabrication of Large-Area Ag Nanoparticle Arrays by Convective Self-Assembly and Their Characterization by Scanning UV-Visible Extinction Spectroscopy. *Langmuir*. 2004; 20, 6927-6931.
  100. Schmidt JP, Cross SE, Buratto SK. Surface-enhanced Raman scattering from ordered Ag nanocluster arrays. *J. Chem. Phys.* 2004; 121, 21.
  101. Baker GA, David E, Moore S. Progress in plasmonic engineering of surface-enhanced Raman-scattering substrates toward ultra-trace analysis. *Anal Bioanal Chem.* 2005; 382: 1751-1770.
  102. Willets KA, Van Duynes RP. Localized Surface Plasmon Resonance Spectroscopy and Sensing. *Annu. Rev. Phys. Chem.* 2007. 58: 267-97.
  103. Kneipp K, Wang Y, Dasari RR. Approach to Single Molecule Detection Using Surface-Enhanced Resonance Raman Scattering (SERRS): A Study Using Rhodamine 6G on Colloidal Silver. *Appl Spectrosc.* 1995; 49,780-784.
  104. Goulet PJG, Pieczonka NPW, Aroca RF. Mapping single-molecule SERRS from Langmuir–Blodgett monolayers on nanostructured silver island films *J. Raman Spectrosc.* 2005; 36, 574-580.
  105. Vo-Dinh T, Stokes DL. Surface-Enhanced Raman Detection of Chemical Vapors and Aerosols Using Personal Dosimeters. *Field Anal. Chem. & Techn.* 1999; 3(6): 346-356.
  106. Taranenko N, Alarie JPe, Stokes DL, Vo-Dinh T. Surface-Enhanced Raman Detection of Nerve Agent Simulant (DMMP and DIMP) Vapor on Electrochemically Prepared Silver Oxide Substrates. *J. Raman Spectrosc.* 1996; 27: 379-384.
  107. Yan F, Wabuyele MB, Griffin GD, Vass AA, Vo-Dinh T. Surface-Enhanced Raman

- Scattering Detection of Chemical and Biological Agent Simulants. *Sensors Journal*. 2005; 5, 4: 665.
108. Rivas L, Murza A, Sanchez-Cortes S, Ramos JVG. Adsorption of acridine drugs on silver: surface-enhanced resonance Raman evidence of the existence of different adsorption sites. *Vib. Spectros*. 2001; 25: 19-28.
109. Sagmullera B, Schwarzeb B, Brehmc G, Trachtac G, Schneider S. Identification of illicit drugs by a combination of liquid chromatography and surface-enhanced Raman scattering spectroscopy. *J. of Mol. Struct*. 2003; 661-662: 279-290.
110. Olson LG, Uibel RH, Harris JM. C18-Modified Metal-Colloid Substrates for Surface-Enhanced Raman Detection of Trace-Level Polycyclic Aromatic Hydrocarbons in Aqueous Solution. *Appl Spectrosc*; 2004, 58: 1394.
111. Lee YH, Farquharson S. SERS sample vials based on sol-gel process for trace pesticide analysis. *Proc SPIE 4206*; 2001: 140.
112. Premasiri WR, Clarke RH, Womble. Surface enhanced Raman detection of CW agents in gel substrates. *ME Proc SPIE 4577*. 2002; 205.
113. *SciFinder Scholar 2004*. Searched for 'SERS explosive detection' and 'Surface enhanced Raman explosive detection' on 13 September 2005.
114. McHugh CJ, Keir R, Graham D, Smith WE. Selective fictionalisation of TNT for sensitive detection by SERRS. *Chem Comm*. 2002; 580-581.
115. McHugh, Callum J, Smith, Ewen W, Graham, Duncan. Chemical manipulation of explosives using novel multifunctional reagents (MFRs) for analysis by SERRS. *Abstracts of Papers, 222nd ACS National Meeting*. 2001; 26-30.
116. Haas, John W, Sylvia, James M, Spencer, Kevin M, Johnston, Thomas M, Clauson, Susan L. Surface-enhanced Raman sensor for Nitro-explosive vapours. *Proc. SPIE-The Inter. Soc. for Optical Eng.*; 1998.
117. Sylvia J M; Janni J A; Klein J D; Spencer K M. Surface-enhanced Raman detection of 2,4-dinitrotoluene impurity vapour as a marker to locate landmines. *Anal. chem*. 2000; 72(23): 5834-5840.
118. Sylvia JM, Spencer KM, Janni JA. Sniffing landmines with surface-enhanced Raman Spectroscopy. *J. Process Anal. Chem*. 2001; 6(4): 146-147.

- 
119. Spencer KM, Sylvia JM, Peter J, Berton JF, Christeen SD. Surface-enhanced Raman spectroscopy for homeland defense. *Proc. of SPIE-The Inter. Soc. Optical Eng.*; 2004.
  120. James AJ, James MS, Susan LC, Kevin MS. SERS detection of the nuclear weapons explosive triaminotrinitrobenzene. *Proc. of SPIE-The Inter. Soc. Optical Eng.*; 2002.
  121. Katrin K, Yang W, Ramachandra D, Michael SRF, Brian GD, James J, Jeffrey S, Harrison GR. Near-infrared surface-enhanced Raman scattering of trinitrotoluene on colloidal gold and silver. *Spectrochimica Acta, A: Mol. and Biomol. Spectros.* 1995; 51A (12): 2171-2175.
  122. Montoya DLC, SERS of Nitro explosives on titanium substrates. *Abs. Papers, 230th ACS National Meeting*, 2005.
  123. Spencer KM, Sylvia JM, Marren PJ, Bertone JF, Christesen SD. Surface enhanced Raman Spectroscopy for Homeland Defence. *Chem. and Bio. Point Sensors for Homeland Def.*; SPIE 5269, 2004
  124. Bertone JF, Cordeiro KL, Sylvia JM, Spencer KM. A nanoengineered sensor to detect vibrational modes of warfare agents/explosives using surface enhanced Raman scatterings. *Sensors, and Command, Control, Comm. and Intelligence (C3I) Techn. for Homeland Def.*; SPIE 5403, 2004
  125. Ahmad SR, Lles A. Pre-resonance Raman excitation profile of the 3400 cm<sup>-1</sup> mode of liquid water. *J. Raman Spectrosc.* 2001; 32: 649-655.
  126. Wu DY, Ren B, Tian ZQ. Progress in the Theory of Surface Enhanced Raman Scattering. *Int. J. Vib. Spect.* 2000; 4, 2: 10.
  127. Otto A. The 'chemical' (electronic) contribution to surface-enhanced Raman scattering. *J. Raman Spectrosc.* 2005; 36: 497-509.
  128. *SciFinder Scholar, version 2006*. Chemical Registry Number 110-86-1.
  129. *SciFinder Scholar, version 2006*. Chemical Registry Number 98-95-3.
  130. *SciFinder Scholar, version 2006*. Chemical Registry Number 67-64-1.
  131. *SciFinder Scholar, version 2006*. Chemical Registry Number 78-11-5.
  132. Yinon J, Zitrin S. *Modern Methods and Applications in Analysis of Explosives*. 1993; John Wiley and Sons. England.
  133. Gruzdkov YA, Gupta YM. Vibrational Properties and Structure of Pentaerythritol
-

- Tetranitrate. *J. Phys. Chem. A*. 2001; 105, 6197-6202.
134. Schulte-Ladbeck R, Kolla P, Karst U. Trace Analysis of Peroxide-Based Explosives. *Anal. Chem.* 2003; 75,731-735.
135. Schulte-Ladbeck R, Vogel M, Karst U. Recent methods for the determination of Peroxide-based explosives. *Anal. Bioanal. Chem.* 2006; 386, 559-565.
136. *SciFinder Scholar, version 2006*. Chemical Registry Number 17088-37-8.
137. McKay GL. Forensic characteristics of organic peroxide explosives. *J. Japan For. Soc.* 2002; 63, 2, 323-329.
138. Oxley JC, Smith JL, Shinde K, Moran. Determination of the Vapor Density of Triacetone Triperoxide (TATP) Using a Gas Chromatography Headspace Technique. *J. Propellants, Expl., Pyrotech.* 2005; 30: 2, 127-130.
139. Quevedo AJP, Calmide NM, Rodriguez N, Nieves D, Cody RB, Rivera SPH. Synthesis, Characterisation and Differentiation of high energy Amine Peroxides by MS and vibrational spectroscopy. *Sensors, and Command, Control, Comm. and Int. (C3I) Techn. for Homeland Def.*; SPIE 6201, 2006.
140. Pena JA, Londono LP, Figueroa j, Montalvo LAR, Valazquez FRR, Rivera SPH. Characterisation and Differentiation of high energy Cyclic Organic Peroxides by GC/FT-IR and Raman Microscopy. *Sensors, and Command, Con., Comm. and Int. (C3I) Techn. for Homeland Def.*; SPIE 5778, 2005. 347-357.
141. Vacque V, Sombret B, Huvenne JP, Legrant P, Suc S. Characterization of O-O peroxide band by vibrational spectroscopy. *Spectromechia Acta A*. 1997; 53, 55-66.
142. *SciFinder Scholar, version 2006*. Chemical Registry Number 283-66-9.
143. Wierzbicki A, Salter EA, Cioffi EA, Stevens ED. Density Functional Theory and X-ray Investigations of P- and M-Hexamethylene Triperoxide Diamine and Its Dialdehyde Derivative. *J. Phys. Chem. A*, 2001; 105, 8763-8768.
144. Chen W, Tan S, Huang Z, Ng T, Ford WT, Tong P. Measured long-ranged attractive interaction between charged polystyrene latex spheres at a water-air interface. *Phys. Rev. E*. 2006; 74, 021406-1-14.
145. Nyquist RA, Kagel RO. *Handbook of infrared and Raman spectra of inorganic compounds and Organic salts*. 1997; Academic press. Vol. 4. 191.

## APPENDIX A

### Summary of work done on Raman spectroscopy of explosive materials

Explosives	Excitation laser line	FTR/ Dispersive	Detector type	Sample type	Remarks	Ref / Year
HMX, TATB	532nm	Dispersive	ICCD	Bulk, liquid	Suitable for only non fluorescent explosives	32/ 2005
23 samples	785nm 830nm	Dispersive	CCD	Bulk	Useful for identification of bulk explosives	22/ 2005
10 samples	1064nm	Dispersive	Ge diode array	Bulk	Fluorescence free region but low S/N due to weak Raman Intensity	21/ 2005
26 samples	1064nm	Dispersive	CCD	Bulk	Fluorescence free region and sensitive detector but weak Raman Intensity due to anti stokes. Good for characterisation.	14/ 2004
11 samples	785nm	Dispersive	CCD	1.5-14% by mass in soil	Fluorescence due to soil gives poor S/N for weak Raman intensities	20/ 2001
TNT, RDX, PETN	532nm	Dispersive	ICCD	Bulk	Identification from 60 meters for non fluorescence material has been demonstrated	17/ 2005
NC, PVN, BAP	514.5nm	Dispersive	CCD	Bulk	Energetic polymers have been characterised by Raman spectroscopy	33/ 2003
TNT, RDX, HMX, NQ	514.5nm	Dispersive	PMT	Bulk	AOTF based Raman spectrometer works from UV to IR but has low sensitivity for detection work	34/ 2000
30 samples	632nm 785nm 1064nm	Dispersive/ FTR	CCD/ GaAs	Bulk	785nm with CCD is better choice for detection work. FTR is good for characterisation and building a spectral data library.	15/ 1995

## APPENDIX B

## Summary of reported results on Surface Enhanced Raman Spectroscopy

SER-active material	Substrate	Method	Roughness Dimension (nm)	Excitation Line (nm)	Analyte	Analyte Concentration (M)	Environment solid/ liquid	Raman System	Remarks	Ref/ Year
Ag colloid	N/A	Lee & Meisel <sup>81</sup>	200 15-40 particles	830	R6G & Crystal violet	$10^{-12} - 10^{-14}$	solution	Raman Microscope & CCD	The concentration of colloid was $10^{-11}$ as compared to $10^{-14}$ of analyte which lead to single molecule detection.	39/ 1998
Ag colloid	N/A	Lee & Meisel <sup>81</sup>	-	1064 647.1 514.5 488	lucigenin	$10^{-4}$	Solution	FTR Bruker, Jobin.Yvon U-1000	Adsorption and orientation of analyte in presence of anions (Cl <sup>-</sup> ) has improved resulting in the SERS enhancement.	69/ 2002
Ag colloid	N/A	Creighton <sup>82</sup>	-	1064 514.5	Cytosine, methyle-cytosine	$10^{-6}$	solution	FTR Bruker, Jobin.Yvon U-1000	Presence of HCl and NaCl (Cl <sup>-</sup> ) resulted in better adsorption. Low pH gave higher SERS by changing the particle coverage.	55/ 2000
Ag colloid	N/A	Lee & Meisel <sup>81</sup> ,	67 particles	1064, 785	Amin-acridine	$10^{-6}$	solution	FTR Bruker FRA, Kaiser HLR 5	In comparison the Hydroxylamine reduced Ag colloids were found to be better than citrate in morphology and in 'hot spots'.	70/ 2003
Ag colloid	N/A	Lee & Meisel <sup>81</sup> ,	10-50 particles	1064	di-methyle-cytosine	$10^{-5}$	solution	FTR Bruker FRA	Optimised morphology for Ag colloids can be achieved by modifying Ag concentration.	56/ 2000
Ag/ Au colloids	Ag on Au, Au on Ag	Lee & Meisel <sup>81</sup>	Ag 40-50 , Au 10-15	1064 457.9 514.5 488	Pyridine	$10^{-2}$	solution	FTR Bruker, Jobin.Yvon U-1000	Coated colloids did not exceed the enhancement offered by Ag alone. Au colloid only work in longer wavelength.	63/ 2000



SER-active material	Substrate	Method	Roughness Dimension (nm)	Excitation Line (nm)	Analyte	Analyte Concentration (M)	Environment solid/ liquid	Raman System	Remarks	SER-active material
Ag colloids	N/A	Lee & Meisel <sup>81</sup>	52 particle	532	R6G	0.1-125x10 <sup>-9</sup> M	solution	Pro 275, CCD	Detection of signal from a single molecule is possible at even higher molecular adsorption, as only few molecules contributed to SER spectra.	71/2005
Ag colloids	N/A	Lee & Meisel <sup>81</sup>	30 particles	CW532, Pulsed 529	Dye ABT. DMOPA	10 <sup>-6</sup>	solution	Spex triplemate, CCD	For SERRS, the use of CW laser was found to be much better than using pulsed laser as it tended to degrade the Ag-analyte bond, decomposition of Ag particles and thus giving poor SER signal.	67/2005
Ag colloids	N/A	Leopold and Lendle <sup>70</sup>	-	1064, 785	Polycyclic hydrocarbons (PAH)	10 <sup>-4</sup>	solution	FTR Bruker, Renishaw Raman Microscope	Adsorption of hydrocarbons on Ag colloids is possible after adding calyx-4-arenes. Likewise SERS is possible for other non adsorbing materials.	68/2004
Ag colloids	Mica	Lee & Meisel <sup>81</sup>	39.8	514.5	R6G	10 <sup>-14</sup>	Solid	Renishaw Raman Microscope	Substrate giving easily reproducible and very high SER signal was demonstrated.	72/2004
Ag nano-wires	glass	Polyol process	100 diameter	442 488 514.5 633 785	R6G	10 <sup>-5</sup>	Solid	Renishaw In Via & Raman Microscope	By isolating 100 diameter nanowires on glass, SERS and SERRS of R6G were recorded. The comparison of spectra confirmed that the use of longer wavelength gave better signal in 'finger print' region.	73/2005

SER-active material	Substrate	Method	Roughness Dimension (nm)	Excitation Line (nm)	Analyte	Analyte Concentration (M)	Environment solid/ liquid	Raman System	Remarks	SER-active material
Ag layer	40 nm diameter fibre-optic	Coating	150	633	triphenol	$10^{-3}$	solid	Renishaw Raman Microscope	The system is complex and non reproducible with lower sensitivity range than other SERS active surfaces.	74/2004
Au	Glass	Scratch	100	632.8	Oxazine	$10^{-6}$	solid	Kaiser spectrograph and CCD	Although the procedure simplifies substrate preparation, it is too crude to make reproducible uniform roughness in a pattern form.	75/2005
Ag	SiO <sub>2</sub> & Glass	Vapour deposited	11	568	R6G		solid	Acton 300i, CCD	Ag layer on SiO <sub>2</sub> gives the required roughness for SERS enhancement. Ag- SiO <sub>2</sub> -Ag-glass gives even larger SERS signal.	76/2005
Ag	Glass	sputtered	50-100	488	Benzoic acid	$10^{-3}$	solid		AgO and Ag <sub>2</sub> O films on glass gave roughness in range of 50-100nm which gave good SERS. The films are reproducible.	77/2003
Ag, Au	Silicon wafer & rough	coating	25-30 , 500-900	632	pyridine	$10^{-4}$	solid	Renishaw Raman Microscope	The SERS of thinner layers, 5-10nm on silica gave better results due to small (25-30) nm cluster formation.	78/2005
Ag	Silicon wafer	chemical deposited	30	514.5	R6G	Single molecule	solid	LabRam MicroRaman	Very high sensitivity was achieved with hotspots at interstices between particles and at clefts.	79/2004

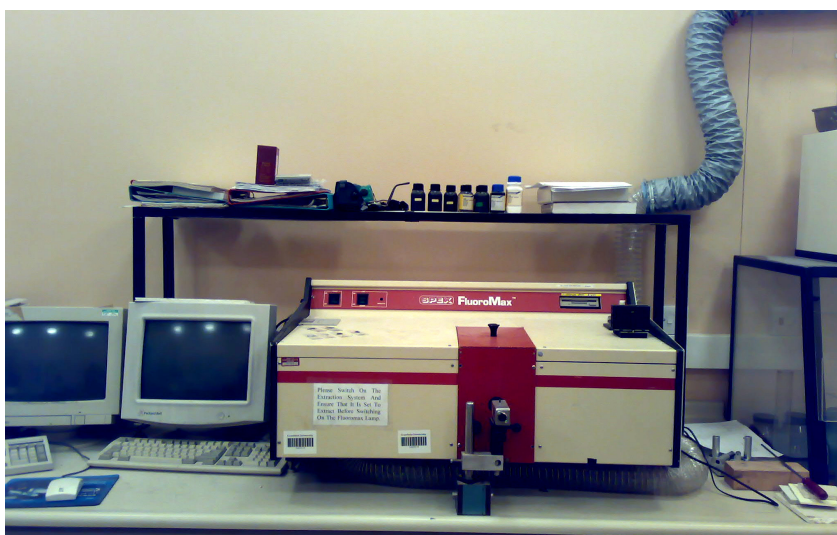
SER-active material	Substrate	Method	Roughness Dimension (nm)	Excitation Line (nm)	Analyte	Analyte Concentration (M)	Environment solid/ liquid	Raman System	Remarks	SER-active material
Ag	Rough Fibre optic	Chemical deposited		702	Thio phenol	$10^{-3}$	solid	DILOR XY CCD	Because of non uniform and higher roughness, the sensitivity was low. it could be useful because of its robustness and simple protocol for the preparation of substrate.	62/2004
Ag	Porous glass	sputtered	5-10	632.8	R6G	$10^{-6}$ M	solid	LabRam MicroRaman	The substrate gave medium level SERS, as the signal is from sharp edges over the pores. For medium level SERS this is economical technique, both in efforts and money.	61/2005
Ag	-	Etched	10-100	488	Amino acridine	$10^{-4}$	solid	1680 B DS, PMT	HNO <sub>3</sub> etching is an old method of surface roughness, but it has many variables and uniform roughness was not always possible.	64/2000
Ag	Silica beads	coating	350-800 diameter	632.8	Benzoic acid	$10^{-7}$	solid	Renishaw Raman Microscope	6nm layer of Ag over 565nm bead gave best results. SER-effect generated from the Ag particles size was not affected much by silica bead diameter.	65/2003
Ag	glass	Polystyrene nanosphere lithography	51		Streptavidin	$10^{-11}$	solid		Highly uniform SER-active surface was prepared. The roughness features was increased by increasing Ag layer thickness	80/2002

## APPENDIX C

### SPEX FluroMax, Spectrofluorometer

It had following main features

1. Source: 150W continuous Xenon lamp.
2. Dispersion: 4.25 nm/mm.
3. Spectrometers: f/3.2 plane grating Czerny-Turner type.
4. Blazing wavelength of the grating: 350nm.
5. Wavelength accuracy:  $\pm 0.5$ nm.
6. Resolution: 0.3nm.
7. Signal detector: Standard: Side on R1527P Photo multiplier tube (PMT), 180-680nm response linearity to  $4 \times 10^6$  cps, 100 counts/second.
8. Reference Detector: Photodiode 200-980nm range.
9. Sensitivity: 160000cps at 397nm peak, Ex at 350nm, Band-pass 5nm, integration of 1 second.
10. Signal to noise ratio: 550/1.
11. A standard PC controls the system.
12. Sample Holder with built in frames for solid and in solution analysis.



## APPENDIX D

### Perkin Elmer Lambda 9 UV/vis/NIR Spectrophotometer

It has following features:

1. Dual monochromator configured in series each having two gratings.
2. Deuterium lamp to cover UV range.
3. Tungsten-Halogen lamp to cover vis-NIR region.
4. Fitted with side window photomultiplier for UV-vis wavelength.
5. A PbS detector for NIR range.
6. Resolution of 0.2 nm in UV-vis region and 0.8 nm in NIR region.
7. Separate sample holders for solid and liquid.
8. Wavelength range from 200-1000 nm.



## **APPENDIX E**

### **Cintra-5 UV/vis Spectrophotometer**

It has following features:

1. A double beam UV/vis spectrophotometer.
2. Enables fixed point measurement (single wavelength, multi-wavelength, concentration photometric measurement).
3. Wavelength scanning.
4. Time scanning.
5. Visionite Scan-Version 1.0 software.



## **APPENDIX F**

### **Custom built high-resolution Raman spectrometer**

It has following features:

1. Spex 1404 double monochromator.
2. Intensified Diode Array detector assembly. The diode array sensitivity was optimised in the UV-vis range of the spectrum, and its response is quoted to be 15 photons per count. In Y-T scanning mode a selected portion of the diode array was grouped to provide a signal of lower resolution but of greater sensitivity.
3. Detector was controlled by a matched (E G & G- type 1460) Optical Multi-channel Analyser (OMA III). The data of each scan is stored on a computer disk, and although the OMA III is not IBM compatible, the data format has been converted to be acceptable to the MS-DOS system.
4. SpectraPhysics 165 Argon ion laser was used in six wavelengths bands; 514.5, 496.5, 488, 476.5, 465.8 and 457.9 nm.
5. Scientech power energy meter was used to determine the power at the sample.
6. Focusing lenses of focal length 5cm and collecting lens of focal length 24cm were used. All lenses were of 5cm diameter.
7. Optics and sample holder were arranged for 90<sup>0</sup> collection of Raman scatterings.
8. A standard blocking filter was used between sample and collecting lens.



## APPENDIX G

### Renishaw Raman microspectrometer RM2000

It had following features:

1. Choice of lasers with 514 nm and 785 nm excitation wavelength at Institute of Material Structures, Madrid, Spain.
2. Laser with 832 nm excitation wavelength with system at Gloucester Royal Hospital, Gloucester.
3. Research grade microscope with digital image capture capability.
4. 100  $\text{cm}^{-1}$  cutoff notch filter
5. 5  $\text{cm}^{-1}$  next cutoff filter for study of near-excitation bands.
6. High Spectral/Spatial resolution.
7. High sensitivity ultra-low noise RenCam CCD detector
8. Powerful WiRE™ 2.0 software for intuitive operation and data manipulation
9. Heating/Freezing stage
10. Allows rapid, non-destructive chemical and structural analysis with easy or no sample preparation (solids, liquids, gases).





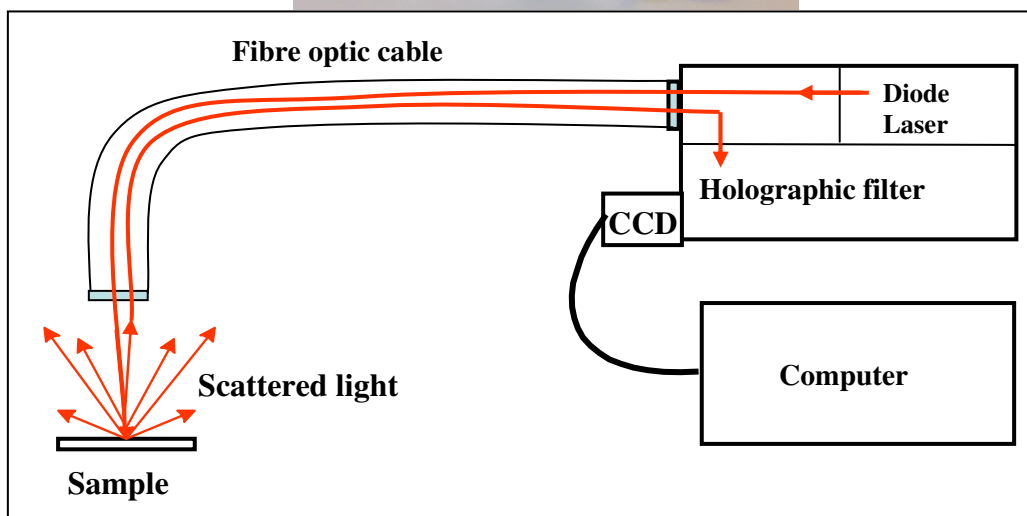
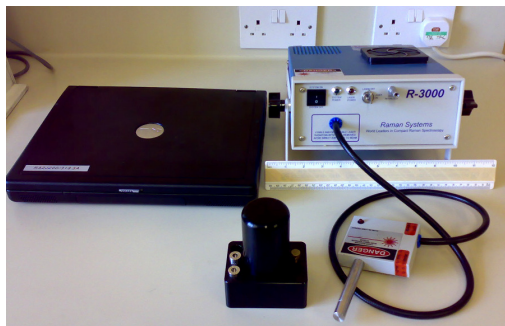
## APPENDIX H

### Ocean Optics Raman Spectrometer R-3000

The Raman Systems R-3000 is a portable fully integrated Raman analyzer for spectral analysis of aqueous solutions, powders, and surface media.

#### Main Features:

1. Integrated System, includes diode laser, CCD-array spectrometer, fiber optic probe and operating software.
2. It has spectral resolution of  $10\text{ cm}^{-1}$ , wavelength stability of  $1\text{ cm}^{-1}$  and output stability of 4%.
3. Fiber optic probe with accessories for calibration and focusing. The fiber length is 1 meter.
4. R-3000 is fitted with an thermoelectrically cooled CCD array, which allows integration times of up to 4 minutes. The CCD is maintained at a constant temperature and has a wavelength range of  $\sim 200\text{-}2700\text{ cm}^{-1}$ .
5. Uses 785 nm (red) solid-state diode laser having an output power of 250mW that is stable enough for use with focused probes.
6. Runs on *RSIBase* software.

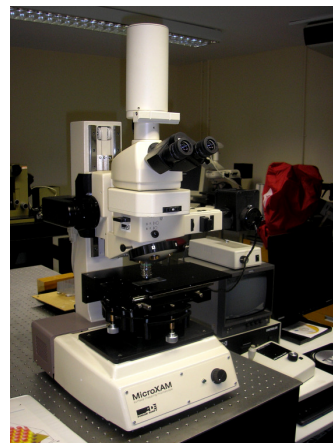


## APPENDIX I

### MicroXAM 3D Interferometric Surface Profiler

Main Features:

1. MicroXAM non contact surface mapping microscope.
2. Works with MapVUE software.
3. Measures step heights from less than a nanometer (.001 micron, or 10 Angstrom) up to millimeters.
4. No stylus.
5. True three-dimensional surface profiling measurements.
6. Ultra-precise surface height sensitivity.
7. Quantitative, visual and confocal modes using optical interferometry.
8. Standard 2D and 3D surface statistics including summit and valley analyses.
9. 3D wire, hybrid and solid plots.
10. Optical microscope with eyepieces and video display of images.



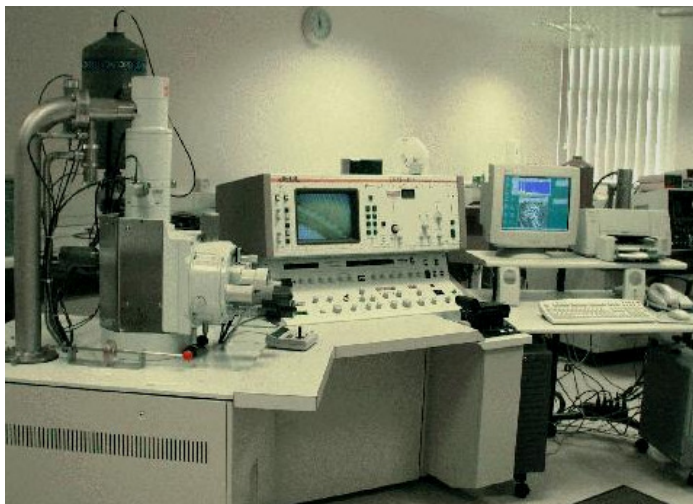
## APPENDIX J

### Scanning Electron Microscopes

#### The JEOL 840A SEM

Main features:

1. Variable accelerating voltage; 200 to 40,000V
2. Variable probe current;  $1 \times 10^{-8}$  to  $1 \times 10^{-12}$  Amps
3. Maximum sample size of 6" in any one dimension
4. Working distances; 8 to 48mm
5. Sample rotation;  $360^\circ$
6. Sample tilting  $90^\circ$
7. Variable magnification; 10x to 300,000x
8. Maximum resolution; 10 nm
9. Secondary and Backscattered Electron detectors
10. Digital image capture and export in electronic form



## LEO 435VP

Main features:

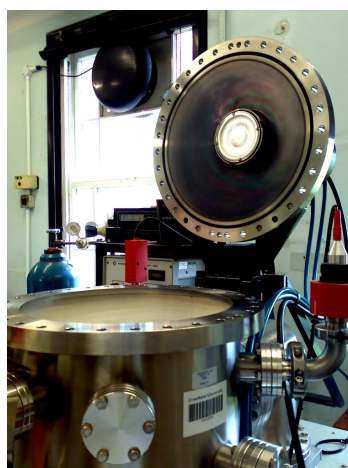
1. High-performance, variable pressure scanning electron microscope.
2. Resolution of 4.0nm.
3. Backscatter detector and enables Digital image acquisition.
4. 5 axis computer controlled stage mounted in a specimen chamber measuring 300 x 265 x 190mm and can accommodate specimens weighing up to 0.5kg.
5. Standard automated features include focus, stigmator, gun saturation, gun alignment, contrast and brightness.



## APPENDIX K

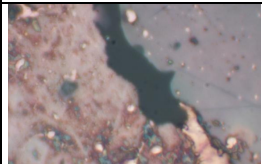
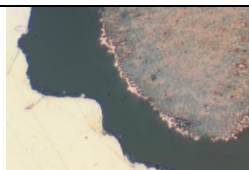
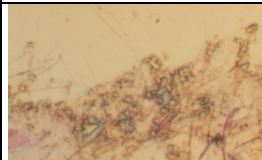
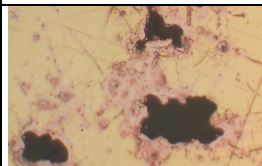
### Magnetron sputtering equipment

1. Reactive DC-Magnetron Sputtering equipment was used to coat silver films in an argon or argon–oxygen environment of closely controlled gas content.
2. Gases were of high purity (99.9%).
3. Target of 75mm diameter Silver disc (purity 99.9%) of 2mm thickness was purchased from *Goodfellow Cambridge Limited*.
4. Turbo-pumped ultra high vacuum (UHV) deposition system was used to ensure very low impurity levels in the deposited films.
5. The metal target disc was fixed in the sputtering chamber roof and substrate holder was in the bottom of the chamber.
6. The substrate (on which the coating was desired) was subjected to high vacuum conditions of  $< 5 \times 10^{-5}$  mbar before injecting Ar gas raising the pressure to  $< 4 \times 10^{-3}$  mbar.
7. The temperature was controlled by internal heating plate (ambient to 400°C) and the substrates were continuously rotated during coating process.
8. Chamber atmosphere could be changed by selecting the oxygen, hydrogen and nitrogen gases.
9. The layers from 10nm to more than a micron could be put on different types of substrates at the rate of 0.2 to 2 nm/s.

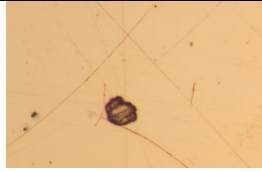
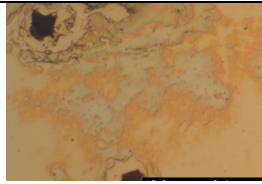
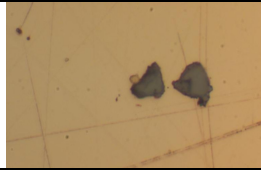


## APPENDIX L

Details for preparation of gold surfaces for SERS study by Nd:YAG (1064 nm) laser ablation

Laser Power (m j)	Number of shots	Laser diameter (mm <sup>2</sup> )	Laser focus	Effect on the surface	Microscope images
59	5	2.5	Focussed	surface burned	
59	2	2.5	Focussed	surface burned	
59	1	2.5	Focussed	surface burned	
59	1	5	without Focusing lens	No effect	
59	5	5	without Focusing lens	No effect	
200	1	5	without Focusing lens	No effect	
200	5	5	without Focusing lens	Surface burned	



200	1	7	Sample placed 5 cm from focal point	No effect	
200	5	7	Sample placed 5 cm from focal point	No effect	
200	10	7	Sample placed 5 cm away from focal point	0.1mm diameter hole in the surface	
200	10	8	Sample placed 6 cm from focal point	surface burned	
200	5	8	Sample placed 6 cm from focal point	surface burned	
200	1	8	Sample placed 6 cm from focal point	Surface burned	

## Appendix M

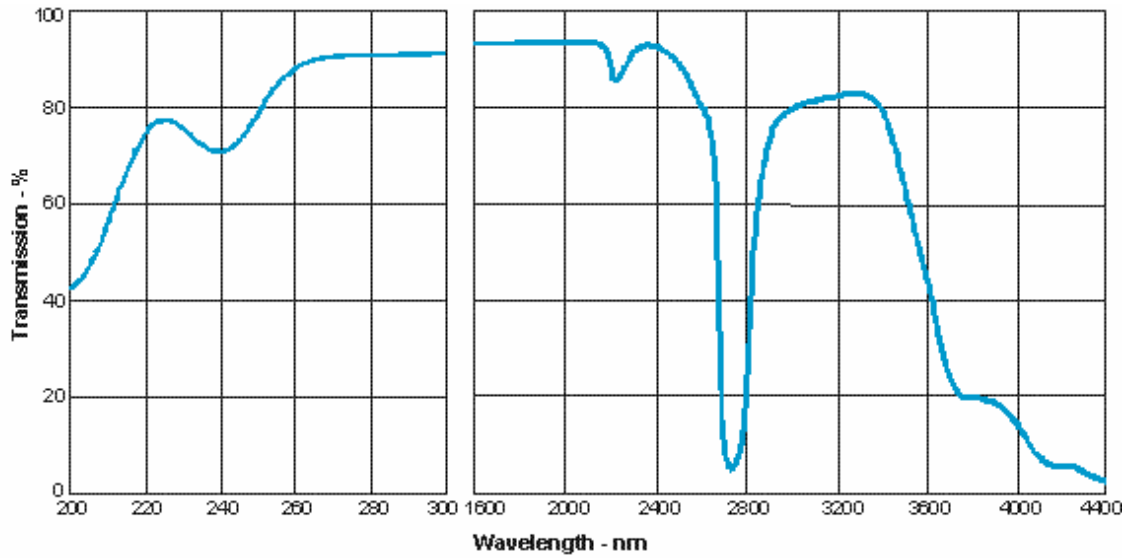
### 1. Optical fused quartz, Vitreosil 077:

- a. Manufactured by flame fusion of naturally occurring high-purity quartz crystal.
- b. 25mm x 25mm x 1mm.
- c. Useful transmission range from <260 nm in the near UV through to >2000 nm in the IR.
- d. Useful transmission range from <260 nm in the UV to >2 000 nm in the infrared. See graph below.
- e. Fluorescence (254nm excitation) blue/violet.
- f. Typical trace elements in ppm:

Al	15
Ca	0.5
Cr	<0.01
Cu	<0.01
Fe	0.1
K	0.2
Li	0.2
Mn	0.01
Na	0.1
Nd	0.01
Ti	1.3
Y	<0.1
Zr	1.3
OH	170



g. Typical external transmission



## 2. Microscope slide glass

- a. Super premium microscope slides from Fisher Scientific, Uk (Menzel-Glaser).
- b. 75 mm x 25 mm x 1mm.
- c. Light transmission (solar) is 91.3%.
- d. Typical composition in percentage:

SiO <sub>2</sub>	72.2
Na <sub>2</sub> O	14.3
K <sub>2</sub> O	1.2
CaO	6.4
MgO	4.3
Al <sub>2</sub> O <sub>3</sub>	1.2
Fe <sub>2</sub> O <sub>3</sub>	0.03
SO <sub>3</sub>	0.3

## APPENDIX N

## Geometry of Silver Nano-structures

The fabrication of SER active substrate by NSL method results in nano-structural array as shown in figure 6.6. This process results in the formation of a single array formed by the assembly of seven nanospheres and is described below.

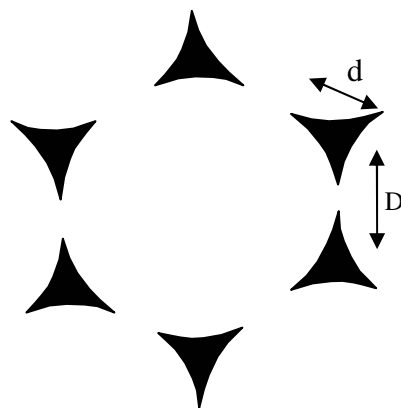


Figure 1 Configuration of a single silver structural array formed by the assembly of seven nanospheres.

This structure array geometry is also described by Hulteen et al <sup>97</sup> in detail. We deduce for the nanospheres of diameter 500 nm will have the distance between any two adjacent structures 'D' (centre to centre distance of two adjacent structures) of 288 nm and the average size of the structure 'd' (the length of the perpendicular bisector of largest inscribed equilateral triangle) of 116 nm. These are calculated as:

Inter-structural distance 'D' is given as:

$$\frac{\text{Nanosphere diameter } (\mu\text{m})}{\sqrt{3}}$$

$$\frac{0.5}{\sqrt{3}} = 0.288\mu\text{m} \quad \text{or} \quad 288 \text{ nm}$$

Nano-structure size ‘d’ is given by:

$$\text{Nano-sphere diameter } (\mu\text{m}) \times \left\{ \sqrt{3} - 1 - \frac{1}{\sqrt{3}} \right\} \times \frac{3}{2}$$

$$0.5 \times 0.233 = 0.116 \mu\text{m} \quad \text{or} \quad 116 \text{ nm}$$

For further calculations consider that the entire surface is distributed into equilateral triangles of 500 nm length of each of its side formed by joining the centre point of each circle made by removing the nanosphere as shown in figure 2. Each of the equilateral triangles will have only one structure within its area.

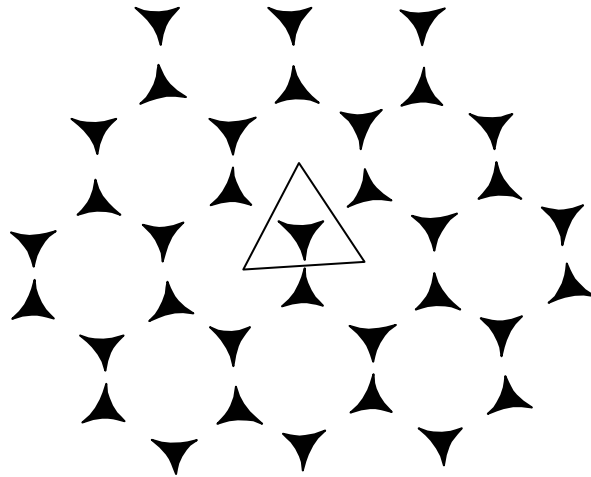


Figure 2 Configuration of uniform structural array divided into equilateral triangles of 500 nm length of each side.

The area of the equilateral triangle would be:

$$= \frac{1}{4}(500)^2\sqrt{3}$$

$$= 108253.08 \text{ nm}^2$$

$$= 1.08 \times 10^5 \text{ nm}^2$$

Area of the laser spot

$$= 0.1\text{mm}^2$$

$$= 1 \times 10^{11} \text{ nm}^2$$

Number of equilateral triangles (or structures) in one laser spot

$$\frac{\text{Area of laser spot}}{\text{Area of equilateral triangle}}$$

$$= \frac{1 \times 10^{11}}{1.08 \times 10^5}$$

$$= 0.9 \times 10^6$$

$$= \sim 1 \text{ million structures in the area of laser spot}$$

Approximate area of one structure can be calculated considering it has straight sides instead of curved so forming an equilateral triangle having perpendicular bisector 'd' 116nm and each side of length 'a'. 'c' being half of 'a'.

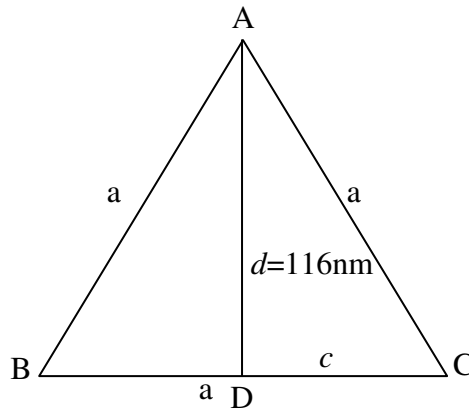


Figure 3 An equilateral triangle being represented by a single structure having perpendicular bisector of 116 nm.

Therefore

$$a = \frac{116}{\sqrt{3}} \times 2$$

$$= 134 \text{ nm}$$

$$c = 67 \text{ nm}$$

$$\text{Area of ADC} = \frac{1}{2} \times 116 \times 67$$

$$= 3886 \text{ nm}^2$$

$$\text{Area of ABC} = 7772 \text{ nm}^2 \quad (\text{Area of one structure})$$

Area of structures within the laser spot;

$$= 7772 \times 1 \times 10^6 \text{ nm}^2$$

$$= 7.7 \times 10^9 \text{ nm}^2$$

Percentage area covered by structures within the laser spot

$$= \frac{7.7 \times 10^9}{1 \times 10^{11}} \times 100$$

$$= 7.7\%$$

Percentage area of exposed substrate within laser spot

$$= 92.3\%$$

**APPENDIX O**

Raman and SER spectra of sample molecules discussed in Chapter 7.

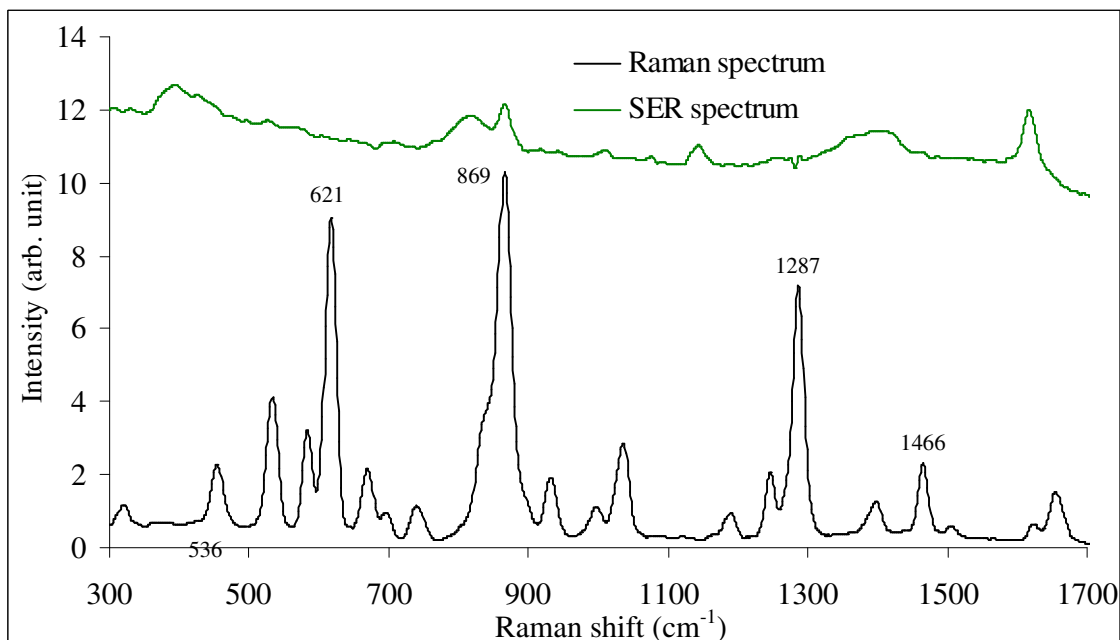


Figure 1 Raman and SER spectrum of PETN ( $t_i=15$ secs) from a glass-based surface exposed to headspace vapour fabricated with 20 nm layer over 250 nm high structures.

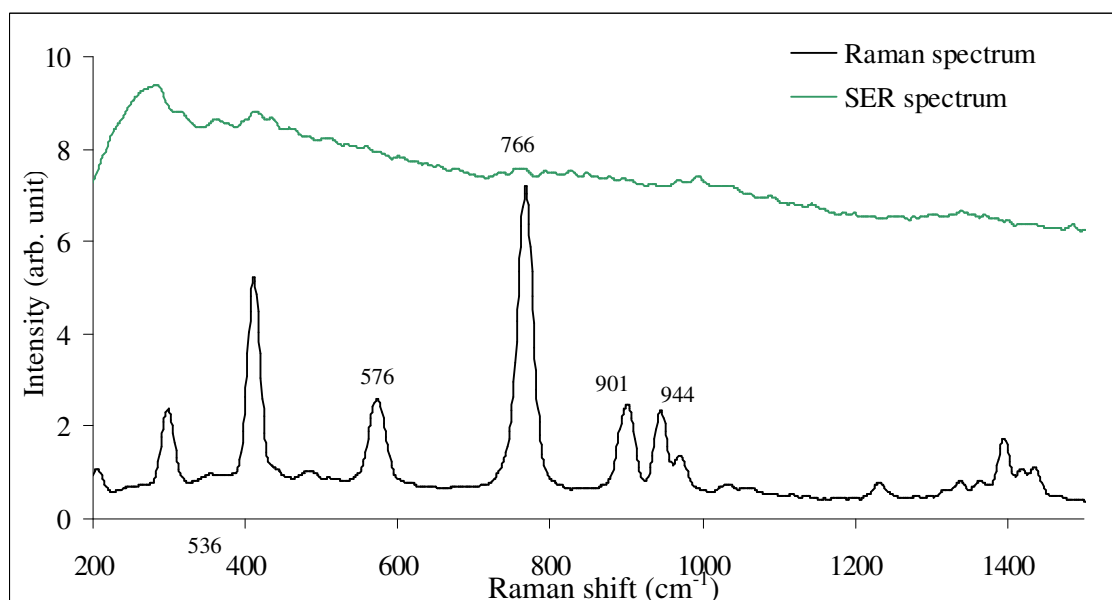


Figure 2 Raman and SER spectra ( $t_i = 10$ seconds) from a glass-based surface having 225 nm high of nano-structures with 20 nm silver overlayer when exposed to headspace vapour from HMTD.

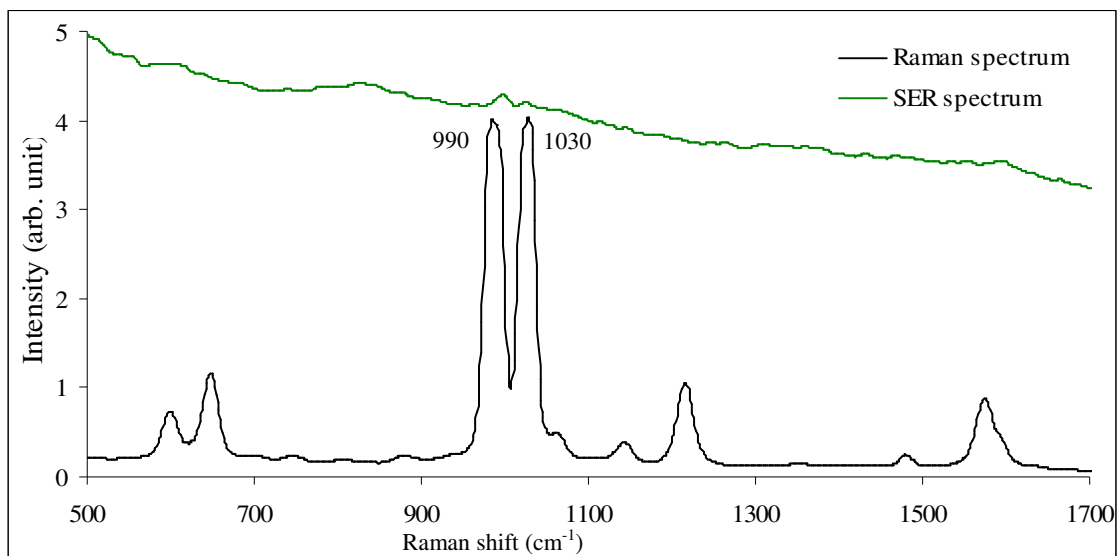


Figure 3 Normal Raman spectrum of pyridine and its SER spectrum recorded from a quartz-based surface having 150 nm high structures exposed to the vapour from pyridine for 20 seconds.  $t_i = 10$  seconds.

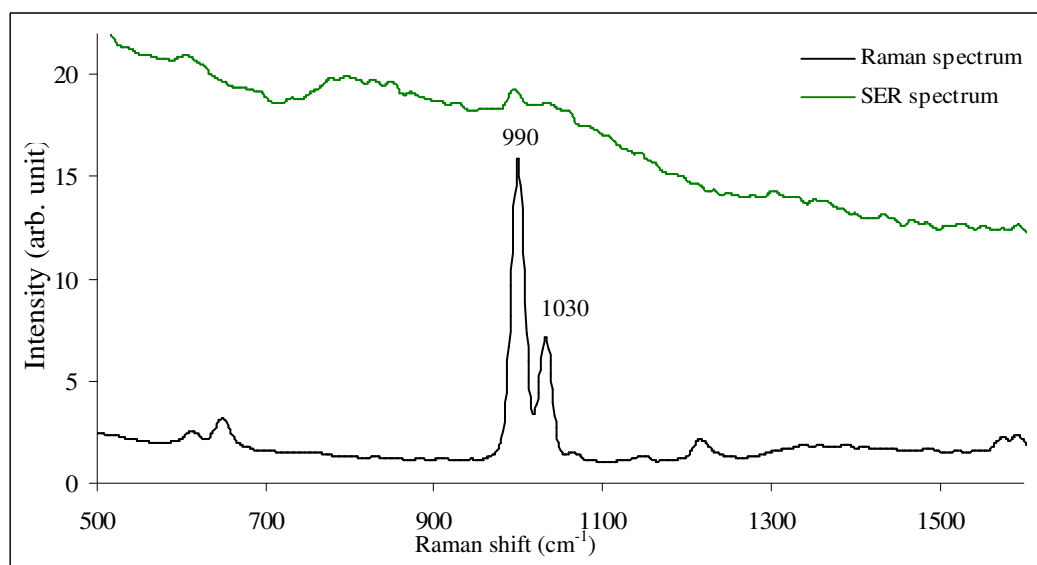


Figure 4 Normal Raman spectrum of pyridine and its SER spectrum recorded from a quartz-based surface having 80 nm high structures exposed to the vapour from pyridine for 10 seconds.  $t_i = 10$  seconds.

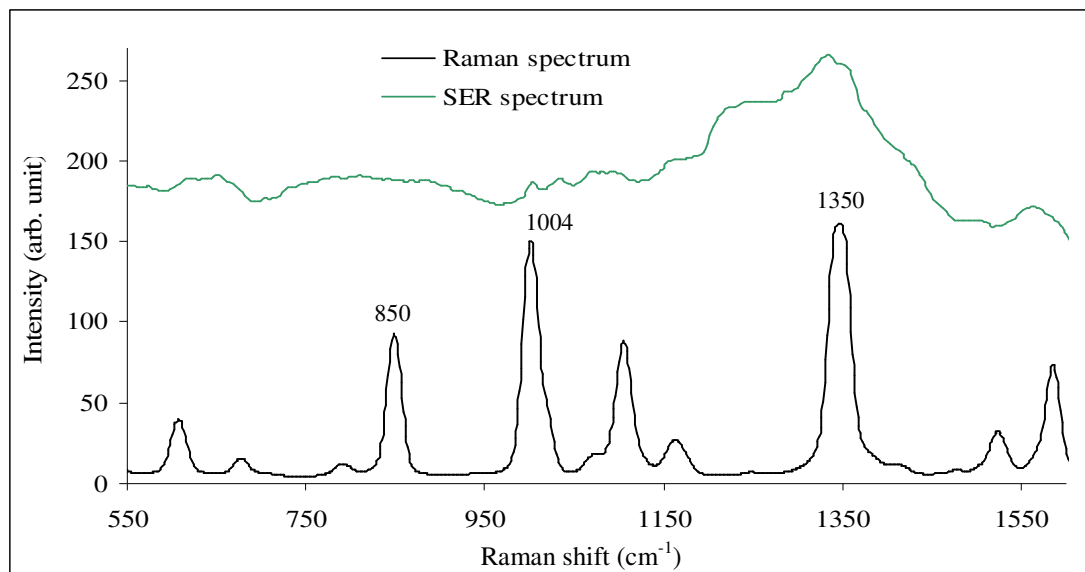


Figure 5 Raman spectrum of nitrobenzene and its SER spectrum from a quartz-based surface with 250 nm structure height exposed to headspace vapour for 60 seconds recorded with Renishaw Raman Microscope.  $t_i = 2$  seconds and 100 accumulations.

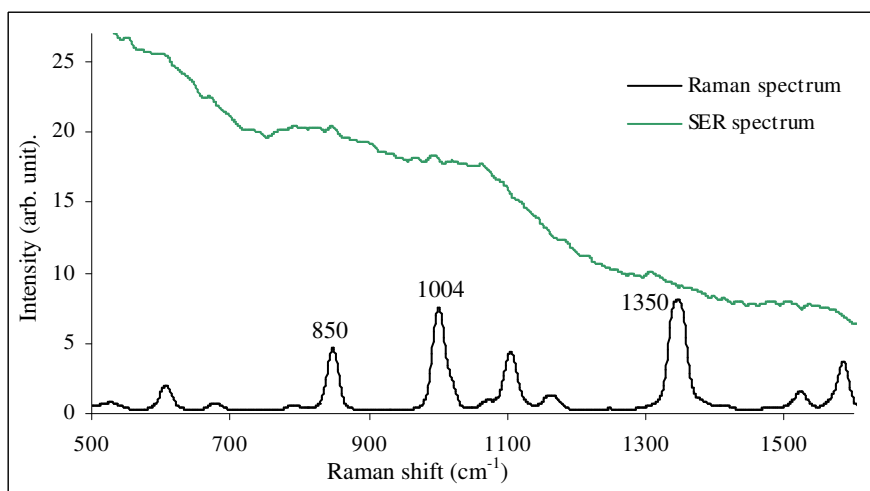


Figure 6 Raman spectrum of nitrobenzene and its SER spectrum from a quartz-based surface having 50 nm structure height exposed to headspace vapour for 20 seconds. Recorded with R3000 with  $t_i = 10$  seconds.



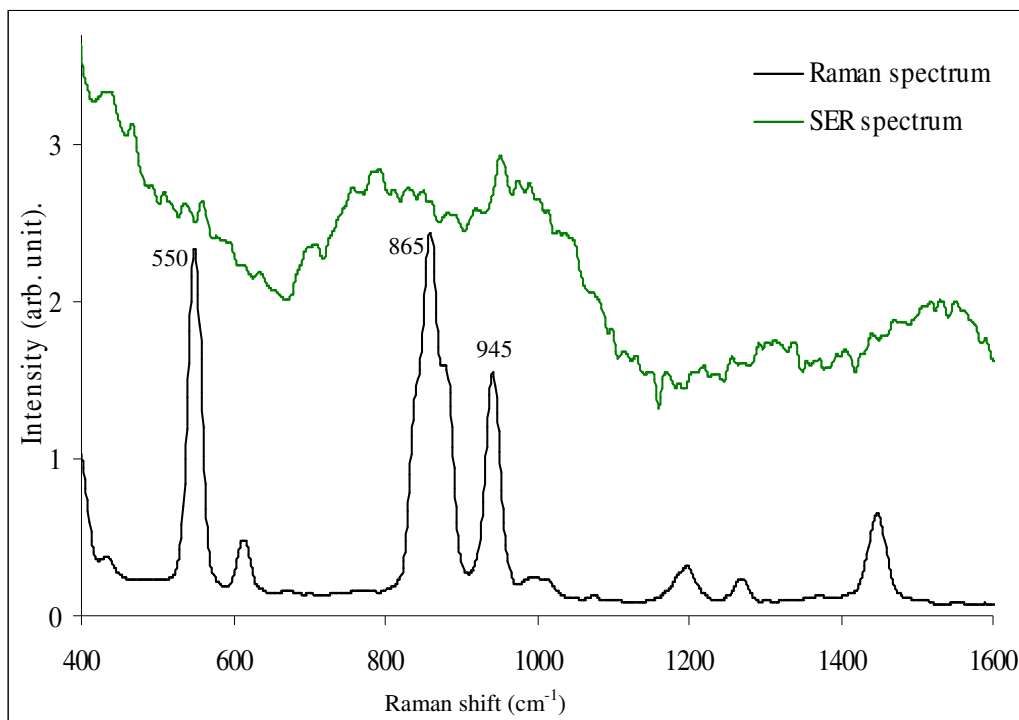


Figure 7 Normal Raman spectrum of TATP and its SER spectrum recorded from a quartz-based surface prepared with 200 nm of sputtered silver layer exposed to the headspace vapour.

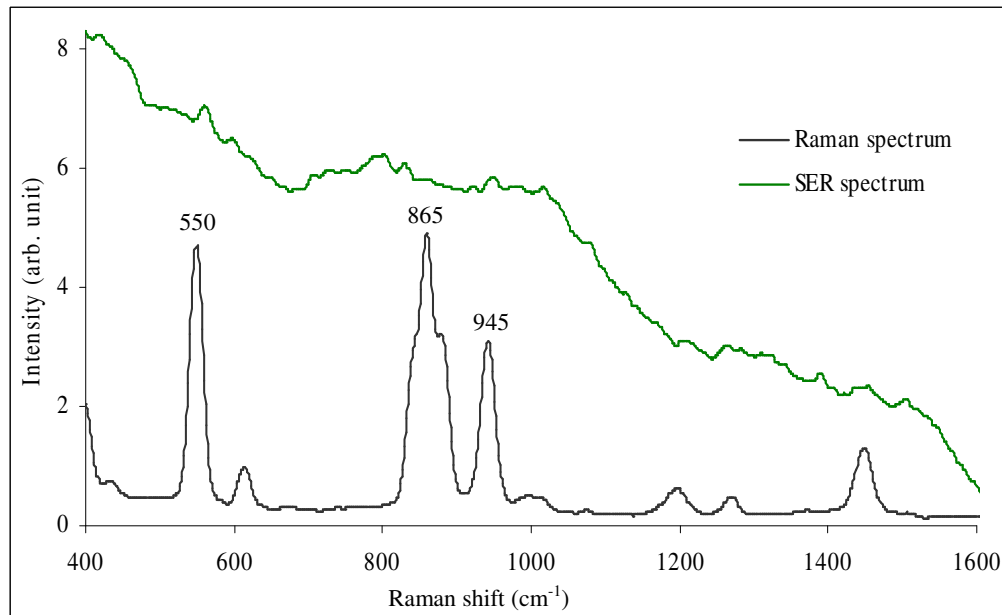


Figure 8 Normal Raman spectrum of TATP and its SER spectrum recorded from a quartz-based surface prepared with 70 nm of sputtered silver layer exposed to the headspace vapour.  $t_i = 10$  seconds.

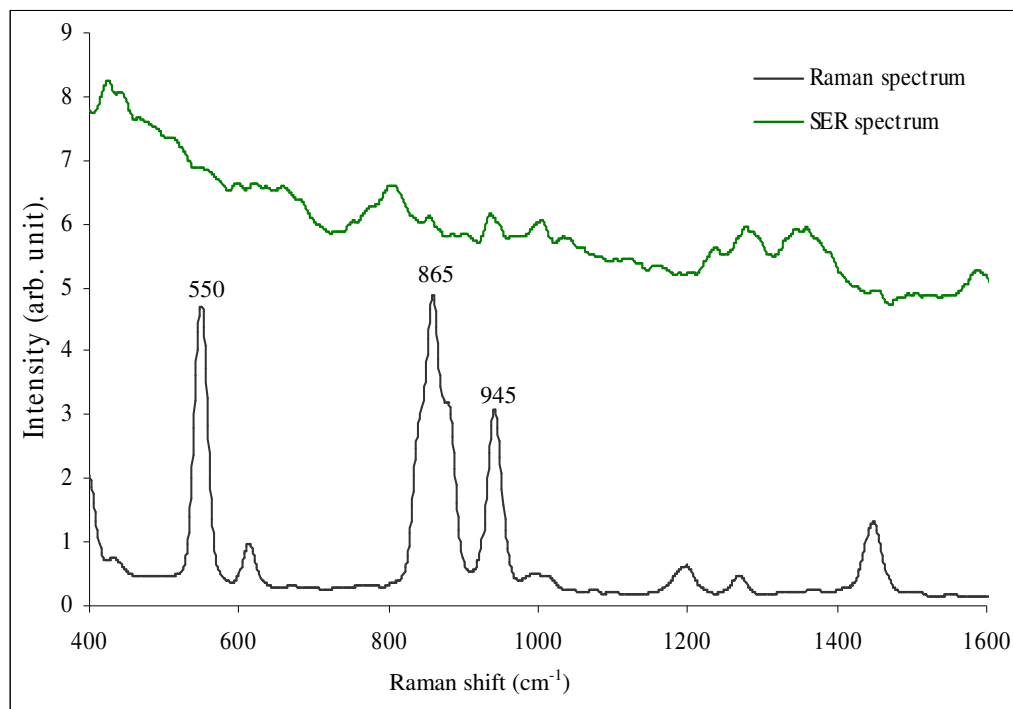


Figure 9 Normal Raman spectrum of TATP and its SER spectrum recorded from a quartz-based surface prepared with 50 nm of sputtered silver layer exposed to the headspace vapour.  $t_i = 5$  seconds.

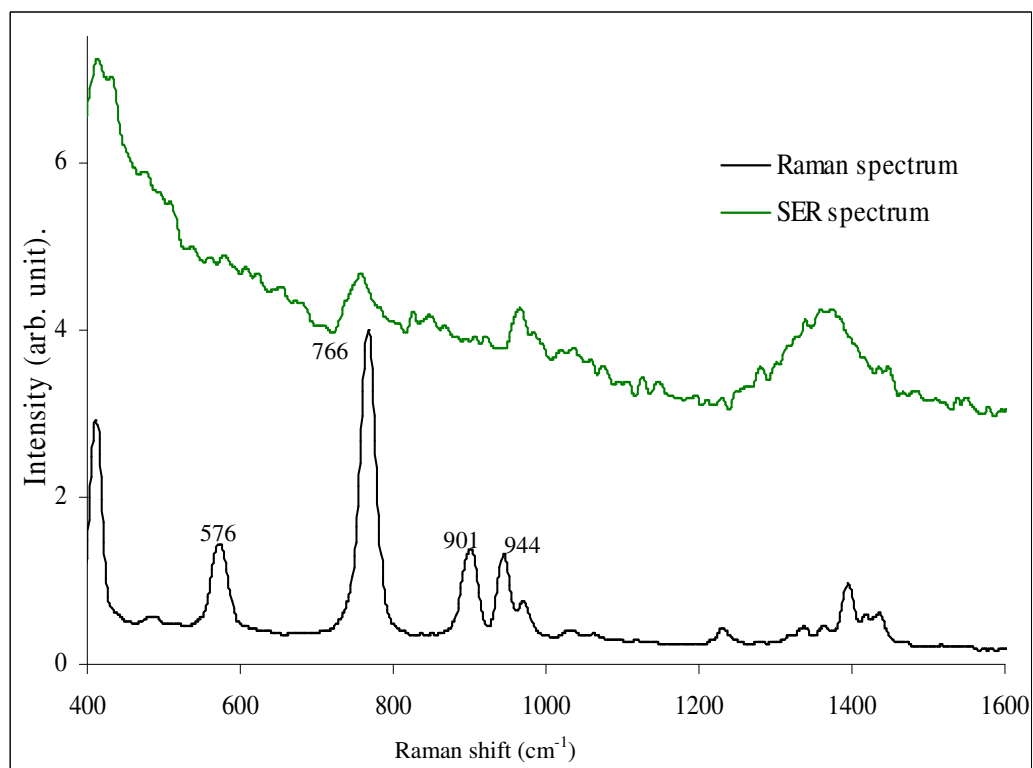


Figure 10 Normal Raman of HMTD and its SER spectra recorded from a quartz-based surface with 250 nm silver structural height exposed to the headspace vapour of.  $t_i = 10$  seconds.

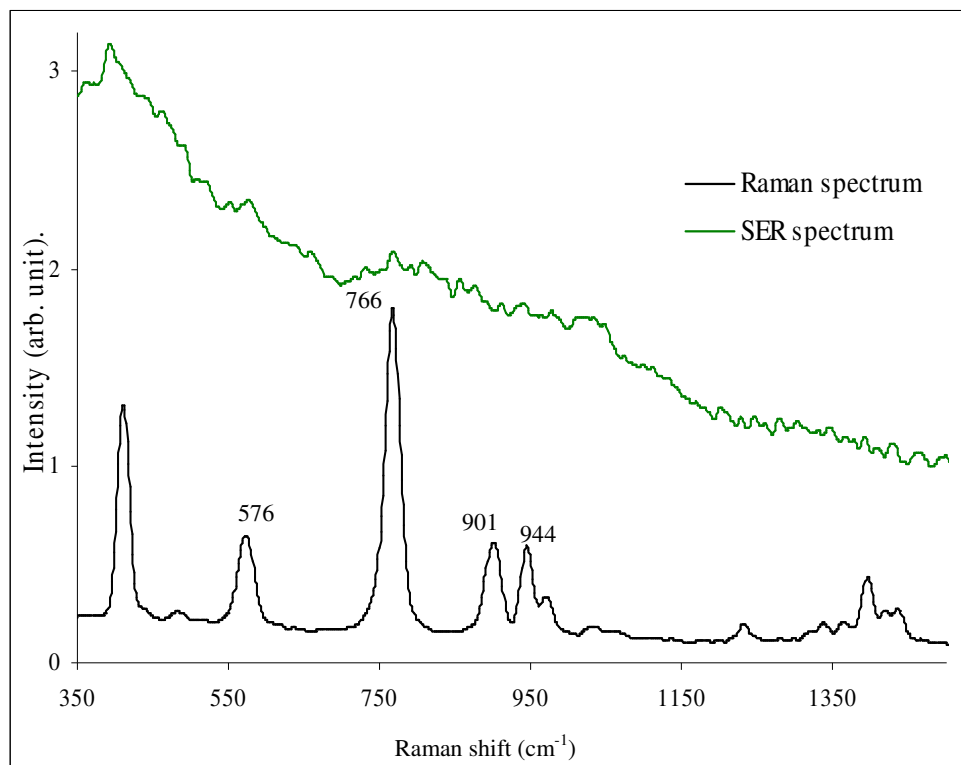


Figure 11 Normal Raman of HMTD and its SER spectra recorded from a quartz-based surface with 225 nm silver structural height exposed to the headspace vapour of.  $t_i = 10$  seconds.

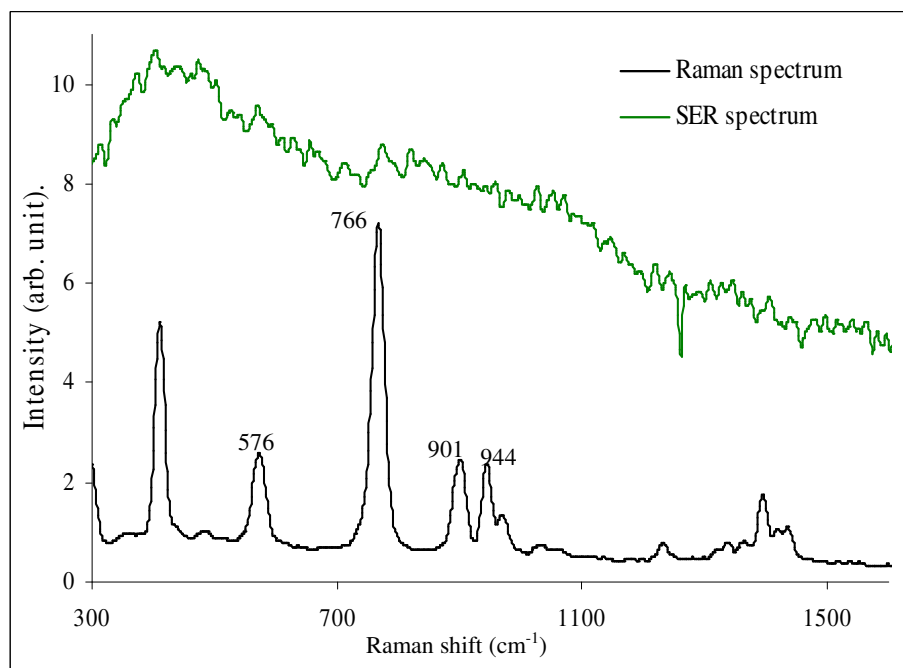


Figure 12 Normal Raman of HMTD and its SER spectra recorded from a quartz-based surface with 100 nm silver structural height exposed to the headspace vapour of.  $t_i = 10$  seconds.

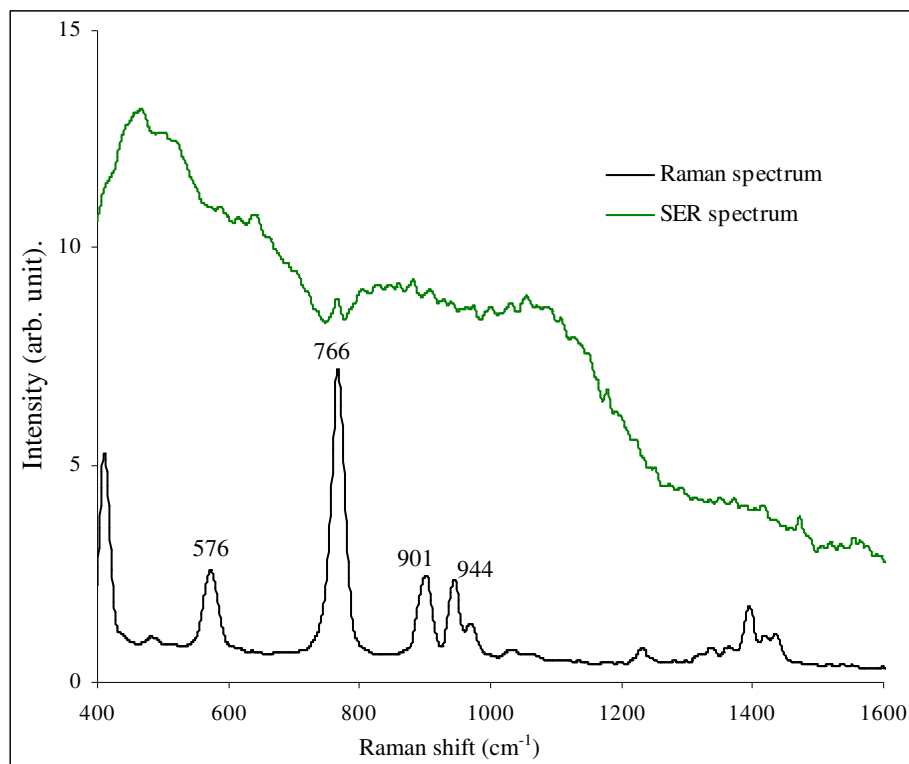


Figure 13 Normal Raman of HMTD and its SER spectra recorded from a quartz-based surface with 70 nm silver structural height exposed to the headspace vapour of.  $t_1 = 10$  seconds.

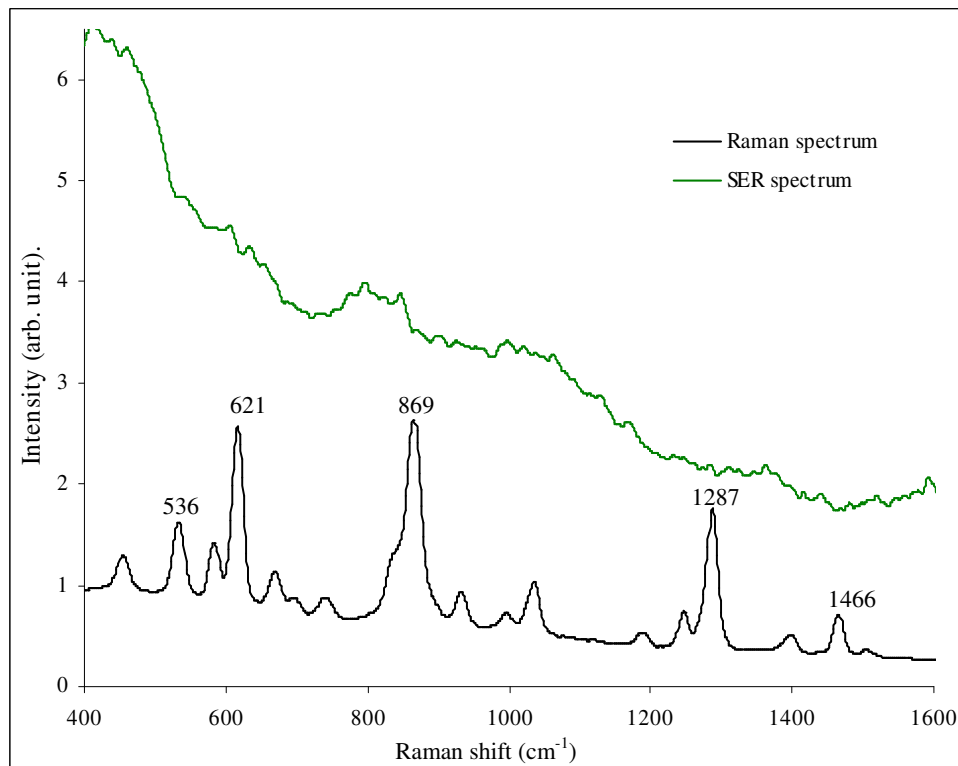


Figure 14 Normal Raman spectrum of solid PETN and its SER spectrum recorded from a quartz-based surface having 250 nm silver structural height, exposed to the headspace vapour.  $t_1 = 10$  seconds.

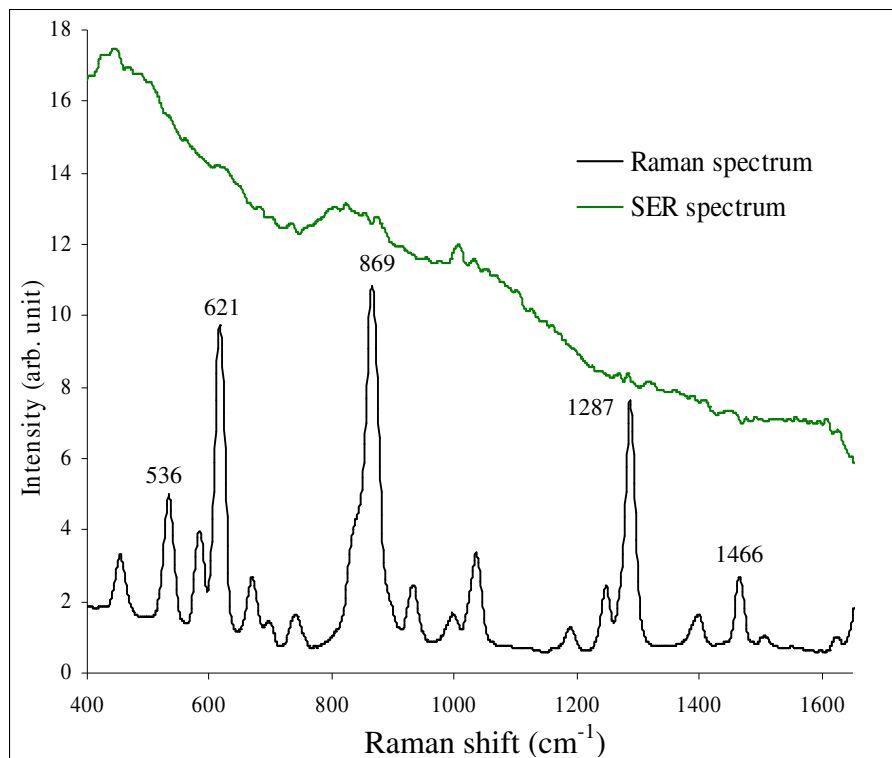


Figure 15 Normal Raman spectrum of solid PETN and its SER spectrum recorded from a quartz-based surface having 225 nm silver structural height, exposed to the headspace vapour.  $t_i = 10$  seconds.

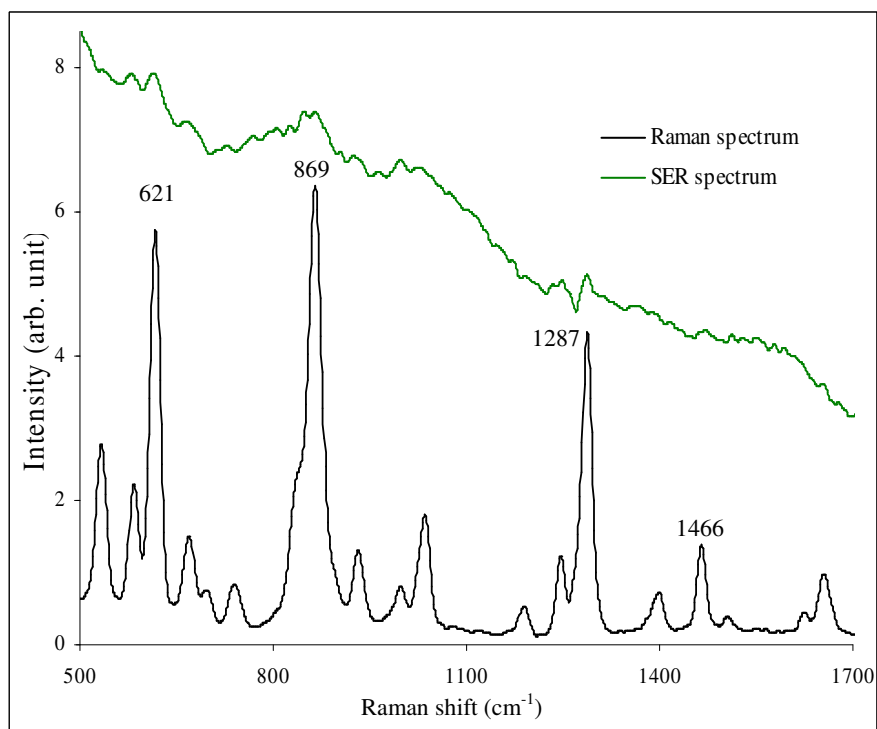


Figure 15 Normal Raman spectrum of solid PETN and its SER spectrum recorded from a quartz-based surface having 80 nm silver structural height, exposed to the headspace vapour.  $t_i = 10$  seconds